Ultrafast Photoisomerization Dynamics of Photochromic Molecular Switches Affected by Their Environment and Ultrafast Energy Transfer

Dissertation
in fulfilment of the requirements for the degree
Dr. rer. nat.
of the Faculty of Mathematics and Natural Sciences
at Kiel University

submitted by
Shuangqing Wang

Kiel, August 2018

First referee: Prof. Dr. Friedrich Temps
Second referee: Prof. Dr. Bernd Hartke

Date of the oral examination: September 21 2018
Approved for publication: September 21 2018

Declaration

I hereby declare that the content and design of the present Thesis is all my own work apart from my supervisor, Prof. Dr. Friedrich Temps' guidance. Parts of this Thesis have been published in scientific journals or submitted for publication. This refers to the following chapters:

Chapter 3
K. Röttger, S. Wang, F. Renth, J. Bahrenburg, and F. Temps, A femtosecond pump–probe spectrometer for dynamics in transmissive polymer films, *Appl. Phys. B*, 2015, **118**, 185 – 193.

Chapter 5
S. Wang, S. Schatz, M. C. Stuhldreier, H. Böhnke, J. Wiese, C. Schröder, T. Raeker, B. Hartke, J. K. Keppler, K. Schwarz, F. Renth, and F. Temps, Ultrafast dynamics of UV-excited *trans*- and *cis*-ferulic acid in aqueous solutions, *Phys. Chem. Chem. Phys.*, 2017, **19**, 30683 – 30694.

Chapter 6
S. Wang, M. Bohnsack, S. Megow, F. Renth, and F. Temps, Ultrafast electronic energy transfer in a benzimidazole–naphthopyran donor–acceptor dyad, *Phys. Chem. Chem. Phys.*, submitted (2018).

This Thesis has been prepared subject to the Rules of Good Scientific Practice of the German Research Foundation.

Shuangqing Wang

Kiel, August 2018

Abstract

The main goal of this Thesis is the investigation of the excited-state dynamics of photochromic molecular switches following photoexcitation in different molecular environments by static and femtosecond time-resolved transient absorption spectroscopy in combination with quantum-chemical calculations.

The time-resolved transient absorption spectroscopy on thin polymethylmethacrylate (PMMA) films doped with azobenzene (AB) derivatives called for an improved experimental setup and data collection strategy combined with a background subtraction scheme. For both isomers of ABs embedded into a thin polymer film, the initial excited-state dynamics of the photo-excited S_1 or S_2 states, i. e., ultrafast $S_2 \rightarrow S_1$ internal conversion in ≤ 1 ps upon S_2 excitation and the early evolution in the S_1 state, are essentially unchanged compared to solution. Conversely, the crucial subsequent slower dynamics in the S_1 state of the *E*-isomer, where a higher energy barrier has to be surmounted, is strongly affected by the embedding in the polymer matrix, shown by a six-fold increase of the excited-state lifetime. The vibrational cooling in the electronic ground state of the ABs is slowed down moderately by a factor of ~ 2 in the polymer film. The observed permanent absorption changes characterized by photo-product signatures provide unambiguous evidence for a successful photoisomerization.

In the neutral, anionic and dianionic forms of *trans*- and *cis*-ferulic acid (FA) in aqueous solution, the initial photoexcitation populates the first $^1\pi\pi^*$ electronic state. For the dianionic *cis*-isomer cFA^{2-}, electronic deactivation takes place with a time constant of only 1.4 ps, whereas in the other isomers, excited-state deactivation happens more than ten times slower on a time scale of ~ 20 ps. Considering these time scales, a barrierless excited-state pathway likely exists only in the case of cFA^{2-}, where the observed formation of the isomerisation photoproduct tFA^{2-} provides clear evidence for a $cis \rightleftarrows trans$ isomerisation. Given the longer excited-state lifetimes of the other isomers, reaction pathways with an excited-state energy barrier are taken, presumably along the same reaction coordinate.

The second goal of this Thesis was the spectroscopic investigation of the ultrafast electronic energy transfer (EET) of a donor–acceptor dyad composed of 1-propyl-2-pyridinyl-benzimidazole (PPBI) as donor linked to 3,3-diphenyl-[3*H*]-naphtho[2,1-b]pyran (DPNP) as acceptor. Global data analysis based on the singular value decomposition method of the measured transient absorption spectra of the dyad and its two building blocks allowed us to determine a value for the timescale of the EET process from the PPBI*–DPNP donor-excited state to the PPBI–DPNP* acceptor-excited state in the dyad with a time constant of $\tau = 2.84 \pm 0.70$ ps. For comparison, Förster theory predicts characteristic FRET times between $1.2 \text{ ps} \leq \tau \leq 4.2$ ps, in good agreement with the experimental result.

Zusammenfassung

Das Hauptziel dieser Arbeit ist die Untersuchung der Dynamik photochromer molekularer Schalter in elektronisch angeregten Zuständen nach Lichtanregung in unterschiedlichen molekularen Umgebungen mittels statischer und femtosekunden-zeitaufgelöster transienter Absorptionsspektroskopie in Kombination mit quantenchemischen Rechnungen.

Die Anwendung von zeitaufgelöster transienter Absorptionsspektroskopie für dünne Polymethylmethacrylat- (PMMA-)Filmschichten dotiert mit Azobenzol- (AB-)Derivaten machte die Verbesserung des experimentellen Aufbaus und der Datenerfassung in Verbindung mit Hintergrundsubtraktion erforderlich. Die Dynamik beider AB-Isomere innerhalb des dünnen Polymerfilms kurz nach Anregung der S_1- oder S_2-Zustände, d.h. ultraschnelle $S_2 \rightarrow S_1$ interne Konversion innerhalb von ≤ 1 ps nach S_2-Anregung sowie die frühe Zeitentwicklung im S_1-Zustand, sind im Vergleich zur Dynamik in Lösung nahezu unverändert. Im Gegensatz dazu ist die relevante spätere Zeitentwicklung im S_1-Zustand des *E*-Isomers, bei dem eine höhere energetische Barriere überwunden werden muss, stark von der Einbettung in die Polymermatrix beeinflusst, was durch eine Versechsfachung der Lebensdauer des angeregten Zustands deutlich wird. Die Schwingungsabkühlung im elektronischen Grundzustand der AB-Isomere im Polymerfilm ist nur gering um einen Faktor ~ 2 verlangsamt. Die beobachtete, dauerhafte Änderung der Absorption, gekennzeichnet durch die charakteristische Absorption des Photoprodukts, belegt zweifelsfrei die vollstände Photoisomerisierung.

Im Fall der neutralen, anionischen und di-anionischen Formen der *trans*- and *cis*-Ferulasäure (ferulic acid, FA) wird durch die Photoanregung der erste $^1\pi\pi^*$-Zustand angeregt. Beim dianionischen *cis*-isomer cFA^{2-} findet die elektronische Deaktivierung mit einer Zeitkonstante von nur 1.4 ps statt, während dieser Vorgang bei den anderen Isomeren zehnmal langsamer innerhalb von ~ 20 ps stattfindet. Unter Berücksichtigung dieser Zeitskalen lässt sich ein barrierefreier Deaktivierungs-Reaktionspfad nur im Fall von cFA^{2-} nachweisen, bei dem die Bildung des Isomerisierungs-Photoproduktes tFA^{2-} einen klaren Beleg für die *cis* $\rightleftarrows$ *trans* Isomerisierung liefert. Bei den anderen Isomeren werden vermutlich Reaktionswege eingeschlagen, die über eine energetische Barriere führen, wobei es sich jedoch wahrscheinlich um dieselbe Reaktionskoordinate handelt.

Ein weiteres Ziel dieser Arbeit besteht in der spektroskopischen Untersuchung des ultraschnellen elektronischen Energietransfers (electronic energy transfer, EET) einer Donor–Akzeptor-Dyade bestehend aus 1-Propyl-2-pyridinyl-benzimidazol (PPBI) als Donor, verbunden mit 3,3-Diphenyl-[3*H*]-naphtho[2,1-b]pyran (DPNP) als Akzeptor. Für die Zeitskala des EET-Prozesses vom PPBI*–DPNP Donor-Zustands zum PPBI–DPNP* Akzeptor-Zustands der Dyade und ihrer beiden Bestandteile konnte durch globale Datenanalyse mittels Singulärwertzerlegung der gemessenen transienten Absorptionsspektren eine Zeitkonstante von $\tau = 2.84 \pm 0.70$ ps bestimmt werden. Zum Vergleich sagt die Förster-Theorie eine charakteristische FRET-Zeit zwischen $1.2 \text{ ps} \leq \tau \leq 4.2$ ps vorher, was sich in guter Übereinstimmung mit dem experimentell bestimmten Wert befindet.

Contents

Chapter 1

Introduction

Molecular switches which show a strong response to chemical and physical stimuli are of great importance in order to achieve high functionality on a molecular level. Numerous families of molecular switches have been developed and investigated over the past six decades, and their unique properties offer promising perspectives for new functional materials and in life sciences. Molecular photoswitches, in particular, have attracted increasing interest in recent years because of their potential applications, e.g., in light-driven molecular machines,[1–5] in optical data storage,[6–9] in biomedical superresolution imaging beyond the diffraction limit,[10–13] and in sunscreen materials to attenuate the biologically harmful UV-A (400 – 315 nm) and UV-B (315 – 280 nm) components of sunlight.[14,15]

Photochromic molecular switches are a class of chemical systems that can be reversibly transformed between two or more forms by electromagnetic radiation. When irradiated with ultraviolet (UV) or visible (VIS) light, photochromic compounds undergo a reversible change between these molecular structures with distinct absorption changes in the UV and VIS spectral regions. In most instances, the photo-induced interconversion of one state of a photochromic compound into another is accompanied by significant changes in their structural and electronic properties, in the dipole moment, in conductivity, in the magnetic state or in the acidity of the molecule. Typically, one isomer is thermodynamically stable, while the thermal lifetime of the other depends strongly on the respective system and its surrounding. A good photoswitch features low photochemical fatigue, usually high thermal stability and well separated absorption bands for both species, as well as high quantum yields for the photoswitching process. The changes in both electronic and geometrical structure can be adopted in various significant modifications of macroscopic properties and thus translated into macroscale applications: for example the changes in electronic structure can be applied to optical memory media and photoswitching devices, while the changes in geometrical structure can potentially be applied to light-driven actuators.[16–20]

Fig. 1.1 depicts the isomerization reactions of several important classes of photochromic compounds, namely ferulic acid, azobenzene, naphthopyran, fulgide/fulgimide, and diarylethene. Photochromic compounds are divided into two types: the photo-generated isomers shown on the right-hand side of Fig. 1.1 which revert to the initial state by light are defined as P types (i.e. fulgide/fulgimide and diarylethene), whereas those that revert thermally are classified as T types (i.e. azobenzene and naphthopyran).[21] The respective chemical transformations include *E/Z*-isomerization of the double bond (C=C in ferulic

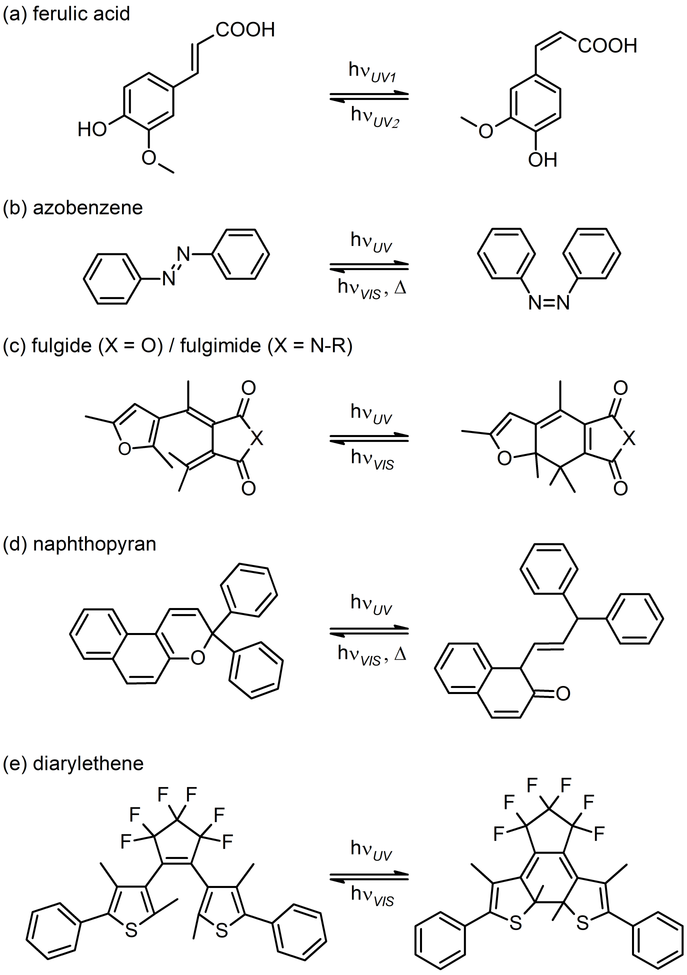

Fig. 1.1 The photoinduced (UV or VIS) and thermal (Δ) transformations of some representative photochromic switches.

acid and N=N in azobenzene), electrocyclic ring opening to the merocyanine form (naphthpyrane), and electrocyclic ring closure of the hexatriene backbone to cyclohexadiene (fulgide/fulgimide and diarylethene). The particular photochemical properties and possible applications of these representative molecules shall be explained in more details in the following:

Ferulic acid (FA, Fig. 1.1a) is a hydroxycinnamic acid derivative that can undergo *E/Z* isomerization about the C=C double bond which is a common photochemical reaction. Because of its fundamental relevance in many biological processes, for example in stilbene or in the photoisomerization of retinal rhodopsin, the *E/Z* isomerization about the central ethylenic double bond was studied extensively.[22,23] FA derivatives are a well-known family of natural compounds primarily present in the free form in seeds and leaves, and thus humans

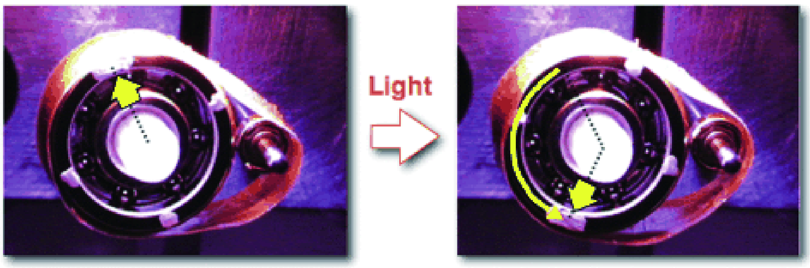

Fig. 1.2 A light-driven motor device actuated by an azobenzene-containing liquid crystalline elastomer (LCE) plastic belt. The belt was a laminated film composed of a LCE film layer connected at both ends, prepared by photopolymerization of a mixture of azobenzene-functionalized monomers, and a flexible polyethylene plastic sheet. Adapted with permission from Yamada, M.; Kondo, M.; Mamiya, J.; Yu, Y.; Kinoshita, M.; Barrett, C. J.; Ikeda, T. *Angew. Chem. Int. Ed.,* **2008**, 47, 4986 – 4988. Copyright (2008) John Wiley and Sons.

absorb a considerable amount of them daily.[24–27] Both isomers are found in plants,[28,29] although the *trans*-isomer predominates. FA is an abundant dietary antioxidant which may offer beneficial effects against cancer, cardiovascular disease, diabetes, and Alzheimer's disease.[30–33] Pharmacokinetic and dietary intake studies[30,31] demonstrated that FA may serve an important antioxidant function in preserving the physiological integrity of cells exposed to both air and impinging UV radiation.[32]

Both the E and Z isomers of FA feature strong absorptions in the UV-A (400 – 315 nm) and UV-B (315 – 280 nm), which are the harmful wavelength regions of the solar spectrum. This property leads to the application of FA as a natural constituent in commercial sunscreens.[28,30,32,34–40] Sunscreens are mainly designed to attenuate the UV-A and UV-B components of the sunlight, in order to reduce the probability of skin cancers like melanoma or squamous cell carcinoma.[41,42] Thus, one of the fundamental photophysical demands for sunscreen molecules used in such photo-protective capacities is a high UV absorption cross section in the critical spectral regions. The other key requirement is a high internal conversion (IC) efficiency following UV photo-excition: The UV-induced electronic excitation energy has to be dissipated without loss of the integrity of the sunscreen molecules *via* one or more non-destructive pathways. FA is one of the most effective molecular constituents currently used in commercial sunscreens because it meets all requirements: strong absorption of UV-A and UV-B light, superior photo-stability,[43,44] efficient ultrafast molecular electronic deactivation, and selective excited-state dynamics on the femto- to picosecond time scale.[37,39]

Azobenzenes (ABs, Fig. 1.1b) form one of the most investigated class of photoswitches. Upon UV irradiation, the thermodynamically favored E isomer converts to the energetically higher-lying *Z* isomer. The back reaction can occur spontaneously in the dark or be photo-induced by VIS light. The isomerization induces not only a large geometrical structural change but also a change in dipole moment.[45] Furthermore, ABs feature extraordinary high photo-stabilities over many switching cycles without showing photochemical fatigue. All these properties make them promising candidates for molecular switches or machines.[17,46–50] A first light-driven plastic motor (Fig. 1.2) was developed by Ikeda and co-workers,[3] which can convert light energy directly into a continuous mechanical rotation without the aid of batteries or electrical connections. The azobenzene-containing liquid crystalline elastomers (LCEs) acting as rotational belt on the pulley system have the potential to show mechanical movement induced by light. By irradiating the belt simultaneously with UV light from the right and VIS light from the left, the pulley could be driven in a counter-clockwise direction. These systems have the potential to drive miniaturized systems such as micro- and nanorobots.

A photoswitching mechanism different to *E/Z* isomerization is displayed by fulgides and fulgimides (Fig. 1.1c), which are based on 1,3-cyclohexadiene (CHD). These molecules undergo an electrocyclic ring-opening reaction in the excited state to form a 1,3,5-hexatriene photo-product, which can also be exploited to implement photochromic transformations. Additionally, due to the arrangement of the phenylic or heterocyclic groups around the hexatriene moiety, the open isomers of fulgides/fulgimides posses an additional *E/Z* isomerization reaction pathway about the hexatriene double bonds. Fulgides exhibit a relatively large spectral separation of the open and closed isomers: the open isomers absorb in the near-UV at about 340 nm, whereas the closed isomers show absorption in the VIS range at about $400-450$ nm due to the rich-electron induced bathochromical shift. Furthermore, they stand out for their thermal irreversibility, excellent photo-stability, and high fatigue resistance.[51] Liang *et al.* developed an optical storage device composed of a photochromic N-(4-aminophenyl)fulgimide and a fluorescent oxazine as shown in Fig. 1.3. Information is stored by irradiating the photochromic component with light at 530 nm wavelength to convert the polar closed form to the open non-polar form of the molecule. The information can be accessed by excitation of the fluorescent moiety at 650 nm to cause fluorescence at 700 nm.

The molecular structure of $3H$-naphthopyran (Fig. 1.1d) instantaneously changes upon UV light irradiation: the heterolytic cleavage of the C(sp^3)-O bond of the pyran ring in the closed ring form (CF, the initial colorless form) is promoted by UV light and results in two colored merocyanine isomers, denoted as *trans-cis* (TC) and *trans-trans* (TT).[52,53] The open forms are colored due to the extended conjugation connecting the naphthalene and the phenyl ring. The two photoisomers reversibly revert back with different rates to the initial colorless

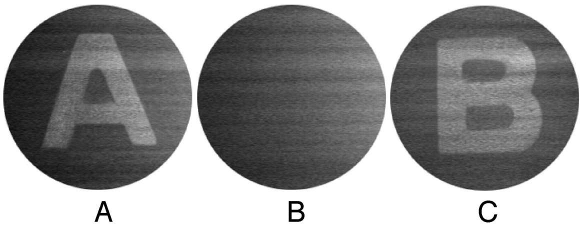

Fig. 1.3 A polymethyl methacrylate (PMMA) film doped with an optical storage molecule composed of a photochromic fulgimide and a fluorescent oxazine. (A) Written image. The polar closed form of fulgimide is illuminated with 530 nm light, which converts it to the open non-polar form. The information is read by excitation at the 650 nm band of the oxazine dye component, causing fluorescence at 700 nm. (B) Erased image. Irradiation below 400 nm converts the open form of the fulgimide moiety to the closed, polar structure. (C) Rewritten image. Adapted with permission from Liang, Y. C.; Dvornikov, A. S.; Rentzepis, P. M. *PNAS* **2003**, 100, 8109 – 8112, Copyright (2003) National Academy of Sciences.

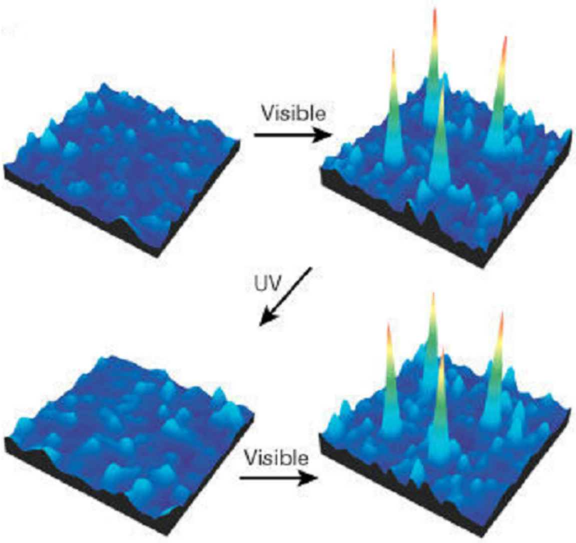

Fig. 1.4 Fluorescence images of the open- and closed-ring forms of single-molecule photoswitches. In this molecule, a photochromic diarylethene derivative is linked to a fluorescent anthracene derivative through an adamantyl spacer. Fluorescence images: top left, before irradiation; top right, after irradiation with visible light 488 nm (deactivating energy acceptors); bottom left, after irradiation with weak ultraviolet light 325 nm (activating energy acceptors); bottom right, after irradiation with visible light for 488 nm. Adapted with permission from Irie, M.; Fukaminato, T.; Sasaki, T; Tamai, N.; Kawai, T. *Nature* **2002**, 420, 759. Copyright (2002) Springer Nature.

closed isomer. While the TC isomer fades quickly (in a few seconds to minutes) to the CF, the TT is converted slowly (in minutes to hours) initially first into the TC isomer. Furthermore, Sallenave *et al.* studied a series of naphthopyran derivatives using NMR methods and found that the ring-closing of the TT form is an unfavoured thermal process, whereas it can revert back very efficiently under irradiation with VIS light.[54] The TT isomer is thermally stable and must overcome a relatively large activation energy barrier to isomerize to the TC form, so it is responsible for the slow thermal response of the system and for the persistent residual color. Among T-type compounds, naphthopyrans are the most widely commercially used photochromic systems, for example in ophthalmic lenses and glasses because they can be easily synthesized at a relatively low cost and are very sensitive to sunlight.[55] Naphthopyran currently attracts great interest because of the breadth of colors generated, the transparency of the closed form, the fine control over the fading kinetics, the good thermal reversibility, and the excellent resistance to photochemical fatigue.[54–58]

Diarylethene derivatives with heterocyclic aryl groups belong to the thermally irreversible (P-type) photochromic compounds. Both closed and open isomers show excellent stabilities for more than a thousand years at 30 °C and can withstand repeated photo-induced coloration/decoloration cycles for more than 10^5 times.[59,60] The quantum yield for coloration is close to unity (i.e. 100 %). Many diarylethene derivatives undergo photochromism even in the single-crystalline phase. The thermal irreversibility of diarylethene is indispensable for the application in optical memories and switches.[18,59,61–66] Based on the mechanism of fluorescence resonance energy transfer (FRET), Irie *et al.*[13] developed a photoswitch (Fig. 1.4), in which a photochromic diarylethene derivative is linked to a fluorescent anthracene derivative through an adamantyl bridge. The fluorescence of this compound embedded in a polymer film can be modulated by irradiation with UV and VIS light at the single-molecule level. Photoreversible fluorescence switching largely contributed to the advances in super-resolution imaging and the application in the design of erasable media for ultrahigh-density optical data storage.[65,67–71]

The selected photochromic molecules presented above feature excellent photochemical and photophysical properties and have been successfully exploited as photoswitchable building blocks in various applications. These promising examples encourage further investigations with respect to not only the fundamental mechanisms, but also real-life applications.

The main focus of this Thesis lies on the investigation of the influence of different environments on the properties of some selected photoswitches. For that, ultrafast spectroscopic techniques were used to study the photodynamics of (i) ABs embedded into polymer matrices, (ii) FA in aqueous solutions of different pH values, and (iii) naphthopyran attached covalently to an excitation energy donor. In the following, an overview of the environmental influences on the photoswitching behaviours of the three families of photochromic molecules is given, followed by a more detailed summary of former works, both experimentally and theoretically, on the ultrafast isomerization dynamics and their applications in extended fields.

Following the Introduction, the applied Experimental methods will be described. In the following Results part, two AB derivatives, 4-[*N*-ethyl-*N*(2-hydroxyethyl)amino]-4′-nitro-azobenzene (Disperse Red 1, DR1, in Chapter 3) and 4-hexyl-4′-(1-propylbutoxy)azobenzene (**1E** and **1Z**, in Chapter 4), are investigated under close to real-life applications. In this case, to obtain detailed mechanistic insight into the fundamental processes on the femtosecond to picosecond time scale, femtosecond time-resolved studies of the photo-induced dynamics and chemical transformations of photo-excited molecular switches embedded in thin polymer films used for applications are mandatory.[48,72–74] The fundamental investigation of the influence of steric restraints on the photoswitching behavior of chromophores could shed light on the rational design of functional photosensitive systems and devices with new properties and improved performance.

The second part of this Thesis focuses on the ultrafast deactivation dynamics of FA in aqueous solution with different pH values from pH $=$ 1.2 to 10.4 (Chapter 5). Both *trans*- and *cis*-ferulic acid with three protonation forms (neutral, anionic and dianionic) in buffered aqueous solutions were investigated by a combination of time-resolved studies and density functional theory (DFT) theoretical calculations.

In the third part, the photochromic molecule naphthopyran acting as an energy acceptor in a dyad was investigated (Chapter 6). After electronic excitation energy is transfered from the donor propyl-pyridylbenzimidazole (PPBI) to the acceptor diphenyl-naphthopyran (DPNP), and the isomerization reaction occurs following the indirect excitation. Special attention is paid to the ultrafast energy transfer process in the dyad by means of femtosecond transient absorption spectroscopy and quantum-chemical calculations.

1.1 Photochemistry of azobenzenes

The photo-induced *E/Z* isomerization of ABs is a well-known unimolecular reaction. ABs can undergo a large and reversible structural change under irradiation with UV/VIS light, transforming between the *E*-isomer and the *Z*-isomer. Thermal $Z \rightarrow E$ back-reaction occurs spontaneously in the dark (see Fig. 1.5).

The static absorption spectrum of *E*-AB (Fig. 1.6, left)[75] consists of two distinct bands: a strong $\pi\pi^*$ transition band in the UV at about 360 nm, and a weak $n\pi^*$ absorption band in the VIS region centered at 480 nm. In contrast to the spectrum of *E*-AB, the *Z*-isomer

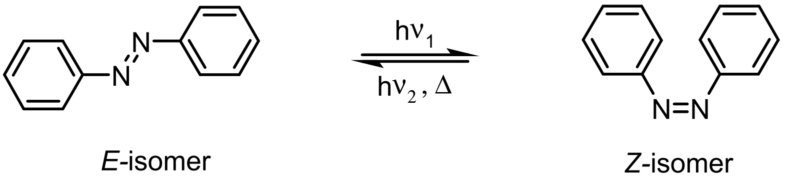

Fig. 1.5 UV-photoinduced *E*-*Z* isomerization and the VIS-photoinduced or thermal *Z*-*E* back-isomerization of AB.

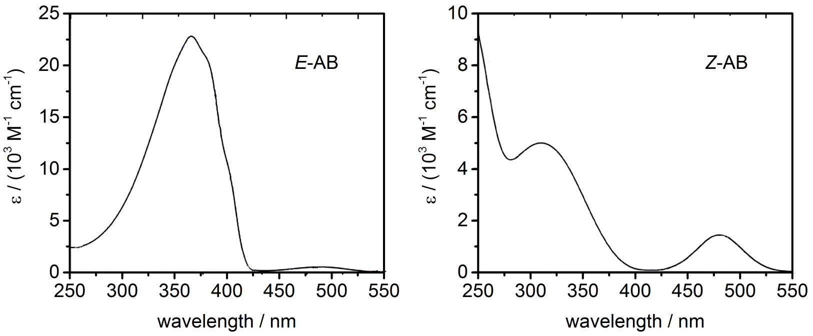

Fig. 1.6 Static UV/VIS spectrum of *E*-AB (left) and *Z*-AB (right) in methanol at 35 °C. Adapted from Ref. [75] with permission from the European Society for Photobiology, the European Photochemistry Association, and The Royal Society of Chemistry.

absorption spectrum features a weaker $\pi\pi^*$ transition at 310 nm, but stronger $n\pi^*$ transition at 480 nm.

The AB isomerization mechanism and quantum yields have been the subject of interest and controversy for decades. While the modification of the quantum yields for isomerization is more important than knowing the isomerization mechanism in practical applications, both properties depend on the isomerization pathway. Steady-state measurements have found that the *E/Z* isomerization quantum yields differ for excitation of the $n\pi^*$ and $\pi\pi^*$ transitions by a factor of two in violation of Kasha's rule, indicating multiple pathways for *E/Z* isomerization.[76,77] A dual mechanism, namely an inversion path for $n\pi^*$ excitation and a torsion path for $\pi\pi^*$ excitation, was proposed to explain observations that the excited AB molecules in the $\pi\pi^*$ state cannot completely reach the state directly populated by $n\pi^*$ excitation. Three possible proposed isomerization mechanisms for AB are sketched in Fig. 1.7. First, the isomerization can occur *via* torsion about the central double bond.[78] Second is the inversion of the phenyl rings moving towards each other in a plane configuration,[79] while the third is the so-called hula-twist mechanism which can be imagined as a pedal-like concerted movement of the nitrogens and phenyls.[80–86] Numerous quantum chemical calculations were

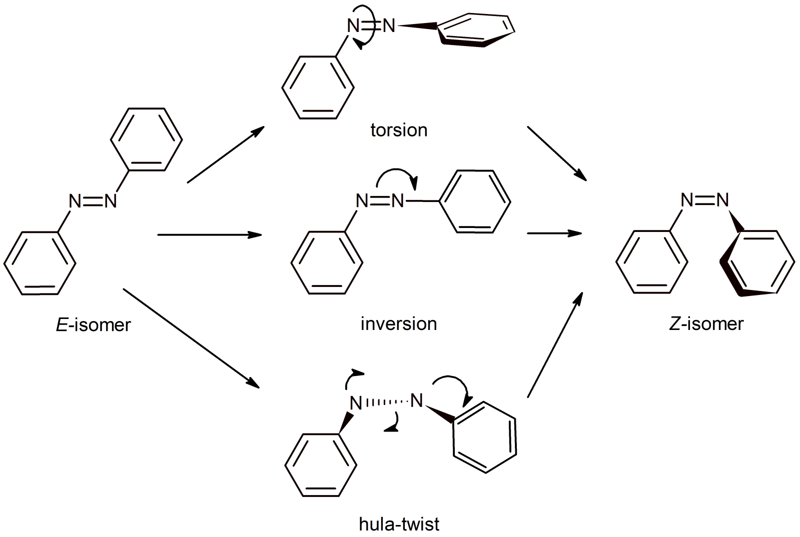

Fig. 1.7 Schematic overview of the mechanisms for the *E/Z* isomerization of AB. Torsion about the central double bond (top); inversion in plane (middle); and hula-twist (pedal-like) concerted motion (bottom).

performed to shed light on the isomerization pathways of AB. Up to now, many studies indicate the concerted torsional pathway to be the most probable mechanism.[87–92]

In the context of the Thesis, the focus was not only on the isomerization mechanism, but also on the nature of the electronically excited states and the time constants of the deactivation dynamics after photo-excitation. A few time-resolved studies were performed on AB providing detailed insight into the controversial photoisomerization mechanisms. Lednev *et al.* investigated the excited-state dynamics of *E*-AB upon $\pi\pi^*$ excitation.[93–95] The resulting time constants of $\tau_1 = 0.2$ ps, $\tau_2 = 1$ ps, and $\tau_3 = 13$ ps were attributed to the decay from the S_2 state to the S_1 state, relaxation in the S_1 state to a local minimum intermediate species, and internal conversion from the intermediate S_1 state to S_0, respectively. Similar time constants were also observed by other experimental studies on the molecular dynamics of AB,[96–102] while their assignments were different. Satzger *et al.* studied the lifetimes of the excited states and relaxation dynamics of AB upon $n\pi^*$ excitation by transient fluorescence spectroscopy.[96] Upon $n\pi^*$ excitation of *E*-AB, the population escapes from the Franck-Condon (FC) region with $\tau_1 = 0.42$ ps. The population then reaches S_0 with a time constant of $\tau_2 = 2.9$ ps *via* a S_1/S_0 conical intersection (CI), where the isomerization occurs. Finally, a third time constant of $\tau_3 = 12$ ps obtained by transient absorption spectroscopy was ascribed to vibrational cooling in the electronic ground state.[101]

After $\pi\pi^*$ excitation of AB, the population created in the S_2 excited state relaxes to S_1 by internal conversion within an additional time constant of ≈ 100 fs. Afterwards, the

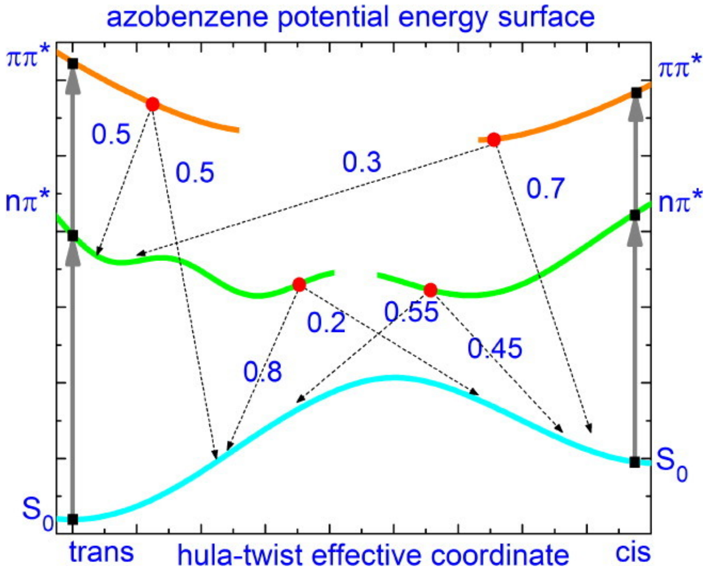

Fig. 1.8 Potential energy surfaces of AB along the hula-twist isomerization coordinate and schematic relaxation pathways for *E*- and *Z*-AB upon $n\pi^*$ (S_1) and $\pi\pi^*$ (S_2) excitation. Adapted with permission from Quick, M.; Dobryakov, A. L.; Gerecke, M.; Richter, C.; Berndt, F.; Ioffe, I. N.; Granovsky, A. A.; Mahrwald, R.; Ernsting, N. P.; Kovalenko, S. A. *J. Phys. Chem. B* **2014**, 118, 8756 – 8771. Copyright (2014) American Chemical Society.

molecule follows the same relaxation pathways as for $n\pi^*$ excitation.[97] These excited-state evolution pathways of AB became mostly accepted.[49] Tahara and coworkers reported that the fluorescence yields from the S_2 and S_1 states of AB were estimated to be nearly identical, indicating that no isomerization occurs in S_2 or during $S_2 \rightarrow S_1$ internal conversion.

Recent studies by Ernsting and coworkers on AB after $n\pi^*$ excitation reported the independence of the dynamics on solvent viscosity,[103] which is in contradiction to the results obtained by fluorescence anisotropy measurements of *E*-AB in solvents of different viscosity.[102] Fig. 1.8 sketches the potential energy surfaces of AB in solution as a function of the hula-twist coordinate and shows the relaxation/isomerization pathways. *E*-AB evolves upon $n\pi^*$ excitation from the FC region to a local minimum on the S_1 potential energy surface with $\tau_1 = 0.3$ ps, reaches a dark intermediate in $\tau_2 = 3$ ps, and finally relaxes to S_0 over a potential energy barrier with $\tau_3 = 16$ ps. Upon $n\pi^*$ excitation, *Z*-AB relaxes to S_1 barrierless with 0.1 ps and subsequently to S_0 with 1.1 ps. Upon $\pi\pi^*$ excitation of *E*-AB, relaxation proceeds *via* an S_n/S_1 CI within 0.1 ps; 50 % of the population reach S_1 and 50 % of the population experience cascade relaxation $S_2 \rightarrow S_1 \rightarrow S_0$ through a different S_1 region that is not accessible by the $n\pi^*$ excitation. For *Z*-AB upon $\pi\pi^*$ excitation, 30 % isomerize to the *E*-isomer *via* an S_n/S_1 CI, resulting in a mixed (*Z/E*) S_1 population. The other 70 %

experience cascade relaxation $S_n \rightarrow S_1 \rightarrow S_0$, mainly *via* an S_1 region not accessible by the $n\pi^*$ excitation.

Upon irradiation with UV/VIS light, AB features large changes both in electronic and geometrical structure, which provides the most promising potentials for applications. Consequently, many azobenzene-based applications in fundamental and technical sciences have been reported. Examples for the use of AB include the life sciences,[104–110] e.g., in biological systems, where light induces orientational changes of AB-functionalized peptides, or in optogenetics, where the function of biomolecules can be turned on and off by light *in vivo*.[111,112] Recently, Heinke *et al.* developed azobenzene-containing pillared-layer metal-organic frameworks (MOFs) that enable the remote-controlled release of guest molecules.[113,114] ABs have also been exploited for optical data storage or in light-driven molecular machines.[14,115–119] A single-component AB-based liquid crystal with promising properties for application in holographic optical memory devices that allows ultrahigh density optical data storage was designed by Sobolewska *et al.*[120] Despite the high application potential of ABs, there are also disadvantages in comparison to other photochromic molecules. In many azobenzene derivatives, the UV/VIS absorption bands for the *E*- and *Z*-isomers differ only in oscillator strength, but are not clearly separated in wavelength, so that efficient *E/Z* switching usually requires UV light and is not quantitative.[49,121] The targeted synthesis of sterically hindered derivatives such as the 5,6-dihydrodibenzo[*c,g*][1,2] diazocine, which shows substantially increased quantum yields and can be switched in both directions almost quantitatively using only visible light,[122,123] or fully ortho-substituted derivatives[124] provide routes to azobenzenes with improved photochromic properties.

Regarding real-life function and practical use, it is of fundamental importance and key to success to integrate molecular switches into a complex environment, i.e. into polymer matrices.[73,125] ABs are still capable of isomerization under strong constraints, for example in the tight environment of solid matrices, or when included in a polymer chain.[122,126–130] Chromophores can either be incorporated into the polymer by covalent attachment, or be embedded into the polymeric matrices. Embedding chromophores into the polymer matrices to form a photoreactive thin film is a popular strategy for application in ophthalmic lenses, memory storage, molecular machines, and biological activity. However, the embedding may alter the functional properties because the photoisomerization processes not only involve a change of the electronic structure, but also a geometrical change of the structure of the chromophore. The latter, however, might be obstructed in the solid film due to the steric hindrance and limited free volume.[131–136]

Understanding the environmental effects on the photoswitching properties now attracts increasing interest. Owing to the complex nature of the investigations, only a few reports on the ultrafast dynamics of solid samples doped with photoswitches exist to date. Most researchers did steady-state investigations on the isomerization kinetics. However, little is know to date about the ultrafast isomerization dynamics of ABs in a polymer matrix.

1.1.1 Investigated azobenzene derivatives and aim of this thesis

The goal of this work was to the investigate the photochemical properties and molecular dynamics of azobenzene switches under the influence of complex and restricting environments, which potentially strongly affect the desired photoisomerization. The experimental details of the employed femtosecond transient absorption spectroscopy setup are described in the Experimental Section (Chapter 2).

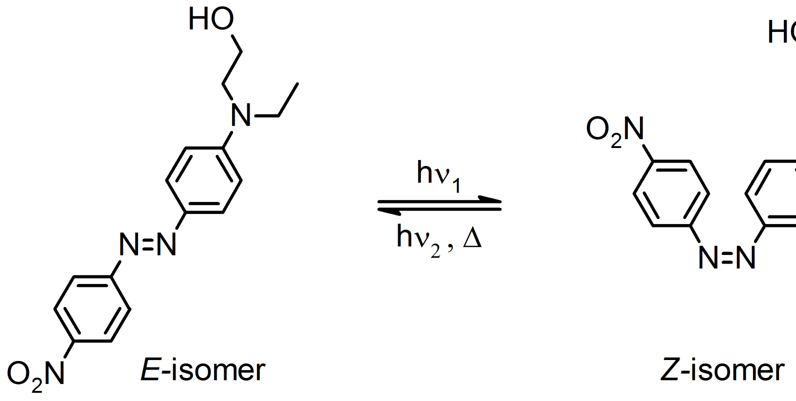

Fig. 1.9 Photoinduced *E*-*Z* isomerization by UV light and the VIS-photoinduced or thermal *Z*-*E* back-isomerization of Disperse Red 1 (DR1).

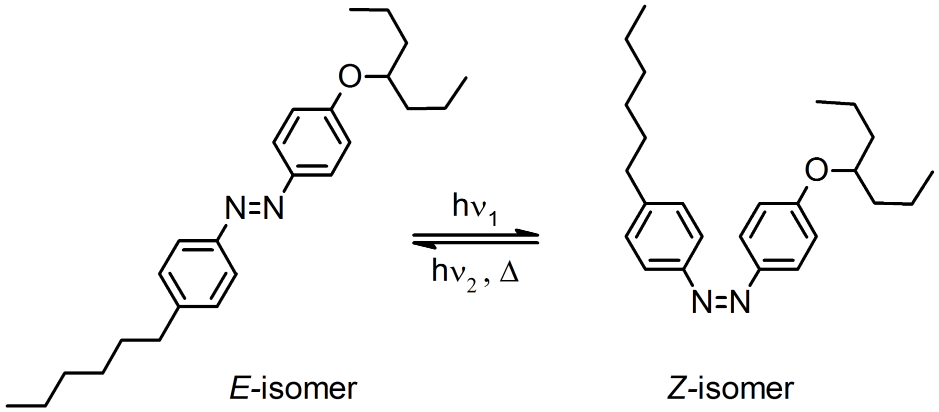

Fig. 1.10 photoinduced *E*-*Z* isomerization by UV light and the VIS-photoinduced or thermal *Z*-*E* back-isomerization of 4-hexyl-4′-(1-propylbutoxy) azobenzene (**1E** and **1Z**).

Two AB compounds, whose chemical structures are shown in Fig. 1.9 and Fig. 1.10, were embedded into polymer matrices and investigated by static and femtosecond time-resolved transient absorption spectroscopies. The solid-phase data of the time-resolved measurements were compared to those for the ABs in solution. The results of this study are presented in Chapters 3 and 4. DR1 embedded into a polymer matrix successfully undergoes isomerization. However, indications for the slower dynamics in the electronic ground state were found. The changes in relaxation times indicate that the molecular motion required for the *E/Z* isomerization is strongly impeded by steric constraints, although the reversible photoisomerization reaction can occur in a thin polymer film. The deactivation dynamics in the excited state of the embedded **1Z** compared with those in solution are quantitatively unchanged. Furthermore, the observed permanent absorption changes characterized by **1E** photo-product signatures provide unambiguous evidence for a successful *cis* $\rightarrow$ *trans* photoisomerization. In contrast, there is no permanent absorption band discernible that could be related to the **1Z** photo-product. The six-fold increase of the excited-state lifetime of **1E** embedded into a PMMA film implies a reduced isomerization quantum yield in volume-restricted environments. The fundamental insights into the molecular dynamics provide valuable information to develop more promising molecular switches that are suitable for the use in polymer matrices. The results prove the excellent capabilities of the new setup that provides the basis for studying the ultrafast dynamics of photoswitching in the solid phase.

1.2 Photochemistry of ferulic acid

Ferulic acid (3-methoxy-4-hydroxycinnamic acid, FA) can be viewed as a substituted phenol or as a substituted cinnamic acid. The side chain in phenol contains a C=C double bond that has the potential to isomerize upon UV photo-excitation. The hydroxy and methoxy groups in phenol have the effect of red-shifting the UV/VIS absorption spectrum. As shown in Fig. 1.11, FA exists as *trans*- and *cis*-isomer, which can be interconverted by photoisomerization about the C=C double bond. Both isomers can be deprotonated to their anionic and dianionic forms in aqueous solution. Depending on the pH value and the environment, FA features different absorption bands in the UV-A and UV-B spectral regions.

Extensive studies have provided considerable insight into the ultrafast photophysics of hydroxycinnamic acid compounds, with particular focus on *p*-coumaric acid chromophores, which triggers the reversible photocycle of the photoactive yellow protein (PYP) by *E/Z* photoisomerization about its C=C double bond.[36,137–144] Other well documented examples of molecules that undergo efficient E/Z photoisomerization about C=C bond upon UV excitation include stilbenes[22,23,145–150] and retinal.[151–157] However, FA has been studied to a

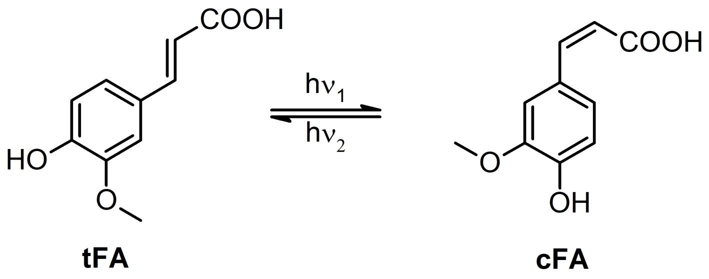

Fig. 1.11 Photochemical interconversion of *trans*- and *cis*-ferulic acid (tFA and cFA).

lesser extent,[28,36,37,39] although it is being widely used as a commercial sunscreen constituent. The strong UV absorption of FA has been studied intensively.[39,158–160] Karsili *et al.*[39] have used highly-correlated multi-reference computational methods to investigate its possible deactivation mechanisms. The calculations show that the $2\,^1\pi\pi^*$ potential energy curve (PEC) in tFA declines slowly, and shows a minimum at a torsional angle of $\Phi = 90°$, where it forms a CI with the S_0 potential. Further CIs to both the $1\,^1\pi\pi^*$ and $1\,^1n\pi^*$ state are accessible at a torsional angle of $\Phi = 140°$. The authors identify the *E/Z* photoisomerization (Fig. 1.12) as dominant relaxation pathway following UV excitation of FA.

Besides gas-phase theoretical calculations for FA, there are so far only two experimental solution-phase studies of the UV-induced dynamics of FA performed by transient absorption spectroscopy. Working with aqueous solutions at pH = 7 and pH = 10.5, corresponding to the anionic and dianionic forms of the *trans*-isomer (tFA^- and tFA^{2-}), Vengris *et al.* observed bi- and tri-exponential dynamics, respectively.[36] The two dominating decay components of $\tau_1 \leq 1$ ps and $\tau_2 = 19$ ps (pH = 7) vs. $\tau_2 = 8.2$ ps (pH = 10.5) were attributed to solvent rearrangement and initial excited-state dynamics, and the decay of the excited state on a much longer time scale, respectively. Despite the lack of evidence for *E/Z* photoisomerization, a torsional reaction coordinate involving a $1\,^1\pi\pi^*/\,1^1n\pi^*$ CI was favoured. More recently, the UV-induced dynamics of the neutral form of the *trans*-isomer (tFA) in aqueous solutions with pH = 2.2, and in the non-protic solvents acetonitrile (ACN) and dioxane were reported.[37] The observed tri-exponential decay behaviour was interpreted identically in all three cases. Accordingly, the fastest time constant, $\tau_1 = 0.08 - 0.4$ ps, was assigned to initial wavepacket motion in the vicinity of the FC region of the initially excited state taking place on the same time scale as the solvation dynamics. The second time constant, $\tau_2 = 0.5 - 2.6$ ps, was interpreted as the time scale of the evolution along the *E/Z* isomerization coordinate, either with or without IC to the $2\,^1\pi\pi^*$ state, followed by electronic deactivation to S_0 with time constant $\tau_3 = 6.3 - 15.4$ ps. The presence of an additional fast time constant compared to the previous study[36] was explained by the superior temporal resolution (~ 80 fs vs. ~ 370 fs)

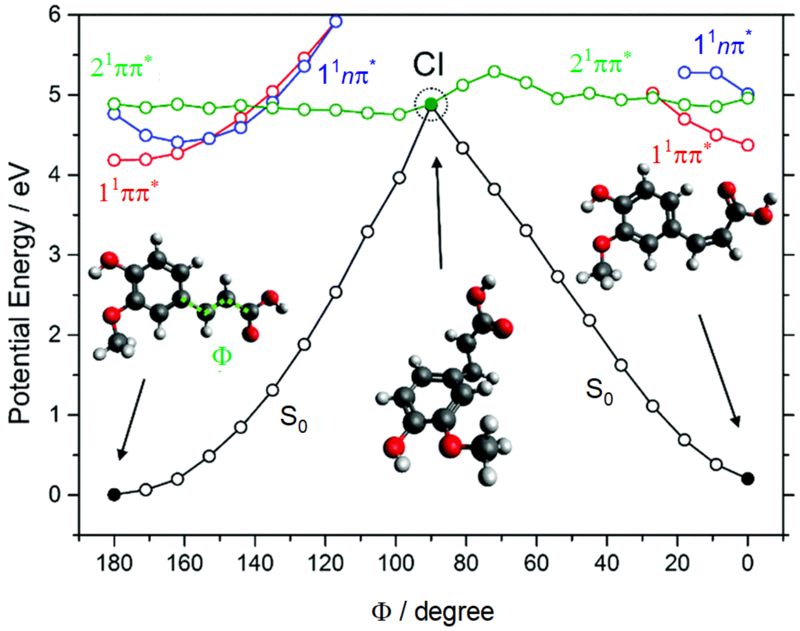

Fig. 1.12 Diabatic potential energy profiles of the lowest four singlet states (S_0, $1\,^1\pi\pi^*$, $1\,^1n\pi^*$, and $2\,^1\pi\pi^*$) of ferulic acid (FA) computed along the *E/Z* photoisomerization coordinate (torsional angle (Φ), in green) at the CASPT2 level. Two independent linear interpolations in internal coordinates (LIICs) were constructed by liking the MP2 optimized geometry of the most stable *E*- and *Z* isomers and the lowest energy $^1\pi\pi^*/S_0$ CI for the E/Z isomerization. The inset structures show the calculated minimum energy geometries of the ground state *E* (left) and *Z* (right) isomers and of the $^1\pi\pi^*/S_0$ CI. Adapted with permission from Karsili, T. N. V.; Marchetti, B.; M. Ashfold, N. R.; Domcke, W. *J. Phys. Chem. A* **2014**, 118, 11999 – 12010. Copyright (2014) American Chemical Society.

of the experiment. However, this comparison is between the neutral form (tFA) and the previously studied two deprotonated forms (tFA^- and tFA^{2-}) by Vengris *et al.*, and it is unclear if this is feasible. Furthermore, the results of Ref. [37] pointed to a significant effect of solvation as indicated by the fairly large range observed for the fast time constants under different solvation conditions and by the varying extent of the stimulated emission (SE) contribution to the transient signals (very strong in aqueous solution, hardly present in dioxane).

1.2.1 Investigated ferulic acid samples and aim of this thesis

One focus of this Thesis lies on the fundamental photochemical properties of ferulic acid as a common sunscreen constituent, and on the dynamical details that control its effectiveness as

UV filter following photo-excitation. Various possible deactivation decay mechanisms were revealed using a combination of DFT theoretical calculations and femtosecond broadband fluorescence and transient absorption spectroscopy. Special attention was paid to the influence of the particular molecular environment, i.e. the pH value of the FA aqueous solutions, on its photoisomerization dynamics.

Considering these environmental effects, some sunscreen components might have an adverse effect on the human skin or physiology. These concerns, often referred to the initiation of chemical reactions, as well as the formation of dangerous by-products and reactive oxygen species (ROS),[161,162] have caused a surge of research focused on gaining a deeper understanding of how sunscreen constituents operate and provide photoprotection. To stay close to its native environment, we studied FA in aqueous solutions which provides better approximations to the environments prevailing in sunscreens.

The ultrafast deactivation dynamics of both *trans*- and *cis*-FA were investigated in three different deprotonation states in buffered solutions (pH = 1.2, 7.4 and 10.4, as shown in Fig. 1.13) by means of broadband Kerr-gating fluorescence and transient absorption spectroscopy. The results of the time-resolved experiments are presented in Chapter 5. In the data, the observation of a complete electronic ground-state recovery and the identification of photo-product formation actually ensures an adequate evaluation of the safety of FA as a sunscreen compound. Gleaning insight into such photoisomerization mechanisms of FA will inevitably assist in developing next-generation sunscreens.

1.3 Electronic energy transfer in donor–acceptor systems

Sunlight, as the most abundant inexhaustible energy resource on our planet, is absorbed by natural compounds, converted to electronic excitation energy, and used to generate chemical energy *via* complex photosynthetic processes.[163–165] The strategy employed by nature is to capture sunlight over a wide spectral and spatial cross section in chromophore arrays, and then funnel the energy to a reaction center (Fig. 1.14).[166] The construction of artificial light-harvesting antenna systems inspired by nature's blueprint has attracted huge interest for decades to research alternative energy sources. The electronic properties of these molecules make them potentially useful in molecular photonics, optoelectronics, nanoscale applications, and in solar energy conversion.[167–169]

The transfer of electronic excitation energy from one excited unit to another is the fundamental physical process in natural light harvesting systems to funnel light from the antenna to the reaction center. Understanding the geometrical and electronic factors influencing the mechanism of excitation energy transfer (EET) is a key factor to the design and construction

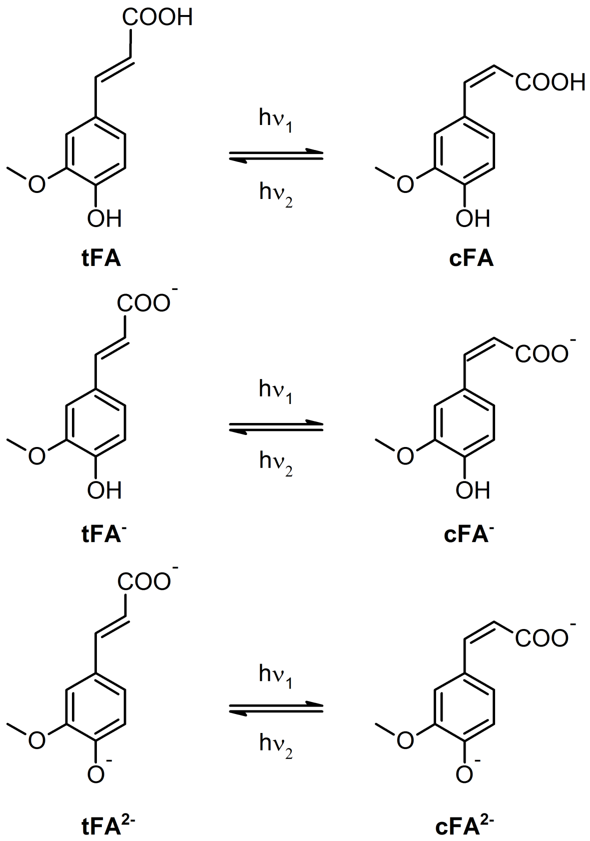

Fig. 1.13 Photoreaction of ferulic acid in its neutral, anionic and dianionic forms (FA, FA$^-$, and FA^{2-}).

of efficient artificial energy harvesting systems. The molecular architectures consisting of energy donors and acceptors are ideal systems for investigating EET processes on a molecular level.

From a general point of view, the rate and efficiency of EET are principally related to the relative magnitude of the electronic coupling between the donor and acceptor. When the two chromophores are strongly coupled, it is the delocalized electronic states that are excited by absorption of a photon, and the excited state is not localized because it is shared among all of the coupled moieties. When there is no orbital overlap between the two chromophores so that electrons can be assigned unambiguously to one moiety or the other, the excitation can be considered to be localized. It is common for weakly coupled moieties that Förster theory adequately describes the effects of distance and spectral overlap between the donor and acceptor moieties on the rate and efficiency of EET. Upon photo-excitation, the donor molecule in the electronic excited state rapidly relaxes to the lowest vibrational sublevel of the first excited singlet electronic state. The EET rate from the excited singlet state to the

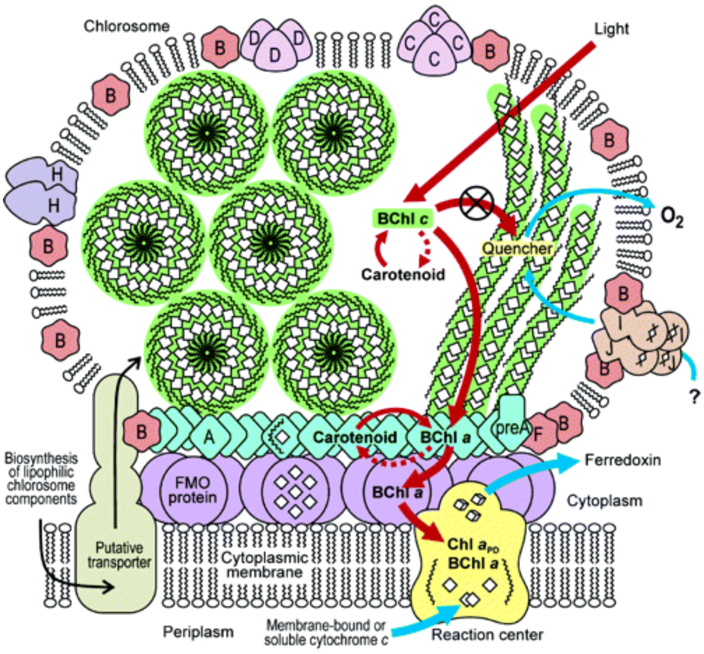

Fig. 1.14 Schematic model of protein organization on the chlorosome envelope including the light-harvesting antennae (chlorosomes), baseplate, the bacteriochlorophyll (BChl) Fenna–Mathews–Olson BChl *a*-binding protein, and reaction center of the green sulfur bacterium. Adapted with permission from Li, H.; Frigaard, N.-U.; Bryant, D. A. *Biochemistry* **2006**, 45, 9095 – 9103. Copyright (2006) American Chemical Society.

ground state of an acceptor molecule due to the Coulombic interaction can be described in the dipole-dipole approximation according to Förster's equation. Three parameters usually define the EET rate between weakly coupled donor and acceptor moieties: (i) the distance separating the dipole moments of the two moieties: the EET rate is dependent by the inverse sixth power of spatial interval; (ii) the relative orientation of the donor and acceptor dipole moments: the electronic coupling relies on the degree of flexibility of the system; (iii) the spectral overlap between the donor emission and acceptor absorption: the energy conservation is assured by the Franck-Condon weighted density of states.[170,171]

Recently, many experimental and theoretical efforts have been put into the development and characterization of molecular systems that are able to perform efficient and (ultra)fast energy transfer upon photo-excitation.[172–176] The development of ultrafast spectroscopic techniques and the increased computational capability certainly provided a more detailed insight into the mechanism of EET. As a further example, Schumacher *et al.* investigated the EET event in an orthogonal molecular dyad (BOD–T4), consisting of tetrathiophene (T4) as donor and a boron dipyromethene (BOD) dye as an acceptor, by means of nonadiabatic *ab*

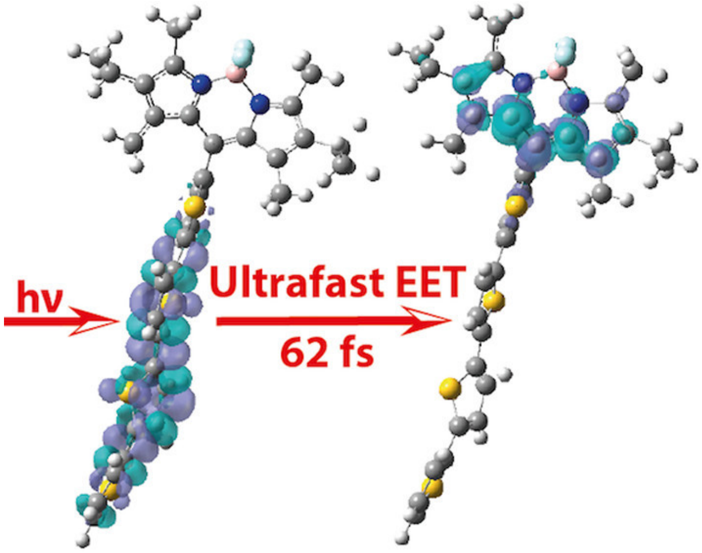

Fig. 1.15 Electronic states of a BOD–T4 dyad consisting of a boron dipyromethene (BOD) and tetrathiophene (T4) moiety based on differences of the electronic densities between the excited state and the electronic ground state. The evolution from the initial excited state (left-hand side) localized on the T4 unit to the excitation localized on the BOD unit (right-hand side) takes place within ≈ 60 fs. Adapted with permission from Wiebeler, C.; Plasser, F.; Hedley, G. J.; Ruseckas, A.; Samuel, I. D. W.; Schumacher, S. *J. Phys. Chem. Lett.,* **2017**, 8, 1086 – 1092. Copyright (2017) American Chemical Society.

initio molecular dynamics simulations.[177] The EET process was found to take place on a time scale of $\lesssim$ 100 fs and to occur through an intermediate charge-transfer state (see Fig. 1.15). Among many others, porphyrins or phthalocyanine-based hetero-dyads have proven as viable model donor–acceptor compounds, since these multi-chromophoric systems provide high absorption cross sections in the visible region. These molecules were extensively studied by Vauthey and coworkers.[178–180]

1.3.1 Naphthopyran as an energy acceptor

Naphthopyrans, also known as benzochromenes, are a group of photochromic molecules that have received considerable attention in the industry, especially for commercial photochromic lenses. UV irradiation of the initial closed form (CF, colorless) results in an electrocyclic ring opening of the pyran moiety *via* heterocyclic cleavage of the C(sp^3)-O bond. This produces the isomeric open form (OF, colorful), often referred to as the merocyanine form that is coloured because of its extended conjugation and quasi-planar conformation. The OF is able to electrocyclize back to the CF in the absence of UV light, either thermally (in the

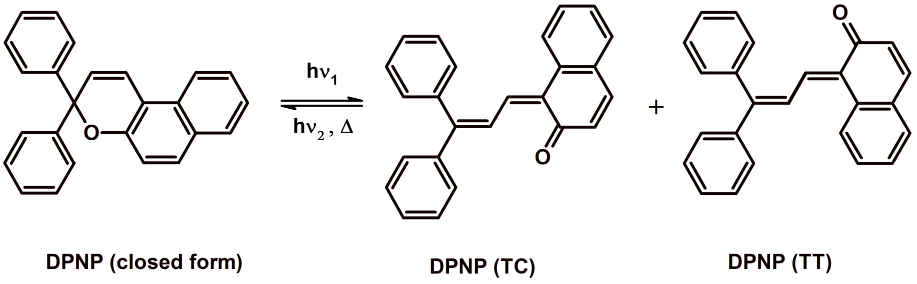

Fig. 1.16 Photochromic reaction between closed form (CF) and two trans isomers (*trans-cis* (TC) and *trans-trans* (TT)) of the photomerocyanine (OF) 3,3-diphenyl-3*H*-naphtho[2,1-*b*]pyran (DPNP).

dark) or photochemically (under VIS light). Furthermore, the OF can interconvert between different geometric conformations referred to as the *trans-cis* (TC) and the *trans-trans* (TT) merocyanine isomer *via* an extra double bond rotation shown in Fig. 1.16. The two main stereoisomeric classes of the OF are known to decay in the following consecutive steps: $\mathrm{OF_{TT}} \xrightarrow{h\nu} \mathrm{OF_{TC}} \xrightarrow{h\nu/\Delta} \mathrm{CF}$. The predominant TC isomer has a faster reversion rate compared to the minor TT isomer, which is thermally relatively stable.[181–185]

Naphthopyrans undergo significant structural changes upon irradiation with UV/VIS light. This leads to significant differences in the electronic properties of the two convertible states of the naphthopyran, as can be seen from Fig. 1.17: upon irradion with a 365 nm LED the CF of the naphthopyran is transformed to the OF, giving rise to a whole new absorption feature in the electronic absorption spectrum. Moreover, naphthopyrans only show little fatigue of their photochromic activity and allow for reversible switching for many times. These properties have been widely employed in applications, e.g., in optical data storage, in ophthalmic lenses, and in optical switching.[186–189] Among such applications, naphthopyrans have recently been engineered to modulate the emission of complementary fluorophores.[190–193] These molecules composed of naphthopyran with certain fluorophore moieties were designed in a way that only the OF isomer absorbs in the wavelength range (VIS region), where the fluorescent component emits. Photo-excitation of the fluorophore moiety can be followed by local excitation of the OF naphthopyran depending on the extent of energy transfer between the two subunits. The efficient suppression of the emission or quenching of the singlet excited state of the fluorophore due to EET to the ground state of the naphthopyran can be described by Föster theory.[194–197] Under these conditions, the emission of the fluorophore can be modulated by interconversion of the photochromic moiety using UV/VIS light. These reversibly switchable fluorescent dyes have attracted considerable interest due to their potential applications in molecular electronics and photonic devices,

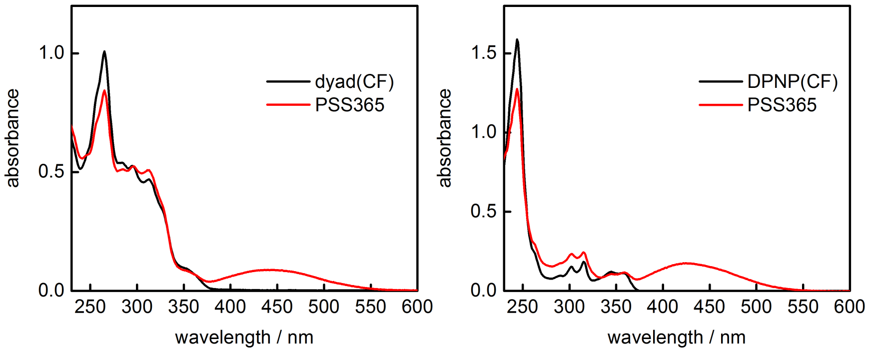

Fig. 1.17 Static absorption spectra of the PPBI–DPNP dyad (left panel) and DPNP (right panel) in ACN. The spectra of the closed forms (CFs) are displayed in black. The ring-opening reactions occur after excitation with UV light. Under continuous UV(365 nm) irradiation, CFs are converted to form a photostationary state (PSS, in red).

in high density optical memory, in reversible saturable optical fluorescence transitions (RESOLFT) microscopy, and in high resolution fluorescence imaging.[65,67–71,198–205]

1.3.2 Investigated donor–acceptor system and aim of this thesis

One of the topics of this Thesis was the investigation of an ultrafast EET process in a donor–acceptor dyad in which a photochromic diphenyl-naphthopyran (DPNP) acted as an acceptor and a propyl-pyridylbenzimidazole (PPBI) moiety as an energy donor by static and femtosecond time-resolved absorption and fluorescence spectroscopy in combination with quantum chemical calculations.

The molecular structure of the dyad is displayed in Fig. 1.18. In order to examine the EET from PPBI to the electronic ground state of the DPNP moiety to induce the isomerization of the latter, a selective excitation of the PPBI moiety is required. The results of this study are presented in Chapter 6. The photo-product (merocyanine form) of DPNP is formed indirectly by excitation energy transfer from the electronically excited state of the PPBI moiety. The photochromic naphthopyran compound can modulate the emission intensity, or the excited-state dynamics of the fluorescent moiety. The experimental results were analyzed using a singular value decomposition (SVD)-based global method which allowed to extract the time of the EET event from the acquired data. Förster theory was used to predict the EET rate in good agreement with the experimental observations, indicating the applicability of the point-dipole approximation at close proximity between donor and acceptor moiety.

Before presenting the results and the discussions for the aforementioned molecular photoswitches in Chapters 3 – 6, the experimental setup with a description of the developments

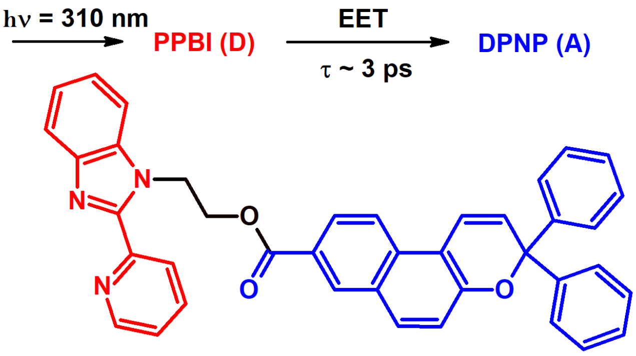

Fig. 1.18 Scheme of EET process from PPBI moiety to DPNP moiety in the PPBI–DPNP molecular dyad.

for solid samples, the new background-subtraction LabView routine, and the methods for data analysis performed on the obtained data are presented in Chapter 2. Finally, a summary regarding implications from the obtained results together with an outlook is given in Chapter 7.

Bibliography

[1] N. Koumura, R. W. J. Zijlstra, R. A. van Delden, N. Harada, B. L. Feringa, *Nature* **1999**, *401*, 152.

[2] T. Muraoka, K. Kinbara, T. Aida, *Nature* **2006**, *440*, 512.

[3] M. Yamada, M. Kondo, J. ichi Mamiya, Y. Yu, M. Kinoshita, C. J. Barrett, T. Ikeda, *Angew. Chem. Int. Ed.* **2008**, *47*, 4986–4988.

[4] Y. Yu, M. Nakano, T. Ikeda, *Nature* **2003**, *425*, 145.

[5] A. Harada, *Acc. Chem. Res.* **2001**, *34*, 456–464.

[6] T. Ikeda, O. Tsutsumi, *Science* **1995**, *268*, 1873–1875.

[7] R. H. Berg, S. Hvilsted, P. S. Ramanujam, *Nature* **1996**, *383*, 505.

[8] F. Ercole, T. P. Davis, R. A. Evans, *Polym. Chem.* **2010**, *1*, 37–54.

[9] D. Gust, J. Andréasson, U. Pischel, T. A. Moore, A. L. Moore, *Chem. Commun.* **2012**, *48*, 1947–1957.

[10] T. L. Andrew, H.-Y. Tsai, R. Menon, *Science* **2009**, *324*, 917–921.

[11] F. M. Raymo, M. Tomasulo, *Chem. Soc. Rev.* **2005**, *34*, 327.

[12] V. Westphal, S. W. Hell, *Phys. Rev. Lett.* **2005**, *94*, 143903.

[13] M. Irie, T. Fukaminato, T. Sasaki, N. Tamai, T. Kawai, *Nature* **2002**, *420*, 759.

[14] K. Szaciłowski, *Chem. Rev.* **2008**, *108*, 3481–3548.

[15] L. A. Baker, M. D. Horbury, S. E. Greenough, F. Allais, P. S. Walsh, S. Habershon, V. G. Stavros, *J. Phys. Chem. Lett.* **2016**, *7*, 56–61.

[16] S. Kobatake, S. Takami, H. Muto, T. Ishikawa, M. Irie, *Nature* **2007**, *446*, 778–781.

[17] H. Koshima, N. Ojima, H. Uchimoto, *J. Am. Chem. Soc.* **2009**, *131*, 6890–6891.

[18] K. Uchida, S. ichiro Sukata, Y. Matsuzawa, M. Akazawa, J. J. D. de Jong, N. Katsonis, Y. Kojima, S. Nakamura, J. Areephong, A. Meetsma, B. L. Feringa, *Chem. Commun.* **2008**, 326–328.

[19] R. Al-Kaysi, C. Bardeen, *Adv. Mater.* **2007**, *19*, 1276–1280.

[20] R. O. Al-Kaysi, A. M. Müller, C. J. Bardeen, *J. Am. Chem. Soc.* **2006**, *128*, 15938–15939.

[21] H. Bouas-Laurent, H. Dürr, *Pure Appl. Chem.* **2001**, *73*, 639–665.

[22] J. Saltiel, A. Marinari, D. W. L. Chang, J. C. Mitchener, E. D. Megarity, *J. Am. Chem. Soc.* **1979**, *101*, 2982–2996.

[23] J. M. Rodier, A. B. Myers, *J. Am. Chem. Soc.* **1993**, *115*, 10791–10795.

[24] E. van der Watt, J. C. Pretorius, *J. Ethnopharmacol.* **2001**, *76*, 87–91.

[25] D. L. Luthria, M. A. Pastor-Corrales, *J. Food Compos. Anal.* **2006**, *19*, 205–211.

[26] T. Masuda, K. Yamada, T. Maekawa, Y. Takeda, H. Yamaguchi, *J. Agric. Food. Chem.* **2006**, *54*, 6069–6074.

[27] H. Yin, L. Xu, N. A. Porter, *Chem. Rev.* **2011**, *111*, 5944–5972.

[28] E. Graf, *Free Radic. Biol. Med.* **1992**, *13*, 435–448.

[29] O. S. Eliane, B. Ronan, *Compr. Rev. Food Sci. Food Saf.* **2017**, *16*, 580–616.

[30] Z. Zhao, M. H. Moghadasian, *Food Chem.* **2008**, *109*, 691–702.

[31] K. J. Gohil, S. B. Kshirsaga, R. S. Sahane, *Int. J. Pharm. Sci. Res.* **2012**, *3*, 700–710.

[32] F. Borges, J. L. Lima, I. Pinto, S. Reis, C. Siquet, *Helv. Chim. Acta* **2003**, *86*, 3081–3087.

[33] K. Ohara, K. Doi, Y. Niizaki, S. ichi Nagaoka, *J. Photochem. Photobiol. A* **2012**, *249*, 1–8.

[34] E. M. M. Tan, M. Hilbers, W. J. Buma, *J. Phys. Chem. Lett.* **2014**, *5*, 2464–2468.

[35] J. C. Dean, R. Kusaka, P. S. Walsh, F. Allais, T. S. Zwier, *J. Am. Chem. Soc.* **2014**, *136*, 14780–14795.

[36] M. Vengris, D. S. Larsen, M. A. Van Der Horst, O. F. A. Larsen, K. J. Hellingwerf, R. Van Grondelle, *J. Phys. Chem. B* **2005**, *109*, 4197–4208.

[37] M. D. Horbury, L. A. Baker, W.-D. Quan, S. E. Greenough, V. G. Stavros, *Phys. Chem. Chem. Phys.* **2016**, *18*, 17691–17697.

[38] L. A. Baker, V. G. Stavros, *Sci. Prog.* **2016**, *99*, 282–311.

[39] T. N. V. Karsili, B. Marchetti, M. N. R. Ashfold, W. Domcke, *J. Phys. Chem. A* **2014**, *118*, 11999–12010.

[40] K. Oehlke, A. Heins, H. Stöckmann, K. Schwarz, *Food Chem.* **2010**, *118*, 48–55.

[41] M. E. Burnett, S. Q. Wang, *Photodermatol. Photoimmunol. Photomed.* **2011**, *27*, 58–67.

[42] H. E. Kanavy, M. R. Gerstenblith, *Semin. Cutan. Med. Surg.* **2011**, *30*, 222–228.

[43] C. Anselmi, M. Centini, M. Ricci, A. Buonocore, P. Granata, T. Tsuno, R. M. Facino, *J. Pharm. Biomed. Anal.* **2006**, *40*, 875–881.

[44] C. Anselmi, M. Centini, M. Maggiore, N. Gaggelli, M. Andreassi, A. Buonocore, G. Beretta, R. M. Facino, *J. Pharm. Biomed. Anal.* **2008**, *46*, 645–652.

[45] G. Füchsel, T. Klamroth, J. Dokić, P. Saalfrank, *J. Phys. Chem. B* **2006**, *110*, 16337–16345.

[46] C. Pakula, C. Hanisch, V. Zaporojtchenko, T. Strunskus, C. Bornholdt, D. Zargarani, R. Herges, F. Faupel, *J. Mater. Sci.* **2011**, *46*, 2488–2494.

[47] K. E. Lee, J. U. Lee, D. G. Seong, M.-K. Um, W. Lee, *J. Phys. Chem. C* **2016**, *120*, 23172–23179.

[48] G. S. Kumar, D. C. Neckers, *Chem. Rev.* **1989**, *89*, 1915–1925.

[49] H. M. D. Bandara, S. C. Burdette, *Chem. Soc. Rev.* **2012**, *41*, 1809–1825.

[50] T. Buffeteau, F. L. Labarthet, M. Pézolet, C. Sourisseau, *Macromolecules* **1998**, *31*, 7312–7320.

[51] Y. Chen, J. P. Xiao, B. Yao, M. G. Fan, *Opt. Mater.* **2006**, *28*, 1068–1071.

[52] R. S. Becker, J. Michl, *J. Am. Chem. Soc.* **1966**, *88*, 5931–5933.

[53] C. Lenoble, R. S. Becker, *J. Photochem.* **1986**, *33*, 187–197.

[54] X. Sallenave, S. Delbaere, G. Vermeersch, A. Saleh, J.-L. Pozzo, *Tetrahedron Lett.* **2005**, *46*, 3257–3259.

[55] W. Sriprom, M. Néel, C. D. Gabbutt, B. M. Heron, S. Perrier, *J. Mater. Chem.* **2007**, *17*, 1885–1893.

[56] E. V. Tulyakova, O. A. Fedorova, J.-C. Micheau, S. V. Paramonov, V. Lokshin, G. Vermeersch, S. Delbaere, *ChemPhysChem* **2011**, *12*, 1294–1301.

[57] C. M. Sousa, J. Berthet, S. Delbaere, A. Polónia, P. J. Coelho, *J. Phys. Org. Chem.* **2015**, *80*, 12177–12181.

[58] P. Sahoo, K. Prakash, S. Kumar, *Supramol. Chem.* **2016**, *29*, 183–192.

[59] M. Irie, *Chem. Rev.* **2000**, *100*, 1685–1716.

[60] T. Shizuka, K. Seiya, K. Tsuyoshi, I. Masahiro, *Chem. Lett.* **2003**, *32*, 892–893.

[61] C. Yun, J. You, J. Kim, J. Huh, E. Kim, *J. Photochem. Photobiol. C* **2009**, *10*, 111–129.

[62] S. C. Pang, H. Hyun, S. Lee, D. Jang, M. J. Lee, S. H. Kang, K.-H. Ahn, *Chem. Commun.* **2012**, *48*, 3745.

[63] M. Irie, *Proc Jpn Acad Ser B Phys Biol Sci.* **2010**, *86*, 472–483.

[64] M. Irie, M. Morimoto, *Bull. Chem. Soc. Jpn.* **2018**, *91*, 237–250.

[65] T. Fukaminato, T. Sasaki, T. Kawai, N. Tamai, M. Irie, *J. Am. Chem. Soc.* **2004**, *126*, 14843–14849.

[66] T. Fukaminato, T. Doi, N. Tamaoki, K. Okuno, Y. Ishibashi, H. Miyasaka, M. Irie, *J. Am. Chem. Soc.* **2011**, *133*, 4984–4990.

[67] H. Tian, S. Yang, *Chem. Soc. Rev.* **2004**, *33*, 85.

[68] T. Fukaminato, T. Doi, M. Tanaka, M. Irie, *J. Phys. Chem. C* **2009**, *113*, 11623–11627.

[69] S. W. Hell, *Nat. Biotechnol.* **2003**, *21*, 1347.

[70] M. Berberich, F. Würthner, *Chem. Sci.* **2012**, *3*, 2771–2777.

[71] M.-Q. Zhu, G.-F. Zhang, C. Li, M. P. Aldred, E. Chang, R. A. Drezek, A. D. Q. Li, *J. Am. Chem. Soc.* **2011**, *133*, 365–372.

[72] M. Häckel, L. Kador, D. Kropp, H. Schmidt, *Adv. Mater.* **2007**, *19*, 227–231.

[73] A. Natansohn, P. Rochon, *Chem. Rev.* **2002**, *102*, 4139–4176.

[74] S. Wiktorowicz, H. Tenhu, V. Aseyev, *Macromolecules* **2013**, *46*, 6209–6216.

[75] L. Vetrakova, V. Ladanyi, J. Al Anshori, P. Dvorak, J. Wirz, D. Heger, *Photochem. Photobiol. Sci.* **2017**, *16*, 1749–1756.

[76] P. Bortolus, S. Monti, *J. Phys. Chem.* **1979**, *83*, 648–652.

[77] G. Zimmerman, L.-Y. Chow, U.-J. Paik, *J. Am. Chem. Soc.* **1958**, *80*, 3528–3531.

[78] J. L. Magee, W. Shand, H. Eyring, *J. Am. Chem. Soc.* **1941**, *63*, 677–688.

[79] D. Y. Curtin, E. J. Grubbs, C. G. McCarty, *J. Am. Chem. Soc.* **1966**, *88*, 2775–2786.

[80] C.-W. Jiang, R.-H. Xie, F.-L. Li, R. E. Allen, *J. Phys. Chem. A* **2011**, *115*, 244–249.

[81] S. Yuan, Y. Dou, W. Wu, Y. Hu, J. Zhao, *J. Phys. Chem. A* **2008**, *112*, 13326–13334.

[82] D. S. Ruiz, A. Cembran, M. Garavelli, M. Olivucci, W. Fuß, *Photochem. Photobiol.* **2002**, *76*, 622–633.

[83] R. S. H. Liu, G. S. Hammond, *Proc. Natl. Acad. Sci. U.S.A.* **2000**, *97*, 11153–11158.

[84] M. Böckmann, N. L. Doltsinis, D. Marx, *J. Phys. Chem. A* **2010**, *114*, 745–754.

[85] M. Böckmann, N. L. Doltsinis, D. Marx, *J. Chem. Phys.* **2012**, *137*, 22A505.

[86] R. S. Liu, A. E. Asato, *Proc. Natl. Acad. Sci. U.S.A.* **1985**, *82*, 259–263.

[87] C. R. Crecca, A. E. Roitberg, *J. Phys. Chem. A* **2006**, *110*, 8188–8203.

[88] G. Granucci, M. Persico, *Theor. Chem. Acc.* **2006**, *117*, 1131–1143.

[89] A. Cembran, F. Bernardi, M. Garavelli, L. Gagliardi, G. Orlandi, *J. Am. Chem. Soc.* **2004**, *126*, 3234–3243.

[90] I. Conti, M. Garavelli, G. Orlandi, *J. Am. Chem. Soc.* **2008**, *130*, 5216–5230.

[91] C. Nonnenberg, H. Gaub, I. Frank, *ChemPhysChem* **2006**, *7*, 1455–1461.

[92] Y. Harabuchi, M. Ishii, A. Nakayama, T. Noro, T. Taketsugu, *J. Chem. Phys.* **2013**, *138*, 064305.

[93] I. K. Lednev, T.-Q. Ye, R. E. Hester, J. N. Moore, *J. Phys. Chem.* **1996**, *100*, 13338–13341.

[94] I. K. Lednev, T.-Q. Ye, L. C. Abbott, R. E. Hester, J. N. Moore, *J. Phys. Chem. A* **1998**, *102*, 9161–9166.

[95] I. Lednev, T.-Q. Ye, P. Matousek, M. Towrie, P. Foggi, F. Neuwahl, S. Umapathy, R. Hester, J. Moore, *Chem. Phys. Lett.* **1998**, *290*, 68–74.

[96] H. Satzger, S. Spörlein, C. Root, J. Wachtveitl, W. Zinth, P. Gilch, *Chem. Phys. Lett.* **2003**, *372*, 216–223.

[97] H. Satzger, C. Root, C. Renner, R. Behrendt, L. Moroder, J. Wachtveitl, W. Zinth, *Chem. Phys. Lett.* **2004**, *396*, 191–197.

[98] T. Fujino, S. Y. Arzhantsev, T. Tahara, *Bull. Chem. Soc. Jpn.* **2002**, *75*, 1031–1040.

[99] T. Fujino, S. Y. Arzhantsev, T. Tahara, *J. Phys. Chem. A* **2001**, *105*, 8123–8129.

[100] T. Fujino, T. Tahara, *J. Phys. Chem. A* **2000**, *104*, 4203–4210.

[101] T. Nägele, R. Hoche, W. Zinth, J. Wachtveitl, *Chem. Phys. Lett.* **1997**, *272*, 489–495.

[102] C.-W. Chang, Y.-C. Lu, T.-T. Wang, E. W.-G. Diau, *J. Am. Chem. Soc.* **2004**, *126*, 10109–10118.

[103] M. Quick, A. L. Dobryakov, M. Gerecke, C. Richter, F. Berndt, I. N. Ioffe, A. A. Granovsky, R. Mahrwald, N. P. Ernsting, S. A. Kovalenko, *J. Phys. Chem. B* **2014**, *118*, 8756–8771.

[104] T. A. Singleton, I. B. Burgess, B. A. Nerger, A. Goulet-Hanssens, N. Koay, C. J. Barrett, J. Aizenberg, *Soft Matter* **2014**, *10*, 1325–1328.

[105] T. E. Schrader, T. Cordes, W. J. Schreier, F. O. Koller, S.-L. Dong, L. Moroder, W. Zinth, *J. Phys. Chem. B* **2011**, *115*, 5219–5226.

[106] F. Zhang, A. Zarrine-Afsar, M. S. Al-Abdul-Wahid, R. S. Prosser, A. R. Davidson, G. A. Woolley, *J. Am. Chem. Soc.* **2009**, *131*, 2283–2289.

[107] O. Sadovski, A. A. Beharry, F. Zhang, G. A. Woolley, *Angew. Chem. Int. Ed.* **2008**, *48*, 1484–1486.

[108] C. Dohno, S.-n. Uno, K. Nakatani, *J. Am. Chem. Soc.* **2007**, *129*, 11898–11899.

[109] J. R. Kumita, O. S. Smart, G. A. Woolley, *Proc. Natl. Acad. Sci. U.S.A.* **2000**, *97*, 3803–3808.

[110] X. Liang, H. Asanuma, M. Komiyama, *J. Am. Chem. Soc.* **2002**, *124*, 1877–1883.

[111] G. Mayer, A. Heckel, *Angew. Chem. Int. Ed.* **2006**, *45*, 4900–4921.

[112] T. Fehrentz, M. Schönberger, D. Trauner, *Angew. Chem. Int. Ed.* **2011**, *50*, 12156–12182.

[113] Z. Wang, L. Heinke, J. Jelic, M. Cakici, M. Dommaschk, R. J. Maurer, H. Oberhofer, S. Grosjean, R. Herges, S. Brase, K. Reuter, C. Woll, *Phys. Chem. Chem. Phys.* **2015**, *17*, 14582–14587.

[114] X. Yu, Z. Wang, M. Buchholz, N. Fullgrabe, S. Grosjean, F. Bebensee, S. Brase, C. Woll, L. Heinke, *Phys. Chem. Chem. Phys.* **2015**, *17*, 22721–22725.

[115] M. Russew, S. Hecht, *Adv. Mater.* **2009**, *22*, 3348–3360.

[116] J. Ma, L. Xuan, *Displays* **2013**, *34*, 293–300.

[117] H. Li, Q. Xu, N. Li, R. Sun, J. Ge, J. Lu, H. Gu, F. Yan, *J. Am. Chem. Soc.* **2010**, *132*, 5542–5543.

[118] D. Gindre, A. Boeglin, A. Fort, L. Mager, K. D. Dorkenoo, *Opt. Express* **2006**, *14*, 9896–9901.

[119] S. Kawata, Y. Kawata, *Chem. Rev.* **2000**, *100*, 1777–1788.

[120] A. Sobolewska, S. Bartkiewicz, J. Mysliwiec, K. D. Singer, *J. Mater. Chem. C* **2014**, *2*, 1409–1412.

[121] A. A. Beharry, G. A. Woolley, *Chem. Soc. Rev.* **2011**, *40*, 4422–4437.

[122] R. Siewertsen, H. Neumann, B. Buchheim-Stehn, R. Herges, C. Näther, F. Renth, F. Temps, *J. Am. Chem. Soc.* **2009**, *131*, 15594–15595.

[123] R. Siewertsen, F. Strübe, J. Mattay, F. Renth, F. Temps, *Phys. Chem. Chem. Phys.* **2011**, *13*, 3800.

[124] A. A. Beharry, O. Sadovski, G. A. Woolley, *J. Am. Chem. Soc.* **2011**, *133*, 19684–19687.

[125] R. Loucif-Saibi, K. Nakatani, J. A. Delaire, M. Dumont, Z. Sekkat, *Chem. Mater.* **1993**, *5*, 229–236.

[126] H. Rau, E. Lueddecke, *J. Am. Chem. Soc.* **1982**, *104*, 1616–1620.

[127] H. Rau, S. Yu-Quan, *J. Photochem. Photobiol. A* **1988**, *42*, 321–327.

[128] A. Khan, C. Kaiser, S. Hecht, *Angew. Chem. Int. Ed.* **2006**, *45*, 1878–1881.

[129] D. Bléger, T. Liebig, R. Thiermann, M. Maskos, J. P. Rabe, S. Hecht, *Angew. Chem. Int. Ed.* **2011**, *50*, 12559–12563.

[130] K. G. Yager, C. J. Barrett, *J. Photochem. Photobiol. A* **2006**, *182*, 250–261.

[131] W. C. Yu, C. S. P. Sung, *Macromolecules* **1988**, *21*, 365–371.

[132] J. G. Victor, J. M. Torkelson, *Macromolecules* **1987**, *20*, 2241–2250.

[133] K. Shima, K. Mutoh, Y. Kobayashi, J. Abe, *J. Phys. Chem. A* **2015**, *119*, 1087–1093.

[134] C. D. Eisenbach, *Polym. Bull.* **1980**, *2*, 169–176.

[135] K. Guo, Y. Chen, *J. Mater. Chem.* **2010**, *20*, 4193–4197.

[136] H. Shen, Z. Chen, T. Xiao, *ChemistrySelect* **2017**, *2*, 5545–5551.

[137] P. Changenet-Barret, A. Espagne, S. Charier, J. B. Baudin, L. Jullien, P. Plaza, K. J. Hellingwerf, M. M. Martin, *Photochem. Photobiol. Sci.* **2004**, *3*, 823–829.

[138] A. Espagne, D. H. Paik, P. Changenet-Barret, M. M. Martin, A. H. Zewail, *ChemPhysChem* **2006**, *7*, 1717–1726.

[139] A. Espagne, P. Changenet-Barret, P. Plaza, M. M. Martin, *J. Phys. Chem. A* **2006**, *110*, 3393–3404.

[140] N. Mataga, H. Chosrowjan, S. Taniguchi, N. Hamada, F. Tokunaga, Y. Imamoto, M. Kataoka, *Phys. Chem. Chem. Phys.* **2003**, *5*, 2454–2460.

[141] D. S. Larsen, M. Vengris, I. H. M. van Stokkum, M. A. van der Horst, F. L. de Weerd, K. J. Hellingwerf, R. van Grondelle, *Biophys. J*. **2004**, *86*, 2538–2550.

[142] E. M. M. Tan, S. Amirjalayer, B. H. Bakker, W. J. Buma, *Faraday Discuss.* **2013**, *163*, 321.

[143] G. Groenhof, M. Bouxin-Cademartory, B. Hess, S. P. de Visser, H. J. C. Berendsen, M. Olivucci, A. E. Mark, M. A. Robb, *J. Am. Chem. Soc.* **2004**, *126*, 4228–4233.

[144] K. Pande, C. D. M. Hutchison, G. Groenhof, A. Aquila, J. S. Robinson, J. Tenboer, S. Basu, S. Boutet, D. P. DePonte, M. Liang, T. A. White, N. A. Zatsepin, O. Yefanov, D. Morozov, D. Oberthuer, C. Gati, G. Subramanian, D. James, Y. Zhao, J. Koralek, J. Brayshaw, C. Kupitz, C. Conrad, S. Roy-Chowdhury, J. D. Coe, M. Metz, P. L. Xavier, T. D. Grant, J. E. Koglin, G. Ketawala, R. Fromme, V. Rajer, R. Henning, J. C. H. Spence, A. Ourmazd, P. Schwander, U. Weierstall, M. Frank, P. Fromme, A. Barty, H. N. Chapman, K. Moffat, J. J. van Thor, M. Schmidt, *Science* **2016**, *352*, 725–729.

[145] A. L. Dobryakov, I. Ioffe, A. A. Granovsky, N. P. Ernsting, S. A. Kovalenko, *J. Chem. Phys.* **2012**, *137*, 244505.

[146] M. Quick, F. Berndt, A. L. Dobryakov, I. N. Ioffe, A. A. Granovsky, C. Knie, R. Mahrwald, D. Lenoir, N. P. Ernsting, S. A. Kovalenko, *J. Phys. Chem. B* **2014**, *118*, 1389–1402.

[147] F. Berndt, A. Dobryakov, M. Quick, R. Mahrwald, N. Ernsting, D. Lenoir, S. Kovalenko, *Chem. Phys. Lett.* **2012**, *544*, 39–42.

[148] S. Kovalenko, A. Dobryakov, I. Ioffe, N. Ernsting, *Chem. Phys. Lett.* **2010**, *493*, 255–258.

[149] I. N. Ioffe, A. A. Granovsky, *J. Chem. Theory Comput.* **2013**, *9*, 4973–4990.

[150] J. Quenneville, T. J. Martínez, *J. Phys. Chem. A* **2003**, *107*, 829–837.

[151] A. Migani, A. Sinicropi, N. Ferre, A. Cembran, M. Garavelli, M. Olivucci, *Faraday Discuss.* **2004**, *127*, 179–191.

[152] G. Bassolino, T. Sovdat, A. Soares Duarte, J. M. Lim, C. Schnedermann, M. Liebel, B. Odell, T. D. W. Claridge, S. P. Fletcher, P. Kukura, *J. Am. Chem. Soc.* **2015**, *137*, 12434–12437.

[153] I. Schapiro, M. N. Ryazantsev, L. M. Frutos, N. Ferré, R. Lindh, M. Olivucci, *J. Am. Chem. Soc.* **2011**, *133*, 3354–3364.

[154] D. Polli, P. Altoè, O. Weingart, K. M. Spillane, C. Manzoni, D. Brida, G. Tomasello, G. Orlandi, P. Kukura, R. A. Mathies, M. Garavelli, G. Cerullo, *Nature* **2010**, *467*, 440.

[155] N. Ferré, M. Olivucci, *J. Am. Chem. Soc.* **2003**, *125*, 6868–6869.

[156] T. Kobayashi, T. Saito, H. Ohtani, *Nature* **2001**, *414*, 531.

[157] R. Schoenlein, L. Peteanu, R. Mathies, C. Shank, *Science* **1991**, *254*, 412–415.

[158] A. Urbaniak, M. Szeląg, M. Molski, *Comput. Theor. Chem.* **2013**, *1012*, 33–40.

[159] G. Mazzone, N. Russo, M. Toscano, *Comput. Theor. Chem.* **2016**, *1077*, 39–47.

[160] G. Prampolini, I. Cacelli, A. Ferretti, *RSC Adv.* **2015**, *5*, 38513–38526.

[161] J. M. Allen, C. J. Gossett, S. K. Allen, *Chem. Res. Toxicol.* **1996**, *9*, 605–609.

[162] K. M. Hanson, E. Gratton, C. J. Bardeen, *Free Radical Biol. Med.* **2006**, *41*, 1205–1212.

[163] D. Gust, T. A. Moore, A. L. Moore, *Acc. Chem. Res.* **2009**, *42*, 1890–1898.

[164] G. D. Scholes, G. R. Fleming, A. Olaya-Castro, R. van Grondelle, *Nat. Chem.* **2011**, *3*, 763–774.

[165] D. A. Bryant, D. P. Canniffe, *J. Phys. B: At. Mol. Opt. Phys.* **2018**, *51*, 033001.

[166] H. Li, N.-U. Frigaard, D. A. Bryant, *Biochemistry* **2006**, *45*, 9095–9103.

[167] D. Gust, T. A. Moore, A. L. Moore, *Acc. Chem. Res.* **2001**, *34*, 40–48.

[168] G. J. Hedley, A. Ruseckas, I. D. W. Samuel, *Chem. Rev.* **2016**, *117*, 796–837.

[169] M. R. Wasielewski, *Acc. Chem. Res.* **2009**, *42*, 1910–1921.

[170] R. P. Haugland, J. Yguerabide, L. Stryer, *Proc. Natl. Acad. Sci. U.S.A* **1969**, *63*, 23–30.

[171] A. N. Glazer in *Photochemical and Photobiological Reviews: Volume 1*, (Ed.: K. C. Smith), Springer US, Boston, MA, **1976**, Chapter 2, pp. 71–115.

[172] D. Badgurjar, K. Sudhakar, K. Jain, V. Kalantri, Y. Venkatesh, N. Duvva, S. Prasanthkumar, A. K. Sharma, P. R. Bangal, R. Chitta, L. Giribabu, *J. Phys. Chem. C* **2016**, *120*, 16305–16321.

[173] C. Azarias, L. Cupellini, A. Belhboub, B. Mennucci, D. Jacquemin, *Phys. Chem. Chem. Phys.* **2018**, *20*, 1993–2008.

[174] E. A. Ermilov, J.-Y. Liu, R. Menting, Y.-S. Huang, B. Roder, D. K. P. Ng, *Phys. Chem. Chem. Phys.* **2016**, *18*, 10964–10975.

[175] G. J. Hedley, A. Ruseckas, A. C. Benniston, A. Harriman, I. D. W. Samuel, *J. Phys. Chem. A* **2015**, *119*, 12665–12671.

[176] M. Fakis, J. S. Beckwith, K. Seintis, E. Martinou, C. Nancoz, N. Karakostas, I. Petsalakis, G. Pistolis, E. Vauthey, *Phys. Chem. Chem. Phys.* **2018**, *20*, 837–849.

[177] C. Wiebeler, F. Plasser, G. J. Hedley, A. Ruseckas, I. D. W. Samuel, S. Schumacher, *J. Phys. Chem. Lett.* **2017**, *8*, 1086–1092.

[178] N. Banerji, S. V. Bhosale, I. Petkova, S. J. Langford, E. Vauthey, *Phys. Chem. Chem. Phys.* **2011**, *13*, 1019–1029.

[179] D. Villamaina, S. V. Bhosale, S. J. Langford, E. Vauthey, *Phys. Chem. Chem. Phys.* **2013**, *15*, 1177–1187.

[180] O. Yushchenko, R. V. Hangarge, S. Mosquera-Vazquez, S. V. Boshale, E. Vauthey, *J. Phys. Chem. B* **2014**, *119*, 7308–7320.

[181] J. Hobley, V. Malatesta, K. Hatanaka, S. Kajimoto, S. L. Williams, H. Fukumura, *Phys. Chem. Chem. Phys.* **2002**, *4*, 180–184.

[182] H. Görner, A. K. Chibisov, *J. Photochem. Photobiol. A* **2002**, *149*, 83–89.

[183] S. Jockusch, N. J. Turro, F. R. Blackburn, *J. Phys. Chem. A* **2002**, *106*, 9236–9241.

[184] G. Ottavi, G. Favaro, V. Malatesta, *J. Photochem. Photobiol. A* **1998**, *115*, 123–128.

[185] S. Delbaere, B. Luccioni-Houze, C. Bochu, Y. Teral, M. Campredon, G. Vermeersch, *J. Chem. Soc. Perkin Trans. 2* **1998**, *2*, 1153–1158.

[186] S. Aiken, J.-P. Cano, C. D. Gabbutt, B. M. Heron, T. Kosa, L. Su, L. Sukhomlinova, B. Taheri, US20100202033A1, **2010**.

[187] D. B. Knowles, US5238981A, **1993**.

[188] A. Kumar, B. V. Gemert, D. B. Knowles, *Mol. Cryst. Liq. Cryst.* **2000**, *344*, 217–222.

[189] C. Crano J., T. Flood, D. Knowles, A. Kumar, B. Van Gemert, *Pure Appl. Chem.* **1996**, *68*, 1395–1398.

[190] L. Bekere, V. Lokshin, M. Sigalov, R. Gvishi, P. Zhao, D. J. Hagan, E. W. V. Stryland, V. Khodorkovsky, *New J. Chem.* **2016**, *40*, 1143–1148.

[191] D. Li, J. Jiang, Q. Huang, G. Wang, M. Zhang, J. Du, *Polym. Chem.* **2016**, *7*, 3444–3450.

[192] Y. He, G. Wang, M. Wang, *J. Mol. Struct.* **2016**, *1116*, 109–115.

[193] Y. Zhang, Y. Zhang, G. Wang, Y. He, *Dyes Pigm.* **2014**, *102*, 107–113.

[194] T. Förster, *Naturwissenschaften* **1946**, *33*, 166–175.

[195] T. Förster, *Annal. Phys.* **1948**, *2*, 55–75.

[196] T. Förster, *Discuss. Faraday Soc.* **1959**, *27*, 7–17.

[197] *Principles of Fluorescence Spectroscopy*, (Ed.: J. R. Lakowicz), Springer, **2006**.

[198] L. Giordano, T. M. Jovin, M. Irie, E. A. Jares-Erijman, *J. Am. Chem. Soc.* **2002**, *124*, 7481–7489.

[199] M. Bossi, V. Belov, S. Polyakova, S. W. Hell, *Angew. Chem. Int. Ed.* **2006**, *45*, 7462–7465.

[200] H. Tian, S. Wang, *Chem. Commun.* **2007**, *0*, 781–792.

[201] L. Zhu, W. Wu, M.-Q. Zhu, J. J. Han, J. K. Hurst, A. D. Q. Li, *J. Am. Chem. Soc.* **2007**, *129*, 3524–3526.

[202] D. Hu, Z. Tian, W. Wu, W. Wan, A. D. Q. Li, *J. Am. Chem. Soc.* **2008**, *130*, 15279–15281.

[203] R. Ando, H. Mizuno, A. Miyawaki, *Science* **2004**, *306*, 1370–1373.

[204] M. Heilemann, E. Margeat, R. Kasper, M. Sauer, P. Tinnefeld, *J. Am. Chem. Soc.* **2005**, *127*, 3801–3806.

[205] G. Jiang, S. Wang, W. Yuan, L. Jiang, Y. Song, H. Tian, D. Zhu, *Chem. Mater.* **2006**, *18*, 235–237.

Chapter 2

Experimental section

Understanding the ultrafast dynamics of different photochromic molecular switches is of particular importance regarding the ambitious design goals for optimal functional devices. The associated processes of the chemical transformations and vibronic relaxation of the photo-excited molecules take place on a femtosecond to picosecond time scale and thus require ultrafast spectroscopic techniques with femtosecond time resolutions. Since the direct transient electronic detection is too slow, femtosecond time-resolved methods are based on the pump-probe principle which is shown schematically in Fig. 2.1. The ultrashort pump pulse is used to excite the sample molecules. The subsequent molecular response is monitored by a second probe pulse that is spatially overlapped, but temporally delayed with respect to the pump pulse *via* an optical delay line. Therefore, the time resolution of the experiment only depends on the duration of the pump and probe pulses, but not on the response time of the detector.

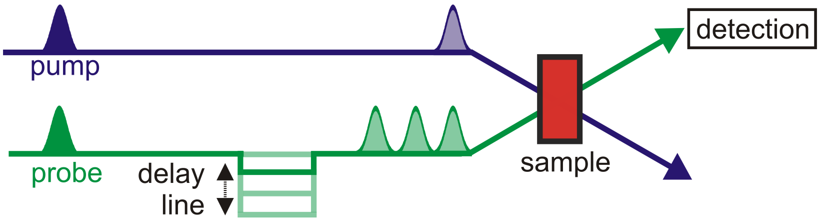

Fig. 2.1 Pump-probe scheme for a femtosecond broadband transient absorption experiment.

In the context of this Thesis, both the deactivation of the electronically excited states and the dynamics in the electronic ground state play a significant role. Therefore, the dynamics of several molecular switches (i.e., FA and ABs) under different circumstances have been investigated by means of femtosecond time-resolved transient absorption spectroscopy to monitor the dynamics in the excited states as well as the recovery of the electronic ground state. The transient absorption spectroscopy is particularly suited for the study of photochromic compounds, which by definition show significant photo-induced changes in their UV/VIS absorption spectra. The required ultrashort laser pulses that realized incorporating initiate the molecular switching process in time-resolved experiments are based on non-linear optical processes. These are described in detail in several previous PhD Theses written within the research group[1–5] and in a number of textbooks.[6–9] This Chapter is therefore kept relatively brief.

A major part of the present Thesis is the development of a versatile transient absorption setup for solid samples. Much effort has been invested to ensure a straightforward, stable and reproducible operation of the setup that can be adjusted to the individual needs of different samples within a reasonable amount of time. A detailed description of setup and operation is given in Section 2.1, while the data processing and explanation of the data analysis procedures can be found in Section 2.4.

2.1 Femtosecond transient absorption setup

A schematic overview of the entire femtosecond time-resolved broadband transient absorption setup in our laboratory in its current status is depicted in Fig. 2.2. A detailed description of the entire laser system can be found elsewhere.[1–3,10] Briefly, a regeneratively amplified Ti:Sa laser (Clark MXR CPA 2001) delivers femtosencond pulses with a duration of 220 fs (Full Width at Half Maximum, FWHM), a center wavelength of $\lambda = 775$ nm and an energy of about 1000 nJ at a repetition rate of 1010 Hz. The experiment consists of three major parts: the generation of the pump pulses, the generation of the supercontinuum broadband probe pulses, and the detection units for the respective probe pulses.

2.1.1 Pump pulse generation

A non-collinear optical parametric amplifier (NOPA) pumped by the frequency-doubled Ti:Sa fundamental ($\lambda = 387$ nm) was used to generate pulses in a wavelength range between 450 nm and 700 nm. The principle and operation of the NOPA is in detail described elsewhere.[2,5] The pulses generated by the NOPA were temporally compressed to of 30 fs − 60 fs using a prism compressor equipped with a pair of BK7 prisms or F2 prisms depending on the amplified wavelength. After passing the compressor, the NOPA pulses were either used directly for excitation in the VIS wavelength range (the lower NOPA in Fig. 2.2) or, for excitation in the UV wavelength range, focused into a β-bariumborate (BBO) crystal for second harmonic generation (SHG) (the upper NOPA in Fig. 2.2).

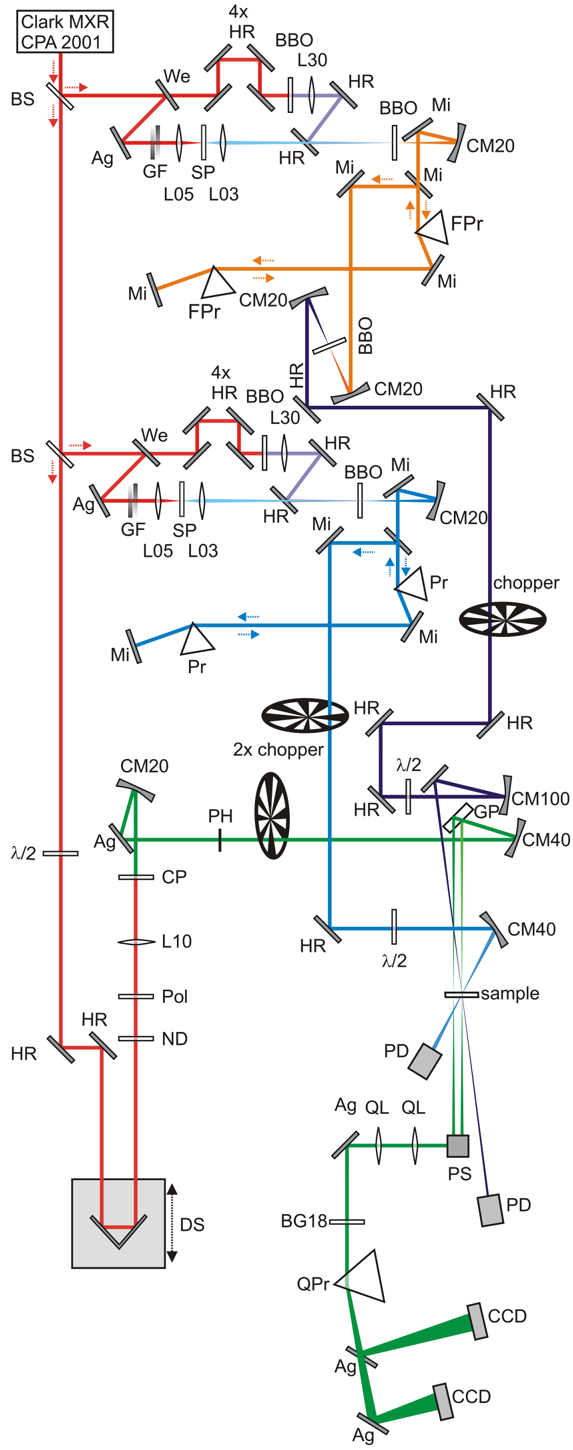

Ag	planar Ag mirror
BBO	β-BaB$_2$O$_4$ crystal
BG18	BG18 filter
BS	beamsplitter
CCD	FFT-CCD camera
CP	CaF$_2$ plate (d = 2 mm)
CM20	concave mirror, rcc = 0.2m
CM40	concave mirror, rcc = 0.4 m
CM100	concave mirror, rcc = 1 m
DS	delay stage with retroreflector
FPr	F2 prism
GF	gradient filter
GP	planar quartz glass plate
HR	high reflective mirror
λ/2	half-wave plate
L03	lens, f = 30 mm
L05	lens, f = 50 mm
L10	lens, f = 0.1 m
L30	lens, f = 0.3 m
Mi	planar Ag or Al mirror
ND	neutral density filter
PD	photodiode
Pol	polarizer
PH	pinhole
Pr	BK7 prism
PS	periscope
QL	quartz lens
QPr	quartz prism
SP	sapphire plate
We	wedge (30´)

Fig. 2.2 Scheme of the broadband transient absorption experimental setup and its optical components. The color of the beam is chosen arbitrarily and does not necessarily reflect the real wavelength.

Finally the beam was focused on the sample with a diameter of 200 μm -300 μm and a pulse energy of about 100 nJ − 300 nJ. A Berek compensator was used to set the polarization to parallel, perpendicular or magic angle (54.7 °) with respect to the probe beam. Additionally, an optical chopper was introduced to the beam path.

2.1.2 Probe pulse generation

In a second part of the pump-probe setup, a small fraction of the laser fundamental ($\approx$ 50 μJ) passed a computer controlled delay stage equipped with a retroreflector, before it is focused in a 2-mm CaF_2 plate to generate broadband probe pulses in a wavelength range between λ_{probe} = 320 nm −750 nm. To avoid damaging the CaF_2 plate, it required a constant movement horizontally and vertically to ensure that a fresh spot was hit by every laser pulse. The supercontinuum white light generation is extremely sensitive to the energy of incoming beam. Therefore, the energy used to generate white light was first attenuated by a set of neutral density filters and afterwards precisely adjusted by the combination of a $\lambda/2$ plate and a polarizer positioned in front of the CaF_2 plate. A detailed description of the obtained white light spectrum, its optimization and stabilization can be found in previous Theses of the work group.[2,4]

The thus generated broadband probe pulses were split into probe and reference beam using an etalon and focused on the sample with a diameter of $\approx$ 200 μm. While the probe beam is overlapped both temporally and spatially with the pump beam, the reference beam passed the unexcited sample. An optical chopper operated at a frequency of 505 Hz is used to block every second probe pulse.

2.1.3 Detection and data acquisition

After passing the sample, the transmitted probe and reference pulses were directed into a prism spectrograph, where they were spectrally dispersed, separated and independently detected by two FFT-CCD cameras (Series 2000, Entwicklungsbüro Stresing, Berlin). A photodiode is used to detect the status of the pump beam chopper, while the status of the probe beam chopper follows directly from the intensity at the CCD cameras. The simultaneous use of the two choppers operated at different frequencies generated a scheme of four different pump probe pulse pairs that was used to obtain background-free datasets on a shot-by-shot basis. In the following, this data acquisition routine is explained in more detail.

Data acquisition using background subtraction routine

The transient absorption (TA) data acquisition procedure for liquid sample shall be explained in the following: An optical chopper (MC2000B, Thorlab) equipped with a symmetric

10-shot blade (MC1F10, Thorlabs) that is synchronized to the amplifier (1010 Hz) is adjusted to half of frequency (505 Hz) and placed in the probe beam path so that every other probe pulse is blocked. Meanwhile, a second synchronized chopper with 10-shot blade (MC1F10, Thorlabs) on the pump path rotated with quarter of the frequency (252 Hz) so that just two continuous pump pulses went through the chopper and the subsequent two consecutive pump pulses were blocked, and so on. Under these conditions, four different states of pump-probe pairs are generated as shown in Fig. 2.3. The resulting pulse sequences are pump off, probe on (A); pump off, probe off (B); pump on, probe on (C); and pump on, probe off (D), where states C and A refer to the excited and unexcited sample signals used to calculate ΔOD (see the following part in more detail); state D contains the complete information of pure pump pulse such as scattered light; state B is regarded as the ambient background. Subsequently, the scattered pump light and background corrections during the data acquirement were implemented straightforward into the LabView program routine. Typically, the signal is accumulated over multiple detection cycles, which requires refreshing the sample between successive laser pulses. For liquid samples this was obtained using a flow cell in combination with a perestaltic pump. For solid film samples a (x/y)-translation stage was used to move the sample to a fresh sample spot. This process is in more detail explained in Section 2.5). To guarantee that each measurement was taken on a fresh sample spot, all pump pulses had to be blocked for a time period, that allowed for the translation of the film. Thus, an independent

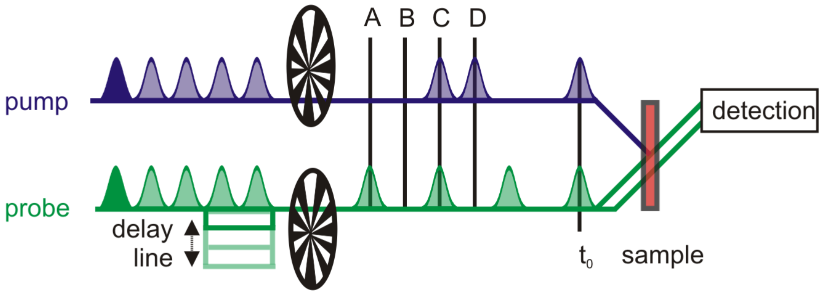

Fig. 2.3 Schematic overview of the pump-probe transient absorption experiment for solution sample using the background subtraction. The ultrashort pump pulses excite the sample at a given time t_0 and the molecular response is monitored using ultrashort probe pulses at discrete delay times. The temporal delay between pump and probe pulses is realized by a variable spatial delay line. In the present transient absorption experiment, the background subtraction is implemented: The chopper frequency of white light (505 Hz, half of the fundamental pulses) is two times that of pump pulse to generate 4 different pump-probe pulse pairs indicated by letters of A, B, C, and D, so that the spectral information of pump or probe pulse alone can be obtained which allows us to do the background subtraction.

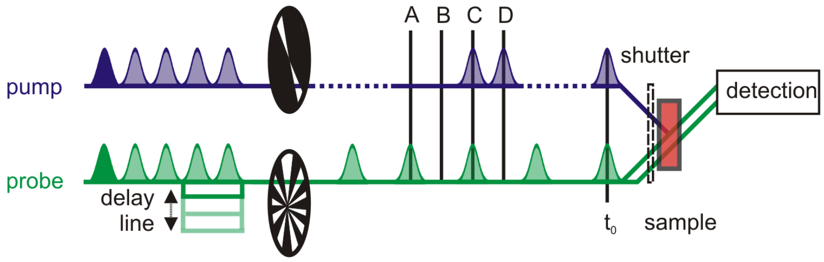

Fig. 2.4 Schematic overview of the pump-probe transient absorption experiment for solid sample using the background subtraction. After an appropriate chopper (50 Hz for pump 2-shot asymmetric chopper *vs.* 505 Hz for probe 10-shot symmetric chopper) setting the same 4 pulse pairs indicated by letters of A, B, C, and D were generated. An additional mechanical shutter blocked all the pulses during the time window of sample movement and data acquisition.

mechanical shutter (Electro-Optical Products Corp.), controlled by computer, was placed just in front of the film sample blocking all pump/ probe pulses. To assure no pump pulse hit the fresh spot during the time period between the opening of the main shutter and the arrival of the four different pump-probe pulse pairs in the correct sequence (A $\rightarrow$ B $\rightarrow$ C $\rightarrow$ D, in Fig. 2.4), an additional blocking time window was needed. Furthermore, the solid sample ((x/y)- translation stages were still shaking after fast sample movement was stopped, so some more milliseconds were required for the stability of the solid sample. Thus, the chopper in the pump beam path was equipped with an asymmetric 2-shot blade (MC1F2P10, Thorlabs) instead of the symmetric 10-shot blade and set to a frequency of 50 Hz allowing only two consecutive pump pulses go through the blade slit. This blade offered another 18 ms more after the opening of main shutter. The optical chopper equipped with a symmetric 10-shot blade (MC1F10, Thorlabs) on the probe beam path is set the same as the liquid sample case with a frequency of 505 Hz. The two choppers were used simultaneously and phase-locked to each other. Under these conditions, the same four pump-probe pulse pairs were achieved, and subsequently, the background subtraction was implemented. The applied background subtraction strategy was capable of reducing noticeable amounts of scattered pump light, specially the scattered pump light artifacts originating at the air/solid-phase interfaces which were so severe that the transient signals positioned in pump wavelength range were completely obstructed (spectral coverage $\sim$ 100 nm).

Calculation of the change in optical density (Δ OD)

The absorbance $A(\lambda,\Delta t)$ of a sample is the negative logarithm of intensity of the probe pulses I$_{pr}$ normalized by the intensity of the reference pulses I$_{ref}$ with absence of the pump pulse, because of the intensity differences between probe and reference beams.

$$A(\lambda,\Delta t) = -\log\left(\frac{I_{pr}}{I_{ref}}\right) \tag{2.1.3.1}$$

The change in optical density is calculated as the difference of absorption of excited molecules A^* and unexcited molucules A^0, respectively:

$$\Delta OD(\lambda,\Delta t) = A^*(\lambda,\Delta t) - A^0(\lambda,\Delta t) \tag{2.1.3.2}$$

According to the description in the previous part, the pulse sequence ((A → B → C → D) allows the detection of A^* (C: pump on, probe on) and A^0 (A: pump off, probe on), which can be used to calculate $\Delta OD(\lambda,\Delta t)$ directly during the measurement. Furthermore, signal contributions from pump pulse (i.e. scattered pump light) were obtained by CCD camera (D: pump on, probe off) and subsequently subtracted from the A^*. The state B (pump off, probe off) supplies the ambient background signals, which also were subtracted from the A^0.

	pulse combination	intensity notation	signal contribution
A	pump off, probe on	$I^0_{pr/ref}\,(\lambda,\Delta t)$	unexcited molecules
B	pump off, probe off	$I^B_{pr/ref}\,(\lambda,\Delta t)$	ambient background
C	pump on, probe on	$I^*_{pr/ref}\,(\lambda,\Delta t)$	excited molecules
D	pump on, probe off	$I^S_{pr/ref}\,(\lambda,\Delta t)$	scattered pump light

In the above table, $I^0_{pr/ref}(\lambda,\Delta t)$ donates the respective pulse intensities detected for unexcited sample molecules, while $I^*_{pr/ref}(\lambda,\Delta t)$ represents the respective pulse intensities for excited sample molecules. $I^S_{pr/ref}\,(\lambda,\Delta t)$ is the ambient background signals, while $I^B_{pr/ref}\,(\lambda,\Delta t)$ corresponds to the scattered pump light. Finally, the background corrected changes in optical density are calculated as follows:

$$\Delta OD(\lambda,\Delta t) = -\log\left(\frac{I^*_{pr}(\lambda,\Delta t) - I^S_{pr}(\lambda,\Delta t)}{I^*_{ref}(\lambda,\Delta t) - I^S_{ref}(\lambda,\Delta t)} \times \frac{I^0_{ref}(\lambda,\Delta t) - I^B_{ref}(\lambda,\Delta t)}{I^0_{pr}(\lambda,\Delta t) - I^B_{pr}(\lambda,\Delta t)}\right) \tag{2.1.3.3}$$

2.2 Molecular contributions to transient absorption signals

Difference absorption spectra obtained by polychromatic detection of the absorption with and without photo-excitation (probe and reference) as a function of the pump-probe delay time yielded a two-dimensional map of the photo-induced transient absorption changes ΔOD (*cf.* $\Delta A(\lambda, \Delta t)$ in the Section 2.1.3). Fig. 2.5 shows a schematic overview of the transient absorption signals consisting of superimposed contributions from various processes: the first contribution appears by negative ground state bleaching (GSB) caused by the decreased number of molecules in the electronic ground state as a fraction of the molecules is promoted to the excited state after pump pulse excitation; The second contribution is given by stimulated emission from the photo-excited state (SE, also negative) induced by the photons of the probe pulse; and the third contribution is provided by positive excited-state absorption (ESA), which results from the absorption of a probe photon at a certain wavelengths where the transition is optically allowed from the electronic excited state S_n to a higher excited state S_m. The temporal evolutions of both SE and ESA reflect the dynamics in the excited state, and the overall ESA decay is usually related to the characteristic time of the photochemical reaction. After returning to the electronic ground state, the vibrationally excited reactant and product molecules give rise of the positive hot ground-state absorption (HGSA). Eventually the GSB is refilled, leading to the contribution of the so called ground-state recovery (GSR). The slow spectral evolution of the HGSA towards the permanent absorption at long delay

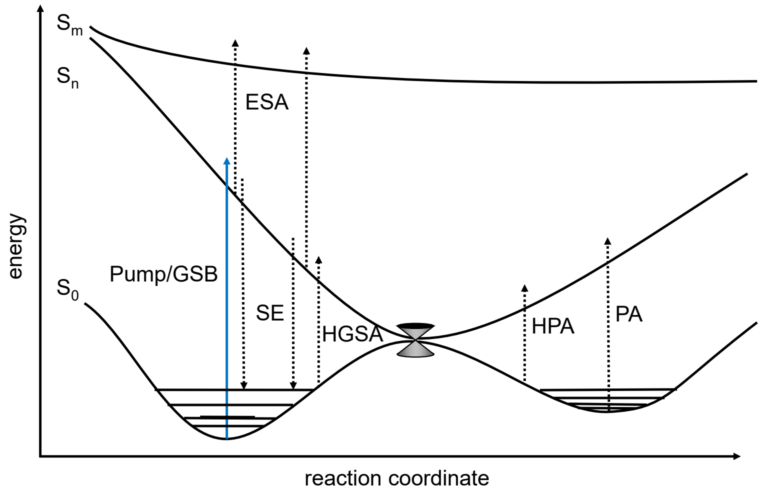

S_0	electronic ground state	HGSA	hot ground state absorption
$S_{m/n}$	excited state (m > n)	GSB	ground state bleach
ESA	excited-state absorption	HPA	hot product absorption
SE	stimulated emission	PA	product absorption

Fig. 2.5 Schematic overview of the different contributions to the transient absorption signal.

times provides information on the cooling processes of the molecules in their electronic ground states. A big advantage of broadband transient absorption spectroscopy is its intrinsic capability of detecting transient populations of non-fluorescent states that allows a complete observation of the dynamics from the FC region of the initial ES all the way to the equilibrated GS product(s).

2.3 Coherent artifacts in transient absorption spectroscopy

The interaction between the intense pump pulse and the weaker probe pulse around $\Delta t = 0$ gives rise to coherent artifacts. The non-molecular contributions to the transient absorption signals include cross-phase modulation (XPM), multi-photon or two-photon absorption (2PA or TPA), and stimulated Raman scattering (SRS).

XPM results from the transient modulation of the refractive indices in the cell window, solvent and substrate (in the case of a solid film) by the intense pump pulse which induces a redistribution of the frequencies of the chirped probe pulse.[11–13] Additionally, 2PA can occur when pump and probe photons are simultaneously absorbed in the windows of the sample cell and the solvent, whereas SRS occurs when the frequency difference of pump and probe photons coherently interact with a vibrational mode of same frequency in such medium. The spectral and temporal properties of the coherent signals strongly depend on the excitation wavelength, the pump energy, the chirp of the probe pulses, the temporal and spectral distribution of the pump pulse, the optical path length of the sample cell, the thickness of cell window and substrate (for a solid film), the solvent and polymer (for a solid film). Before or after the sample measurement, a measurement of the pure solvent (in the case of solution samples) or non-doped polymer films (solid samples) under the same conditions as the sample measurement enables one to characterize the XPM and SRS contributions. In the step of data preprocessing these were subtracted from the results of the sample measurements with suitable scaling factors.[12] If present, SRS signal can be described as the pump-probe cross-correlation function and therefore be used to determine the time resolution of the experiment.[12] Details on the transient artifacts and their correction in the present transient absorption setup can be found elsewhere.[10,14]

All other details regarding the measurements such as excitation wavelengths and energies can be found in the corresponding experimental section of Chapter 3 – 6.

2.4 Data processing

2.4.1 Data preprocessing

Wavelength calibration of the measured two-dimensional transient absorption data matrices was done by using a number of bandpass interference filters covering the wavelength range of $\lambda_{\text{probe}} = 330 - 650$ nm.[10] Unless corrected, the whitelight pulses are chirped, which means they posses a certain temporal shape, in which – caused by so-called group velocity dispersion (GVD) – the blue wavelengths propagate slower than the red wavelengths, resulting in different arrival times at the sample. A time-zero correction of the obtained transient absorption spectra was accounted for before deeper data analysis. In order to correct this temporal shape, the XPM signals in the respective solvent/ non-doped film were fitted at multiple wavelengths. A number of time zero values from each of the fits were extracted and described by polynomial function with respect to the wavelength. The resulting function was used to correct the chirp in the transient data matrices according to a procedure already explained in detail in earlier works.[14] The solvent contributions (i.e. XPM) were subtracted from the results of the sample measurements with suitable scaling factors as described in section 2.3. Time-zero correction and solvent-contributions subtraction were performed with a self-written MATHEMATICA program.[10,14]

2.4.2 Singular value decomposition (SVD)

In this Thesis, a non-linear least-squares fitting based on singular value decomposition (SVD) of all the data under study was performed for a quantitative global analysis .[15] The software toolbox was developed by Dr. F. Renth in MATHEMATICA environment. Before deeper data analysis, the data matrices under study needs to be pre-processed with regards to time-zero correction and solvent-contributions subtraction.

The principle of SVD analysis has been explained in previous works of the work group[16,17] and books.[18,19] Here, the present Thesis only describes briefly the theory and mainly the procedures of data analysis under study using the software toolbox. The TA data were collected in a matrix Ψ of dimensions $m \times n$, where m and n are, respectively, the number of different time delays and wavelengths. The matrix element Ψ_{ij} then contains the measurement at time delay t_i and wavelength λ_j. Using the matrix notation allows the use of matrix decomposition technique. The singular value decomposition of Ψ is given by

$$\Psi = U \cdot S \cdot V^T \tag{2.4.2.1}$$

where U and V are orthogonal matrices of dimensions $m \times n$ and $n \times n$, respectively, whose columns contain the left singular vectors (concentration profiles of components) and right singular vectors (component spectra). The matrix S of dimension $m \times n$ is its diagonal, which contains the singular values. When there is linear independencies between the spectra (or concentration profiles) of the components, and thus no linear relationship between the columns of the matrix, the matrix is of full *rank*. The *rank* is equal to the number of the components (*rank* = n_{comp}). In the TA data, we do not know the number of the components, so we can estimate *rank* of a data matrix Ψ.

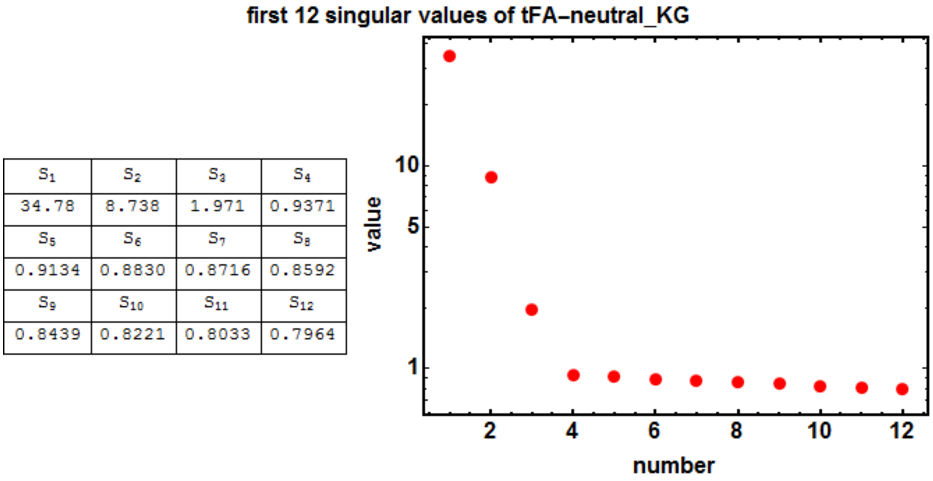

S_1	S_2	S_3	S_4
34.78	8.738	1.971	0.9371
S_5	S_6	S_7	S_8
0.9134	0.8830	0.8716	0.8592
S_9	S_{10}	S_{11}	S_{12}
0.8439	0.8221	0.8033	0.7964

Fig. 2.6 . Singular-value scree plot for tFA obtained from the SVD analysis on a logarithmic scale.

The important information obtained from SVD is the rank of the data matrix. So the first step of the SVD analysis here is to estimate the number of relevant SVD components n_{comp} (also referred to as *rank*) based on the following three step of inspections: (i) by inspection of the scree plots with respect to the number of singular values, it shows clearly the fall-off of singular values of the most significant components. Since we are not dealing with noise-free data sets, the baseline of the scree plot does not go to zero. In general, the larger singular values indicate mostly signals, while the significant small singular values contain noise. One can straightforward estimate the number of components needed, since singular values of signals are significantly higher than the rest noise-related ones. (ii) the obtained SVD spectra and SVD time traces after decomposition are evaluated. The minimum number of the SVD spectra and SVD time traces containing the spectral and temporal information of signals, respectively, is needed to reconstruct the approximation the *rank* n_{comp}. (iii) the two-dimensional approximations of the *rank* n_{comp} inspected for remaining systematic deviations with respect to the input matrices. Using the estimated number of singular values,

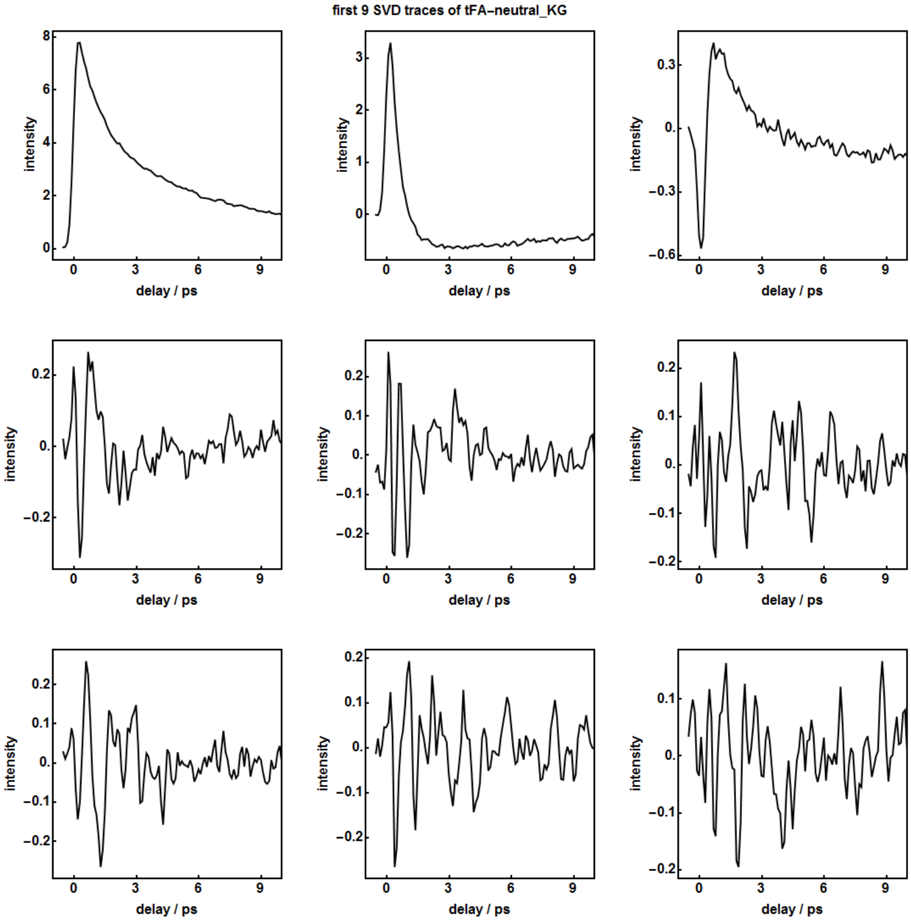

Fig. 2.7 The first nine SVD traces for tFA obtained from the SVD analysis.

one can reconstruct the data matrices described as a linear combinations of a subset to extract the signal out of the data, effectively filtering the noise.[20–22]

A representative determination of the singular value number n_{comp} for the broadband transient fluorescence data of tFA has clearly indicated that $n_{comp} = 3$ singular values are sufficient to reconstruct the majority of the signals present in the data matrix. In the present data set, the scree plot (Fig. 2.6) shows the first three singular value are significantly higher than the rest which are the experimental noise. Note that the difference from the fourth singular value to the twelfth one is ~ 0.1 reflecting the experimental noise contributions. The first nine time traces (the left singular vectors (U matrices) in matrix) obtained from SVD are shown in Fig. 2.7. As can be seen, almost only the first three time traces contain temporal signals of the data matrix. The corresponding first nine SVD spectra (the right singular vectors (W matrices) in matrix) are presented in Fig. 2.8. It is more obvious that only the first three SVD spectra contain spectral structure from the data. On the other word,

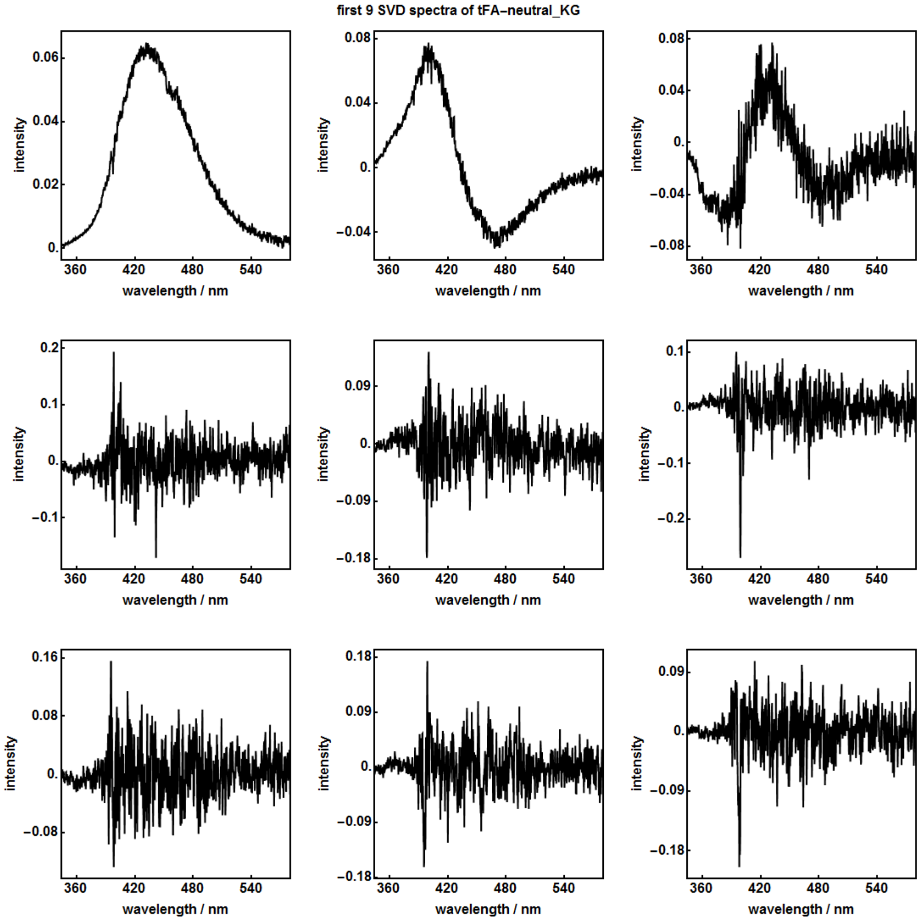

Fig. 2.8 The first nine SVD spectra for tFA obtained from the SVD analysis.

the noise-time trace and noise-spectra can be recognized by the absence of the structure in the left and right singular vectors. By inspecting the scree plot, SVD time traces and SVD spectra, the first three components ($n_{comp} = 3$) are appropriate to reconstruct data set present only the sample signals. However, it is not always so obvious to determine the number of singular values, because of the linearly dependent information between concentration profiles and spectra of the components or physical significance of the noise components.

Subsequently the n_{comp} sets of spectra and time traces resulting from SVD can be fitted as well in a user-friendly graphical user interface (GUI) which makes it straightforward to use. Each of the single time trace is then fitted quantitatively by nonlinear least-squares fitting using a sum of n_{comp} exponential functions convoluted with the instrument response function (IRF). The resulting time constants can be used as starting values for the subsequent global fit. In case of a permanent absorption changes caused by the formation of equilibrated product species, this can be described by a step function. If the solvent signals in certain wavelengths are not fully subtracted, which is most of the case, the residual coherent artifacts (e.g. stimulated Raman or XMP) become apparent close to time zero and can be written as an additional Gaussian function with ultrashort temporal width. Subsequently, the global analysis can be performed straightforward by fitting all time profiles simultaneously, yielding a matrix of amplitudes a_{ij} and global decay constants τ_j. The spectrum resulting from the SVD can be fitted with a sum of Gaussian. As a result an entire two-dimensional matrix can be rebuilt based on the fitted spectral and temporal profiles.

The spectral evolution needs to be elucidated followed by the dynamics evolution obtained from the above global fit. We treat the data matrix with the linear combinations of the spectral or temporal profiles. The non-linear least-squares fitting is independent of the estimated kinetic models. Without a priori knowledge about a defined kinetic and spectral model, fit the data with a sufficient number of exponential decays and their amplitudes, which constitute the decay associated difference spectra (DADS). In general, the DADS do not correspond to physically meaningful spectra.

Global analysis using a kinetic scheme, i.e. a sequential mode (scheme 2.2.3.1), results in evolution associated difference spectra (EADS) and corresponding time constants.[23,24] Each EADS with associated times is for every component. Here, the term "component" is a complicated issue to be clarified. Generally, the resulting EADS are not associated to certain molecular species because they may contain contributions from different molecular species or state. In this scenario the EADS reflect the spectral evolution: The first evolution associated difference spectra (EADS (A)) correspond to the time-zero transient difference spectra of the molecules in the FC region after populated by an input excitation pulse and subsequently form the EADS (B). The EADS (B) rise with the time constant of τ_1 and decay with the time constant of τ_2. This series continues until the $\mathrm{n^{th}}_{\mathrm{comp}}$ component decays into the final electronic ground state (GS) with time constant τ_n.

$$A \xrightarrow{\tau_1} B \xrightarrow{\tau_2} C \xrightarrow{\tau_3} D \xrightarrow{\tau_4} \cdots \xrightarrow{\tau_n} (GS) \qquad (2.2.3.1)$$

where, the arrows indicate successive monoexponential decays of time constants of EADS. The individual letters (A, B, C, and D) thus represent consecutive states of the molecules that can be distinguished by their differing spectral properties. Note that the estimated EADS may contain contributions from different molecular states (species). But this procedure enables a clear visualization of the evolution of the states (species).

What remains then is the actual physical interpretation of the estimated time constants from SVD-based global analysis. Although the underlying kinetic scheme in the EADS might not correspond exactly to the true kinetics, the EADS helps in the interpretation of the results, as they provide a clear representation of the time-dependent spectral changes caused by the evolution of the system; further state- or species-specific information can hardly be extracted from the transient spectra.

Additional details of the SVD-based data analysis for each data set are given in the respective Chapters 4 – 6.

2.5 Sample preparation

All transient absorption measurements in *n*-hexane, acetonitrile (ACN) and buffered aqueous solutions were performed in home-made flow cells with 0.2 mm quartz windows and 1 mm optical pathlength. The cell was connected to a sample reservoir with tubings and the solution was pumped through the cell with a peristaltic pump to provide fresh sample for every laser shot. Unless stated otherwise every measurement was repeated three times to verify reproducibility of the results.

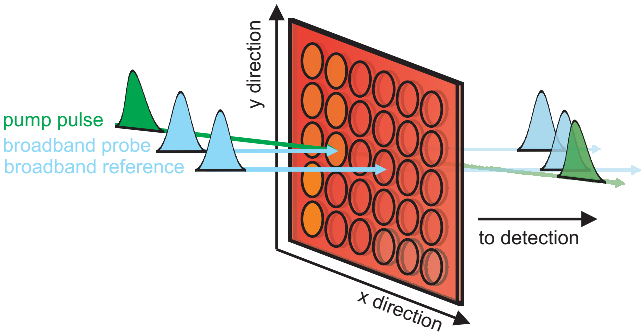

Fig. 2.9 Detailed scheme of the optical pathways at the solid sample. The sample can be moved vertically and horizontally so that the pump always hits a fresh, unexcited spot. The reference pulse has to hit a fresh sample spot as well.

The solid samples were prepared by spincoating on a quartz plate (20 mm $\times$ 20 mm, $d = 0.5$ mm) with the following recipe: (i) 500 rpm for 6 s; (ii) 2500 rpm for 33 s; and (iii) 4000 rpm for 11 s, to form a PMMA film. The solid films created by spincoating were annealed for 2 h at 45 °C. The prepared solid films were stored in the dark. The film was prepared with high filling factor of doped chromophores in order to provide higher signal-to-noise ratio for certain measurements of respective chromophore (i.e. nπ^* transition state for ABs).

As presented previously, investigating the ultrafast dynamics of molecular switches embedded into the polymer matrices requires refreshing the sample in between two successive laser shots to avoid photo-degradation or accumulation of photo-products. Using computer-controlled (x/y)- translation stages (M-404.1PD and M-403.1PD) allowed for a precise and fast transversal motion of a polymer film. The film was moved by 300 μm in the x- or y-direction for the diameter of the pump focus is 200 μm. Furthermore, a main shutter was placed in front of the sample to block all the laser shots for a time window that allowed for the translation of the film. A sketch of the detailed beam pathways in the proximity of the film sample is given in Fig. 2.9.

Further details of the static UV/VIS absorption, fluorescence spectra and the preparation of solid and solution samples are given in the respective experimental sections of Chapter 3 – 6

Bibliography

[1] T. Pancur, PhD thesis, Christian-Albrechts-Universität zu Kiel, **2004**.

[2] M. Foca, PhD thesis, Christian-Albrechts-Universität zu Kiel, **2005**.

[3] H. Studzinski, PhD thesis, Christian-Albrechts-Universität zu Kiel, **2007**.

[4] N. Schwalb, PhD thesis, Christian-Albrechts-Universität zu Kiel, **2009**.

[5] R. Siewertsen, F. Renth, F. Temps, F. Sönnichsen, *Phys. Chem. Chem. Phys.* **2009**, *11*, 5952.

[6] *Laserspektroskopie: Grundlagen und Techniken*, (Ed.: W. Demtröder), Springer, **2000**.

[7] *Optik, Licht und Laser*, (Ed.: D. Meschede), Teubner, **2005**.

[8] *Nonlinear Optics*, (Ed.: R. W. Boyd), Elsevier Inc., **2008**.

[9] *Principles of Nonlinear Optical Spectroscopy, Oxford Series in Optical and Imaging Sciences*, (Ed.: S. Mukamel), Oxford University Press, **1995**.

[10] K. Röttger, PhD thesis, Christian-Albrechts-Universität zu Kiel, **2013**.

[11] K. Ekvall, P. van der Meulen, C. Dhollande, L.-E. Berg, S. Pommeret, R. Naskrecki, J.-C. Mialocq, *J. Appl. Phys.* **2000**, *87*, 2340–2352.

[12] M. Lorenc, M. Ziolek, R. Naskrecki, J. Karolczak, J. Kubicki, A. Maciejewski, *Appl. Phys. B* **2002**, *74*, 19–27.

[13] A. L. Dobryakov, S. A. Kovalenko, N. P. Ernsting, *J. Chem. Phys.* **2005**, *123*, 044502.

[14] S. Siewertsen, PhD thesis, Christian-Albrechts-Universität zu Kiel, **2011**.

[15] S. Wang, S. Schatz, M. C. Stuhldreier, H. Bohnke, J. Wiese, C. Schroder, T. Raeker, B. Hartke, J. K. Keppler, K. Schwarz, F. Renth, F. Temps, *Phys. Chem. Chem. Phys.* **2017**, *19*, 30683–30694.

[16] R. Marschan, MA thesis, Christian-Albrechts-Universität zu Kiel, **2015**.

[17] S. R., MA thesis, Christian-Albrechts-Universität zu Kiel, **2016**.

[18] *Principal Components Analysis*, (Ed.: G. H. Dunteman), SAGE Publications, **1989**.

[19] *Essential Numerical Computer Methods*, (Ed.: M. L. Johnson), Elsevier, **2010**.

[20] E. Henry, J. Hofrichter in *Numerical Computer Methods*, Methods in Enzymology, Academic Press, **1992**, pp. 129–192.

[21] L. L. Scharf, *Signal Process.* **1991**, *25*, 113–133.

[22] A. A. Istratov, O. F. Vyvenko, *Rev. Sci. Instrum.* **1999**, *70*, 1233–1257.

[23] I. H. van Stokkum, D. S. Larsen, R. van Grondelle, *Biochim. Biophysica. Acta Bioenergetics.* **2004**, *1657*, 82–104.

[24] R. Berera, R. van Grondelle, J. T. M. Kennis, *Photosynth. Res.* **2009**, *101*, 105–118.

Chapter 3

A femtosecond pump–probe spectrometer for dynamics in transmissive polymer films

Katharina Röttger,* Shuangqing Wang, Falk Renth,* Julia Bahrenburg, and Friedrich Temps

Institut für Physikalische Chemie, Christian-Albrechts-Universität zu Kiel, Olshausenstr. 40, 24098 Kiel, Germany

K. Röttger, S. Wang, F. Renth, J. Bahrenburg, and F. Temps, A Femtosecond Pump–Probe Spectrometer for Dynamics in Transmissive Polymer Films, *Appl. Phys. B*, 2015, **118**, 185 – 193.
Reproduced by permission of Springer Berlin Heidelberg

Own contribution to this munuscript:

- ☐ Construction of the femtosecond pump–probe spectrometer
- ☐ Static absorption spectroscopy
- ☐ Analysis of the transient absorption data

---

* To whom correspondence should be addressed. E-mails: roettger@phc.uni-kiel.de and renth@phc.uni-kiel.de

Abstract

An experimental setup and data collection strategy for femtosecond transient absorption spectroscopy on thin (< 1 μm) solid polymer film samples is described. The experiment allows for parallel detection of the changes in optical density ΔOD via broadband supercontinuum probing in the VIS/UV range and single-color detection at an independently selected wavelength from the deep UV to the IR with a sensitivity of $\Delta\text{OD} \approx 10^{-3}$ per laser shot (r.m.s. standard deviation) and a time resolution below 40 fs. A fast and reproducible bi-directional translation of a two-dimensional film sample of 20×20 mm^2 in size is used to measure fresh sample spots at each detection interval. Signal readout at a 1 kHz rate enables single-shot analysis and automated signal discrimination, as well as detailed statistics on sample homogeneity, signal evolution with increasing number of pump pulses, and reproducibility. The technique was employed to study the photoisomerization of Disperse Red 1 (DR1) in films of polymethylmethacrylate (PMMA) after $\pi\pi^*$ photoexcitation at $\lambda = 473$ nm. The results revealed excited-state dynamics characterized by time constants of $\tau_1 = 0.06$ and $\tau_2 = 1.0$ ps, almost identical as in solution, but evidently enhanced vibrational excitation and slower vibrational cooling (time constant $\tau_3 = 14$ ps) after return to the electronic ground state due to the constraining polymer environment.

3.1 Introduction

Photochromic molecules such as azobenzenes, fulgides or diarylethenes[1–7] have proved as successful photoswitchable building units for applications ranging from optical data storage devices to biomedical superresolution imaging[5,8–12]. In most cases, the photoswitchable molecules need to be embedded in complex environments such as bulk polymer materials or thin films in order to translate the molecular response into the desired macroscopic effects.[13–23] Under these conditions, the particular molecular environment and specific multi-chromophore interactions may affect the photoswitching properties to unkown extent. To obtain detailed mechanistic insight into the fundamental processes on the femtosecond to picosecond time scale[24–28] that govern important photochemical properties such as product quantum yields, photostability and fluorescence, time-resolved studies of the photo-induced dynamics and chemical transformations of photo-excited molecular switches embedded in the complex environments used for applications are mandatory. Beyond fundamental interest, the results provide a basis for a rational design of functional photosensitive systems and devices with new properties and improved performance.

The required femtosecond time-resolved experiments rely on the pump–probe scheme, where an ultrashort pump pulse is used for photoexcitation and is followed by a time-delayed probe pulse that monitors the molecular response. This is repeated for many different delay times to obtain a complete set of time-dependent data set.[5,26,29] To acquire the desired information over an extended spectral and temporal range with adequate sensitivity, typical experimental implementations accumulate the signals over multiple detection cycles, which requires refreshing the sample between successive laser shots to avoid photodegradation or buildup of photoproducts. In case of gas- or liquid-phase samples, this is conveniently achieved by flow techniques. However, this approach cannot easily be extended to photoreactive molecules in solid phases because sample refreshing is too slow or cannot be repeated often enough.

Several techniques capable of simultaneous detection at multiple delay times have been developed to reduce the number of pump–probe cycles for femtosecond measurements of crystalline or amorphous solids. In the dual-echelon method, a two-dimensional spatial delay pattern is imposed on the probe pulse by inserting two orthogonally oriented step prisms (echelons) into the beam path, and the resulting array of probe pulses with predetermined time delays is imaged onto a two-dimensional detector.[30–32] The method is intrinsically restricted to single-wavelength detection, and requires replacement of the echelons for a different set of delay steps. For pump–probe imaging spectroscopy[33–36], the pump and probe pulses incident on the sample are line-shaped and intersect at a fairly large angle, so that the time delay varies across the illuminated sample area. The time resolution (typically ≥ 100 fs) and the accessible temporal range depend on the particular experimental geometry. Reported largest delay times are ≈ 20 ps using a large lateral spot size, and sensitivities for the detection of the transient absorption changes are of the order of $\Delta\text{OD} \approx 0.01$. An alternative approach that works without the need for multiple-delay detection has gained popularity recently. Optimization of the single-shot sensitivity in combination with precise single-axis transversal sample translation allowed for signal detection at $50 - 100$ different delay times with $10 - 20$ accumulations resulted in a typical noise of $\Delta\text{OD} \approx 3 \times 10^{-3}$.[37] This technique has been applied for monitoring the shape transformation of spherical Ag nanoparticles in a glass matrix upon photoexcitation.[37]

In the present publication, we report femtosecond transient absorption spectroscopy on solid polymer films doped with photoreactive molecules by making use of a high-sensitivity setup for parallel ΔOD measurements via broadband supercontinuum probing in the VIS/UV range and single-color probing at a selected wavelength from deep-UV to IR. Combined with bi-directional fast sample translation and data collection with real-time data discrimination, we achieve a sensitivity of $\Delta\mathrm{OD} \approx 10^{-3}$ (r.m.s. standard deviation) for single-shot detection and a time resolution below 50 fs. Experimental results after $\pi\pi^*$ photoexcitation of Disperse Red 1 (DR1, Scheme 3.1) doped in films of polymethylmethacrylate (PMMA) at $\lambda = 473$ nm are reported as a test case.

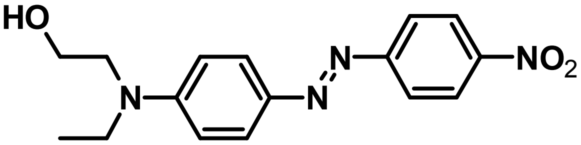

Scheme 3.1 Disperse Red 1 (DR1)

3.2 Experimental section

3.2.1 Transient absorption experiment

The experimental setup is based on our previously reported time-resolved broadband absorption spectrometer.[38] Two probe pulses are applied, one spectrally broad pulse covering the wavelength range of 310 nm $< \lambda_{\mathrm{probe}} <$ 750 nm and a second, spectrally narrower pulse which can be set to any desired wavelength in the UV to the near-IR. Usually, we select a deep-UV wavelength $\leq$ 300 nm to follow the ground state recovery and vibrational cooling processes when exciting in the deep UV. Most of the general description refers to both liquid and solid samples. For solids, translation stages allow for a precise and fast transversal (x-y) sample motion. With this setup, solid samples can be moved to a fresh spot between successive laser shots to ensure their integrity even in case of samples prone to photodegradation. In the following, the experimental details with regard to beam pathways and the timing of the translational stages will be given. A sketch of the setup is given in Fig. 3.1.

The experiment was driven by a Ti:Sa laser (Clark-MXR CPA 2001) delivering pulses with pulse lengths of 150 fs (FWHM) at 775 nm. Half of the overall output of 1000 μJ was used for the transient absorption experiment, the other half for a fluorescence up-conversion experiment and laser pulse diagnostics. The excitation and single-color probe pulses were each generated in a non-collinear optical parametric amplifier (NOPA) with subsequent temporal compression and, if necessary, frequency doubling. The broadband probe pulses were generated using supercontinuum generation (SCG) in CaF_2. All pulses were recollimated using reflective optics to reduce the chirp and obtain an optimal time resolution of the experiment.[39] To characterize both, the cross-phase molulation (XPM) and stimulated Raman scattering (SRS) contributions for the pure solvent (in the case of liquid

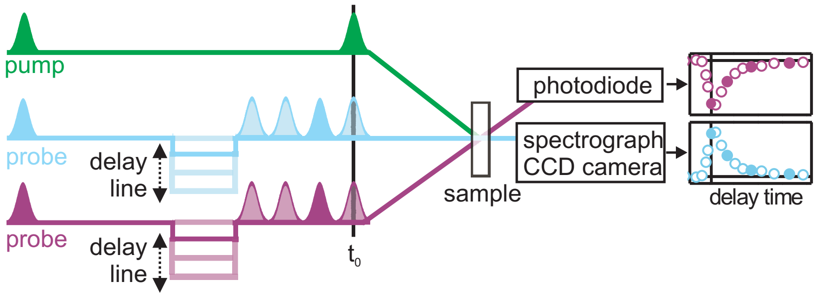

Fig. 3.1 Schematic overview of the transient absorption experiment. Two probe pulses are available to allow for simultaneous detection of transient absorption changes at 310 nm $\leq \lambda_{\mathrm{probe}} \leq$ 750 nm (shown in blue) and at a freely selected single wavelength (shown in purple).

samples) or non-doped polymer films (for solid samples) were measured independently. The center positions of the XPM at many wavelengths were then fitted with a fifth-order polynomial to obtain the time-zero function, which was subsequently employed to correct the raw transient absorption data matrices for the white light continuum chirp. For the displayed two-dimensional transient absorption maps and transient spectra, the respective time-corrected solvent and non-doped polymer film contributions were subtracted from the sample data with a suitable scaling factor accounting for the pump pulse absorption.[40,41]

A detailed view of the optical pathways near the sample and detection units is given in Fig. 3.2. The broadband and single-color probe pulses were split into probe and reference using the front and back reflection of planar quartz glass plates ($d = 5$ mm). All pulses were focused into the sample cell using reflective optics. In the sample, the probe pulses (broadband and single-color) were spatially overlapped with the pump pulse. The angles between the incident pulses were kept as small as possible to reduce the chirp of the pump and probe pulses and consequently the intensity of coherent signals.[42] Since the spectrally broad pulses are especially prone to chirping, tilting of this beam path was avoided as much as possible. A reproducible and straightforward adjustment of the broadband probe beam diameter was ensured using two focusing mirrors after the CaF_2 plate. The first mirror was placed so that a slight pre-focussing was achieved, and the second mirror focused the pulses into the sample cell. This resulted in smaller focus diameters than with only one focussing mirror after the CaF_2 plate. Generally, the probe foci were of the order of ≈ 100 μm and the pump pulse focus of the order of ≈ 200 μm. Overlapping of the two reference pulses was avoided by placing the two glass plates at an angle of $\approx 90^\circ$ (see Fig. 3.2) in case of liquid samples. In case of solid samples, the reference pulses should hit a fresh spot on the sample as is shown in Fig. 3.3 for the broadband detection pulses.

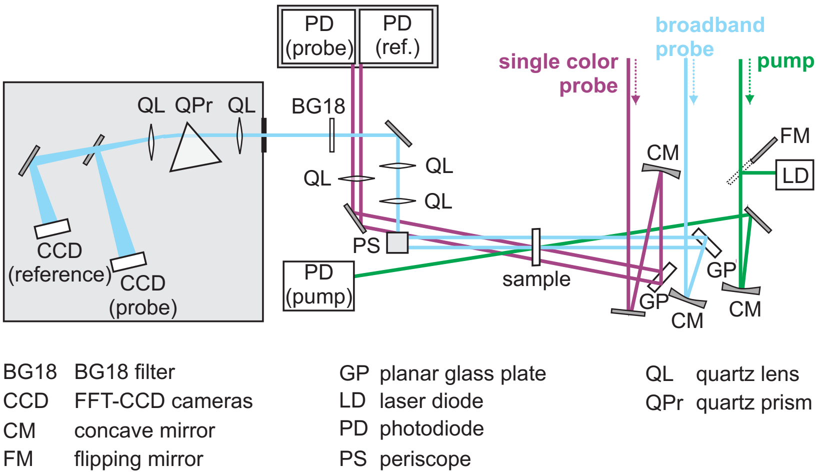

Fig. 3.2 Sketch of the pulse propagation at the sample and the detection units. The broadband probe pulses are traveling perpendicular to the sample and are spatially and temporally overlapped with the pump and the single-color probe pulses. The two reference pulses are located on the right and left of the pump and probe pulses.

After passing the sample, the relative displacement of the broadband probe and reference pulses was rotated from horizontal to vertical using a periscope. The pulses were then recollimated and focused onto the entrance slit of a prism spectrometer using either one or a combination of two quartz lenses. An optical filter (BG18, Schott) was used to lower the intensity of residual 775 nm light. In the spectrometer box, the pulses passed a quartz lens, an equilateral quartz prism and a second quartz lens. The vertically displaced probe and reference pulses were separated with a set of two square aluminum mirrors and aligned toward the CCD cameras for detection. The optical pathlength after passing the prism had to be equal for probe and reference pulses to ensure equal horizontal widths of the dispersed pulses on the cameras. The positions were adjusted so that the same lateral pixels of both cameras are illuminated by the same wavelengths using a set of interference filters. For this, a LabView routine allowing for a live scan of the camera signals was employed. The CCD cameras (Series 2000, Entwicklungsbüro Stresing, Berlin) were equipped with back-thinned full frame transfer (FFT) CCD image sensors (S7030-0906, Hamamatsu) with quantum efficiencies of ≈ 40 % in the $300-380$ nm range and up to 90 % in the visible range of the spectrum. The sensor area was 512 (H) $\times$ 58 (V) pixels (12.3×1.4 mm). Both FFT-CCD cameras were read out with the laser repetition rate of 1010 Hz.

The single-color probe and reference pulses were detected using a set of slow matched Si photodiodes (S1227-66BQ, Hamamatsu) that were read out using differential signaling to reduce noise due to electromagnetic interference. Additionally, the pump pulse intensity was monitored with a third photodiode to monitor the chopper status for every laser shot (see below). The photodiode signals were streamed into the data flow of the CCD cameras. The detection unit consisting of prism spectrometer, CCD cameras, photodiodes and controller was developed in close collaboration with G. Stresing (Entwicklungsbüro Stresing, Berlin).

Measurements were carried out in the following sequence: An optical chopper equipped with a 2-shot blade (MC1F2, Thorlabs) was used to block all pump pulses for a time window that allowed for the translation of the film to a fresh sample spot. For the given pump focus diameter of 200 μm, the pump pulses were blocked for 380 ms and the film was moved by 250 μm in the x or y direction (cf. Figs. 3.3 and Fig. 3.4) using computer-controlled translation stages mounted perpendicular to each other (Physik Instrumente, M-404.1PD and M-403.1PD).

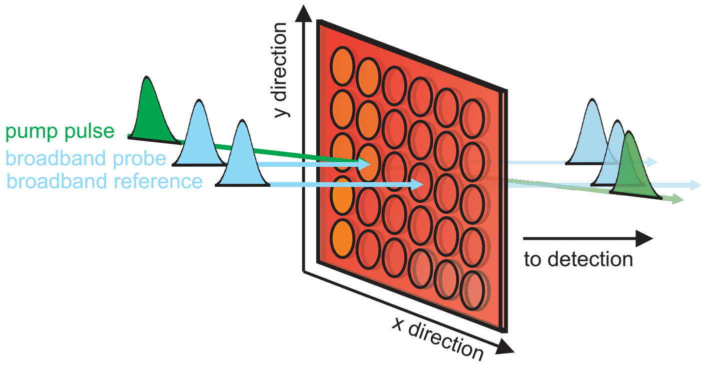

Fig. 3.3 Detailed scheme of the optical pathways at the solid sample. The sample can be moved vertically and horizontally so that the pump always hits a fresh, unexcited spot (cf. Fig. 3.4). The reference pulse have to hit a fresh sample spot as well. The single-color pulses have been omitted for clarity.

A second chopper (MC2000, Thorlabs) equipped with a 10-shot blade (MC1F10, Thorlabs) was used to block every second pump pulse, thus enabling the measurement of the sample (pump pulse unblocked) and background (pump pulse blocked) signals. The change of transient absorption was calculated from the respective probe and reference intensities.[39]

For a typical polymer film of 20 × 20 mm, taking into account the area that is needed for the reference pulses, 7 × 7 test areas of 2.5 × 2.5 mm^2 each are accessible. With a typical focus diameter of 250 μm, transient absorption changes at 10 × 10 spots per test area can be measured (cf. Fig. 3.4).

To obtain reliable results, two parameters need to be carefully checked: First, the film needs to be placed exactly perpendicular to the plane of incidence so that moving of the sample does not change the spatial overlap of the probe and pump pulses in the sample (Fig. 3.3). This can easily be achieved by adjusting the tilt angles of the film so that the

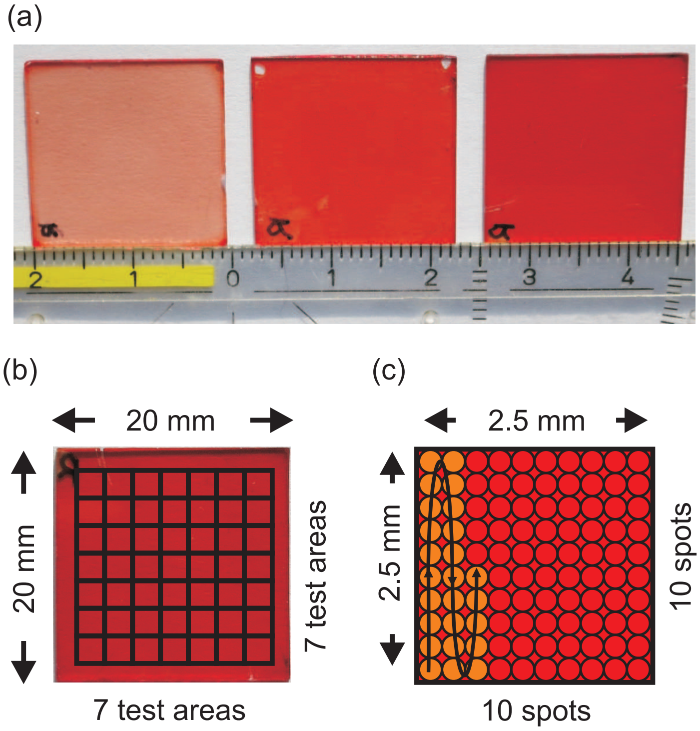

Fig. 3.4 (a) Photographs of three polymer film samples with optical densities of 0.2, 0.5, and 1.0 (from left to right). (b) Scheme of the 7 × 7 test areas on the film that can be used for time-resolved measurements. (c) Schematic drawing of one test area with 10 × 10 spots. The horizontal and vertical movement is depicted by arrows. Excited spots are depicted in orange, fresh ones in dark red.

back-reflected broadband probe pulse is traveling exactly opposite to the incoming pulses. Second, the homogeneity of the sample needs to be checked in advance. In case of sensitive samples, the use of the pump or probe pulses is not advised because of a potential damage of the sample and the inherent pulse-to-pulse fluctuations. A non-invasive alternative is to use a weak, stable laser diode at a suitable wavelength that can be coupled into the pump pulse path by a flipping mirror (cf. Fig. 3.2) and focused on the same spot as the pump pulses. The transmitted intensity can be monitored with one of the photodiodes and the change in optical density at each sample spot relative to the mean intensity can be calculated. This procedure is routinely used to check the homogeneity of the polymer films after preparation.

3.2.2 Single-shot analysis and sensitivity of the setup

The single-shot readout enables a shot-to-shot analysis of the transient absorption signals. This increases the sensitivity since the pulse-to-pulse noise of the laser fundamental is only

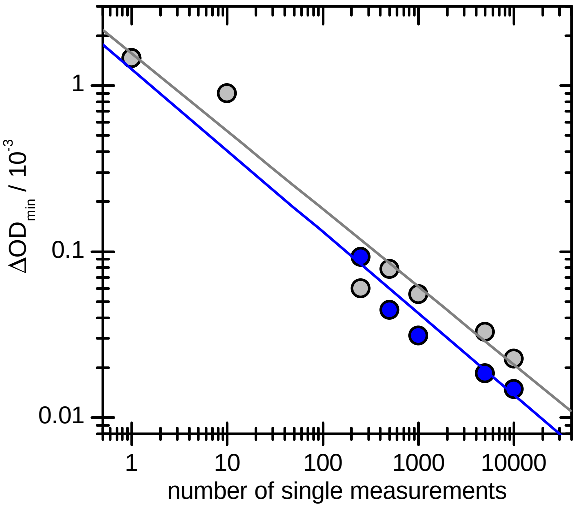

Fig. 3.5 Standard deviations of ΔOD with broadband probe at $\lambda_{\text{probe}} = 350$ nm as function of number of single measurements before (gray) and after (blue) single-shot analysis. The sensitivity of the single-color probe measurements were about three times better.

of the order of ≤ 0.5 % (r.m.s.), but on the time scale of a few seconds, laser fluctuations are more pronounced[43]. Consequently, if sample and background transmissions ($T^*(\lambda,\Delta t)$ and $T^0(\lambda)$) are averaged over long times before calculating $\Delta\text{OD}(\lambda,\Delta t)$, the correlation of both is at least partially lost after several hundred laser shots, which results in higher noise.[39] The detection sensitivities with broadband probe pulses achieved in the single-shot readout mode are depicted in Fig. 3.5 as function of the number of measured shots. The respective measurements have been performed with a liquid sample in a flow cell and thus are not affected by sample inhomogeneities. The correlation is linear with a slope of ≈ 0.5, and transient absorption measurements with sensitivities ranging from $\Delta\text{OD} \approx 1 \times 10^{-3}$ for a single shot to $\approx 2 \times 10^{-5}$ after averaging over several thousand single measurements is feasible. The single-shot readout also allows for a pulse discrimination to eliminate poor single measurements resulting from, e.g. dust particles in the optical pathway. This is performed on the fly with a LabVIEW routine. Towards these ends, the mean value $\langle \Delta\text{OD}(\lambda) \rangle$ and the deviations $|\langle \Delta\text{OD}(\lambda) \rangle - \Delta\text{OD}(\lambda)|$ of each single measurement is calculated. If the deviation from the mean exceeds a preset limit, the respective single measurement is discarded. Typically, this applies to a fraction of < 1 % of single measurements. In Fig. 3.5, the sensitivities after applying this correction are shown in blue. The sensitivity increase by this single-shot discrimination analysis for ≥ 500 single measurements per delay step is evident. For a smaller number of shots, the applied simple discrimination method is not feasible. A more sophisticated approach would require more computing capacity or computing time (leading to longer overall accumulation times) than available for our experiment.

3.3 Measurement of DR1-doped PMMA films

3.3.1 Sample preparation

DR1 was dissolved together with polymethylmethacrylate (PMMA, 100 kg/ mol, $M_W =$ 99400 kg mol^{-1}, polydispersity index 1.08) powder in toluene (Uvasol, $\leq 99\%$) or chloroform ($\leq 99\%$), and mixtures with dye content of 6 %, 10, % and 18.5 % in the solid film were prepared. PMMA was purchased from PSS GmbH, all other components were purchased from Sigma Aldrich and used without further purification. Solutions of DR1 in chloroform and toluene were purified by filter devices (Puradisc 25 TF-25 mm) prior to preparing films. Borosilicate glass (Schott, D263M, 20 × 20 mm, $d = 0.5$ mm) was used as a substrate. The thin polymer films were prepared by spin-coating[23,44] on the glass plate for 63 s at a speed of 2400 rpm and dried for 63 s at a speed of 3600 rpm.[45]

3.3.2 Static absorption spectra

The static UV/VIS absorption spectra of DR1 in solution in toluene and in the PMMA matrix are displayed in Fig. 3.6.

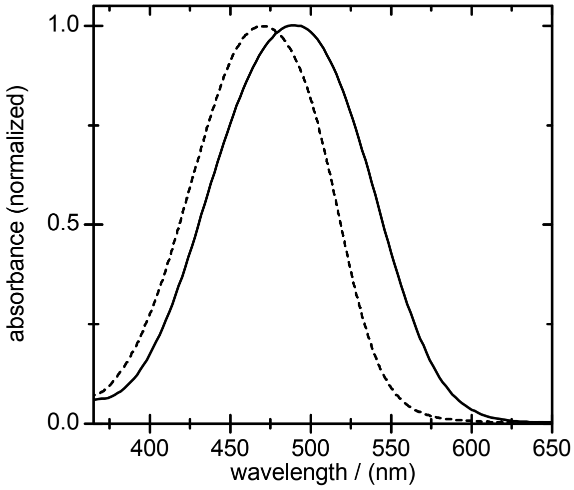

Fig. 3.6 Normalised absorbance spectra of DR1 in toluene (dashed line) and in PMMA (solid line).

The absorption band of DR1 in solution features a maximum at 469 nm attributed to a $\pi\pi^*$ transition. The weak nπ^* transition that is present in azobenzene is hidden underneath.[46,47] The static absorption spectrum of DR1 embedded in the PMMA film features a red shift of the maximum to 489 nm and a slight broadening of the band. This behavior of push-pull azobenzenes is well-known and attributed to the different polarity in the PMMA film compared to the solvent and possible formation of DR1 aggregates in polymeric environments.[40,47–49]

3.3.3 Time-resolved measurement of PMMA films doped with DR1

The excitation wavelength for the time-resolved measurement of DR1 in the PMMA matrix was $\lambda_{\text{pump}} = 473$ nm. The single-color detection was not used for these measurements. To avoid high energy densities at the test spot and potential thermal excitation of neighboring spots, the excitation energy was reduced to ≤ 200 nJ. Measurements of the transient absorption at different spots (spot-by-spot stability) on the film were done to check the film homogeneity and orientation relative to the pump and probe pulses (cf. Sec. 3.2.1). The delay time was fixed to $\Delta t = 1$ ps for these measurements. The results are displayed in Fig. 3.7(a) and show a standard deviation of $\Delta\text{OD} = 1 \times 10^{-3}$. This sensitivity is of the same order as for liquid samples (see above). It shows the correct positioning of the film as well as the high homogeneity of the film.

The shot-by-shot stability is shown by 190 single measurements at the delay time $\Delta t = 1$ ps on one test spot of the film in Fig. 3.7(b). The standard deviation is $\Delta\text{OD} \approx 1 \times 10^{-3}$. It can be seen that the signal height drops from $\approx 10 \times 10^{-3}$ to $\approx 9 \times 10^{-3}$ after 190 single measurements, indicating a slow photodegradation of the DR1 molecules. Averaging over the first 50 single measurements can thus safely be done in case of DR1. The analysis of these plots could be used for the analysis of thermal back-reactions as it was done by Warth et al.[37]

3.3.4 Results of time-resolved transient absorption measurements

For the time-resolved measurements, data were taken on one 2.5×2.5 mm^2 test area at 100 delay times (each at a fresh spot). The measurements were repeated at several other test areas on the sample to ensure the reproducibility of the results. The probe wavelength range was limited to 360 nm $\leq \lambda_{\text{probe}} \leq$ 750 nm due to the strong absorption of DR1 at $\lambda_{\text{probe}} \leq 360$ nm. Three films with dye concentrations corresponding to optical densities between 0.2 and 1.0 were measured. The time-resolved results were virtually identical and in the following only the results for the PMMA film doped with 6 % DR1 (OD = 0.2) are shown. Fig. 3.8

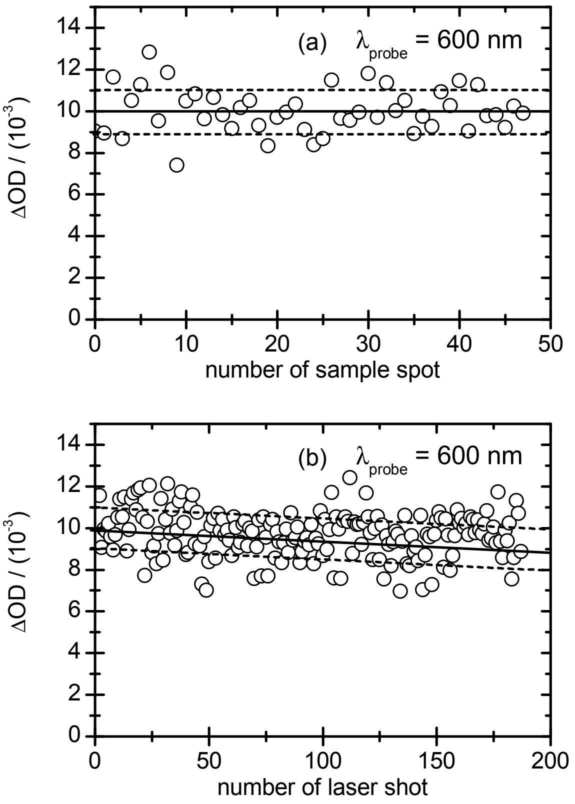

Fig. 3.7 Transient absorption changes of DR1 embedded in a PMMA matrix after excitation at $\lambda_{\text{pump}} = 473$ nm. The delay time was fixed to $\Delta t = 1$ ps. (a) *Spot-by-spot* stability of ΔOD measured at 50 neighboring spots each with a diameter of 250 μm on the film. (b) *Shot-by-shot* stability of ΔOD for 190 consecutive single measurements performed at one selected test spot.

depicts the two-dimensional (2–D) spectro-temporal transient absorption map after excitation at $\lambda_{\text{pump}} = 473$ nm.

The map features four overlapping bands: three positive absorption signals at $\lambda \approx 400$, 590 and 750 nm and a negative signal around $\lambda \approx 470$ nm which is partially obscured by scattered pump light. The negative band can be attributed to the ground state recovery (GSR) and to stimulated emission (SE). The transient spectra in Fig. 3.9 provide a closer look at the spectro-temporal behavior.

The longer-lived positive band centered at 590 nm features a pronounced red-shift during the first 400 fs, which could be due to the rapid decay of the stimulated emission contribution overlapping with the positive ESA band. The subsequent blue-shift is typical for the absorption of vibrationally excited molecules in the electronic ground state. The band is therefore assigned to hot ground state absorption (HGSA). The bands at 400 nm and 750

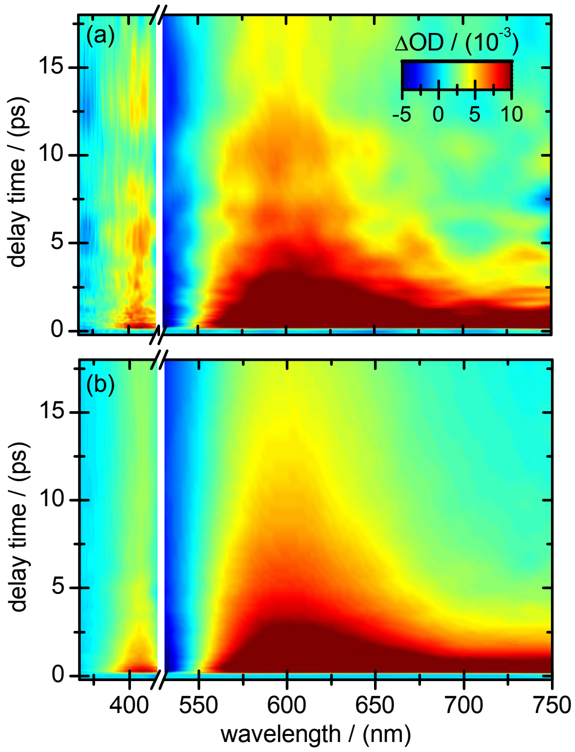

Fig. 3.8 2D spectro-temporal absorption map of the change in optical density ΔOD (transient absorption) following excitation of PMMA film doped with DR1 at $\lambda_{\text{pump}} = 473$ nm for delay times up to $\Delta t = 18$ ps. (a) Result for the single-shot mode, (b) transient signals averaged over 50 single shots. The range at $\lambda = 420$ to 530 nm is cut out because of a strong contribution of scattered pump light.

nm feature no pronounced shifts and are attributed to excited-state absorption (ESA). The signals at probe wavelengths ≤ 700 nm show a residual absorption after the maximum delay time of 18 ps which is attributed to the absorption of the *Z* isomer of DR1 and vibrationally excited *E* and *Z* isomers.

A more detailed look into the dynamics was provided by a non-linear least-squares fitting analysis of four selected time profiles at probe wavelengths $\lambda_{\text{probe}} = 400$, 531, 590 and 700 nm. The time resolution of the experiment was determined to be $\Delta r = 35 \pm 5$ fs. In accordance with our earlier study of DR1 in solution,[40] the following relaxation scheme was employed:

$$\mathrm{E} \xrightarrow{+h\nu} \mathrm{E}^{*} \xrightarrow{\tau_1} \mathrm{E}^{**} \xrightarrow{\tau_2} [\mathrm{E}^{\#}+\mathrm{Z}^{\#}] \xrightarrow{\tau_3} [\mathrm{E}+\mathrm{Z}]\,.$$

Here, E^{*} and E^{**} denote excited molecules in two different electronically excited “states” which give rise to prompt and delayed ESA, respectively, and $\mathrm{E}^{\#}$ and $\mathrm{Z}^{\#}$ denote vibrationally hot molecules in the electronic ground state. E and Z are the final products. The data analysis

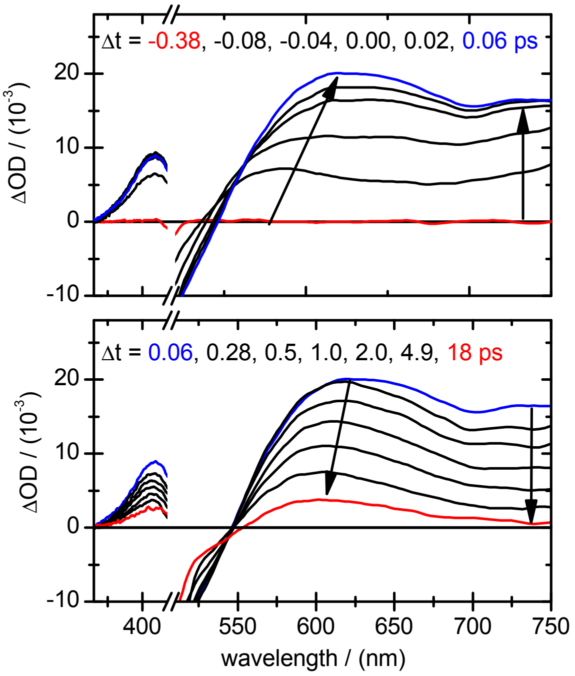

Fig. 3.9 Transient spectra of DR1 at different delay times between (a) 0 ps $\leq \Delta t \leq$ 0.06 ps and (b) 0.06 ps $\leq \Delta t \leq$ 18 ps. The range at $\lambda = 420$ to 530 nm is cut out because of a strong contribution of scattered pump light.

resulted in decay times of

$$\tau_1 = 0.06 \pm 0.01 \ \text{ps},$$
$$\tau_2 = 1.0 \pm 0.1 \ \text{ps},$$
$$\tau_3 = 14 \pm 1 \text{ ps}.$$

Additionally, a constant contribution was necessary for the description of the product absorption.

The results are shown in Fig. 3.10. The fast-decaying component (τ_1) is assigned to internal conversion of initially excited molecules E^* to E^{**}. The latter species gives rise to the delayed appearance of the ESA contribution decaying with τ_2. This decay time is in turn the rise time of the HGSA contribution of hot E and E isomers ($E^\#$ and $Z^\#$) decaying to the vibrational ground state with τ_3. The product formation of the *Z* isomer and the permanent GSR contribution is accounted for by a step function with an IRF-limited rise as it cannot be separated from the ESA and HGSA at early times.

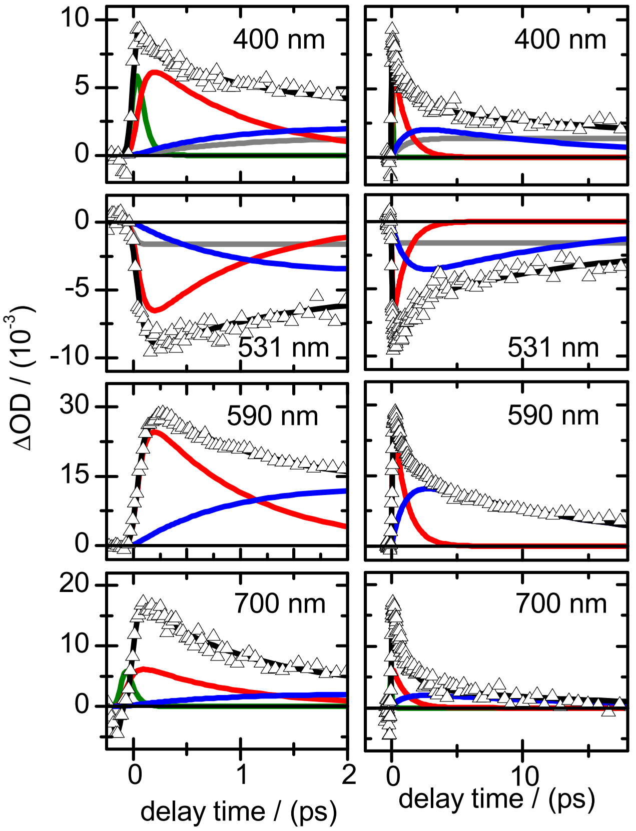

Fig. 3.10 Absorption-time profiles at four representative probe wavelengths for delay times up to $\Delta t = 2.0$ ps (left column) and $\Delta t = 18$ ps (right column). Triangles represent the data points and black lines the overall fit curves. The individual contributions to the latter are shown in green (τ_1), red (τ_2), and blue (τ_3). The contribution of product absorption is shown in gray.

3.4 Discussion

3.4.1 Transient absorption experiment

The reported femtosecond time-resolved transient absorption experiment for transmissive solid samples allows for highly sensitive measurements of broadband transient absorption spectra in the wavelength range 310 – 750 nm and the simultaneous detection of transient absorption at a single additional wavelength. In a single-shot mode, typical sensitivities of the order of $\Delta\text{OD} \approx 1 \times 10^{-3}$ enables the investigation of sensitive samples that are prone to photodegradation. Data accumulation over a larger number of laser shots on the same spot or, if necessary, after x-y-translation of the sample to a new spot, enables a corresponding improvement of detection sensitivity.

Furthermore, the setup can easily be transformed to a pump–repump–broadband probe or pump–dump–broadband probe experiment in the solid state. This only requires a third chopper in the single-color probe beam path which then serves as the second pump or dump pulse. Such experiments could be useful for the investigation of multichromophores[50,51] or the control of complicated photo-induced reactions such as the ring closure and opening of fulgides as was already shown for indolylfulgides.[52–57]

3.4.2 Time-resolved experiments of DR1 in PMMA matrices

The time-resolved experiments on DR1-doped PMMA films on glass substrates revealed molecular dynamics that are comparable with those obtained in solution.[40,46] The initial dynamics and the subsequent isomerization via a conical intersection are virtually unaffected, apart from minor shifts of the ESA bands, by the polymeric environment. The similar relaxation behavior of DR1 in solution and embedded in the PMMA matrix can be rationalized by the fact that the DR1 molecules are not covelently linked to the polymer and hence the isomerization is less hindered compared to systems in which the azobenzene unit is sterically unrestrained. In contrast, the dynamics of azobenzene derivatives cross-linked into a polymer matrix via covalent bonds has been found to be drastically slower compared to the free monomeric switches in solution.[51] These effects are currently under investigation in solid films.

The ensuing vibrational cooling dynamics in the electronic ground state is slowed down compared to the vibrational cooling dynamics in the solvent. The differences include spectral broadening of the HGSA contribution and an increase of the vibrational cooling time from $\tau_3 = 6.0 \pm 0.1$ ps to $\tau_3 = 14 \pm 1$ ps. The dependence of the rate of vibrational relaxation on the environment is most likely due to a viscosity effect. It is known that vibrational relaxation is highly dependent on the solvent viscosity and that higher viscosity leads to slower vibrational cooling.[58,59]

3.5 Conclusion

In this paper, we presented a highly sensitive femtosecond time-resolved transient absorption experiment that allows us to observe transient absorption changes in transmissive solid samples with a broadband probe pulse and simultaneously with a single-color probe pulse. With this setup, complex reaction and deactivation dynamics in the solid state can be investigated. In a single shot mode, the detection sensitivity of 1×10^{-3} allows for the investigation of sensitive samples that are easily photodegraded. Using a combination of optical choppers, the sample can be moved between successive laser shots and the transient absorption at each delay time can be monitored at a fresh sample spots. A detailed description of the setup including a convenient, non-invasive method to check the homogeneity of the sample in advance of time-resolved experiments was given. The setup can easily be extended to a pump–repump or pump–dump experiment that could be useful for the investigation of coupled chromophore systems or complex molecular switching mechanisms under solid-state conditions similar as in applications. The setup has been tested with PMMA films doped with the push-pull azobenzene Disperse Red 1 and the results were discussed in comparison with corresponding solution phase experiments.

Acknowledgments

Financial support by the DFG through the CRC 677 “Function by Switching” is gratefully acknowledged. We cordially thank Prof. Dr. F. Faupel, Dr. T. Strunskus and V. Schneider from the University of Kiel for valuable information on the sample preparation and characterization.

Bibliography

[1] *Molecular Switches*, (Ed.: B. L. Feringa), Wiley-VCH, Weinheim, **2001**.

[2] A. A. Beharry, G. A. Woolley, *Chem. Soc. Rev.* **2011**, *40*, 4422–4437.

[3] H. M. D. Bandara, S. C. Burdette, *Chem. Soc. Rev.* **2012**, *41*, 1809–1825.

[4] Y. Yokoyama, *Chem. Rev.* **2000**, *100*, 1717–1740.

[5] F. Renth, R. Siewertsen, F. Temps, *Int. Rev. Phys. Chem.* **2013**, *32*, 1–38.

[6] M. Irie, *Chem. Rev.* **2000**, *100*, 1685–1716.

[7] K. Matsuda, M. Irie, *J. Photochem. Photobiol. C* **2004**, *5*, 169–182.

[8] S. Kawata, Y. Kawata, *Chem. Rev.* **2000**, *100*, 1777–1788.

[9] D. Gust, J. Andréasson, U. Pischel, T. A. Moore, A. L. Moore, *Chem. Commun.* **2012**, *48*, 1947–1957.

[10] F. Ercole, T. P. Davis, R. A. Evans, *Polym. Chem.* **2010**, *1*, 37–54.

[11] S. W. Hell, *Science* **2007**, *316*, 1153–1158.

[12] B. Huang, M. Bates, X. Zhuang, *Annu. Rev. Biochem* **2009**, *78*, 993–1016.

[13] G. S. Kumar, D. C. Neckers, *Chem. Rev.* **1989**, *89*, 1915–1925.

[14] A. Natansohn, P. Rochon, *Chem. Rev.* **2002**, *102*, 4139–4176.

[15] T. Hugel, N. B. Holland, A. Cattani, L. Moroder, M. Seitz, H. E. Gaub, *Science* **2002**, *296*, 1103–1106.

[16] N. B. Holland, T. Hugel, G. Neuert, A. Cattani-Scholz, C. Renner, D. Oesterhelt, L. Moroder, M. Seitz, H. E. Gaub, *Macromolecules* **2003**, *36*, 2015–2023.

[17] M. Häckel, L. Kador, D. Kropp, H. Schmidt, *Adv. Mater.* **2007**, *19*, 227–231.

[18] I. Willerich, F. Gröhn, *Macromolecules* **2011**, *44*, 4452–4461.

[19] S. Wiktorowicz, H. Tenhu, V. Aseyev, *Macromolecules* **2013**, *46*, 6209–6216.

[20] Z. Sekkat, D. Morichère, M. Dumont, R. Loucif-Saïbi, J. A. Delaire, *J. Appl. Phys.* **1992**, *71*, 1543–1545.

[21] C.-C. Hsu, Y.-T. Wang, A. Yabushita, C.-W. Luo, Y.-N. Hsiao, S.-H. Lin, T. Kobayashi, *J. Phys. Chem. A* **2011**, *115*, 11508–11514.

[22] F. Fabbri, D. Garrot, K. Lahlil, J. P. Boilot, Y. Lassailly, J. Peretti, *J. Phys. Chem. B* **2011**, *115*, 1363–1367.

[23] C. Pakula, C. Hanisch, V. Zaporojtchenko, T. Strunskus, C. Bornholdt, D. Zargarani, R. Herges, F. Faupel, *J. Mater. Sci.* **2011**, *46*, 2488–2494.

[24] *Excited states and photochemistry of organic molecules*, *Vol. 53*, (Eds.: M. Klessinger, J. Michl), VCH Publishers, New York, **1995**.

[25] *Conical Intersections: Electronic Structure, Dynamics and Spectroscopy*, (Eds.: W. Domcke, D. R. Yarkony, H. Köppel), World Scientific, Singapore, **2004**.

[26] *Conical Intersections: Theory, Computation and Experiment*, (Eds.: W. Domcke, D. R. Yarkony, H. Köppel), World Scientific, Singapore, **2011**.

[27] *Analysis and Control of Ultrafast Photoinduced Reactions*, (Eds.: O. Kühn, L. Wöste), Springer, New York, **2007**.

[28] *Modern molecular photochemistry of organic molecules*, (Eds.: N. Turro, V. Ramamurthy, J. Scaiano), University Science Books, **2010**.

[29] A. H. Zewail, *J. Phys. Chem. A* **2000**, *104*, 5660–5694.

[30] G. P. Wakeham, K. A. Nelson, *Opt. Lett.* **2000**, *25*, 505–507.

[31] G. P. Wakeham, D. D. Chung, K. A. Nelson, *Thermochim. Acta* **2002**, *384*, 7–21.

[32] P. R. Poulin, K. A. Nelson, *Science* **2006**, *313*, 1756–1760.

[33] N. Furukawa, C. E. Mair, V. D. Kleiman, J. Takeda, *Appl. Phys. Lett.* **2004**, *85*, 4645–4647.

[34] Y. Makishima, N. Furukawa, A. Ishida, J. Takeda, *Jpn. J. App. Phys.* **2006**, *45*, 5986–5989.

[35] J. Takeda, A. Ishida, Y. Makishima, I. Katayama, *Sensors* **2010**, *10*, 4253–4269.

[36] Y. Minami, H. Yamaki, I. Katayama, J. Takeda, *Appl. Phys. Express* **2014**, *7*, 022402.

[37] A. Warth, J. Lange, H. Graener, G. Seifert, *J. Phys. Chem. C* **2011**, *115*, 23329–23337.

[38] K. Röttger, R. Siewertsen, F. Temps, *Chem. Phys. Lett.* **2012**, *536*, 140–146.

[39] A. L. Dobryakov, S. A. Kovalenko, A. Weigel, J. L. Pérez-Lustres, J. Lange, A. Müller, N. P. Ernsting, *Rev. Sci. Instrum.* **2010**, *81*, 113106.

[40] J. Bahrenburg, K. Röttger, R. Siewertsen, F. Renth, F. Temps, *Photochem. Photobiol. Sci.* **2012**, *11*, 1210–1219.

[41] F. Renth, R. Siewertsen, F. Strübe, J. Mattay, F. Temps, *Phys. Chem. Chem. Phys.* **2014**, *16*, 19556.

[42] M. Lorenc, M. Ziolek, R. Naskrecki, J. Karolczak, J. Kubicki, A. Maciejewski, *Appl. Phys. B* **2002**, *74*, 19–27.

[43] C. Schriever, S. Lochbrunner, E. Riedle, D. J. Nesbitt, *Rev. Sci. Instrum.* **2008**, *79*, 013107.

[44] N. Semaltianos, *Microelectronics Journal* **2007**, *38*, 754–761.

[45] C. B. Walsh, E. I. Franses, *Thin Solid Films* **2003**, *429*, 71–76.

[46] M. Poprawa-Smoluch, J. Baggerman, H. Zhang, H. P. A. Maas, L. De Cola, A. M. Brouwer, *J. Phys. Chem. A* **2006**, *110*, 11926–11937.

[47] C. Toro, A. Thibert, L. De Boni, A. E. Masunov, F. E. Hernandez, *J. Phys. Chem. B* **2008**, *112*, 929–937.

[48] D. Brown, A. Natansohn, P. Rochon, *Macromolecules* **1995**, *28*, 6116–6123.

[49] T. Buffeteau, F. L. Labarthet, M. Pézolet, C. Sourisseau, *Macromolecules* **1998**, *31*, 7312–7320.

[50] J. Bahrenburg, C. M. Sievers, J. B. Schönborn, B. Hartke, F. Renth, F. Temps, C. Näther, F. D. Sönnichsen, *Photochem. Photobiol. Sci.* **2013**, *12*, 511–518.

[51] J. Bahrenburg, F. Renth, F. Temps, F. Plamper, W. Richtering, *Phys. Chem. Chem. Phys.* **2014**, *16*, 11549.

[52] A. Rupenyan, I. H. M. van Stokkum, J. C. Arents, R. van Grondelle, K. J. Hellingwerf, M. L. Groot, *J. Phys. Chem. B* **2009**, *113*, 16251–16256.

[53] Z. Wei, T. Nakamura, S. Takeuchi, T. Tahara, *J. Am. Chem. Soc.* **2011**, *133*, 8205–8210.

[54] S. Draxler, T. Brust, S. Malkmus, J. A. DiGirolamo, W. J. Lees, W. Zinth, M. Braun, *Phys. Chem. Chem. Phys.* **2009**, *11*, 5019–5027.

[55] S. Draxler, T. Brust, J. Eicher, W. Zinth, M. Braun, *Opt. Commun.* **2010**, *283*, 1050–1054.

[56] T. Brust, S. Malkmus, S. Draxler, S. A. Ahmed, K. Rück-Braun, W. Zinth, M. Braun, *J. Photochem. Photobiol. A* **2009**, *207*, 209–216.

[57] T. Brust, S. Draxler, J. Eicher, W. J. Lees, K. Rück-Braun, W. Zinth, M. Braun, *Chem. Phys. Lett.* **2010**, *489*, 175–180.

[58] R. M. Stratt, M. Maroncelli, *J. Phys. Chem.* **1996**, *100*, 12981–12996.

[59] I. Martini, G. V. Hartland, *J. Phys. Chem.* **1996**, *100*, 19764–19770.

Chapter 4

Ultrafast dynamics of a photochromic azobenzene embedded into polymer films

Shuangqing Wang,[a] Thomas Strunskus,[b] Franz Faupel,[b] Falk Renth,*[a] and Friedrich Temps*[a]

[a] Institut für Physikalische Chemie, Christian-Albrechts-Universität zu Kiel, Olshausenstr. 40, 24098 Kiel, Germany.
[b] Institut für Materialwissenschaft, Christian-Albrechts-Universität zu Kiel, Kaiserstr. 2, 24143 Kiel, Germany.

Manuscript in preparation.

Own contribution to this munuscript:

- ☐ Synthesis of the azobenzene derivative
- ☐ Static absorption spectroscopy
- ☐ Time-resolved absorption spectroscopy
- ☐ Analysis of the transient absorption data
- ☐ Writing of the manuscript

---

* To whom correspondence should be addressed. E-mail: renth@phc.uni-kiel.de, temps@phc.uni-kiel.de

Abstract

The photoisomerization of the *cis*- and *trans*-isomers of an azobenzene (AB) derivative embedded into a thin polymethylmethacrylate (PMMA) film was studied by static and femtosecond time-resolved absorption spectroscopy following visible $S_1\,(n\pi^*)$ and UV $S_2\,(\pi\pi^*)$ excitation. For both isomers, the initial excited-state reaction pathways, comprising dynamics in the vicinity of the Franck-Condon region of the photo-excited S_1 or S_2 states, ultrafast $S_2 \rightarrow S_1$ internal conversion upon S_2 excitation in ≤ 1 ps, and the early evolutions in the S_1 state are essentially unchanged compared to solution. Conversely, the crucial subsequent slower dynamics in the S_1 state is strongly affected by the embedding in the polymer matrix. Whereas the *trans*-isomer exhibits six-fold increase of excited-state lifetime, the ground-state dynamics of *cis*-isomer is slowed down moderately by a factor of 2 in a polymer film. The volume constraints by the polymeric environment impede the *trans* → *cis* photoisomerization much more strongly than the reverse reaction. The findings provide a rationale for reduced isomerisation quantum yields of ABs in volume-restricted environments.

4.1 Introduction

Photochromic molecules capable of undergoing photochemical transformations by irradiation with light of two different wavelengths[1,2] are intensively studied for applications such as high-density optical data storage,[3] signal processing,[3–6] super-resolution imaging,[7] light-driven molecular machines,[8,9] or ophtalmic lenses.[10,11] To achieve a desired macroscopic function, the photoswitches are embedded into polymers,[12–16] liquid crystals,[17–19] or thin solid films.[20,21] In such complex environments, the molecular switching may be strongly affected by cooperative effects, interactions between the chromophores, and the lack of free reaction volume.[22–26] Among optical molecular switches, azobenzenes (ABs) have received particular interest due to the large-amplitude changes in length, volume, dipole moment, and non-linear properties associated with the photo-reversible *trans* → *cis* isomerisation of the N=N double bond, their remarkable photostability, and the relative ease of chemical modifications.[27–32] Furthermore, ABs have been shown to isomerize even under strong inter- and intramolecular steric constraints.[33–39]

The UV-VIS absorption spectra of both the *trans* and *cis* AB isomers show a weak band in the visible related to the $S_1(n\pi^*)$ transition, and a much stronger band in the UV due to the allowed $S_2(\pi\pi^*)$ transition. Irradiation in the UV is usually performed to affect *trans* $\rightarrow$ *cis* isomerisation, whereas the *cis*-isomer is switched back by visible excitation, where its absorption is slightly higher than for *trans*-AB (see, e.g., Refs. [31] and [32] for recent reviews on AB photoisomerization). Extensive studies by ultrafast spectroscopy and quantum chemical calculations have shown that the extraordinary photostability of ABs is related to internal conversion (IC) processes on the femto- to picosecond time scale mediated by conical intersections (CIs).[31,32,40,41] Upon $S_2(\pi\pi^*)$ excitation in the UV, the first step is ultrafast IC to the S_1 state, so that isomerisation and deactivation into th e electronic ground state occurs from the S_1 state irrespective of the excitation wavelength.[31,32,42–44] Previously suggested isomerisation pathways via simple rotation about the central N=N double bond, in-plane inversion on one of the nitrogen atoms, or concerted inversion via a linear transition state have now been disapproved in favour of a pedal-like torsional motion of the central C−N=N−C moiety is generally seen as the relevant isomerisation coordinate.[31,32,42–44] This so-called hula-twist mechanism, initially suggested as volume-conserving *trans* $\rightarrow$ *cis* isomerisation pathway for polyenes,[45,46] can explain the observed photoisomerization of rotation-restricted ABs, and might provide a rationale for the capability of ABs to isomerise even in strongly confined environments and under external forces.[12,20,37,38,47–50]

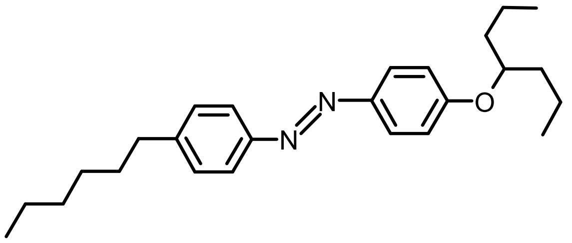

Scheme 4.1 *trans*-isomer of the studied AB derivative 4-hexyl-4′-(1-propylbutoxy) azobenzene (**1E**).

We have employed femtosecond time-resolved absorption spectroscopy to obtain detailed insight into the photo-induced processes of the AB derivative 4′-hexyl-4-(propyl-butoxy)-azobenzene **1**, see Scheme 4.1) embedded into a PMMA matrix and in *n*-hexane solution. The long alkyl side chains of **1** increase the solubility in the polymer matrix and prevent phase separation even at high filling factors, enabling its successfull application of light-controlled capacitance switching of metal/polymer nanocomposites[16] and in a photo-responsive organic field-effect transistor.[6] Our findings are highly relevant for optical switching of ABs subjected to strict volume constraints, as is common in light-responsive polymeric application materials.[13,18,35,51]

4.2 Experimental

4.2.1 Materials & static spectroscopy

The synthesis of the *trans*-isomer of 4-hexyl-4′-(1-propylbutoxy) azobenzene (**1E**, see Scheme 4.1) was performed following Ref. [16] from *trans*-4-(4′-hexylphenyl)-diazophenol and 4-bromoheptane. Purification of the reaction product by column chromatography on silica gel with chloroform yielded **1E** as a highly viscous orange-red liquid with a purity of $> 99\,\%$ as determined by ^{1}H NMR. Solutions of **1Z** in toluene or *n*-hexane (Uvasol Sigma-Aldrich, 99 %) were prepared photochemically by irradiation into the photostationary state at λ = 365 nm (PSS365) using light-emitting diodes (LEDS, Nichia NCSU034A, 11 nm spectral width). The PSS365 in *n*-hexane (toluene) contained $\geq 97\,\%$ ($\sim 87\,\%$) of **1Z** according to ^{1}H NMR.

Thin solid polymethylmethacrylate (PMMA) films with a dye load of 60 wt.-% were made from solutions of PMMA and **1E** or **1Z** (PSS365) in toluene via the spin coating technique using a P6808P programmable spin coater (SCS).[52] The required solutions with a 2:3 mass ratio of PMMA ($M_W = 99400$ g mol^{-1}, $M_W/M_n = 1.08$, PSS GmbH) and the isomers of **1** were prepared by mixing measured amounts of a 15 wt.-% polymer solution, sonicated before mildly for 30 min to ensure homogeneity, and a 30 wt.-% solution of **1E** or **1Z** (PSS365). Spin coating was performed by casting 60 μL of the solutions onto quartz substrates of 0.5 mm thickness, spun at 500 rpm for the first 6 s, then at 2500 rpm for 33 s and finally at 4000 rpm for 11 s. Cleanliness of the substrates was ensured by immersion into a 3:1 mixture of H_2SO_4 and H_2O_2 (Piranha solution) for 5h, followed by thorough rinsing with acetone, isopropanol and deionized water prior to usage. The resulting dye-loaded PMMA films were annealed for 2 h at 45 °C and had a typical thickness between 0.6 and 1 μm as measured by a DektakXT profilometer. The optical density for the thin film samples used in the transient absorption experiments was OD $\sim$ 0.06 and OD $\sim$ 0.5 at the excitation wavelengths of $\lambda_{\text{pump}} = 460$ nm and 330 nm, respectively.

All static absorption spectra were taken on a Shimadzu UV-2401 UV-VIS spectrometer. The solutions for the transient absorption experiments in *n*-hexane as solvent had a concentration adjusted to an optical density of OD $\sim$ 0.06 and OD $\sim$ 0.5 at the excitation wavelengths of $\lambda_{\text{pump}} = 460$ nm and 330 nm, respectively. During the time-resolved measurements of **1Z**, the solution reservoir was continuously irradiated by LEDs at 365 nm to maintain the photostationary state.

4.2.2 Femtosecond transient spectroscopy

All femtosecond measurements were done at room temperature. The experimental setup was based on a regeneratively amplified Ti:Sa laser system (Clark CPA2001) and has been described in some detail before.[53–55] Pulses for excitation in the visible at $\lambda_{\mathrm{pump}} = 460$ nm were generated from a home-built non-collinear optical parametric amplifier (NOPA), excitation pulses at $\lambda_{\mathrm{pump}} = 330$ nm were created by frequency-doubling of NOPA pulses at 660 nm. Pulse energy was adjusted to ~ 0.2 nJ in both cases. Broadband probe and reference pulses ranging from $\lambda_{\mathrm{probe}} = 335$ to 675 nm were provided by the front and back reflections off a planar quartz glass plate placed in the beam path of a supercontinuum generated in CaF_2. A Berek variable wave plate was used to ensure magic angle polarisation of the probe relative to the pump beam. Spectrally resolved pulse-by-pulse detection with signal readout at a 1 kHz rate was achieved by two full frame transfer (FFT) back-thinned CCD cameras (S7030-0906, Hamamatsu).[55] Phase-locked optical choppers (MC2000B, Thorlabs) were used to control the sequence of pump and probe pulses. For the solution-phase samples, every other pump beam was blocked, allowing for the detection of probe and reference transmission spectra with and without excitation at two successive laser pulses. For the solid samples each detection cycle consisted of four successive pulses that were selectively blocked in order to realise all combinations of blocked pump and probe/reference beams. The background-corrected changes in optical density at a delay time Δt are then calculated (further details regarding the data collection with background subtraction, ESI).

The data collection for the thin polymer film samples relied on fast and reproducible bi-directional translation of the two-dimensional samples to measure fresh sample spots at each detection interval. At each spot, 50 successive detection cycles were recorded, and a minimum of three different spots were used for each pump–probe delay. Independent measurements on pure solvent samples and non-doped PMMA films were carried out to characterize the cross-phase modulation (XMP) and stimulated Raman scattering (SRS) signal contributions, from which the width of the instrument response function (IRF) of ~ 50 fs (Gaussian standard deviation) and the time-zero function were obtained.

4.3 Results

4.3.1 Static spectra

The static UV-VIS spectra of **1E** and **1Z** in *n*-hexane and embedded into PMMA films are shown in Fig. 4.1 as dashed and solid lines, respectively. As the absolute values of the extinction cannot be determined with sufficient accuracy for the film samples, the *trans*-

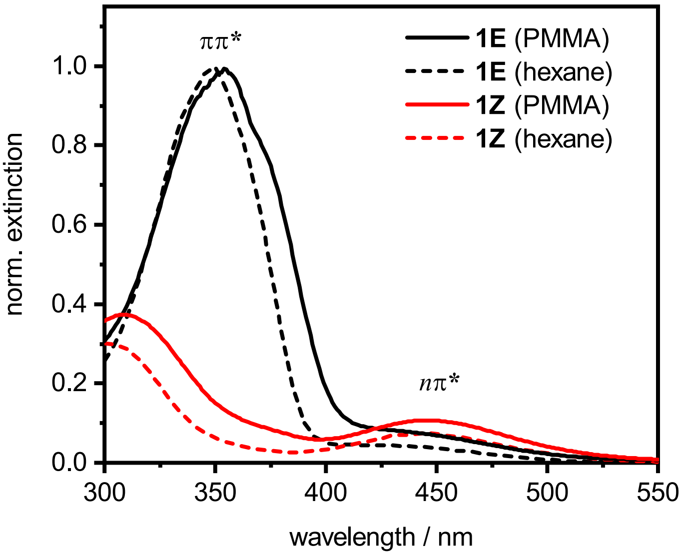

Fig. 4.1 Scaled static absorption spectra of **1E** (black) and **1Z** (PSS365, red) in PMMA films (solid lines) and in *n*-hexane (dashed lines).

isomer spectra were normalized to a maximum intensity of unity, and the resulting scaling factors were also employed for the *cis*-isomer. The stronger absorption band in the UV belongs to the $S_2(\pi\pi^*)$ transition and is centered at $\sim$ 350 nm for the *trans*-isomer and at $\sim$ 310 nm for the *cis*-isomer. The weaker band in the visible around 450 nm is due the $S_1(n\pi^*)$ transition. Compared to solution, a weak shift towards longer wavelengths and a slight broadening of the $\pi\pi^*$ band is observed in the polymer matrix. For the *cis*-isomer in PMMA, the relative intensity of both bands appears enhanced; however, this might just be due to the difficulties of proper scaling. Furthermore, it should be noted that the *cis*-film samples inevitably contain $\sim 10-15\,\%$ of the *trans*-isomer due to the preparation from toluene solutions, cf. Experimental Section).

4.3.2 Time-resolved spectroscopy

Figure 4.3 shows two-dimensional maps of the transient absorption changes of *trans*-isomer embedded into PMMA films after S_2 $(\pi\pi^*)$ photo-excitation in the UV at 330 nm and *cis*-isomer after S_1 $(n\pi^*)$ excitation at 460 nm, respectively, i.e., at the excitation wavelengths commonly used for effective photoswitching of these isomers in applications. The corresponding data obtained for solutions of **1E** and **1Z** in *n*-hexane can be found in Fig. 4.7 (ESI). The data were acquired up to much longer delay times of several hundred picoseconds, but are displayed here only for delay times up to 20 ps for the sake of clarity, as negligible spectro-temporal changes were observed at longer delay times. (Fig. 4.3b).

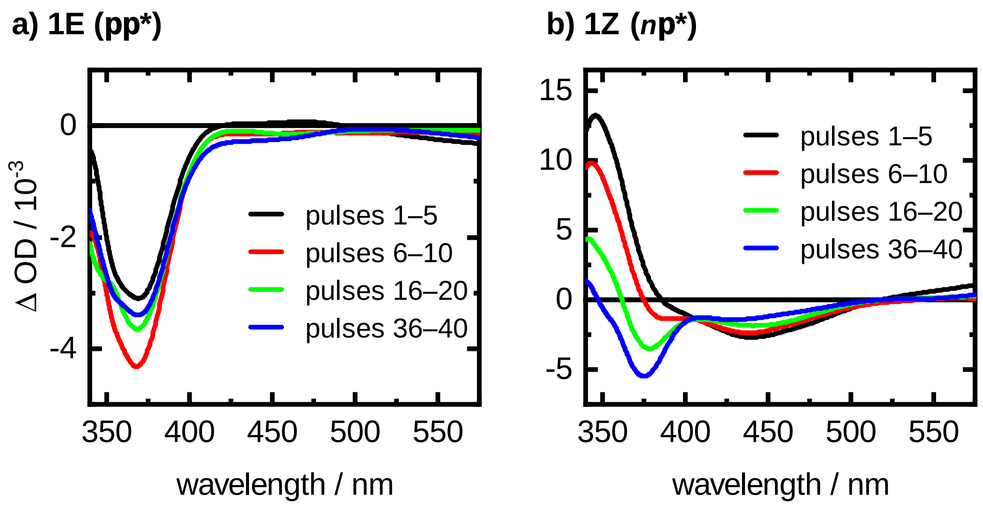

Fig. 4.2 The final transient absorption spectra (Δt = 407 ps) as a function of the number of laser pulses for **1E** (a) and **1Z** (b) embedded into PMMA. At each spot of a solid film doped with chromophores (**1E** or **1Z**), 50 successive detection cycles were recorded. The pulse dependence of the final spectra of **1Z** (b) shows clearly increasing amounts of **1E** photo-product.

The transient absorption signals in the case of photo-excited **1E** were averaged for up to 50 detection cycles for each sample spot, as there was no sign of photodegradation or accumulation of the *cis*-isomer photoproduct (Fig. 4.2a). Conversely, only the first five detection cycles were taken and averaged for **1Z** to ensure that the dominating contribution to the transient absorption signal comes from the photo-excited *cis*-isomer, as there were clear effects of the accumulation of the **1E** photo-product for increasing numbers of detection cycles

The transient absorption map of the *trans*-isomer (Fig. 4.3a) features two dominant contributions that both arise immediately after photo-excitation. A broad negative band at probe wavelengths below $\lambda_{\text{probe}} \sim 375$ nm can be safely assigned to ground-state bleaching (GSB) of the *trans*-isomer by comparison with the static UV-VIS absorption spectrum. As the signal-to-noise ratio in this wavelength region is unfavourable due to the fairly low probe light intensities, any time-dependent amplitude changes of this band are difficult to see by visual inspection. The second contribution is a positive band around $\lambda_{\text{probe}} \sim 400$ nm due to excited-state absorption (ESA). The decay of the ESA happens mostly within several picoseconds, but a part decays up to several tens of picoseconds.

The transient absorption changes for **1Z** show a broad negative band ranging from $\lambda_{\text{probe}} = 420$to ~ 480 nm due to GSB. The rise of the GSB appears to be non-instantaneous.

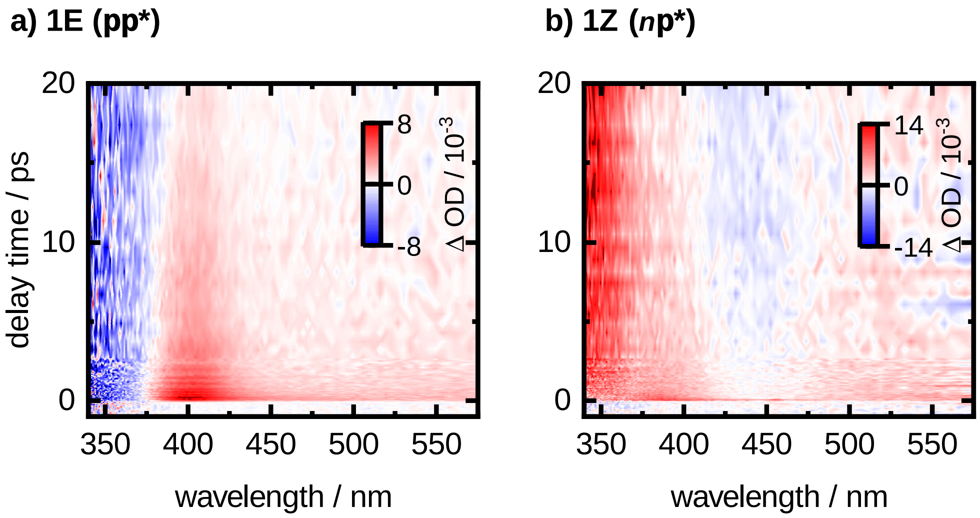

Fig. 4.3 (a) Two-dimensional spectro-temporal absorption maps of the change in optical density (ΔOD) following excitation of **1E** in PMMA at $\lambda_{\text{pump}} = 330$ nm (left) and (b) after excitation of **1Z** at $\lambda_{\text{pump}} = 460$ nm (right) for probe wavelengths in the range of $340 \leq \lambda_{\text{probe}} \leq 575$ nm and delay times between $-1 \leq \Delta t \leq 20$ ps.

However, this impression can be traced back to the presence of spectrally overlapping positive signal contributions caused by ESA, which decay on a time scale of a few picoseconds. The ESA is also seen with a low amplitude but partially obscured by noise at $\lambda_{\text{probe}} \geq 500$ nm and likely contributes to the transient absorption changes in the UV region. The most prominent signal component, however, is a strong positive band at probe wavelengths below $\lambda_{\text{probe}} \sim 375$ nm that also exhibits a delayed rise happening mostly within a few picoseconds. This band is clearly related to the formation of the **1E** photoproduct, which has a higher absorption coefficient than **1Z** at these wavelengths (cf. Fig. 4.1).

A quantitative global analysis of the data was performed by singular value decomposition[56] (SVD) of the time-zero corrected data matrices with prior subtraction of coherent signal contributions such as cross-phase modulation (XPM) and stimulated Raman scattering obtained by independent measurements of the solvent and undoped PMMA films. The global fit was achieved by a simultaneous non-linear least-squares fit of the relevant SVD time traces using a sum of exponential decays convolved with the instrument response function (IRF), where one exponential was replaced with a convoluted step function to account for conserved of species. The resulting time constants are collected in Table 4.1. Three time constants were needed for the solution measurements, with the smallest time constant τ_0/τ_1 of $0.1 - 0.2$ ps. For the **1Z** isomer in solution, the fit had to be restricted to delay times > 0.2 ps, as the earlier temporal behavior was highly non-exponential, so that the fitted value represents an

Table 4.1 Time constants from global fits to the spectro-temporal absorption data of **1Z** following S_1 $(n\pi^*)$ photo-excitation and **1E** following S_2 $(\pi\pi^*)$ photo-excitation in *n*-hexane and PMMA. The 2σ error limits are given as error of the last significant figure(s) in parentheses.

isomer	medium	$\tau_0{}^a$/ps	τ_1/ps	τ_2/ps	τ_3/ps
1E $(\pi\pi^*)$	*n*-hexane	0.09(1)	1.17(16)	3.84(12)	–
	PMMA	–	1.17(34)	23.4(61)	–
1Z $(\mathrm{n}\pi^*)$	*n*-hexane	–	0.20(1)	1.77(11)	12.3(20)
	PMMA	–	0.08(5)	1.29(36)	24.5(80)

[a] internal conversion from $S_2 \rightarrow S_1$

upper limit. This time constant is also seen for the **1Z** isomer in PMMA; due to the higher noise levels in the PMMA film data for S_2 photo-excitation of the *trans*-isomer, only two signifcant singular values remain, so that only the two larger time constants (τ_1 and τ_2) could be recovered reliably. To make further progress, a quantification of the spectral evolution by evolution-associated absorption difference spectra (EADS) was attempted assuming a sequential kinetic scheme, given here for the *cis*-isomer as

$$1\mathrm{Z} \xrightarrow{h\nu} 1\mathrm{Z}^{(1)} \xrightarrow{\tau_1} 1\mathrm{Z}^{(2)} \xrightarrow{\tau_2} 1\mathrm{Z}^{(3)} \xrightarrow{\tau_3} 1\mathrm{Z} + 1\mathrm{E}. \qquad (4.3.2.1)$$

In the specific form given, the numbered species are assumed to correspond to electronically or vibrationally excited molecules and the non-numbered species are assumed to be molecules that do not undergo further changes on the time scale of the experiment, e.g., deactivated molecules in the electronic ground state. The resulting EADS for **1Z** after S_1 $(n\pi^*)$ excitation at $\lambda_{\mathrm{pump}} = 460$ nm and of **1E** following photo-excitation into its S_2 $(\pi\pi^*)$ state at $\lambda_{\mathrm{pump}} = 330$ nm are shown in Fig. 4.4 (see ESI for the corresponding measurements of both isomers in *n*-hexane solution). It should be stressed, however, that these EADS need not be associated to a particular real molecular species and may contain contributions from different molecular species or states, i.e., individual items only represent states of the molecules that can be distinguished by their differing spectral properties and transform to each other via the corresponding time constants τ_j.[56,57] The last step of Scheme 4.3.2.1 assumes that the electronic deactivation eventually leads back to the **1Z** and possibly **1E** isomers in their S_0 electronic ground states. Although the underlying strictly sequential kinetic scheme might not correspond exactly to the true kinetics, the EADS in Fig. 4.4 provide a clear representation of the evolution of the spectral changes caused by the photo-induced dynamics of the molecules that should aid the interpretation of the results.

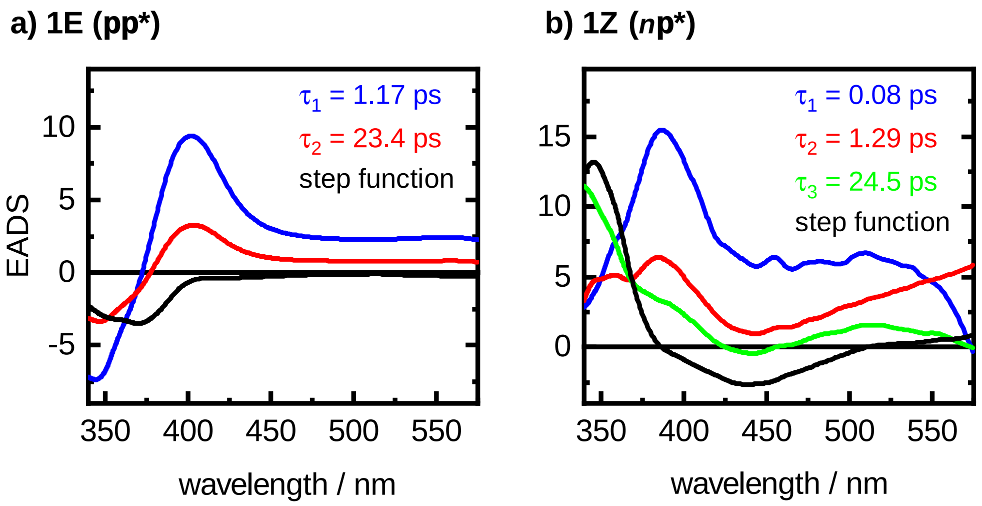

Fig. 4.4 (a) Evolution-associated difference spectra (EADS) following excitation of **1E** in PMMA at $\lambda_{\text{pump}} = 330$ nm and (b) after excitation of **1Z** at $\lambda_{\text{pump}} = 460$ nm displayed for probe wavelengths in the range of $340 \leq \lambda_{\text{probe}} \leq 575$ nm (the small hump at 460 nm is caused by residual scattered pump light). The spectra are labelled according to the time constants obtained from a global fit analysis using a consecutive (sequential) kinetic model.

Fig. 4.4a shows the three EADS required to describe the spectro-temporal changes of **1E** in PMMA after photo-excitation at $\lambda_{\text{pump}} = 330$ nm. The first EADS (blue spectrum in Fig.4.4a) corresponds to the short-time absorption of the molecules and features positive values due to ESA for probe wavelengths > 370 nm. An intense ESA band with a maximum at ~ 400 nm and a weaker, broad band at probe wavelengths between 450 nm $\leq \lambda_{\text{probe}} \leq 575$ nm can be discerned. The GSB leads to negative signals below 370 nm. This band decays with $\tau_2 = 1.17$ ps towards the second EADS, which is fairly similar in shape, but with overall lower positive and negative amplitudes. This spectrum evolves into the final EADS corresponding to the permanent absorption differences (on the time scale of the experiment) with $\tau_3 = 23.4$ ps. These absorption changes are characterized by persisting negative signals mainly for $\lambda_{\text{probe}} < 400$ nm, but discernible even up to 440 nm, that mirror the static *trans*-isomer UV-VIS absorption (cf. Fig. 4.1), and virtually no amplitude elsewhere.

Four EADS are needed in case of **1Z** in PMMA after S_1 photo-excitation (Fig. 4.4b). The time-zero EADS is purely positive due to ESA and shows two maxima around 400 and 500 nm with a broad dip in between that could be related to GSB of the *cis*-isomer. Very fast decreases in amplitude and changes in spectral shape in particular at longer probe wavelengths happening with $\tau_1 = 0.08$ ps lead to the second EADS. The subsequent spectral evolution with $\tau_2 = 1.17$ ps is characterized by a further decay of the ESA absorption and the emergence of a new intense positive band with a maximum near the blue edge of the detection range ($\lambda_{\text{probe}} \leq 340$ nm) that is indicative of the formation of **1E** photo-product molecules. The final EADS reached with $\tau_3 = 24.5$ ps shows negative signals corresponding to the GSB of **1Z**, and a corresponding strong positive peak at ~ 350 nm by **1E** product absorption. This is unambiguous evidence for a successful photo-induced *cis* → *trans* isomerisation.

4.4 Discussion

The experimental results obtained in this study give detailed insight into the photo-induced dynamics of the *cis*- and *trans*-isomers for the AB derivative **1** embedded into PMMA films compared to *n*-hexane solution. In this discussion, we first deal with the results for **1Z** and **1E** in *n*-hexane solution followed by the results in PMMA films. Eventually, we consider the excited-state and isomerization pathways of the *cis*- and *trans*-isomers upon $S_1(n\pi^*)$ and $S_2(\pi\pi^*)$ excitation, respectively.

4.4.1 Observed ultrafast dynamics in solution

The time-resolved femtosecond transient absorption data for **1E** in *n*-hexane solution can be quantified by two sub-picosecond time constants $\tau_0 = 0.09$ ps and $\tau_1 = 1.17$ ps, and one slower time constant $\tau_2 = 3.85$ ps, and thus exhibit very similar spectro-temporal behavior compared to previous experimental studies of photo-excited parent *trans*-AB.[42,58] The EADS of **1E** in *n*-hexane (Fig. 4.8a, ESI) show that the spectral shape of the time-zero EADS with a time constant of $\tau_0 = 0.09$ ps differs from the other EADS. Furthermore, a delayed rise (0.09 ps component) was observed in the ESA band centered at ~ 380 nm (cf. Fig. 4.9a, ESI). Thus, this time constant of $\tau_0 = 0.09$ ps allows to identify the time scale of the IC from the directly populated S_2 state evoluting to the buildup of a population in the S_1 state ($S_2 \rightarrow S_1$ IC). Subsequently, $\tau_1 = 1.17$ ps is related to dynamics in the S_1 state. The *trans*-isomer encounters an excited-state barrier that is responsible for the slower deactivation dynamics $\tau_2 = 3.85$ ps which describes the decay of the S_1 ESA components in the visible range. It is not related to the deactivation to the ground state, but describes excited-state dynamics. The weak-intensity probe light in the UV region prevent further analysis, thus the ESA component in the UV and the recovery of the bleach can not be followed. Quick *et al.*[42] extracted the long-lived component (17 ps) from the recovery of the bleach, however, the long-time bleach evolution is sensitive to solvent polarity/proticity. Our data did not allow to discriminate the proposed direct CNN in-plane inversion channel originating from the S_2 excited state.[42,44]

In contrast to the *trans* → *cis* isomerization, the reverse isomerisation pathway is steep or nearly barrier-less via a CI, and high isomerization quantum yields were reported.[59–61] For the *cis* → *trans* isomerization reaction following $n\pi^*$ excitation, the sum of three exponentials plus a step function are required to describe the transient absorption data. The first time component of $\tau_1 = 0.20$ ps represents an upper limit value, since the data were cut at 0.2 ps due to the higly non-exponential decay behavior.[42,59] This fast time component in good agreement with Quick *et al.*, describes the movement out of the Franck-Condon region.[42] The slower time constant ($\tau_2 = 1.77$ ps) is the conversion of the S_1 excited state to the electronic ground state via a S_1/S_0 CI. Finally, the ensuring vibrational cooling in the electronic ground state ($\tau_3 = 12.3$ ps) is indicated by the spectral narrowing from EADS3 to the step function (green and black spectra in Fig. 4.8, ESI).

For the *cis*- and *trans*-isomers in *n*-hexane upon $S_1\,(n\pi^*)$ and $S_2\,(\pi\pi^*)$ excitation, respectively, both final EADS (black lines in Fig. 4.8) show positive photoproduct absorption at 350 nm for **1Z** → **1E** and at 475 nm for **1E** → **1Z**. This provides unambiguous evidence for successful photoisomerization of both isomers in solution.

4.4.2 Ultrafast dynamics in PMMA films

The SVD analysis of the transient absorption data for **1E** embedded into a PMMA film required only two independent components for adequate fitting. While the time constant of $\tau_1 = 1.17$ ps is surprisingly similar in solution and in the polymer film, subsequent dynamics ($\tau_2 = 23.4$ ps) is significantly slowed down as compared to solution ($\tau_2 = 3.85$ ps). EADS spectral shapes being well-known from the results obtained in solution and can be associated to the same relaxation dynamics. Due to the lower signal-to-noise ratio and the larger delay steps in the solid sample measurements, the $S_2 \rightarrow S_1$ dynamics of sub-ps time component in analogy to solution cannot be resolved in the solid samples. The EADS features of the fast component (blue lines in Fig. 4.4 and Fig. 4.8) is similar to that observed in solution, and hence corresponds to the initial dynamics on the PES of S_1, exhibiting no effect by the volume-restricted environment. However, the subsequent slow time constant of $\tau_2 = 23.4$ ps is associated to the process along S_1 overcoming a high energetic barrier. The six-fold increase of this excited-state lifetime is attributed to the strict volume constraints or the aliphatic chains tangled up in PMMA microviscosity.

The final EADS (black line in Fig. 4.4a) characterized by persisting negative signals at $\sim$ 350 nm, that mirror the static *trans*-isomer UV-VIS absorption (cf. Fig. 4.1), but there is no positive absorption band discernible that could be related to the **1Z** photo-product. The *trans*-isomer appears to be possibly trapped in a optically dark long-lived triplet state through other competing pathways or the low signal-to-noise ratio of a PMMA film measurement does not allow to discern such small amplitude changes (cf. the solution case with higher quantum yield and data quality in Fig. 4.8, ESI).

For **1Z** in PMMA upon S_1 ($n\pi^*$) excitation, both fast time constants (τ_1 and τ_2) agree well with the solution case. EADS1 (blue spectrum in Fig. 4.4) associated with a time constant of $\tau_1 = 0.08$ ps shows fairly similar feature to that in solution: a broad band in the visible and a sharper band in the UV. Hence, it should correspond to escape of the excited population from the FC region and then deactivation along S_1 surface to the electronic ground state with $\tau_2 = 1.29$ ps. The time constant $\tau_3 = 24.5$ ps would reflect vibrational cooling in the electronic ground state, which is moderately slowed down by a factor of 2 as compared to solution. In our previous study of Disperse Red 1 (DR1) in a PMMA film, the same scale of the matrix effect on the ground-state process was reported.[55] An inspection of the 2D spectro-temporal map (Fig. 4.3b) and the final EADS (black line in Fig. 4.4b) shows a strong positive peak at ~ 350 nm and negative signals at ~ 450 nm matching well with the difference absorption of **1E** product and **1Z** reactant. This is unambiguous evidence for a successful photo-induced *cis* → *trans* isomerisation.

In summary, the volume constraints in the polymer film do not affect the early excited-state dynamics decried by τ_0 and τ_1 very much. While the process in the electronic ground state for *cis*-isomer is slowed down by a factor of 2, a significant six-fold slow-down in the excited-state dynamics is observed for the *trans*-isomer.

4.4.3 Excited-state deactivation and isomerization pathways

Based on the agreement with previous experimental studies of AB upon $S_2(\pi\pi^*)$ excitation in solution,[42] all our observed time constants are unambiguously related to excited-state processes. The increased excited-state lifetime of τ_2 in a PMMA film (23.4 ps resp. 3.85 ps) is due to the volume constraints for the *trans* → *cis* isomerization on the S_1 state. This excited-state dynamics of $\tau_2 \sim 3$ps was associated to the relaxation of the $n\pi^*$ population overcoming a potential energy barrier through a torsional isomerization pathway.[44,62] The torsional mechanism for isomerization is energetically preferable and the double bond torsion is the most important geometrical change leading to the isomerization and/or to the excited state decay.[44] So, the excited-state dynamics and the isomerization quantum yields are strongly influenced by the environment. The six-fold increase of the excited-state lifetime τ_2 for **1E** in PMMA indicates the wave-packet overcome a higher energy barrier to reach an intermediate excited state. On the other hand, the quantum yield of *trans* → *cis* isomerization in a PMMA film is reduced as compared with solution,[63] due to the insufficient free volume for the $S_2 \rightarrow S_1$ IC in the rotational coordinate.

In contrast to the matrix effect on the excited-state dynamics of **1E**, the only effect on the process of electronic ground state of **1Z** is moderately slowed down by a factor of 2. The same order of magnitude effect on the electronic ground-state dynamics was also observed by our previous study on a push-pull AB (Disperse Red 1, DR1). It implies no environmental effect for the excited states (τ_1 and τ_2) when the excited-state PES is barrier-less. The *cis*-isomer undergoes a much prompter torsion than the *trans*-isomer because on the slope of the PES is steeper and drives more forcefully the motion along the torsional coordinate.

According to Harms *et al.*,[64] the free volume in a PMMA film is decreased by the order of 10 % when undergoing the *trans* → *cis* photoisomerization. The *cis* → *trans* reaction demands higher free volume for isomerization. The excited-state dynamics of **1Z** are not affected by the environment, indicating a small amplitude pedal-like torsional motion as the isomerization coordinate.[65] The strongly restricted free volume for **1E** (by 21.6 %) compared to the hole free volume in the pure PMMA matrix,[64] leads to an apparent suppression of the isomerization.

4.5 Conclusions

The present study of **1Z** and **1E** embedded into thin solid PMMA films with high chromophore load upon $S_1(n\pi^*)$ and $S_2(\pi\pi^*)$ excitation, respectively, with reference to the observed dynamics of the molecule in *n*-hexane yielded detailed insight into the ultrafast electronic deactivation processes and *trans* ⇄ *cis* isomerization in volume-restricted environments. For both isomers in PMMA films, the early excited-state reaction pathways are quantitatively unchanged, with deactivation to the electronic ground state via S_1 state irrespective of the excitation wavelength and $S_2 \rightarrow S_1$ internal conversion in ≤ 1 ps as a preceding step after UV-excitation. Whereas excited-state dynamics of *cis*-isomer are barely affected by the environment, the vibrational cooling in the electronic ground state is slowed dwon by a factor of two. The embedded *cis*-isomer undergoes successful isomerisation. The six-fold increase of excited-state lifetime of *trans*-isomer compared to *n*-hexane solution indicates the molecular motions is strongly hindered in the PMMA matrix by steric volume constraints, implying a reduced *trans* → *cis* isomerization quantum yields.

Conflicts of interest

There are no conflicts to declare.

Acknowledgements

This work has been supported by the Deutsche Forschungsgemeinschaft through sub-project A1 of the SFB 677 “Function by Switching” (SW, FR, FT) and by a PhD grant (Grant no. 201306620029) by the China Scholarship Council (SW).

Bibliography

[1] H. Bouas-Laurent, H. Dürr, Organic photochromism, tech. rep., INTERNATIONAL UNION OF PURE and APPLIED CHEMISTRY, **2001**.

[2] H. Dürr, *Angew. Chem.* **2004**, *116*, 3404–3418.

[3] S. Kawata, Y. Kawata, *Chem. Rev.* **2000**, *100*, 1777–1788.

[4] K. Szaciłowski, *Chem. Rev.* **2008**, *108*, 3481–3548.

[5] D. Gust, J. Andréasson, U. Pischel, T. A. Moore, A. L. Moore, *Chem. Commun.* **2012**, *48*, 1947–1957.

[6] K. J. Lee, J. H. Woo, E. Kim, Y. Xiao, X. Su, L. M. Mazur, A.-J. Attias, F. Fages, O. Cregut, A. Barsella, F. Mathevet, L. Mager, J. W. Wu, A. D'Aléo, J.-C. Ribierre, *Phys. Chem. Chem. Phys.* **2016**, *18*, 7875–7887.

[7] S. W. Hell, *Angew. Chem. Int. Ed.* **2015**, *54*, 8054–8066.

[8] B. L. Feringa, *Angew. Chem. Int. Ed.* **2018**, *56*, 11060–11078.

[9] V. Balzani, A. Credi, M. Venturi, *Chem. Soc. Rev.* **2009**, *38*, 1542–1550.

[10] R. A. Evans, T. L. Hanley, M. A. Skidmore, T. P. Davis, G. K. Such, L. H. Yee, G. E. Ball, D. A. Lewis, *Nat. Mater.* **2005**, *4*, 249–253.

[11] N. Ishii, J. Abe, *Appl. Phys. Lett.* **2013**, *102*, 163301.

[12] G. S. Kumar, D. C. Neckers, *Chem. Rev.* **1989**, *89*, 1915–1925.

[13] A. Natansohn, P. Rochon, *Chem. Rev.* **2002**, *102*, 4139–4176.

[14] F. Ercole, T. P. Davis, R. A. Evans, *Polym. Chem.* **2010**, *1*, 37–54.

[15] Y. Yu, M. Nakano, T. Ikeda, *Nature* **2003**, *425*, 145.

[16] C. Pakula, C. Hanisch, V. Zaporojtchenko, T. Strunskus, C. Bornholdt, D. Zargarani, R. Herges, F. Faupel, *J. Mater. Sci.* **2011**, *46*, 2488–2494.

[17] T. Ikeda, O. Tsutsumi, *Science* **1995**, *268*, 1873–1875.

[18] C. J. Barrett, J. Mamiya, K. G. Yager, T. Ikeda, *Soft Matter* **2007**, *3*, 1249–1261.

[19] T. Fujii, S. Kuwahara, K. Katayama, K. Takado, T. Ube, T. Ikeda, *Phys. Chem. Chem. Phys.* **2014**, *16*, 10485–10490.

[20] Z. Sekkat, D. Morichère, M. Dumont, R. Loucif-Saïbi, J. A. Delaire, *J. Appl. Phys.* **1992**, *71*, 1543–1545.

[21] C.-C. Hsu, Y.-T. Wang, A. Yabushita, C.-W. Luo, Y.-N. Hsiao, S.-H. Lin, T. Kobayashi, *J. Phys. Chem. A* **2011**, *115*, 11508–11514.

[22] C. D. Eisenbach, *Makromol. Chem.* **1978**, *179*, 2489–2506.

[23] C. D. Eisenbach, *Polym. Bull.* **1980**, *2*, 169–176.

[24] J. Royal, J. Victor, J. Torkelson, *Macromolecules* **1992**, *25*, 729–734.

[25] G. Such, R. A. Evans, L. H. Yee, T. P. Davis, *J. Macromol. Sci. Polym. Rev.* **2003**, *43*, 547–579.

[26] A. Fihey, A. Perrier, W. R. Browne, D. Jacquemin, *Chem. Soc. Rev.* **2015**, *44*, 3719–3759.

[27] J. A. Delaire, K. Nakatani, *Chem. Rev.* **2000**, *100*, 1817–1846.

[28] A. A. Beharry, G. A. Woolley, *Chem. Soc. Rev.* **2011**, *40*, 4422–4437.

[29] F. Renth, R. Siewertsen, F. Temps, *Int. Rev. Phys. Chem.* **2013**, *32*, 1–38.

[30] C. Garcia-Iríepa, M. Marazzi, L. M. Frutos, D. Sampedro, *RSC Adv.* **2013**, *3*, 6241–6266.

[31] H. M. D. Bandara, S. C. Burdette, *Chem. Soc. Rev.* **2012**, *41*, 1809–1825.

[32] T. Kumpulainen, B. Lang, A. Rosspeintner, E. Vauthey, *Chem. Rev.* **2017**, *117*, 10826–10939.

[33] H. Rau, S. Yu-Quan, *J. Photochem. Photobiol. A* **1988**, *42*, 321–327.

[34] I. K. Lednev, T.-Q. Ye, L. C. Abbott, R. E. Hester, J. N. Moore, *J. Phys. Chem. A* **1998**, *102*, 9161–9166.

[35] K. G. Yager, C. J. Barrett, *J. Photochem. Photobiol. A* **2006**, *182*, 250–261.

[36] A. Khan, C. Kaiser, S. Hecht, *Angew. Chem. Int. Ed.* **2006**, *45*, 1878–1881.

[37] T. Pancur, F. Renth, F. Temps, B. Harbaum, A. Krüger, R. Herges, C. Näther, *Phys. Chem. Chem. Phys.* **2005**, *7*, 1985–1989.

[38] R. Siewertsen, F. Renth, F. Temps, F. Sönnichsen, *Phys. Chem. Chem. Phys.* **2009**, *11*, 5952.

[39] J. Bahrenburg, PhD thesis, Christian-Albrechts-Universität zu Kiel, **2014**.

[40] S. Matsika, P. Krause, *Annu. Rev. Phys. Chem.* **2011**, *62*, 621–643.

[41] *Conical Intersections: Theory, Computation and Experiment*, (Eds.: W. Domcke, D. R. Yarkony, H. Köppel), World Scientific, Singapore, **2011**.

[42] M. Quick, A. L. Dobryakov, M. Gerecke, C. Richter, F. Berndt, I. N. Ioffe, A. A. Granovsky, R. Mahrwald, N. P. Ernsting, S. A. Kovalenko, *J. Phys. Chem. B* **2014**, *118*, 8756–8771.

[43] J. Casellas, M. J. Bearpark, M. Reguero, *ChemPhysChem* **2016**, *17*, 3068–3079.

[44] A. Nenov, R. Borrego-Varillas, A. Oriana, L. Ganzer, F. Segatta, I. Conti, J. Segarra-Marti, J. Omachi, M. Dapor, S. Taioli, C. Manzoni, S. Mukamel, G. Cerullo, M. Garavelli, *J. Phys. Chem. Lett.* **2018**, *9*, 1534–1541.

[45] R. S. H. Liu, *Acc. Chem. Res.* **2001**, *34*, 555–562.

[46] R. S. Liu, A. E. Asato, *Proc. Natl. Acad. Sci. U.S.A.* **1985**, *82*, 259–263.

[47] Y.-C. Lu, E. W.-G. Diau, H. Rau, *J. Phys. Chem. A* **2005**, *109*, 2090–2099.

[48] S. Siewertsen, PhD thesis, Christian-Albrechts-Universität zu Kiel, **2011**.

[49] T. A. Singleton, K. S. Ramsay, M. M. Barsan, I. S. Butler, C. J. Barrett, *J. Phys. Chem. B* **2012**, *116*, 9860–9865.

[50] N. B. Holland, T. Hugel, G. Neuert, A. Cattani-Scholz, C. Renner, D. Oesterhelt, L. Moroder, M. Seitz, H. E. Gaub, *Macromolecules* **2003**, *36*, 2015–2023.

[51] J. Vapaavuori, C. G. Bazuin, A. Priimagi, *J. Mater. Chem. C* **2018**, *6*, 2168–2188.

[52] C. B. Walsh, E. I. Franses, *Thin Solid Films* **2003**, *429*, 71–76.

[53] F. Renth, M. Foca, A. Petter, F. Temps, *Chem. Phys. Lett.* **2006**, *428*, 62–67.

[54] F. Renth, R. Siewertsen, F. Strübe, J. Mattay, F. Temps, *Phys. Chem. Chem. Phys.* **2014**, *16*, 19556.

[55] K. Röttger, S. Wang, F. Renth, J. Bahrenburg, F. Temps, *Appl. Phys. B* **2015**, *118*, 185–193.

[56] I. H. van Stokkum, D. S. Larsen, R. van Grondelle, *Biochim. Biophysica. Acta Bioenergetics.* **2004**, *1657*, 82–104.

[57] R. Berera, R. van Grondelle, J. T. M. Kennis, *Photosynth. Res.* **2009**, *101*, 105–118.

[58] H. Satzger, C. Root, C. Renner, R. Behrendt, L. Moroder, J. Wachtveitl, W. Zinth, *Chem. Phys. Lett.* **2004**, *396*, 191–197.

[59] T. Nägele, R. Hoche, W. Zinth, J. Wachtveitl, *Chem. Phys. Lett.* **1997**, *272*, 489–495.

[60] H. Satzger, S. Spörlein, C. Root, J. Wachtveitl, W. Zinth, P. Gilch, *Chem. Phys. Lett.* **2003**, *372*, 216–223.

[61] H. Rau in *Photochromism: Molecules and Systems*, (Eds.: H. Dürr, H. Bouas-Laurent), Elsevier, Amsterdam, **2003**, p. 165.

[62] Y. Harabuchi, M. Ishii, A. Nakayama, T. Noro, T. Taketsugu, *J. Chem. Phys.* **2013**, *138*, 064305.

[63] Y.-Q. Shen, H. Rau, *Makromol. Chem.* **1991**, *192*, 945–957.

[64] S. Harms, K. Rätzke, C. Pakula, V. Zaporojtchenko, T. Strunskus, W. Egger, P. Sperr, F. Faupel, *J. Polym. Sci. Part B Polym. Phys.* **2011**, *49*, 404–408.

[65] M. Böckmann, N. L. Doltsinis, D. Marx, *J. Phys. Chem. A* **2010**, *114*, 745–754.

4.6 Electronic supplementary information

4.6.1 Femtosecond transient spectroscopy of thin solid films

Data collection strategy

In femtosecond time-resolved experiments, a full set of time-dependent data is obtained by probing the molecular response after photo-excitation by an ultrashort pump pulse by a time-delayed probe pulse, repeated for many different delay times.[1–3] To acquire the desired information with high sensitivity, the signals are accumulated over multiple detection cycles, which requires refreshing the sample between successive laser shots to avoid photo-degradation or buildup of photo-products. As described in detail before,[4] we have employed an experimental setup and data collection strategy that relies on a fast and reproducible bi-directional translation of the two-dimensional polymer film samples for refreshing, combined with signal readout at a 1 kHz rate. This allows us to perform single-shot analysis and automated signal discrimination, and to monitor the signal evolution with increasing number of pump pulses.

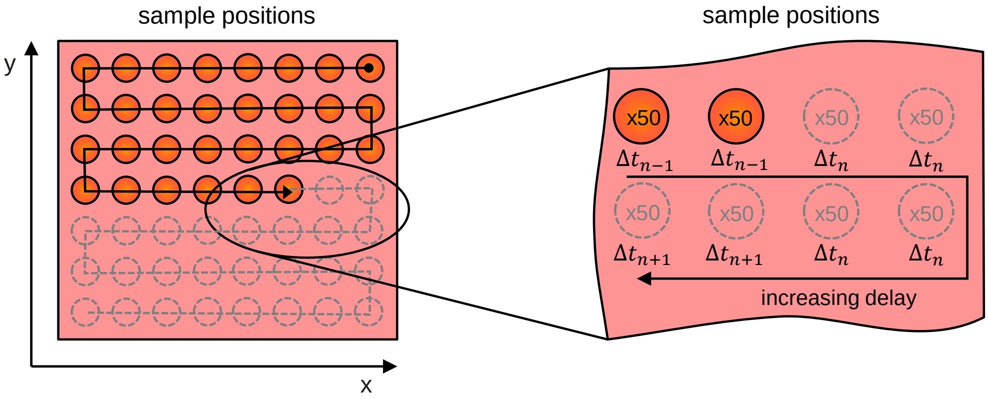

Fig. 4.5 Sketch of the data collection scheme. The filled orange circles represent sample positions already hit by the pump beam, the dashed circles upcoming positions. A total of 200 detection cycles per delay step Δt_n is realized by collecting data for 50 cycles at each sample spot and keeping the delay constant for four spots.

Figure 4.5a illustrates the data collection scheme. At each sample spot, probe and reference spectra were recorded for 50 detection cycles. After blocking the pump beam with a mechanical shutter (see Fig. 2.3), the sample was then translated to a new position, keeping the pump–probe delay unchnaged for four successive sample positions resulting in a total of 200 detection cycles per delay.

Subtraction of scattered pump light

Scattering of the incident pump light at the front and rear air-sample interfaces leads to an unwanted negative signal component that dominates the total absorption changes close to the excitation wavelength, where it obscures the molecular signal contributions. We have therefore implemented a background subtraction scheme involving selective blocking of four successive pump and probe laser pulses per detection cycle as illustrated in Fig. 4.6.

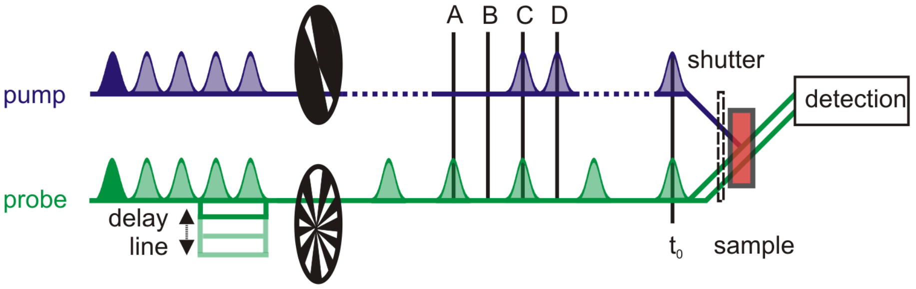

Fig. 4.6 Sketch of the phase-locked chopping of the pump and probe beams. The optical chopper placed in the probe beam has 10 symmetrically space slits each 18° wide, the pump chopper is either identical (for liquid samples) or has two such slits opposite each other for solid samples. In the latter case, an additional mechanical shutter is used to block all pump and probe pulses during sample movement. Rotation of the pump chopper with $1/20$ of the laser repetition rate, $\omega_{\text{rot}} = f_{\text{rep}}/20 \approx 50$ Hz results in two successive pump pulses passing, and the next 2 resp. 18 pulses being blocked. For the probe light, every other pulse is blocked by rotation of the probe chopper with $\omega_{\text{rot}} = f_{\text{rep}}/10 \approx 100$ Hz. The resulting pump/probe pulse pairs are indicated by the letters A–D.

Phase-locked optical choppers (MC2000B, Thorlabs) were used to realise a scheme comprising all possible combinations of blocked pump and probe/reference beams during four successive laser shots, indicated by letters A–D in Fig. 4.6. On the detection side, combination A are the pure probe and reference spectra *without* excitation I^0, B are the ambient background intensities I^{BG}, C corresponds to the probe and reference spectra *with* excitation I^*, and D represents the scattered pump light I^{SC}. The background-corrected changes in optical density at a delay time Δt are then calculated via:

$$\Delta OD(\lambda, \Delta t) = -\log \frac{\left(I^*_{\text{pr}} - I^{\text{SC}}_{\text{pr}}\right) \times \left(I^0_{\text{ref}} - I^{\text{BG}}_{\text{ref}}\right)}{\left(I^*_{\text{ref}} - I^{\text{SC}}_{\text{ref}}\right) \times \left(I^0_{\text{pr}} - I^{\text{BG}}_{\text{pr}}\right)} \tag{4.6.1.1}$$

It is worth noting: since the sample is not refreshed between the required four successive laser shots in case of the solid sample, only the sequence A-B-C-D allows for application of Eq. 4.6.1.1 without transient absorption changes due to the second pump pulse.

4.6.2 Measurements in *n*-hexane

Spectro-temporal transient absorption maps of 1E and 1Z in *n*-hexane

Two-dimensional maps of the spectro-temporal transient absorption data on **1E** in *n*-hexane following $\pi\pi^*$ excitation at $\lambda_{\text{pump}} = 330$ nm and **1Z** in *n*-hexane following $n\pi^*$ excitation at $\lambda_{\text{pump}} = 460$ nm are presented in Fig. 4.7. The delay times are displayed from -1 to 20 ps, while the probe wavelengths for the data are between 340 and 575 nm. The data were measured up to $\Delta t = 1.3$ ns, but the changes at longer delay times are negligible.

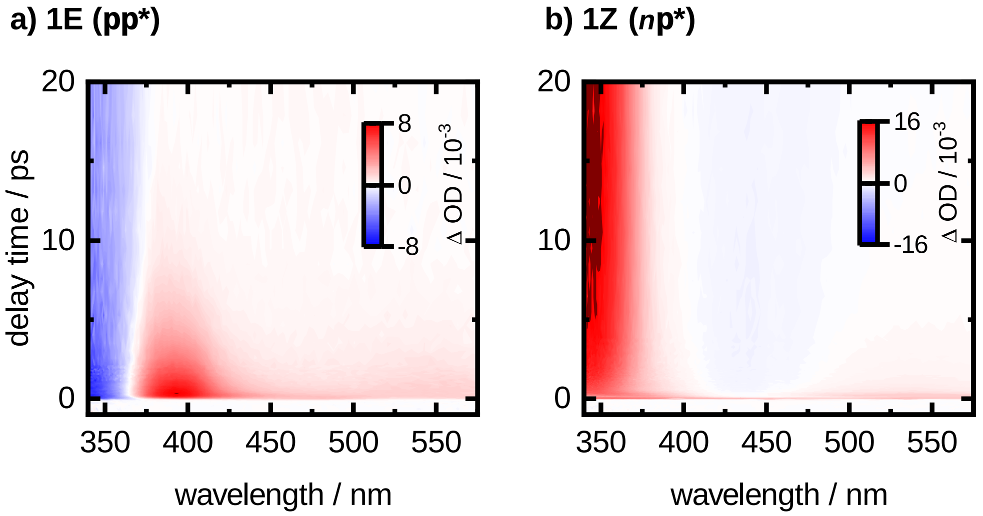

Fig. 4.7 (a) Two-dimensional spectro-temporal absorption maps of the change in optical density (ΔOD) following excitation of **1E** in *n*-hexane at $\lambda_{\text{pump}} = 330$ nm and (b) after excitation of **1Z** at $\lambda_{\text{pump}} = 460$ nm for probe wavelengths in the range of $340 \leq \lambda_{\text{probe}} \leq 575$ nm and delay times between $-1 \leq \Delta t \leq 20$ ps.

The spectro-temporal transient absorption data (Fig. 4.7a) of **1E** in *n*-hexane following $\pi\pi^*$ excitation are characterized by the presence of a strong ground-state bleaching (GSB) signal at $\lambda_{\text{probe}} \leq 370$ nm, where the corresponding $\pi\pi^*$ transition in the static absorption spectrum (Fig. 4.1), leaving permanent absorption changes up to $\Delta t = 1.3$ ns. At longer wavelengths ($\lambda_{\text{probe}} > 375$ nm) the data show two excited-state absorption (ESA) contributions at $\lambda_{\text{probe}} \approx 400$ nm and 520 nm. The 2D map of **1Z** (Fig. 4.7b) in *n*-hexane following $n\pi^*$ excitation at $\lambda_{\text{pump}} = 460$ nm presents the following features: a positive ESA band at $\lambda_{\text{probe}} \leq 400$ nm; a weak and broad positive ESA band at $\lambda_{\text{probe}} \geq 500$ nm; and a negative GSB signal at $\lambda_{\text{probe}} = 450$ nm.

Evolution-associated difference spectra (EADS) of 1E and 1Z in *n*-hexane

Fig. 4.8a shows four EADS are needed to describe the spectro-temporal changes of **1E** in *n*-hexane upon $\pi\pi^*$ excitation at $\lambda_{\text{pump}} = 330$ nm. The time-zero EADS associated with time constant of $\tau_0 = 90$ fs (blue spectrum in Fig. 4.8a) shows negative bands at 400 nm and positive bands at 475 and 650 nm, which can be explained as a buildup of a population of the S_1 state followed evolution from the S_2 state. The qualitative spectral shape and associated time constants along the S_1 potential energy surface followed evolution from $S_2 \rightarrow S_1$ were observed indicating that the subsequent S_1 evolution is the comparable to that following directly $n\pi^*$ excitation.

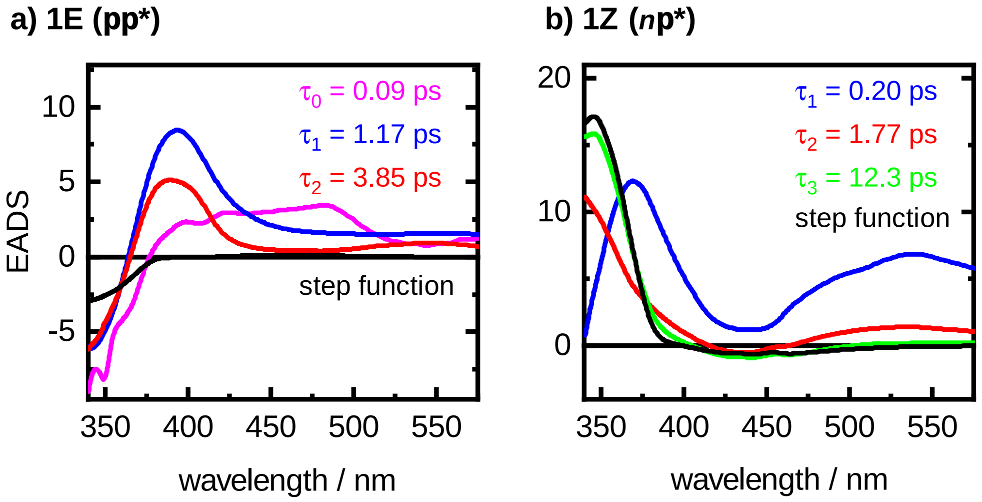

Fig. 4.8 (a) Evolution-associated difference spectra (EADS) following excitation of **1E** in *n*-hexane at $\lambda_{\text{pump}} = 330$ nm and (b) after excitation of **1Z** at $\lambda_{\text{pump}} = 460$ nm displayed for probe wavelengths in the range of $340 \leq \lambda_{\text{probe}} \leq 575$ nm. The spectra are labelled according to the time constants obtained from a global fit analysis using a consecutive kinetic model.

For **1Z** in *n*-hexane upon $n\pi^*$ excitation, four components were required to fit the SVD time profiles for the transient absorption data. A fast component of $\tau_1 = 0.20$ ps in *n*-hexane is associated to the population movement out of the Franck-Condon region. The time constants $\tau_2 = 1.77$ ps is assigned to that the wavepacket moves on the S_1 potential energy surface via a S_1/S_0 CI, before it reaches the product ground state. EADS1 shows a broad band in the visible and a sharper band in the UV (blue spectrum in Fig. 4.8b). The spectra of the slower components for **1Z** in *n*-hexane, EADS2 and EADS3 (red and green spectra in Fig. 4.8b), show very similar features, different from the evolution in the excited S_1 state. Particularly, the EADS3 is almost overlapping with permanent spectra, which indicates an evolution in the ground state. Thus, the time constant of $\tau_3 = 12.3$ ps is associated to the ground-state vibrational cooling.

Time traces and transient absorption spectra from 1E in *n*-hexane upon $\pi\pi^*$ excitation

Fig. 4.9a shows two time profiles for **1E** in *n*-hexane upon $\pi\pi^*$ excitation after integration over the transient absorption bands of $370 \leq \lambda_{\text{probe}} \leq 395$ nm and $475 \leq \lambda_{\text{probe}} \leq 590$ nm. The fit of the time profile at the wavelengths $370 \leq \lambda_{\text{probe}} \leq 395$ nm results in an ultafast positive contribution of 90 fs, whereas a negtive components (90 fs) was required to fit the time profile at $475 \leq \lambda_{\text{probe}} \leq 590$ nm indicating a internal conversion from $\mathrm{S}_2 \rightarrow S_1$.

Fig. 4.9b shows transient absorption spectra at selected delay times and reveal ultrafast decay in the red and growth in the blue at early delays from 0.05 to 0.30 ps. An ultrafast decay in the wavelength range $475 \leq \lambda_{\text{probe}} \leq 590$ nm is associated with the $\mathrm{S}_2 \rightarrow S_1$ relaxation.[5]

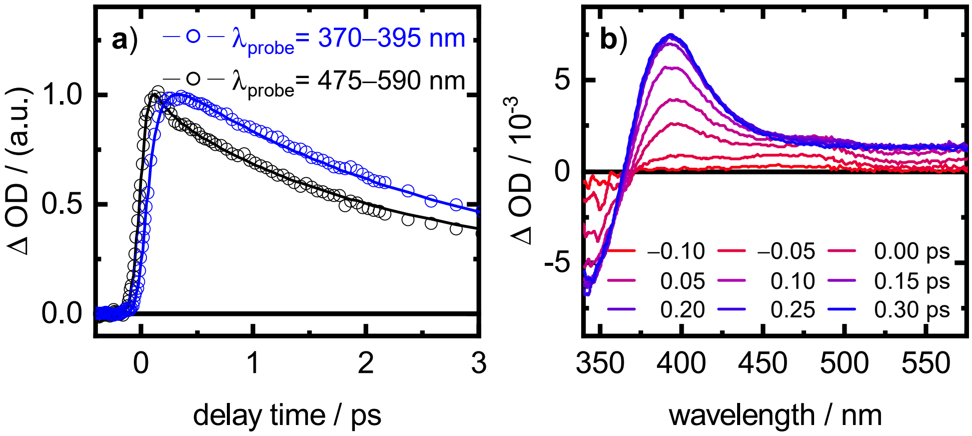

Fig. 4.9 (a) Transient absorption time profiles of **1E** in *n*-hexane upon $\pi\pi^*$ excitation in two selected probe windows: $370 \leq \lambda_{\text{probe}} \leq 395$ nm and $475 \leq \lambda_{\text{probe}} \leq 590$ nm. (b) Transient absorption spectra following excitation of **1E** in *n*-hexane at $\lambda_{\text{pump}} = 330$ nm for the selected delay times from $\Delta t = -0.10$ ps – 0.30 ps, which shows a delayed rising at about 390 nm indicating the internal conversion from $\mathrm{S}_2 \rightarrow \mathrm{S}_1$

Bibliography

[1] A. H. Zewail, *J. Phys. Chem. A* **2000**, *104*, 5660–5694.

[2] R. Berera, R. van Grondelle, J. T. M. Kennis, *Photosynth. Res.* **2009**, *101*, 105–118.

[3] F. Renth, R. Siewertsen, F. Temps, *Int. Rev. Phys. Chem.* **2013**, *32*, 1–38.

[4] K. Röttger, S. Wang, F. Renth, J. Bahrenburg, F. Temps, *Appl. Phys. B* **2015**, *118*, 185–193.

[5] M. Quick, A. L. Dobryakov, M. Gerecke, C. Richter, F. Berndt, I. N. Ioffe, A. A. Granovsky, R. Mahrwald, N. P. Ernsting, S. A. Kovalenko, *J. Phys. Chem. B* **2014**, *118*, 8756–8771.

Chapter 5

Ultrafast dynamics of UV-excited *trans*- and *cis*-ferulic acid in aqueous solutions

Shuangqing Wang,[a] Sebastian Schatz,[a] Mayra C. Stuhldreier,[a‡] Hendrik Böhnke,[a] Joss Wiese,[a¶] Carsten Schröder,[a] Tim Raeker,[a] Bernd Hartke,[a] Julia K. Keppler,[b] Karin Schwarz,[b] Falk Renth,[*a] and Friedrich Temps[*a]

[a] Institut für Physikalische Chemie, Christian-Albrechts-Universität zu Kiel, Olshausenstr. 40, 24098 Kiel, Germany.
[b] Institut für Humanernährung und Lebensmittelkunde, Christian-Albrechts-Universität zu Kiel, Heinrich-Hecht-Platz 10, 24118 Kiel, Germany.
‡ Present address: TNG Technology Consulting GmbH, Betastraße 13a, 85774 Unterföhring, Germany.
¶ Present address: Center for Free-Electron Laser Science (CFEL), Deutsches Elektronen-Synchrotron DESY, 22607 Hamburg, Germany

S. Wang, S. Schatz, M. C. Stuhldreier, H. Böhnke, J. Wiese, C. Schröder, T. Raeker, B. Hartke, J. K. Keppler, K. Schwarz, F. Renth, and F. Temps, *Phys. Chem. Chem. Phys.*, 2017, **19**, 30683 – 30694.
Reproduced by permission of the PCCP Owner Societies.

Own contribution to this munuscript:

- ☐ Synthesis of *cis*-ferulic acid
- ☐ Static absorption spectroscopy
- ☐ Time-resolved absorption spectroscopy
- ☐ Analysis of the transient absorption and fluorescence up-conversion data

---

[*] To whom correspondence should be addressed. E-mail: roettger@phc.uni-kiel.de and renth@phc.uni-kiel.de

Abstract

The ultrafast UV-induced processes of the neutral, anionic and dianionic forms of *trans*- and *cis*-ferulic acid (FA) in aqueous solution were studied by static and femtosecond time-resolved emission and absorption spectroscopy combined with quantum chemical calculations. In all cases, initial excitation populates the first $^1\pi\pi^*$ state. For the dianionic *cis*-isomer cFA^{2-}, electronic deactivation takes place with a time constant of only 1.4 ps, whereas in all other cases, excited-state deactivation happens more than ten times slower, on a time scale of $\approx$20 ps. The data suggest sequential de-excitation pathways, where initial sub-picosecond solvent rearrangement and structural changes are followed by internal conversion to an intermediate excited electronic state from which deactivation to the ground state proceeds. Considering the time scales, barrierless excited-state pathways are suggested only in the case of cFA^{2-}, where the observed formation of the isomerisation photoproduct tFA^{2-} provides clear evidence for a *cis* $\rightleftarrows$ *trans* isomerisation coordinate. In the other cases, pathways with an excited-state energy barrier, presumably along the same coordinate, are likely, given the longer excited-state lifetimes.

5.1 Introduction

Ferulic acid (3-methoxy-4-hydroxycinnamic acid, FA) is a phytochemical cinnamic acid derivative that shows anti-inflammatory, cardio- and neuroprotective as well as anti-cancerogenic capabilities and is naturally abundant in all kinds of plant food such as grains, fruits, and vegetables.[1–5] As Fig. 5.1 shows, FA exists as *trans*- and *cis*-isomers, which can be interconverted by isomerisation about the C=C double bond, and are deprotonated to their anionic and dianionic forms in aqueous solution, depending on pH and environment.[6–8] Although the *trans*-isomer predominates, both isomers are found in plants,[4,5] e.g., the *cis*-*trans* isomer ratio in the cell walls of corn, a rich source for FA, is 0.16.[9] Besides being a potent antioxidant, FA features strong absorptions of UV-A (400 – 315 nm) and UV-B (315 – 280 nm) light. This combination enables FA to act as a natural sun-protectant and has created considerable research interest recently.[10–15] Since fundamental application requirements such as photostability and absence of reactive intermediates or side products rely on efficient molecular ultrafast electronic deactivation processes and selective excited-state dynamics on the femto- to picosecond time scale,[16–20] detailed insight into the molecular mechanisms using time-resolved laser spectroscopy is indispensible as a basis for a rational design of

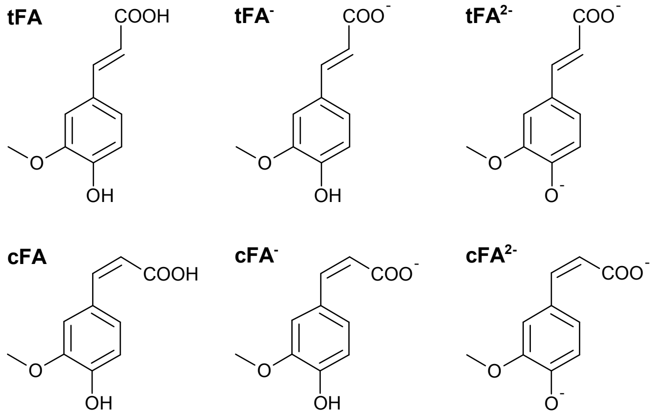

Fig. 5.1 Top row: Neutral, anionic and dianionic forms of *trans*-ferulic acid (tFA, tFA^- and tFA^{2-}). Bottom row: Corresponding forms of *cis*-ferulic acid (cFA, cFA^- and cFA^{2-}).

artificial sunscreen molecules. Extensive studies along these lines targeting the ultrafast photophysics of hydroxycinnamic acid compounds have so far been performed with particular focus on the *p*-coumaric acid chromophore, which triggers the reversible photocycle of the photoactive yellow protein (PYP),[12,21–30] whereas FA has been studied to a lesser extent.[12,13,31] According to gas-phase theoretical calculations, the UV-induced dynamics of *trans*-FA (tFA) are determined by several electronically excited singlet states, of which only the $1\,^1\pi\pi^*$ and $2\,^1\pi\pi^*$ states are optically bright and can be accessed directly, whereas the $1\,^1n\pi^*$ and $1\,^1\sigma\pi^*$ states might be populated efficiently by internal conversion (IC) via conical intersections (CIs) along out-of-plane ring deformation and *trans*-*cis* isomerisation coordinates.[31] These calculations suggest that electronic deactivation upon excitation to the $1\,^1\pi\pi^*$ state can occur via several pathways, depending on the excitation energy. With only little excess energy, i.e. excitation in the red wing of the absorption band, the molecule shows fluorescence. At slightly higher excitation energies, a $1\,^1\pi\pi^*/S_0$ CI with the electronic ground state becomes accessible. Eventually, at even higher energies, a $2\,^1\pi\pi^*/S_0$ CI related to the *trans*-*cis* isomerisation provides a feasible de-excitation pathway. In addition, the formation of radical product species by O−H bond fission via the $^1\pi\sigma^*$ state as an intermediate was discussed as an alternative pathway.[31]

Previous experimental solution-phase studies of photo-excited *trans*-FA were performed using transient absorption spectroscopy. For the anionic and dianionic forms (tFA^- and tFA^{2-}) in aqueous solutions, Grondelle *et al.* observed bi- and tri-exponential decays towards only weak final absorption changes.[12] The latter were assigned to the formation of solvated electrons and the corresponding radicals, and a very low *trans*-*cis* isomerisation yield $\leq 3\%$ was estimated. The fastest decay component, $\tau_1 \leq 1$ ps, was attributed to substantial spectral shifts due to solvent rearrangement and initial excited-state dynamics, whereas slower time constants of $\tau_2 = 19$ ps (tFA) and of $\tau_2 = 8.2$ and $\tau_3 = 44$ ps (tfA^{2-}) were assigned to an excited-state decay via an aborted *trans*-*cis* isomerisation. Tri-exponential decays were also observed in a recent comparative study of the photo-induced dynamics of tFA in aqueous solution and in the non-protic solvents acetonitrile and dioxane,[13] where the fastest time constants in the range of $\tau_1 = 0.08 - 0.4$ ps were interpreted the same way. For the slower dynamics characterised by time constants $\tau_2 = 0.52 - 2.6$ ps and $\tau_3 = 6.3 - 15.4$ ps, two alternative scenarios were given: either evolution along the *trans*-*cis* isomerisation coordinate within the initially excited $1\,^1\pi\pi^*$ state and subsequent electronic deactivation via a CI with the electronic ground state S_0, or internal conversion to the $2\,^1\pi\pi^*$ state followed by *trans*-*cis* isomerisation via a $2\,^1\pi\pi^*/S_0$ CI. In both cases, successful *trans*-*cis* isomerisation was assumed with reference to the quantum chemical calculations of Ref. [31] and static irradiation experiments.

Here, we report on the UV-induced ultrafast dynamics of *trans*-FA and, for the first time, also *cis*-FA in aqueous solutions in their neutral, anionic and dianionic forms. In order to elucidate details of the ensuing complex dynamics, combined probing in absorption and emission using femtosecond time-resolved transient absorption spectroscopy and Kerr-gated broadband fluorescence spectroscopy was used. The experiments were supplemented by density functional theory (DFT) calculations performed using the Turbomole 7.0 program package,[32] employing the Conductor-like Screening Model (COSMO) to treat effects of solvation.[33]

5.2 Experimental

5.2.1 Materials & static spectroscopy

Trans-4-hydroxy-3-methoxycinnamic acid (*trans*-ferulic acid, tFA) was purchased from Sigma-Aldrich (99%) and used without further purification. The *cis*-isomer cFA was synthesized photochemically according to literature[34] from ionic liquid solutions of *trans*-ammoniumferulate in acetonitrile by irradiation in the UV at 350 nm for 24 h, using a mercury lamp with suitable filters. The resulting solid *cis*-ammoniumferulate precipitate was filtered off and redissolved in aqueous HCl solution. After extraction with CH_2Cl_2, *cis*-ferulic acid (cFA) was obtained with a purity of 97% as determined by ^{1}H NMR.

Using oxalate, phosphate, and carbonate buffer solutions, aqueous solutions of both isomers were prepared at pH = 1.2, 7.4 and 10.4, at which the content of the neutral, anionic and dianionic forms is $\geq 99.9\%$ in chemical equilibrium.[8,35,36]

All sample solutions used in the time-resolved fluorescence experiments had a concentration of $c_0 = 400\,\mu$M. For the transient absorption experiments, the concentration was $c_0 = 300\,\mu$M, except for the anionic *cis*-isomer cFA$^-$, where c_0 was set to $500\,\mu$M to ensure a similar optical density at the excitation wavelength. Static absorption spectra were taken on a Shimadzu UV-2401 UV/VIS spectrometer. Static fluorescence spectra were measured on a Jobin-Yvon FluoroMax-4 spectrophotometer at 330 nm excitation using a continuous flow of fresh sample solution to avoid photoisomerisation during the irradiation inside the fluorescence spectrometer. This was verified by UV/VIS absorption spectra taken before and after acquisition of the fluorescence spectra.

5.2.2 Femtosecond time-resolved spectroscopy

All femtosecond measurements were done at room temperature using flow cells with optical path lengths of $d = 1$ mm. Time resolved emission spectra were recorded via the Kerr-gating method[37,38] utilizing a Ti:Sa laser system (Coherent LibraHE) delivering pulses with pulse lengths of 80 fs (FWHM) at 800 nm. Magic-angle excitation was performed with pump pulses of 180 nJ pulse energy and <100 fs duration (FWHM) at $\lambda_{\text{pump}} = 330$ nm, generated from compressed 560 nm pulses of a home-built noncollinear optical parametric amplifier (NOPA) by sum frequency mixing with the laser fundamental. Gating was achieved by collecting and refocusing the fluorescence together with $16\,\mu$J laser fundamental gate pulses into a flow cell of 1 mm path length filled with carbon tetrachloride ($\geq 99.9\%$, Merck) as Kerr medium placed in between two crossed wire-grid polarisers (WP25L-UB, Thorlabs). The gated fluorescence was then focused onto the entrance slit of an imaging spectrograph equipped with a CCD-camera (Princeton Instruments/Acton Research 2150i and PI-MAX). Separate measurements on pure solvents were performed to allow for subtraction of possible unwanted background signals, and fluorometric intensity correction using secondary emission standards[39] was applied. The width of the instrument response function (IRF) was ≈ 150 fs (Gaussian standard deviation).

The time-resolved broadband absorption setup based on a regeneratively amplified Ti:Sa laser system (Clark CPA2001) has been described in detail before.[40–42] Excitation pulses of 150 nJ at $\lambda_{\text{pump}} = 300$ and 330 nm were created by frequency-doubling of compressed pulses from a home-built NOPA. Broadband supercontinuum probe pulses between $\lambda_{\text{probe}} = 335$ and 675 nm were generated in CaF_2, where the polarisation was adjusted relative to the pump beam to the magic angle using a Berek variable wave plate. Signal and reference probe pulses from the front and back reflections of a planar quartz glass plate placed in the probe beam were detected spectrally resolved pulse-by-pulse by two full frame transfer (FFT) back-thinned CCD cameras (S7030-0906, Hamamatsu). Measurements on pure solvent samples were performed to determine the cross-phase modulation (XPM) and stimulated Raman scattering (SRS) solvent signal contributions, from which an IRF width of ≈ 50 fs (Gaussian standard deviation) and the time-zero function were obtained.

5.2.3 DFT calculations

DFT calculations employed the PBE0 functional,[43] which performs on the same level as other common hybrid DFT functionals regarding ground and excited state energies.[44,45] All calculations were carried out using the Turbomole 7.0 program package[32], with the def2-TZVPP basis set[46] and a finer integration grid (m4). Where applicable, the resolution of identity (RI) approximation was used to speed up the calculations.[47,48] To fix the inherent problem of van der Waals interactions in DFT, Grimme's D3 dispersion correction[49] was used. Excited state properties were obtained from the random phase approximation (RPA) for DFT as implemented in Turbomole.[50–54] The characters of the individual electronic ground and excited states and the corresponding classifications of the $S_0 \rightarrow S_n$ excitations up to $n = 4$ were derived from visual inspection of the dominant orbitals. The Conductor-like Screening Model (COSMO) continuum solvation model[33,55,56] implemented in Turbomole was employed to treat the effects of solvation on the excited state properties and gradients. The solvent properties of water were described taking a dielectric constant of 80.4 and a refractive index of 1.33.

5.3 Results

5.3.1 Static spectra

The static UV/VIS absorption and fluorescence spectra of the neutral, anionic and dianionic forms of both FA isomers in aqueous solutions are shown in Fig. 5.2 as blue, red and green lines, respectively. The UV/VIS spectra in Fig. 5.2a feature strong structured absorptions in the UV-A and UV-B range that extend to $\approx 350-400$ nm. Compared to the neutral forms, the absorptions of the anions occur blue-shifted. Conversely, the longest-wavelength bands of the dianions are red-shifted. The structured appearance of the UV/VIS spectra gives indications of at least two optically accessible singlet excited electronic states in the near UV, in accord with previous gas-phase calculations for tFA and cFA, where allowed transitions into the $1\,^1\pi\pi^*$ (S_1) and $2\,^1\pi\pi^*$ states (S_2 for tFA and S_3 for cFA) were found.[31] Compared to the *trans*-isomers, the absorptions of the *cis*-isomers occur at slightly shorter wavelengths and are weaker by a factor of ≈ 2. As seen in Fig. 5.2b, the fluorescence spectra upon excitation at $\lambda_{\text{exc}} = 330$ nm display single structureless broad bands. The fluorescence

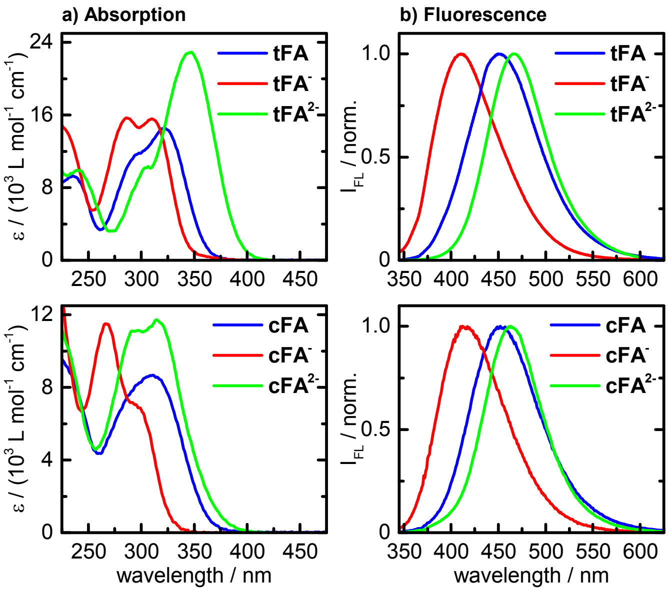

Fig. 5.2 Static spectra of *trans*- and *cis*-FA in aqueous solution for the neutral, anionic and dianionic forms. a) UV/VIS absorption spectra, b) normalized fluorescence spectra upon excitation at $\lambda_{\text{exc}} = 330$ nm.

of the anionic form of both isomers occurs significantly blue-shifted (30 – 50 nm) compared to the emission of the respective neutral and dianionic forms.

5.3.2 Time-resolved spectroscopy of the *trans*-isomers

Figure 5.3 shows two-dimensional maps of the time-resolved emission and transient absorption spectra for *trans*-FA in its different protonation states following photo-excitation at $\lambda_{\text{pump}} = 330$ nm. The data were acquired up to much longer delay times of several hundred picoseconds in fluorescence and beyond 1 ns in absorption, where any further changes were negligible, but are displayed here only for delay times up to 50 ps for the sake of clarity.

The time-resolved fluorescence intensities are given in Fig. 5.3a for emission wavelengths between $345\,\text{nm} \leq \lambda_{\text{FL}} \leq 580$ nm. They were normalized to the strongest fluorescence signal (tFA^{2-}) to reflect the changes in relative intensity for the different degrees of deprotonation. The spectro-temporal behaviour is characterized in all cases by an immediate rise of a broad fluorescence band ranging from $\lambda_{\text{FL}} = 345 - 520$ nm for tFA and tFA^{2-} and from $\lambda_{\text{FL}} = 345 - 470$ nm for tFA^{-}. The bands undergo significant spectral shifts towards longer wavelengths in the first few picoseconds, and decay on time scales slower than 10 ps. The fluorescence of the anion tFA^{-} not only occurs at the shortest wavelengths, but also has the lowest overall intensity and displays the smallest spectral shift.

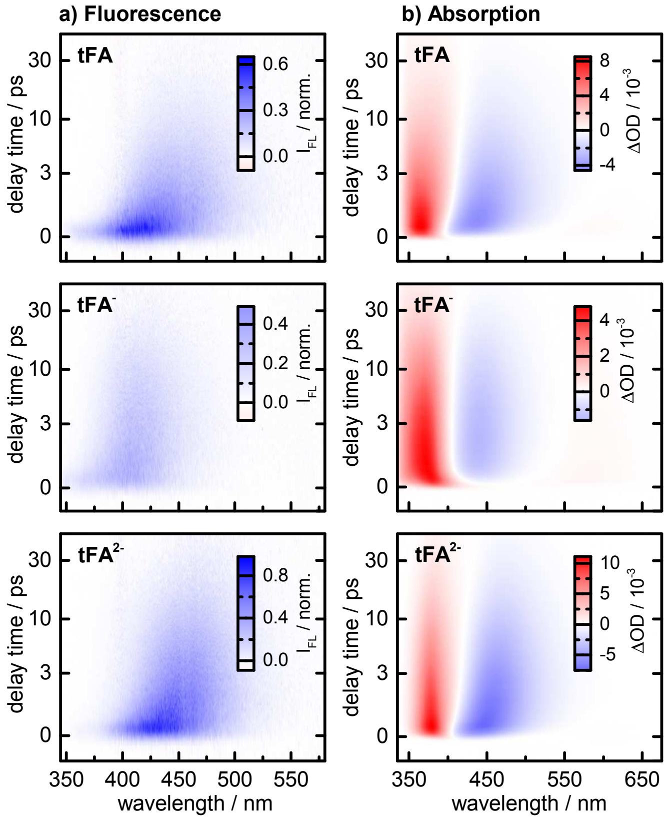

Fig. 5.3 a) Maps of the normalized time-resolved emission intensities I_{FL} and b) transient absorption changes ΔOD of *trans*-FA in its neutral, anionic and dianionic forms following photo-excitation at $\lambda_{\mathrm{pump}} = 330\,\mathrm{nm}$ for delay times between 0.5 and 50 ps (see note[57] for an explanation of the logarithmic delay scale).

The spectro-temporal transient absorption maps in Fig. 5.3b for probe wavelengths between $335\ \mathrm{nm} \leq \lambda_{\mathrm{probe}} \leq 675\ \mathrm{nm}$ are very similar for all tFA forms. The two dominant contributions are a broad negative signal that mirrors the spectro-temporal behaviour of the fluorescence and can thus safely be assigned to stimulated emission (SE), and an intense positive band due to excited-state absorption (ESA) present from $\lambda_{\mathrm{probe}} = 345$ nm to $\approx$ 420 nm. During the first couple of picoseconds, a spectral blue-shift of the ESA bands and a spectral red-shift of the SE component are clearly discernible. ESA overlaps with the blue wing of the SE, so that the signals change sign at $\lambda_{\mathrm{probe}} \approx 375$ nm. The zero-crossing moves to shorter wavelengths initially, a shift back towards longer wavelengths at longer delay times is only observed for tFA and tFA^{2-}. The overall decay of ESA and SE happens concomitantly within ≤ 50 ps and leaves only small if any permanent absorption changes.

For a quantitative global analysis of the data, non-linear least-squares fitting based on singular value decomposition (SVD) of the data matrices was performed.[58] Briefly, SVD

Table 5.1 Globally fitted time constants for the fluorescence (FL) and transient absorption (TA) SVD time traces of tFA, tFA^- and tFA^{2-} with 2σ error limits given as error of the last significant figure in parentheses.

	method	τ_1 / ps	τ_2 / ps	τ_3 / ps	τ_4 / ps
tFA	FL	–	0.49(1)	2.9(1)	18(1)
	TA	0.16(1)	0.58(3)	4.0(1)	20(1)
tFA^-	FL	–	0.81(6)	8.2(15)	23(2)
	TA	0.12(1)	0.45(2)	11.5(9)	23(1)
tFA^{2-}	FL	–	0.63(2)	4.5(2)	21(1)
	TA	0.11(1)	0.57(2)	5.5(2)	25(1)

was run on the time-zero corrected matrices, where background and solvent-contributions had been subtracted before. To decide on the number of relevant SVD components n_{comp}, scree plots of the singular values as well as the SVD time traces and SVD spectra were inspected, and the two-dimensional approximations of rank n_{comp} were checked for remaining systematic deviations with respect to the input matrices. The resulting set of SVD time traces was then described quantitatively by simultaneous non-linear least-squares fitting using a sum of n_{comp} exponential decays convolved with the instrument response function (IRF), yielding a matrix of amplitudes $\{a_{ij}\}$ and global decay constants τ_j. The permanent absorption changes due to the formation of equilibrated product species that are missing in emission were taken into account by replacing the last exponential with a convoluted step function. The resulting time constants are collected in Table 5.1, where numbering starts with $j = 2$ for fluorescence for better comparison with the absorption results.

Two sub-picosecond time constants (τ_1 and τ_2) were required to describe the SVD time profiles for the transient absorption data, whereas only one sub-picosecond time constant (τ_2) was needed to describe the fluorescence profiles, because the time resolution of the transient absorption method is higher than for the Kerr-gated fluorescence method. In accord, the fastest time constant in absorption, $\tau_1 \approx 0.15$ ps, is within the instrumental resolution of the time-resolved fluorescence detection. The values of $\tau_2 \approx 0.6$ ps for both methods agree well with each other. The slower time constants τ_3 and τ_4 are observed in absorption and in emission and must therefore be related to excited-state processes. While time constant $\tau_4 \approx 20$ ps agrees remarkably well for both methods and for the different tFA forms, time constant $\tau_3 = 3 - 11$ ps roughly doubles for tFA^- compared to tFA and tFA^{2-}.

To elucidate details of the spectral evolution, a sequential kinetic scheme was assumed to calculate the evolution-associated fluorescence spectra (EAFS) and the corresponding evolution-associated absorption difference spectra (EADS).[58] For the neutral form, the sequential scheme is given by

$$\mathrm{tFA}^{*,1} \xrightarrow{\tau_1} \mathrm{tFA}^{*,2} \xrightarrow{\tau_2} \mathrm{tFA}^{*,3} \xrightarrow{\tau_3} \mathrm{tFA}^{*,4} \xrightarrow{\tau_4} \mathrm{tFA} + \mathrm{cFA}. \qquad (5.3.2.1)$$

As mentioned, the numbering of the time constants τ_j starts with $j = 2$ in the case of fluorescence. The resulting EAFS and EADS are, in general, not associated to molecular species and may contain contributions from different molecular species or states. The individual items $\mathrm{tFA}^{*,j}$ thus represent states of the molecules that can be distinguished by their differing spectral properties, e.g., in the FC region or due to solvation, but need not be distinct electronic states.[58,59] The last step of Scheme 5.3.2.1 further assumes that electronic deactivation eventually leads back to the thermally equilibrated tFA and possibly cFA isomers in their S_0 electronic ground states. Although the underlying kinetic scheme might not correspond exactly to the true kinetics, the EAFS and EADS shown in Fig. 5.4 help in the interpretation of the results, as they provide a clear representation of the spectral changes caused by the evolution of the system; further state- or species-specific information can hardly be extracted from both types of transient spectra.

The EAFS are purely positive. The first spectra occur at the shortest wavelengths and correspond to the time-zero transient fluorescence by the molecules in the FC region of the initially excited state. They undergo a fast spectral red-shift of 20 – 30 nm with time constant τ_2 into the second, intermediate EAFS. As seen most clearly for tFA and tFA^{2-}, these EAFS are characterized by very broad wings towards longer wavelengths. The spectral evolution with τ_3 towards the last EAFS related to the final excited-state species $\mathrm{tFA}^{*,4}$ is much slower and dominated by a decrease in intensity with a slight spectral narrowing and only small further spectral red-shifts. The decays of these species and EAFS happen with τ_4.

The EADS are more complex due to the overlap of the strongly positive, blue-shifting ESA with the negative, red-shifting signals caused by SE, but can be disentangled at least qualitatively considering the known behaviour of the EAFS. The first EADS near time-zero show positive values due to ESA up to probe wavelengths of $\approx 500 - 550$ nm, and display maxima around 360 – 380 nm. The superimposed SE is visible as an intermediate minimum around 400 nm in the case of tFA and tFA^{2-} that is not discernible for tFA^{-} most likely due to the weaker SE amplitude. The evolution of the time-zero EADS with the sub-picosecond time constants τ_1 and τ_2 towards the third EADS is characterized by an apparent spectral red-shift of the positive band associated with ESA, while the SE shows a spectral blue-shift in accordance with the emission EAFS. The subsequent slower spectral evolution towards the final excited-state EADS with time constants τ_3 corresponds to a partial decay of the ESA and SE contributions. The further decay with τ_4 leaves final EADS with only low amplitudes

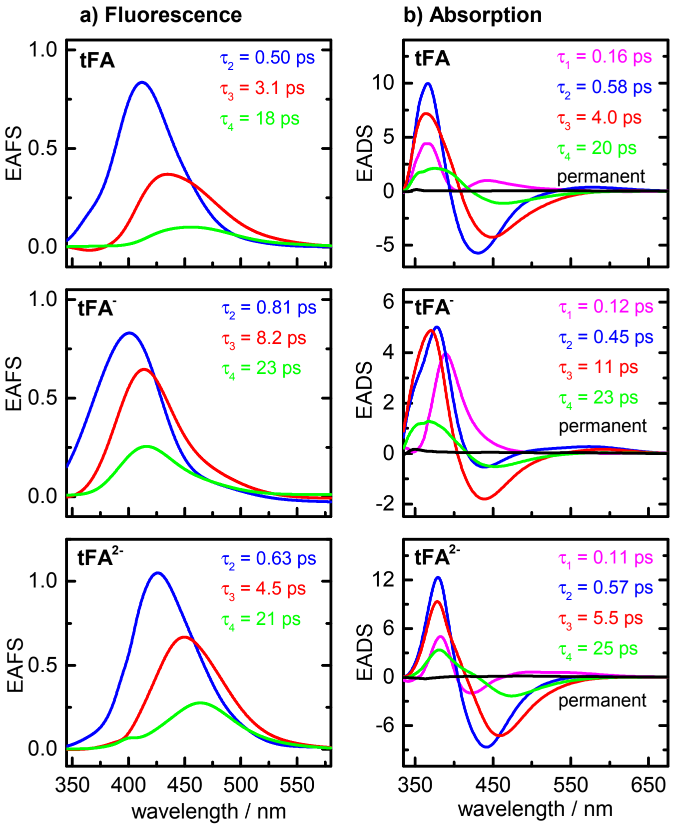

Fig. 5.4 Evolution-associated fluorescence spectra (EAFS) and absorption difference spectra (EADS) of photo-excited *trans*-FA in different protonation states obtained via SVD-analysis. The spectra are labelled according to their decay times within Scheme 5.3.2.1.

(black lines in Fig. 5.4) corresponding to small permanent absorption changes. Physical assigments for these different time constants will be given in the Discussion below.

5.3.3 Time-resolved spectroscopy of the *cis*-isomers

The two-dimensional maps of the changes in optical density following photoexcitation of the neutral, anionic and dianionic forms of *cis*-FA at $\lambda_{\text{pump}} = 330$ nm are shown in Fig. 5.5a for probe wavelengths between 335 nm $\leq \lambda_{\text{probe}} \leq$ 675 nm and delay times of -0.5 ps $\leq \Delta t \leq$ 50 ps. As before, the measurements were continued up to delay times around 1 ns, where the observed transient absorption remained constant. Here, we present only results of our transient absorption measurements, as the weak intensities of the transient fluorescence spectra for the cFA forms, in particular for cFA$^-$ and cFA^{2-}, impaired their accurate measurement.

The recorded signals for the three cases are distinctly different. The map for cFA is similar to those for the three tFA forms, with a broad negative signal due to SE at probe wavelengths > 410 nm, and an ESA band from $\lambda_{\mathrm{probe}} = 335$ nm to $\lambda_{\mathrm{probe}} \approx 420$ nm overlapping with the blue wing of the SE. The ESA undergoes a spectral blue-shift, whereas the SE shifts to longer wavelengths. The concurrent overall decay of both bands happens within ≤ 50 ps and leaves only small permanent absorption changes. In the case of cFA$^-$, the behaviour at early delay times is dominated by a fast sub-picosecond decay of a spectrally broad positive ESA band ranging from $335 - 550$ nm. Positive signals beyond delay times of 1 ps occur only below $\lambda_{\mathrm{probe}} = 375$ nm, with much reduced amplitude. The SE is much weaker than for cFA and the corresponding tFA anion, so that negative optical density changes can only be observed at probe wavelengths > 430 nm and after the initial ESA has decayed. The weak, short-wavelength ESA band, as well as the SE component disappear within ≈ 50 ps

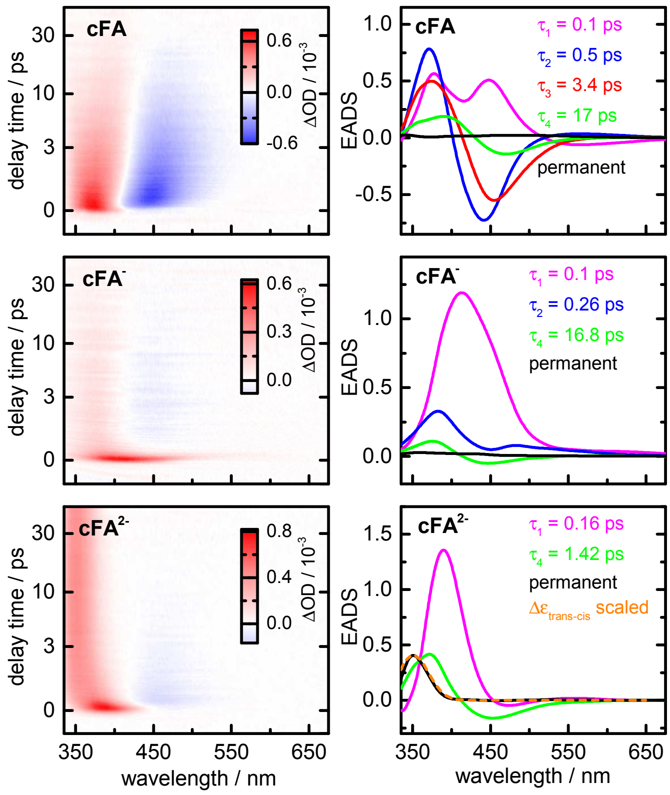

Fig. 5.5 a) Two-dimensional transient absorption changes ΔOD of *cis*-FA in the neutral, anionic and dianionic forms following photo-excitation at $\lambda_{\mathrm{pump}} = 330$ nm for delay times between 0.5 and 50 ps (see note[57] for an explanation of the logarithmic delay scale). b) Evolution-associated absorption difference spectra (EADS) obtained via SVD-analysis. The spectra are labelled according to their decay times within Scheme 5.3.2.1.

Table 5.2 Time constants from global fits of the transient absorption maps of neutral, anionic and dianionic *cis*-FA (2σ error limits given as error of the last significant figure in parentheses).

	method	τ_1 / ps	τ_2 / ps	τ_3 / ps	τ_4 / ps
cFA	TA	0.10(1)	0.49(6)	3.4(3)	17(2)
cFA$^-$	TA	0.10(1)	0.26(5)	–	17(3)
cFA^{2-}	TA	0.16(1)	–	–	1.4(1)

and leave only small permanent absorption changes. The transient absorption map of cFA^{2-} features a strong ESA component overlapped by a weak SE component at probe wavelengths above 420 nm. The simultaneous ESA and SE decays happen within just a few picoseconds, leaving fairly large and constant positive signals below 375 nm. Table 5.2 collects the global decay times τ_j obtained by quantitative analysis of the data, where the permanent absorption changes were described by a convoluted step function as for the *trans*-isomer.

For cFA, the number of components, as well as the values of the fitted time constants correspond to the case of the *trans*-isomer. For cFA$^-$, the SVD analysis yields one component less. However, apart from the missing component corresponding to the intermediate time constant τ_3, the values of the other time constants conform to those found for cFA and tFA$^-$. However, compared to the other *cis*-forms and the dianionic *trans*-isomer, cFA^{2-} shows distinct differences. Its behaviour can be described with only three components, of which one is related to the strong permanent absorption changes, leaving only time constants $\tau_1 = 0.16$ ps, and the short value of $\tau_4 = 1.4$ ps as the slowest decay component.

The EADS calculated using a sequential kinetic scheme analogous to the *trans* case for the photo-excited *cis*-isomers are displayed in Fig. 5.5b. The EADS for cFA behave very similar to those of tFA; a strong SE component is present that cuts off the maximum of the positive ESA in the time-zero EADS, and subsequently leads to negative amplitudes for wavelengths above $\lambda_{\text{probe}} \approx 420$ nm in the other excited-state EADS. For the two deprotonated forms, the amplitudes of the SE component are significantly lower so that the time-zero EADS are dominated by the positive ESA. For cFA$^-$ an intermediate second EADS is present that is significantly decreased in intensity compared to the first EADS. In all cases, the EADS related to the last excited-state species (equivalent to the second EADS for cFA^{2-}, the third EADS for cFA$^-$ and the fourth EADS for cFA) have similar spectral shapes in all three cases despite of the distinctly different decay constants τ_4. Finally, the permanent absorption changes (last EADS) in the case of cFA^{2-} correspond almost quantitatively to the *trans*-*cis* absorption difference spectrum calculated using the static UVVIS spectra shown in Fig. 5.2b. This is unambiguous evidence for a photo-induced *cis* $\rightarrow$ *trans* isomerisation of cFA^{2-} with the time constant of $\tau_4 = 1.4$ ps. For cFA and cFA$^-$, the observed permanent absorption changes are much smaller, in line with the related absorption difference spectra, which have amplitudes within the spectral detection range that are lower by a factor of ≈ 8 and ≈ 20 for the neutral and anionic forms, respectively, compared to the dianionic form. It is therefore difficult to judge the extent of *cis* → *trans* photoisomerisation for cFA and cFA$^-$ using the present time-resolved absorption data for $\lambda_{\text{probe}} \geq 340$ nm

5.3.4 Computational results

DFT calculations establishing the nature of the involved transitions and their energetic order were performed on the electronic ground state S_0 and the excited electronic states S_n up to $n = 4$ in Turbomole 7.0,[32] using the Conductor-like Screening Model (COSMO)[33,55,56] to include solvation effects implictly. Table 5.3 lists the calculated relative energies E_{rel} of the electronic ground states S_0, as well as the vertical excitation energies ΔE and the oscillator strengths f for the $S_0 \rightarrow S_n$ transitions up to $n = 4$ for both FA isomers in their neutral, anionic and dianionic forms with and without solvation effects. Also given are the types of the respective transitions as judged from the predominant character of the relevant orbitals (see ESI† for pictorial representations of the molecular orbitals).

The evident main trends can be summarized as follows:

(i) The relative S_0 energies show that the *trans*-isomers are slightly more stable than the *cis*-isomers. The molecules are stabilised by solvation.

(ii) The $^1\pi\pi^*$ excited singlet states are optically bright, whereas the $^1n\pi^*$ states have typically much lower oscillator strengths.

(iii) The vertical excitation energies of the optically bright $1\,^1\pi\pi^*$ excited states are highest for the anionic forms when solvation effects are included. Lower excitation energies are found for the *trans*-isomer forms compared to the corresponding *cis*-isomers. Both findings reproduce the observed trends in the absorption spectra (cf. Fig. 5.2).

(iv) For anionic forms, the $^1n\pi^*$ excitation energies are reduced relative to those of the $^1\pi\pi^*$ states, such that for tFA$^-$ the $1\,^1n\pi^*$ state becomes the lowest electronically excited state irrespective of solvation. For the bare dianions, the calculations also indicate energetically low-lying states with $^1\pi\sigma^*$ character.

Table 5.3 Calculated ground state energies E_{rel} as well as vertical excitation energies ΔE, oscillator strengths f, and transition types for the $S_0 \rightarrow S_n$ transitions of the neutral, anionic and dianionic forms of tFA and cFA. Values with inclusion of solvent effects are indicated by the subscript *aq*.

	S_0	$S_0 \rightarrow S_1$			$S_0 \rightarrow S_2$			$S_0 \rightarrow S_3$			$S_0 \rightarrow S_4$		
	E_{rel}/eV	type	ΔE/eV	f	type	ΔE/eV	f	type	ΔE/eV	f	type	ΔE/eV	f
tFA	0.0	$\pi\pi^*$	4.00	0.48	$\pi\pi^*$	4.55	0.08	$n\pi^*$	4.64	0.00	$\pi\pi^*$	5.29	0.39
tFA^-	15.4	$n\pi^*$	2.90	0.00	$n\pi^*$	3.05	0.00	$\pi\pi^*$	3.59	0.01	$n\pi^*$	4.67	0.00
tFA^{2-}	33.23	$\pi\sigma^*$	3.69	0.00	$\pi\pi^*$	3.84	0.40	$n\pi^*$	3.90	0.00	$n\pi^*$	4.14	0.00
$\mathrm{tFA}_{\mathrm{aq}}$	0.0	$\pi\pi^*$	3.74	0.50	$\pi\pi^*$	4.40	0.18	$n\pi^*$	4.84	0.00	$\pi\pi^*$	5.18	0.40
$\mathrm{tFA}_{\mathrm{aq}}^-$	12.82	$n\pi^*$	4.17	0.00	$\pi\pi^*$	4.19	0.54	$n\pi^*$	4.47	0.00	$\pi\pi^*$	4.63	0.02
$\mathrm{tFA}_{\mathrm{aq}}^{2-}$	25.99	$\pi\pi^*$	3.55	0.66	$\pi\pi^*$	4.32	0.09	$n\pi^*$	4.44	0.00	$n\pi^*$	4.52	0.00
cFA	0.36	$\pi\pi^*$	4.16	0.24	$n\pi^*$	4.46	0.00	$\pi\pi^*$	4.76	0.02	$\pi\pi^*$	5.32	0.25
cFA^-	15.48	$\pi\pi^*$	3.70	0.05	$\pi\pi^*$	3.81	0.11	$n\pi^*$	4.09	0.00	$\pi\pi^*$	4.22	0.00
cFA^{2-}	33.63	$\pi\sigma^*$	3.44	0.00	$\pi\pi^*$	3.85	0.15	$\pi\pi^*$	3.93	0.42	$n\pi^*$	4.22	0.01
$\mathrm{cFA}_{\mathrm{aq}}$	0.36	$\pi\pi^*$	3.64	0.31	$\pi\pi^*$	4.35	0.16	$n\pi^*$	4.73	0.02	$\pi\pi^*$	5.18	0.31
$\mathrm{cFA}_{\mathrm{aq}}^-$	13.03	$\pi\pi^*$	4.49	0.44	$\pi\pi^*$	4.67	0.01	$n\pi^*$	5.10	0.00	$\pi\pi^*$	5.22	0.14
$\mathrm{cFA}_{\mathrm{aq}}^{2-}$	26.28	$\pi\pi^*$	3.74	0.46	$\pi\pi^*$	4.33	0.12	$n\pi^*$	4.73	0.00	$n\pi^*$	4.91	0.10

5.4 Discussion

The comprehensive results for the differently protonated forms of the two FA isomers obtained by static and femtosecond time-resolved emission and absorption spectroscopies in combination with quantum chemical calculations provide detailed insight into the ultrafast processes leading to electronic deactivation. For the sake of clarity, the following discussion is structured into three parts dealing with the quantum chemical calculations, the observed spectro-temporal dynamics and assignment of the time scales, and finally the implications regarding details of the reaction pathways.

5.4.1 Quantum chemical calculations

The results for the vertical excitations into the first three singlet excited states for the neutral molecules tFA and cFA without inclusion of solvation effects can be compared to CASSCF/CASPT2 gas-phase calculations for these molecules in the literature.[31] In accordance with these, our DFT calculations show two optically bright $^1\pi\pi^*$ states, and one energetically higher-lying $^1n\pi^*$ excited singlet state with much lower oscillator strength. The good qualitative agreement with the CASSCF/CASPT2 calculations demonstrates that the chosen DFT method is adequate, and it can be assumed that a similar level of accuracy should also hold for the two deprotonated forms. The aforementioned CASSCF/CASPT2 calculations for tFA and cFA also provide evidence for an optically dark $\pi\sigma^*$ state, as seen in our DFT results for tFA^{2-} and cFA^{2-} *in vacuo*. For phenolic molecules, such $\pi\sigma^*$ states provide a route for the photo-deactivation by IC to the electronic ground state along a RO−H stretch coordinate (cf. discussion on pathways below).[31,60–62]

For the calculated results with inclusion of solvation effects via COSMO, direct comparison with the static UV/VIS-spectra (Fig. 5.2) is feasible. Both main trends, i.e. the observed blue-shift of the absorption of the anionic forms compared to the neutral and dianionic forms, and the absorption at longer wavelengths for the respective *trans*-isomers compared to the *cis*-isomers, are reproduced by the calculated lowest $S_0 \rightarrow {}^1\pi\pi^*$ vertical excitation energies. This establishes that for all studied molecules, initial excitation populates the $1\,{}^1\pi\pi^*$ states. The underlying transitions have HOMO-LUMO character, where an electron from a bonding C=C π orbital is promoted to a π^* orbital that is antibonding with respect to the C=C double bond, so that the double bond should be weakened upon photo-excitation in the near UV. This might be taken as an indication for a possible torsional *cis* ⇄ *trans* isomerisation coordinate in accordance with the standard expectation regarding photo-excited C=C double bonds.[63,64] The results indicate further that the excited states are partly re-ordered by solvation. In particular, the $^1n\pi^*$ excitation energies are reduced relative to those of the $^1\pi\pi^*$ states, such that for tFA^{-}_{aq}, the $1\,^{1}n\pi^{*}$ state becomes the lowest electronically excited state at the FC geometry. This suggests that the $^{1}n\pi^{*}$ states might be relevant for electronic deactivation, in accordance with previous calculations on hydroxycinnamic acid derivatives.[11,31]

However, we caution against drawing conclusions regarding relevant coordinates and participating states from these DFT results alone, for several reasons: First, our calculations were done only at the optimized ground-state geometries, i.e., single points on the potential energy surfaces. Comparison to previous *ab initio* results is only feasible at those geometries. Second, the reaction pathways will be strongly affected by the couplings between different electronic states and very likely involve conical intersections (CIs). In such regions, (TD)DFT and other single-reference electronic structure methods produce qualitatively wrong descriptions, multireference methods would be needed for correct treatment. In addition, notations such as HOMO and LUMO become ill-defined when configuration interaction is important (see ESI† for additional discussion). Extended exploration of the photoisomerisation pathways using expensive multi-reference methods like CASSCF/CASPT2, would be desirable, but is beyond the scope of the present work.

5.4.2 Observed ultrafast dynamics

The time-resolved emission and absorption data for the neutral, anionic and dianionic tFA forms all exhibit very similar spectro-temporal behaviours quantified by two sub-picosecond time constants, $\tau_1 \approx 0.15$ ps (observed in absorption only) and $\tau_2 \approx 0.6$ ps, on average, and two slower time constants ($\tau_3 = 3 - 11$ ps and $\tau_4 \approx 20$ ps). The strong spectral shifts of $> 2000\,\mathrm{cm}^{-1}$ observed in particular at early (< 1 ps) delay times are reproduced by the changes between the first two EAFS and three EADS, respectively (cf. Fig. 5.4). The subsequent changes with τ_3 towards the final excited-state EAFS/EADS are similar for all three forms. The permanent absorption changes described by the final EADS are small and consistent with fairly low *trans* → *cis* isomerisation yields, in line with previous transient absorption studies of tFA,[12,13] and in agreement with inefficient photoconversion observed in static irradiation experiments.[6,65]

The present results on UV-excited tFA agree well with the observed behaviour in previous studies,[12,13] where only one sub-picosecond time constant was used to model the data, however. The existing differences can be related partly to the increased time resolution of 50 fs in our experiments (compared to 370 fs in Ref. [12]), and partly to the advantageous properties of the SVD-based data analysis for the selected number of components, which acts as a noise filter when higher SVD components mostly related to random noise are discarded, and reduces the dimensionality of the least-squares fits.[66] In fact, while in any type of data analysis, descriptions of the signals by purely delay-dependent time profiles and wavelength-dependent spectra become necessarily inaccurate in the presence of spectral shifts, SVD provides a rationale for the estimation of the number of required components, yielding an optimal least-squares solution for the selected number of components.[66,67]

The assignment of the time constants is made taking into account the behaviour of the evolution-associated spectra in fluorescence and absorption. In this context, it should be noted that within Scheme 5.3.2.1, the first EAFS and EADS correspond to the time-zero spectra that decay with the respective fastest time constant (τ_1 in absorption, τ_2 in emission). The subsequent spectra rise and decay according to the sequential kinetics, e.g., the second EADS rise with τ_1 and decay with τ_2. The final EADS build up with τ_4 and do not decay on the time scale of the experiment. Furthermore, the first EAFS and EADS can be associated to photo-excited *trans*-isomer molecules in the Franck-Condon (FC) region of the excited electronic state (even if Scheme 5.3.2.1 should not reflect the true molecular dynamics), and the final EADS corresponds to the permanent absorption changes due to product formation.

Based on the agreement between the results probed in emission and absorption, all four time constants are unambiguously related to excited-state processes, and the slowest time constant τ_4 can be related to the deactivation to the electronic ground state. The spectro-temporal changes within the first picosecond featuring pronounced spectral shifts and described by one sub-picosecond time constant in emission and two time constants in absorption are consistent with the behaviour expected from solvation dynamics in polar solvents.[68] In particular, the solvation dynamics in water is known to be extremely fast, with a strong sub-100 fs Gaussian response and multi-exponential decays with time constants ranging from < 1 ps to a few picoseconds.[68–72] However, a noticeable decrease in intensity happens on the same time scale, e.g., the amplitude of the second EAFS is only about 50% compared to the first EAFS in the case of tFA. This indicates a decrease of the Franck-Condon factors likely to be caused by molecular motion on the excited-state potential energy surface (PES) on the same time scale. Therefore, we assign time constants τ_1 and τ_2 to initial concurrent solvent rearrangement and molecular dynamics out of the Franck-Condon region of the initially excited $^1\pi\pi^*$ states in accordance with the literature.[12,13,31] A quantitative assessment of the solvation dynamics is difficult for several reasons: First, the superimposed effects of molecular dynamics need to be disentangled. Second, the time resolution of the time-resolved fluorescence measurements is limited, so that the initial solvation dynamics happens within instrumental resolution. And finally, the additional overlap of the SE and ESA contributions is a further complication that prevents a more detailed analysis in absorption. Nevertheless, tFA^- behaves unlike the other two *trans* forms in that spectral shifts are virtually absent beyond $\approx 1 - 2$ ps (cf. Fig. 5.3). One might speculate that this could be due to the negative charge at the carboxylic group, however, alternative explanations such as a different gradient of the involved PES, are conceivable as well.

There are several plausible explanations for time constant τ_3. First, it could be related to vibrational cooling in the initially excited state prior to electronic deactivation. In that case, a spectral blue-shift of the emission and a corresponding red-shift of the absorption, accompanied by spectral narrowing of the corresponding bands would be expected. Inspection of the EAFS and EADS related by τ_3 (red and green spectra in Fig. 5.4) reveals that minor spectral shifts are present, but there are no clear indications of spectral narrowing. Rather, the dominating feature is a significant intensity decrease, that is unlikely to be caused solely by vibrational cooling. Alternatively, τ_3 could be interpreted as the time scale of a separate pathway for electronic deactivation to the electronic ground state. Pathways originating from a different region of the same electronic excited state have indeed been observed, e.g., in the electronic deactivation of styrene with different amounts of vibrational excess energy.[73] It is, however, not clear how such a splitting of pathways in the excited state should occur in the case of tFA. Moreover, an alternative description of the emission data by a kinetic scheme including a parallel reaction as final step yielded contradictory evidence, as the resulting associated fluorescence spectra showed unphysical, partially negative amplitudes.

The observed spectral changes with τ_3 are consistent instead with an interpretation of τ_3 either as the time scale of a slow evolution in a fairly flat region of the initially excited $1\,^1\pi\pi^*$ potential energy surface, or as the time scale for internal conversion (IC) to an intermediate excited electronic state. The latter case is in accord with recent quantum chemical calculations of tFA in the gas phase that predicted IC to the $2\,^1\pi\pi^*$ state followed by deactivation to the electronic ground state as a viable pathway for *trans*-*cis* isomerisation. Both scenarios have also been adopted for the interpretation of the observed time scales in previous experimental studies of photo-excited ferulic acid.[12,13]

The results for the neutral, anionic and dianionic *cis* isomers exhibit distinct differences between them, with cFA behaving essentially identical to the three tFA forms so that its results can be interpreted the same way. Conversely, both anionic forms (cFA^- and cFA^{2-}) have much weaker SE contributions and lack the intermediate τ_3 component. The evolution of the time-zero spectra (first EADS) within less than a picosecond described by τ_1, and additionally τ_2 in the case of cFA^-, shows a significant decrease in intensity and leads to EADS (green spectra in Fig. 5.5) composed of negative signal contributions by SE and positive signals due to ESA. Both spectra are fairly similar to each other and to the final excited-state EADS of cFA and the tFA forms. The presence of SE indicates that they originate from molecules in the excited state. The time scale of the decay (τ_4) towards the final EADS representing the permanent absorption changes therefore corresponds to the lifetime of the excited-state. Time constants τ_1, and τ_2 describe complex excited-state dynamics that cannot be disentangled easily and might involve simultaneous solvent rearrangement, initial excited-state dynamics originating the FC region and possibly even IC to other excited electronic states. Despite the apparent similarities at early delay times, cFA$^-$ and cFA^{2-} differ strikingly in that the latter has the short excited-state lifetime of $\tau_4 = 1.4$ ps, more than ten times smaller than for cFA$_1^-$ and cFA. Considering this, an almost barrierless pathway seems certain for cFA^{2-}. The almost perfect match of the permanent absorption changes (final EADS) of cFA^{2-} with the corresponding static *trans-cis* UV/VIS difference spectrum (cf. Fig. 5.5) provides clear evidence for *cis* → *trans* photoisomerisation.

5.4.3 Excited-state pathways

Further insight into the pathways of the ultrafast de-excitation processes is feasible by cross-comparison between all data sets. The main points can be summarized as follows:

(i) Based on the large similarities of the observed spectro-temporal behaviour of tFA, tFA$^-$, tFA^{2-} and cFA, very similar electronic deactivation pathways can be assumed for these. The observed excited-state lifetimes of ≈ 20 ps in all cases favour the existence of a low excited-state potential energy barrier, in agreement with the calculations of Ref. [31] done for tFA and cFA. The observed permanent absorption changes indicate fairly low *trans* → *cis* isomerisation quantum yields in line with previous time-resolved studies[12,13] and static irradiation experiments.[6,65]

(ii) The results for cFA^{2-} provide unambiguous evidence that the *trans*-isomer is formed. Since the electronic deactivation of cFA^{2-} happens with a time constant of 1.4 ps, a barrierless excited-state pathway along a *cis* $\rightleftarrows$ *trans* isomerisation coordinate is likely.

(iii) The anionic form of the *cis*-isomer constitutes an intermediate case. Its sub-picosecond spectro-temporal dynamics, the weak SE, and the absence of the τ_3 decay component are all quite similar to the case of cFA^{2-}, yet the much larger excited-state lifetime ($\tau_4 = 17$ ps), and the small permanent absorption changes correspond to the behaviour of the *trans*-isomer forms and cFA.

(iv) Despite the apparent dissimilarities, a common underlying scenario for all cases is thus conceivable, where the observed differences are caused by just minor changes in the relevant potential energy surfaces, such as slightly different locations of the involved CIs and/or different energy gradients in their vicinity, and smaller (or larger) energy barriers along the excited-state pathway. On account of the observed *cis* → *trans* isomerisation, the reaction coordinate is likely to involve torsion about the C=C double bond.

Figure 5.6 shows schematic sketches of the proposed relaxation pathways following photoexcitation into the $S_1(1\,^1\pi\pi^*)$ state that explain the present findings, are in line with

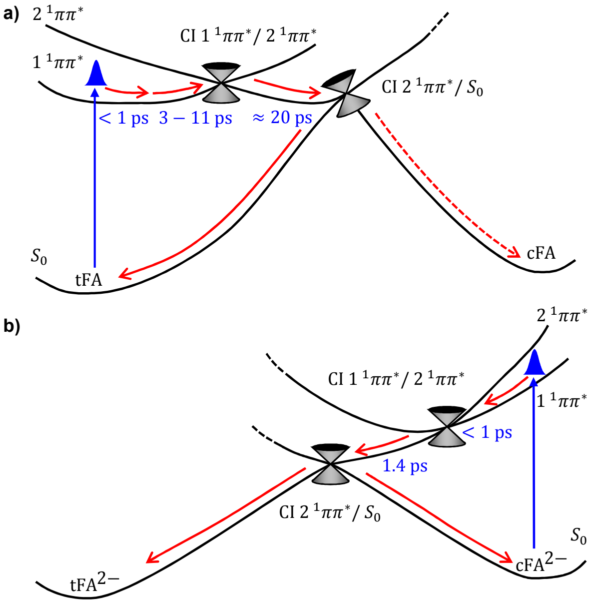

Fig. 5.6 Schematic sketch of the suggested pathways of ferulic acid upon excitation to the $1\,^1\pi\pi^*$ state. a) Scenario for the *trans*-isomers. b) Suggested isomerisation pathway for the dianionic *cis*-isomer.

results from previous time-resolved studies.[12,13] and take into account the quantum chemical calculations on photo-excited tFA and cFA in the gas phase.[12,13,31] In line with the calculations, the scenario assumes a sequential pathway comprising IC to the $2\,^1\pi\pi^*$ state as intermediate state, followed by deactivation to the electronic ground state via a $2\,^1\pi\pi^*/S_0$ CI involving torsion about the C=C double bond, i.e., the *cis* $\leftrightarrows$ *trans* isomerisation coordinate. For the *trans*-isomer forms (cf. Fig. 5.6a), the fast sub-picosecond dynamics given by τ_1 and τ_2 is due to initial solvent rearrangement and concurrent molecular dynamics out of the Franck-Condon region of the initially excited $^1\pi\pi^*$ state, time constant τ_3 corresponds to the time scale of the IC to the $2\,^1\pi\pi^*$ state, and τ_4 describes the deactivation to the electronic ground state. The comparatively slow latter steps are rationalized by excited-state pathways that are not barrierless. A tilted topography of the $2\,^1\pi\pi^*/S_0$ CI is suggested in line with the calculations.[31] This could explain why most molecules return to the electronic ground state of the *trans*-isomer and do not isomerise, resulting in fairly low isomerisation quantum yields consistent with the observed small permanent absorption changes for the *trans*-isomers and in agreement with previous irradiation experiments.[6,65]

As is illustrated in Fig. 5.6b, the distinct behaviour of cFA^{2-} could be caused by just slightly different locations of the involved CIs, and an excited-state pathway involving no or only small energy barriers. Here, solvation rearrangement, initial dynamics and IC to the $2\,^1\pi\pi^*$ state are assumed to happen simultaneously on a sub-picosecond timescale. As a consequence, the individual processes cannot be disentangled in our experiments, explaining why only two related time constants are observed and the τ_3 component is missing. The final deactivation to the electronic ground state (τ_4) happens via a $2\,^1\pi\pi^*/S_0$ CI as above.

The suggested relaxation pathways are plausible because they provide a unified and consistent explanation of the observed ultrafast dynamics following photo-excitation of the neutral, anionic and dianionic forms of both *trans*- and *cis*-FA, as well as previous results from static irradiation. Furthermore, the scenario is in accord with *ab initio* calculations for tFA and cFA,[31] however, other pathways are conceivable considering that FA is not only a cinnamic acid derivative with an isomerisable C=C double bond, but could also be classified as a substituted phenol.[15,60–62] Indeed, the calculations of Ref. [31] also showed direct electronic deactivation via a $1\,^1\pi\pi^*/S_0$ CI along an out-of-plane ring deformation coordinate and $\pi\sigma^*$-mediated fission of the phenolic O−H bond[61] as possible pathways. Although the former pathway cannot be ruled out completely, it does seem unlikely to be a major contributing pathway since it does not lead to *cis* ⇆ *trans* isomerisation. Our data do not indicate that deactivation to the electronic ground state involving a $\pi\sigma^*$ state has much relevance either, as there are no significant absorption contributions from phenolic radicals formed by O−H or O−CH_3 bond fission.[74] Furthermore, $\pi\sigma^*$-mediated dissociation should be possible only at higher excitation energies according to the calculations for tFA suggesting a sizeable excited-state energy barrier, and also by comparison with other molecules stufdied in the literature.[31,60–62,75]

It should be noted further that the proposed scenario relates to gas-phase calculations, but solvation shifts the energies of the participating states. In particular, in our DFT calculations, the $^1n\pi^*$ excitation energies were found to be reduced relative to those of the $^1\pi\pi^*$ states, suggesting that the $1\,^1n\pi^*$ state might be relevant in solution, as has been discussed for structurally related hydroxycinnamic acid derivatives.[10,11] Given the variety of relaxation pathways discussed in the literature for this class of molecules, it is clear that further high-level theoretical studies as well as additional experimental work targeting possible IC steps, e.g. using structure-sensitive methods such as time-resolved vibrational spectroscopy, measurements in other solvent environments, or anisotropy measurements are desirable.

5.5 Summary and conclusions

The present comprehensive study of the photo-excited neutral, anionic and dianionic forms of *trans*- and *cis*-ferulic acid in aqueous solutions using femtosecond time-resolved emission and absorption spectroscopies and DFT calculations yields detailed insight into the ensuing ultrafast processes promoting electronic deactivation. According to the calculations, the initially excited optically bright electronic state is the first ${}^1\pi\pi^*$ state. The multi-exponential spectro-temporal dynamics observed in emission and absorption indicate that the initial excitation to the Franck-Condon region is immediately followed by solvent rearrangement, wavepacket motion along PES gradients and minor geometry changes on the sub-picosecond time scale for all molecules. For the dianionic *cis*-isomer cFA^{2-}, the observed permanent absorption changes show unambiguously that the *trans*-isomer photoproduct is formed. The electronic deactivation of cFA^{2-} happens with a time constant of 1.4 ps, making a barrierless excited-state pathway along a *cis* $\rightleftarrows$ *trans* isomerisation coordinate likely. For all other molecules, excited-state deactivation is more than ten times slower, with an average time constant of $\approx$ 20 ps, suggesting low excited-state potential energy barriers along the de-excitation pathway. Although alternative routes, e.g. involving ring deformations, cannot be fully excluded, the data in these cases are consistent with a step-wise electronic deactivation most likely involving internal conversion to the $2\,{}^1\pi\pi^*$ state and further deactivation via a $2\,{}^1\pi\pi^*/S_0$ CI by torsion about the C=C double bond. Regarding photoprotection in plants as well as sunscreen applications, the ultrafast pathways for electronic deactivation suggested here would lead only to mutual interconversion of the *trans* and *cis* isomers, i.e. both isomers could equally act as photoprotectant, and within the resulting closed cycle, radiation energy would be simply dissipated to the surrounding solvent.

Acknowledgements

The authors thank Markus Ott for assistance in the measurement of the initial static fluorescence spectra. This work has been supported by the Deutsche Forschungsgemeinschaft through sub-project A1 of the SFB 677 “Function by Switching” (FR, FT, BH) and by a PhD grant (Grant no. 201306620029) by the China Scholarship Council (SW).

Bibliography

[1] Z. Zhao, M. H. Moghadasian, *Food Chem.* **2008**, *109*, 691–702.

[2] R. J. Robbins, *J. Agric. Food. Chem.* **2003**, *51*, 2866–2887.

[3] K. J. Gohil, S. B. Kshirsaga, R. S. Sahane, *Int. J. Pharm. Sci. Res.* **2012**, *3*, 700–710.

[4] E. Graf, *Free Radic. Biol. Med.* **1992**, *13*, 435–448.

[5] E. de Oliveira Silva, R. Batista, *Compr. Rev. Food Sci. Food Saf.* **2017**, *16*, 580–616.

[6] G. Kahnt, *Phytochemistry* **1967**, *6*, 755–758.

[7] F. Borges, J. L. Lima, I. Pinto, S. Reis, C. Siquet, *Helv. Chim. Acta* **2003**, *86*, 3081–3087.

[8] K. Oehlke, A. Heins, H. Stöckmann, K. Schwarz, *Food Chem.* **2010**, *118*, 48–55.

[9] J. F. Kennedy, P. Methacanon, L. L. Lloyd, *J. Sci. Food Agric.* **1999**, *79*, 464–470.

[10] E. M. M. Tan, M. Hilbers, W. J. Buma, *J. Phys. Chem. Lett.* **2014**, *5*, 2464–2468.

[11] J. C. Dean, R. Kusaka, P. S. Walsh, F. Allais, T. S. Zwier, *J. Am. Chem. Soc.* **2014**, *136*, 14780–14795.

[12] M. Vengris, D. S. Larsen, M. A. Van Der Horst, O. F. A. Larsen, K. J. Hellingwerf, R. Van Grondelle, *J. Phys. Chem. B* **2005**, *109*, 4197–4208.

[13] M. D. Horbury, L. A. Baker, W.-D. Quan, S. E. Greenough, V. G. Stavros, *Phys. Chem. Chem. Phys.* **2016**, *18*, 17691–17697.

[14] L. A. Baker, V. G. Stavros, *Sci. Prog.* **2016**, *99*, 282–311.

[15] L. A. Baker, B. Marchetti, T. N. V. Karsili, V. G. Stavros, M. N. R. Ashfold, *Chem. Soc. Rev.* **2017**, *46*, 3770–3791.

[16] *Excited states and photochemistry of organic molecules*, *Vol. 53*, (Eds.: M. Klessinger, J. Michl), VCH Publishers, New York, **1995**.

[17] F. Renth, R. Siewertsen, F. Temps, *Int. Rev. Phys. Chem.* **2013**, *32*, 1–38.

[18] *Conical Intersections: Electronic Structure, Dynamics and Spectroscopy*, (Eds.: W. Domcke, D. R. Yarkony, H. Köppel), World Scientific, Singapore, **2004**.

[19] *Conical Intersections: Theory, Computation and Experiment*, (Eds.: W. Domcke, D. R. Yarkony, H. Köppel), World Scientific, Singapore, **2011**.

[20] S. Matsika, P. Krause, *Annu. Rev. Phys. Chem.* **2011**, *62*, 621–643.

[21] P. Changenet-Barret, A. Espagne, S. Charier, J. B. Baudin, L. Jullien, P. Plaza, K. J. Hellingwerf, M. M. Martin, *Photochem. Photobiol. Sci.* **2004**, *3*, 823–829.

[22] A. Espagne, P. Changenet-Barret, P. Plaza, M. M. Martin, *J. Phys. Chem. A* **2006**, *110*, 3393–3404.

[23] A. Espagne, D. H. Paik, P. Changenet-Barret, M. M. Martin, A. H. Zewail, *ChemPhysChem* **2006**, *7*, 1717–1726.

[24] H. Kuramochi, S. Takeuchi, T. Tahara, *J. Phys. Chem. Lett.* **2012**, *3*, 2025–2029.

[25] K. Pande, C. D. M. Hutchison, G. Groenhof, A. Aquila, J. S. Robinson, J. Tenboer, S. Basu, S. Boutet, D. P. DePonte, M. Liang, T. A. White, N. A. Zatsepin, O. Yefanov, D. Morozov, D. Oberthuer, C. Gati, G. Subramanian, D. James, Y. Zhao, J. Koralek, J. Brayshaw, C. Kupitz, C. Conrad, S. Roy-Chowdhury, J. D. Coe, M. Metz, P. L. Xavier, T. D. Grant, J. E. Koglin, G. Ketawala, R. Fromme, V. Rajer, R. Henning, J. C. H. Spence, A. Ourmazd, P. Schwander, U. Weierstall, M. Frank, P. Fromme, A. Barty, H. N. Chapman, K. Moffat, J. J. van Thor, M. Schmidt, *Science* **2016**, *352*, 725–729.

[26] N. Mataga, H. Chosrowjan, S. Taniguchi, N. Hamada, F. Tokunaga, Y. Imamoto, M. Kataoka, *Phys. Chem. Chem. Phys.* **2003**, *5*, 2454–2460.

[27] D. S. Larsen, M. Vengris, I. H. M. van Stokkum, M. A. van der Horst, F. L. de Weerd, K. J. Hellingwerf, R. van Grondelle, *Biophys. J*. **2004**, *86*, 2538–2550.

[28] E. M. M. Tan, S. Amirjalayer, B. H. Bakker, W. J. Buma, *Faraday Discuss.* **2013**, *163*, 321.

[29] G. Groenhof, M. Bouxin-Cademartory, B. Hess, S. P. de Visser, H. J. C. Berendsen, M. Olivucci, A. E. Mark, M. A. Robb, *J. Am. Chem. Soc.* **2004**, *126*, 4228–4233.

[30] F. F. García-Prieto, A. Muñoz-Losa, M. Luz Sánchez, M. Elena Martín, M. A. Aguilar, *Phys. Chem. Chem. Phys.* **2016**, *18*, 27476–27485.

[31] T. N. V. Karsili, B. Marchetti, M. N. R. Ashfold, W. Domcke, *J. Phys. Chem. A* **2014**, *118*, 11999–12010.

[32] TURBOMOLE V7.0 2015, a development of University of Karlsruhe and Forschungszentrum Karlsruhe GmbH, 1989-2007, TURBOMOLE GmbH, since 2007; available from `http://www.turbomole.com`.

[33] A. Klamt, G. Schuurmann, *J. Chem. Soc., Perkin Trans. 2* **1993**, 799–805.

[34] M. L. Salum, C. J. Robles, R. Erra-Balsells, *Org. Lett.* **2010**, *12*, 4808–4811.

[35] F. H. Yassin, D. S. Marynick, *J. Mol. Struct. (Theochem.)* **2006**, *766*, 137–141.

[36] S. P. Ozkorucuklu, J. L. Beltrán, G. Fonrodona, D. Barrón, G. Alsancak, J. Barbosa, *J. Chem. Eng. Data* **2009**, *54*, 807–811.

[37] S. Arzhantsev, M. Maroncelli, *Appl. Spectrosc.* **2005**, *59*, 206–220.

[38] B. Schmidt, S. Laimgruber, P. Gilch in Quantum Electronics Conference, 2003. EQEC '03. European, *Vol. 814*, **2003**, p. 177.

[39] J. A. Gardecki, M. Maroncelli, *Appl. Spectrosc.* **1998**, *52*, 1179–1189.

[40] F. Renth, M. Foca, A. Petter, F. Temps, *Chem. Phys. Lett.* **2006**, *428*, 62–67.

[41] F. Renth, R. Siewertsen, F. Strübe, J. Mattay, F. Temps, *Phys. Chem. Chem. Phys.* **2014**, *16*, 19556.

[42] K. Röttger, S. Wang, F. Renth, J. Bahrenburg, F. Temps, *Appl. Phys. B* **2015**, *118*, 185–193.

[43] C. Adamo, V. Barone, *J. Chem. Phys.* **1999**, *110*, 6158–6170.

[44] M. R. Momeni, A. Brown, *J. Phys. Chem. A* **2016**, *120*, 2550–2560.

[45] L. A. Burns, À. Vàzquez-Mayagoitia, B. G. Sumpter, C. D. Sherrill, *J. Chem. Phys.* **2011**, *134*, 084107.

[46] F. Weigend, R. Ahlrichs, *Phys. Chem. Chem. Phys.* **2005**, *7*, 3297–3305.

[47] R. Ahlrichs, *Phys. Chem. Chem. Phys.* **2004**, *6*, 5119–5120.

[48] M. Arnim, R. Ahlrichs, *J. Comput. Chem* **1998**, *19*, 1746–1757.

[49] S. Grimme, J. Antony, S. Ehrlich, H. Krieg, *J. Chem. Phys.* **2010**, *132*, 154104.

[50] R. Bauernschmitt, R. Ahlrichs, *Chem. Phys. Lett.* **1996**, *256*, 454–464.

[51] R. Bauernschmitt, M. Häser, O. Treutler, R. Ahlrichs, *Chem. Phys. Lett.* **1997**, *264*, 573–578.

[52] F. Furche, R. Ahlrichs, *J. Chem. Phys.* **2002**, *117*, 7433–7447.

[53] D. Rappoport, F. Furche, *J. Chem. Phys.* **2005**, *122*, 064105.

[54] F. Furche, D. Rappoport, *Theor. Comput. Chem.* **2005**, *16*, 93–128.

[55] A. Klamt, *J. Phys. Chem.* **1996**, *100*, 3349–3353.

[56] G. Scalmani, M. J. Frisch, B. Mennucci, J. Tomasi, R. Cammi, V. Barone, *J. Chem. Phys.* **2006**, *124*, 094107.

[57] The logarithmic delay scale for an optimal display of the spectrotemporal evolution was obtained by taking log(t / ps + 0.5) and relabelling the scales to the correct delay values.

[58] I. H. van Stokkum, D. S. Larsen, R. van Grondelle, *Biochim. Biophysica. Acta Bioenergetics.* **2004**, *1657*, 82–104.

[59] R. Berera, R. van Grondelle, J. T. M. Kennis, *Photosynth. Res.* **2009**, *101*, 105–118.

[60] A. L. Sobolewski, W. Domcke, C. Dedonder-Lardeux, C. Jouvet, *Phys. Chem. Chem. Phys.* **2002**, *4*, 1093–1100.

[61] O. P. J. Vieuxmaire, Z. Lan, A. L. Sobolewski, W. Domcke, *J. Chem. Phys.* **2008**, *129*, 224307.

[62] M. N. R. Ashfold, G. A. King, D. Murdock, M. G. D. Nix, T. A. A. Oliver, A. G. Sage, *Phys. Chem. Chem. Phys.* **2010**, *12*, 1218–1238.

[63] A. Nenov, R. de Vivie-Riedle, *J. Chem. Phys.* **2011**, *135*, 034304.

[64] B. G. Levine, C. Ko, J. Quenneville, T. J. Martinez, *Mol. Phys.* **2006**, *104*, 1039–1051.

[65] R. D. Hartley, E. C. Jones, *J. Chromatogr. A* **1975**, *107*, 213–218.

[66] E. R. Henry, *Biophys. J .* **1997**, *72*, 652–73.

[67] H. Marciniak, S. Lochbrunner, *Chem. Phys. Lett.* **2014**, *609*, 184–188.

[68] B. Bagchi, B. Jana, *Chem. Soc. Rev.* **2010**, *39*, 1936–1954.

[69] W. Jarzeba, G. C. Walker, A. Johnson, M. A. Kahlow, P. F. Barbara, *J. Phys. Chem.* **1988**, *92*, 7039–7041.

[70] P. F. Barbara, W. Jarzeba, *Acc. Chem. Res.* **1988**, *21*, 195–199.

[71] R. Jimenez, G. R. Fleming, P. V. Kumar, M. Maroncelli, *Nature* **1994**, *369*, 471–473.

[72] M. J. Lang, X. J. Jordanides, X. Song, G. R. Fleming, *J. Chem. Phys.* **1999**, *110*, 5884–5892.

[73] A. D. G. Nunn, R. S. Minns, R. Spesyvtsev, M. J. Bearpark, M. A. Robb, H. H. Fielding, *Phys. Chem. Chem. Phys.* **2010**, *12*, 15751–15759.

[74] S. Foley, S. Navaratnam, D. J. McGarvey, E. J. Land, T. Truscott, C. A. Rice-Evans, *Free Radical Biol. Med.* **1999**, *26*, 1202–1208.

[75] B. Marchetti, T. N. V. Karsili, M. N. R. Ashfold, W. Domcke, *Phys. Chem. Chem. Phys.* **2016**, *18*, 20007–20027.

5.6 Electronic supplementary information

Calculated molecular orbitals of the *trans*- and *cis*-ferulic acid isomers

The DFT calculations were carried out using the Turbomole 7.0 program package[1], employing the Conductor-like Screening Model (COSMO)[2–4] to take into account solvation effects (see Sec. 2.3 of the main article). The relevant molecular orbitals (MOs) for the electronic transitions $S_0 \rightarrow S_n$ up to $n = 4$ of the bare neutral, anionic and di-anionic forms of *trans*- and *cis*-ferulic acid (FA) are displayed in Figures 5.7 and 5.8.

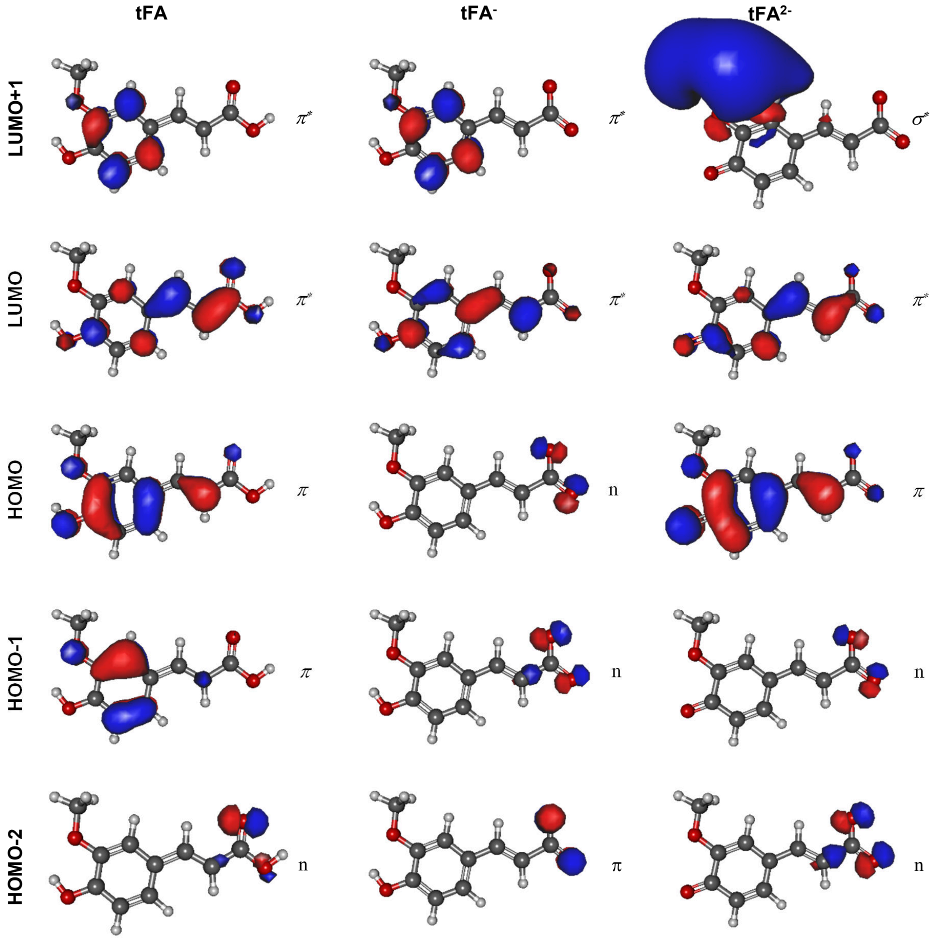

Fig. 5.7 Relevant molecular orbitals and their deduced characters of *trans*-FA in its neutral, anionic and di-anionic forms (tFA, tFA^- and tFA^{2-}) *in vacuo*.

The characters of the orbitals judged from visual inspection are indicated to their right. Mutual comparison of the *trans* and *cis* isomers reveals that the neutral tFA and cFA forms,

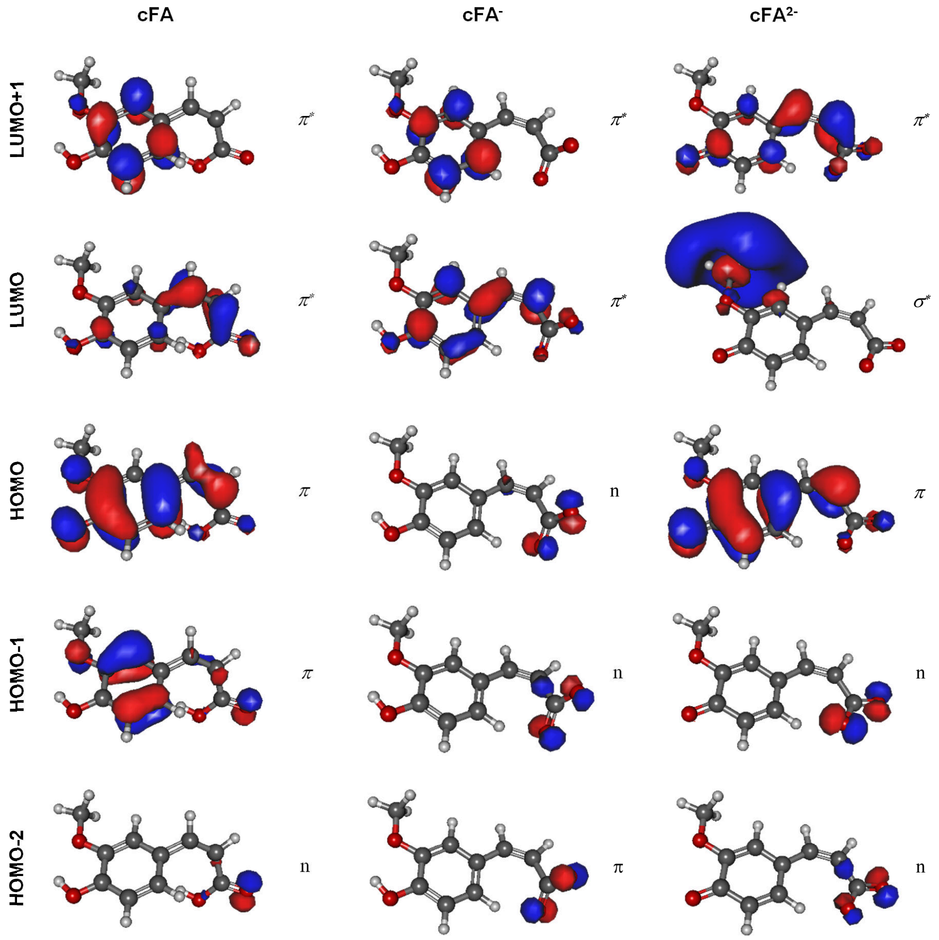

Fig. 5.8 Relevant molecular orbitals and their deduced characters of *cis*-FA in its neutral, anionic and di-anionic forms (cFA, cFA^- and cFA^{2-}) *in vacuo*.

and likewise the anionic tFA^- and cFA^- forms share the same sequence of orbitals. For the dianionic forms, the LUMO and LUMO+1 orbitals are interchanged. The unoccupied orbitals have π^* character and show electron density at the benzene ring (LUMO+1) and at the C=C double bond (LUMO). Only for the dianionic forms, a σ^*-like orbital replaces the π^* LUMO+1 orbital (tFA^{2-}) or the π^* LUMO orbital (cFA^{2-}). Indications for optically dark $\pi\sigma^*$ states have also been found in recent CASSCF/CASPT2 calculations for tFA and cFA, and they do play an important role in the photophysics of phenolic molecules.[5–8] However, we refrain from drawing any conclusions, considering that the calculations with inclusion of solvation effects do not show such states, and being cautious when interpreting DFT results regarding excited-state pathways (see further below). The occupied orbitals have either π- or n-character, and the transitions from the highest-lying π-orbital to the π^* LUMO (LUMO+1 for cFA^{2-}) are optically allowed $S_0 \rightarrow {}^1\pi\pi^*$ transitions in all cases.

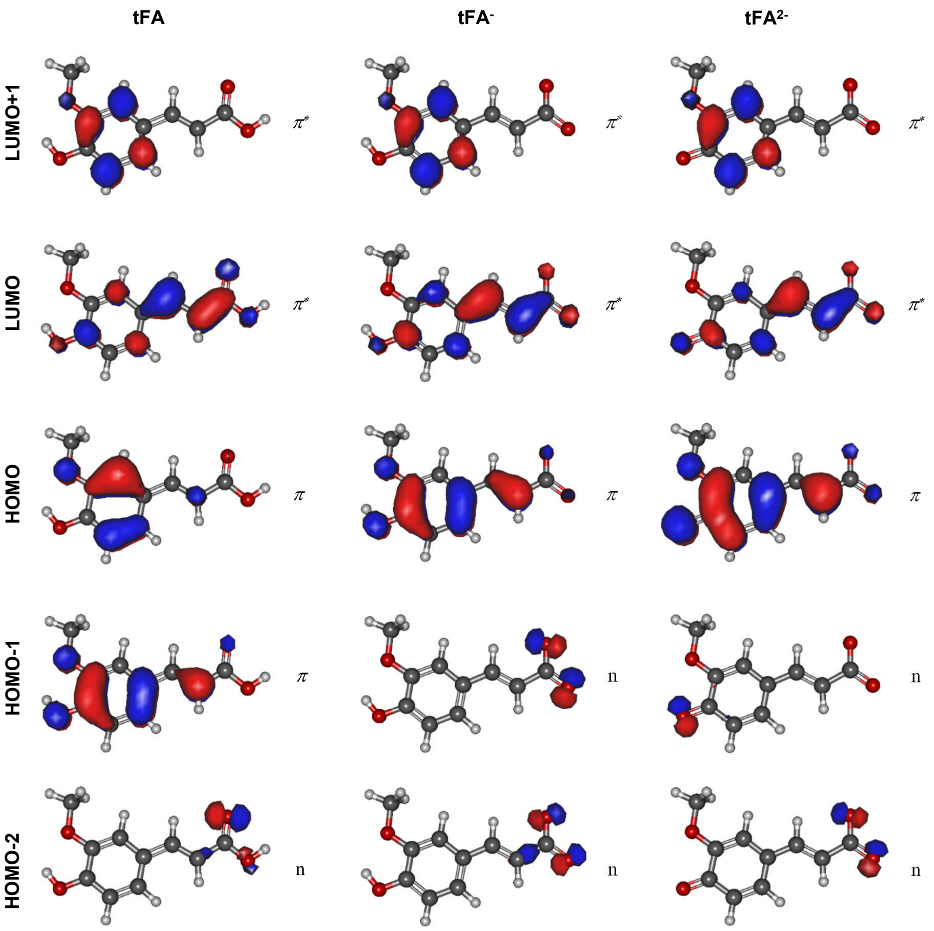

Fig. 5.9 Relevant molecular orbitals and their deduced characters for the neutral, anionic and di-anionic forms of *trans*-FA with solvation effects taken into account.

Figures 5.9 and 5.10 show the relevant MOs for the electronic transitions $S_0 \rightarrow S_n$ up to $n = 4$ for the different forms of *trans*- and *cis*-FA obtained with inclusion of solvation effects. As can be seen, the respective *trans*- and *cis*-forms have the same sequences of orbital characters. The unoccupied orbitals are all of π^* character, located either at the benzene ring (LUMO+1) or the C=C double bond (LUMO), the HOMO is always of π character. The neutral forms tFA and cFA have a second, lower-lying π orbital as HOMO-1, which is replaced by a n orbital for the anionic and dianionic forms. The HOMO-2 orbitals are n orbitals located at the oxygen atoms of the acid group, except for cFA^{2-}, where the phenolic O-atom is also involved. In the latter case, the visual difference between the HOMO-1 and HOMO-2 orbitals is rather small, which is also reflected in the strong mixing character for the excitations involving these orbitals.

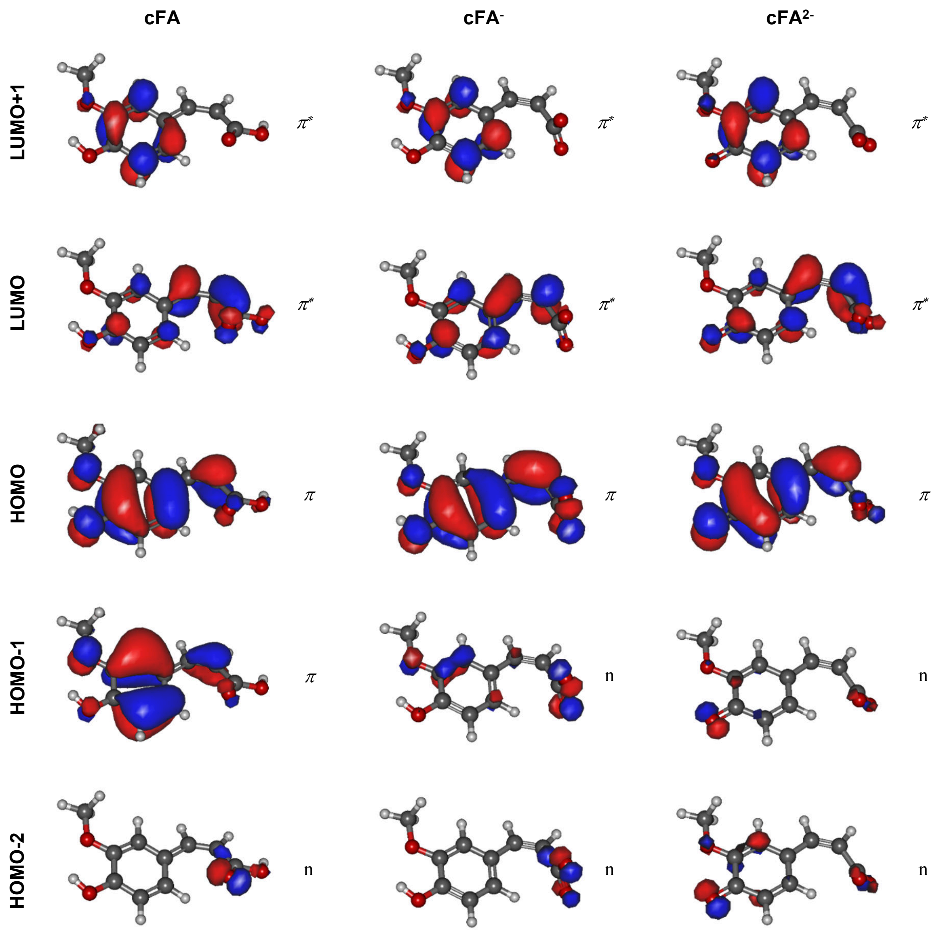

Fig. 5.10 Relevant molecular orbitals and their deduced characters for the neutral, anionic and di-anionic forms of *cis*-FA with solvation effects taken into account.

As stated in the paper, vertical excitation populates the $1\,{}^1\pi\pi^*$ state via an optically allowed $S_0 \rightarrow {}^1\pi\pi^*$ transition in all cases. Judged from the orbitals in Figures 5.9 and 5.10, these HOMO-LUMO transitions move an electron from a bonding C=C π orbital to an anti-bonding π^* orbital. This could be interpreted in favour of a photo-induced *cis* ⇄ *trans* isomerisation coordinate, conforming to the standard expectation at photo-excited double bonds.[9] However, such a conclusion should be drawn only with great caution, since molecular orbitals are just convenient computational constructs (which could be transformed via arbitrary linear transforms) and do not correspond to observables. Furthermore, when multi-configuration interaction is taken into account, concepts like HOMO and LUMO become ill-defined. Second, for an investigation of the de-excitation pathways, even a scan of the C=C dihedral angle would provide little evidence on how much this particular mechanism contributes; only unbiased, full-dimensional direct-dynamics simulations could provide these answers. For (TD)DFT or any other type of single-reference electronic structure method, such calculations are hardly adequate because of the expected strong coupling between the participating electronic states, and the likely involvement of conical intersections (CIs), which cannot be treated correctly by these methods.[10]. It should be noted that our calculations could be interpreted in favour the $^1n\pi^*$ states playing a role in the FA photochemistry, in line with previous calculations *in vacuo* on these molecules.[8,11] However, our calculations were done only at the optimized ground-state geometries, where indeed a good agreement with earlier CASSCF/CASPT2 results[8] was found (see paper). But given the approximations inherent in our method (RPA-DFT) and other standard TDDFT variants, this does not imply good results in other regions of the potential energy surfaces (PES); in fact, qualitative failures at conical intersections are to be expected. Therefore, our results provide a hint at a possible involvement of the $^1n\pi^*$ states, but their exact role and importance cannot be deduced.

Bibliography

[1] TURBOMOLE V7.0 2015, a development of University of Karlsruhe and Forschungszentrum Karlsruhe GmbH, 1989-2007, TURBOMOLE GmbH, since 2007; available from `http://www.turbomole.com`.

[2] A. Klamt, G. Schuurmann, *J. Chem. Soc., Perkin Trans. 2* **1993**, 799–805.

[3] A. Klamt, *J. Phys. Chem.* **1996**, *100*, 3349–3353.

[4] G. Scalmani, M. J. Frisch, B. Mennucci, J. Tomasi, R. Cammi, V. Barone, *J. Chem. Phys.* **2006**, *124*, 094107.

[5] A. L. Sobolewski, W. Domcke, C. Dedonder-Lardeux, C. Jouvet, *Phys. Chem. Chem. Phys.* **2002**, *4*, 1093–1100.

[6] O. P. J. Vieuxmaire, Z. Lan, A. L. Sobolewski, W. Domcke, *J. Chem. Phys.* **2008**, *129*, 224307.

[7] M. N. R. Ashfold, G. A. King, D. Murdock, M. G. D. Nix, T. A. A. Oliver, A. G. Sage, *Phys. Chem. Chem. Phys.* **2010**, *12*, 1218–1238.

[8] T. N. V. Karsili, B. Marchetti, M. N. R. Ashfold, W. Domcke, *J. Phys. Chem. A* **2014**, *118*, 11999–12010.

[9] A. Nenov, R. de Vivie-Riedle, *J. Chem. Phys.* **2011**, *135*, 034304.

[10] B. G. Levine, C. Ko, J. Quenneville, T. J. Martinez, *Mol. Phys.* **2006**, *104*, 1039–1051.

[11] L. A. Baker, B. Marchetti, T. N. V. Karsili, V. G. Stavros, M. N. R. Ashfold, *Chem. Soc. Rev.* **2017**, *46*, 3770–3791.

Chapter 6

Ultrafast electronic energy transfer in a photochromic donor–acceptor dyad

Shuangqing Wang,[a] Mats Bohnsack,[a] Sebastian Megow,[a] Falk Renth[a] and Friedrich Temps*[a]

[a] Institut für Physikalische Chemie, Christian-Albrechts-Universität zu Kiel, Olshausenstr. 40, 24098 Kiel, Germany.

S. Wang, M. Bohnsack, S. Megow, F. Renth, and F. Temps, *Phys. Chem. Chem. Phys.*, submitted (2018).

Own contribution to this munuscript:

- ☐ Syntheses of the dyad and reference molecules
- ☐ Static absorption spectroscopy
- ☐ Time-resolved absorption spectroscopy
- ☐ Analysis of the transient absorption data
- ☐ Writing of the manuscript

---

* To whom correspondence should be addressed. E-mail: temps@phc.uni-kiel.de

Abstract

The excited-state dynamics of a donor–acceptor dyad composed of 1-propyl-2-pyridinyl-benzimidazole (PPBI) as donor and diphenylnaphthopyran (DPNP) as acceptor linked via an ester bridge has been investigated by a combination of static and time-resolved spectroscopies and quantum chemical calculations. The UV absorption spectrum of the dyad is virtually identical to the sum of the spectra of its individual constituents, indicating only weak electronic coupling between the donor and acceptor in the electronic ground state. After selective photoexcitation of the PPBI chromophore in the dyad at λ_{pump} = 310 nm, however, a fast electronic energy transfer (EET) from the donor to the acceptor is observed, by which the lifetime of the normally long-lived excited state of PPBI is reduced to a few ps. The singular value decomposition-based global analyses of the measured femtosecond time-resolved transient absorption spectra of the dyad and its two building blocks as reference compounds allowed us to determine a value for the EET time constant in the dyad of $\tau = 2.84 \pm 0.70$ ps. For comparison, Förster theory predicts characteristic FRET times between 1.2 ps $\leq \tau \leq$ 4.2 ps, in good agreement with the experimental result.

6.1 Introduction

Electronic energy transfer (EET) plays a key role in many complex photo-induced processes, including natural and artificial photosynthesis[1–6] and the photophysics of solar cells.[7–15] For instance, the light harvesting antennae in the photosynthetic complexes of bacteria and plants not only collect the energy of the sunlight, but also ensure the subsequent efficient transfer of the excitation energy to the reaction centers, where the actual chemical transformations happen. A quantitative understanding of the underlying EET mechanisms is therefore of fundamental importance for rational designs of artificial light harvesting antenna analogues and other working energy transfer devices.[6,10,16,17]

A variety of molecular architectures based on energy donor–acceptor dyads and donor–bridge–acceptor triads have been developed to understand and utilise EET.[18–24] The respective chromophores can be connected at different distances and relative orientations by electronically insulating aliphatic spacers or by electronically conducting π-conjugating linkers.[25] The ensuing EET can thus take place "through-space" via dipole–dipole coupling as described by Förster resonance energy transfer (FRET) theory,[26–32] "through-bond" via electron exchange as described by the Dexter model,[19,33,34] or via some mixture of or deviation from these two classical mechanisms.[35–37] FRET commonly requires weak coupling, i.e. the donor–acceptor distance should be larger than the size of the individual dipoles or the dipoles should be oriented near-orthogonally. Dexter EET, on the other hand, requires strong coupling, i.e. the donor and acceptor should be close to each other, connected through a conjugated bridge, and possess favourable relative orientations.[38–40] As a radiationless relaxation process, FRET funnels the electronic energy that was supplied to the donor by the absorption of a photon to the acceptor that originally missed absorption and was left in its electronic ground state. The efficiency and rate of this transition depend on the donor–acceptor distance and on the overlap integral between the fluorescence spectrum of the donor and the absorption spectrum of the acceptor.[41–43]

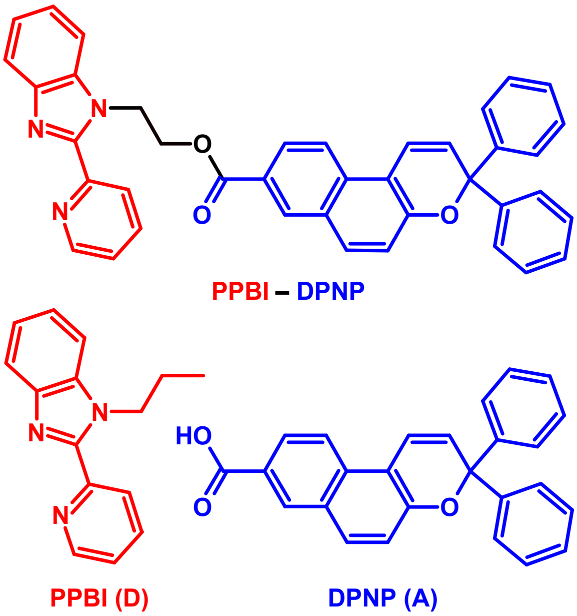

Fig. 6.1 Molecular structures of the PPBI–DPNP dyad and its constituents PPBI (donor, D, red) and DPNP (acceptor, A, blue).

Here, we report on a study of the excited-state dynamics of a donor–acceptor dyad consisting of 1-propyl-2-($2'$-pyridyl)-benzimidazole (PPBI) as donor (D) and 3,3-diphenyl-[3*H*]-naphtho[2,1-b]pyran (DPNP) as acceptor (A) linked by an ester bridge as shown in Fig. 6.1. Benzimidazoles like 2-($2'$pyridyl)-benzimidazole (PBI) form an interesting class of organic chromophores that have mostly attracted attention in the context of excited-state intramolecular proton transfer (ESIPT).[44–48] In addition, when the H atom at the N^1 position of the imidazole ring is replaced by some potential linker group, they exhibit many desirable characteristics for excitation energy donors, including simplicity in molecular structure, facile synthesis, high molar absorption coefficients, and compatibility with a variety of acceptor chromophores for practical realisation of light harvesting antennae.[48–53] Likewise, naphthopyrans are frequently used photochromic systems, especially in the ophthalmic lens industry, due to their versatile photoswitching properties with high sensitivity to sunlight, excellent resistance to photochemical fatigue, and easy synthetic access at relatively low cost.[54–59] Whereas the closed form (CF) of DPNP does not absorb in the visible (VIS) region of the electromagnetic spectrum and has only a small fluorescence quantum yield, the open form (OF) obtained by irradiation of the CF with ultraviolet (UV) light exhibits a new electronic absorption band at longer wavelengths because of the extended π-conjugation in the planar ring-opened molecules. The dynamics of the complex ring-opening[56,60–63] and the slower reverse ring-closure[57,58] have been elucidated in several laboratories by detailed time-resolved spectro-kinetic absorption measurements down to the femtosecond time scale. The combination of PPBI and DPNP thus turns out as an excellent candidate for a donor–acceptor dyad with a favourable energetic match between the electronic states of both moieties that enhances the EET rate and efficiency.

In this work, the photophysical properties of the PPBI–DPNP dyad are investigated by static and time-resolved spectroscopies in combination with quantum chemical theoretical calculations. From the static absorption spectra and the computed electronic transitions, the dyad shows only weak electronic coupling between the two chromophores in their ground states. Information on the rate of the observed fast EET after photoexcitation of the PPBI chromophore in the dyad at $\lambda_{\text{pump}} = 310$ nm to a PPBI*–DPNP donor-excited state to the subsequent PPBI–DPNP* acceptor-excited state was obtained by a singular value decomposition-based global analysis of the measured transient electronic absorption (TEA) spectra and by measurement of the accompanying transient absorption anisotropy decay. Corresponding measurements on the individual constituents were taken for reference. The experimental results are compared with theoretical calculations using the Förster model which indicate the predominance of a FRET mechanism.

6.2 Experimental section

6.2.1 Sample preparation

The synthesis and chemical characterisation of the PPBI–DPNP dyad (full chemical name: 3,3-diphenyl-[3*H*]-naphtho[2,1-b]pyran-8-carboxylic acid 2-[2-(2-pyridyl)-1H-benzoimidazole-1-yl]ethyl ester) and the free constituents PPBI (1-propyl-2-(2’-pyridyl)-benzimidazole) and DPNP (3,3-diphenyl-[3*H*]naphtho[2,1-b]pyran-8-carboxylic acid) as reference compounds have been described in some detail before.[64,65] The experimental procedures are detailed in the ESI. The concentrations of the sample solutions used in the time-resolved experiments and their respective optical densities at the excitation wavelength of λ_{pump} = 310 nm were c_0 = 0.12 mM (OD = 0.31) for the dyad, c_0 = 0.15 mM each (OD = 0.39) for an equimolar mixture of PPBI and DPNP, c_0 = 0.16 mM (OD = 0.38) for free PPBI, and c_0 = 0.30 mM (OD = 0.11) for free DPNP. The reservoirs containing the PPBI–DPNP and DPNP solutions were constantly irradiated during the transient absorption measurements using a light-emitting diode (LED) at λ = 500 nm to avoid product accumulation by converting the OF isomers generated by the 310 nm pump pulses back to their CF state.

6.2.2 Static spectroscopy

The static UV absorption spectra of the dyad and its constituents were measured on a Shimadzu UV-2410 desktop spectrometer. Static fluorescence spectra were recorded on a Jobin-Yvon FluoroMax-4 spectrophotometer using sample solutions with an optical density of $\sim$0.05 at the excitation wavelength (λ = 310 nm). The fluorescence quantum yields (Φ) were determined using 2-aminopyridine (Sigma-Aldrich, Φ = 0.66) as standard for PPBI and phenanthrene (Sigma-Aldrich, Φ = 0.125) as standard for the dyad.[66–69]

6.2.3 Time-resolved spectroscopy

The femtosecond transient electronic absorption (TEA) spectrometer in our laboratory has been described in several previous publications.[70–72] All measurements were carried out at room temperature under flow-through conditions in dry acetonitrile (ACN; Sigma-Aldrich) as solvent. The required pump pulses at λ_{pump} = 310 nm were generated by frequency-doubling the output of a home-built non-collinear optical parametric amplifier (NOPA) operated at 620 nm. Probe pulses were obtained by supercontinuum generation (SCG) in CaF_2 using the 775 nm Ti:Sa fundamental. The pump–probe time delay was set using a computer-controlled delay stage (Physik Instrumente). The obtained broadband pulses (320 nm $\leq \lambda_{\text{probe}} \leq$ 750 nm) were split into probe and reference by a glass plate and focused into the sample cell with the probe spatially overlapped with the pump. After the sample cell, the probe and reference pulses were dispersed in a prism spectrograph and detected by two matched fast frame transfer CCD cameras (S7030-0906, Hamamatsu) connected to a desktop PC. For overall transient absorption experiments, the polarization of the pump was set to the magic angle (54.7 °) with respect to the polarization of the probe. Additional transient absorption anisotropy measurements were carried out with parallel ($\|$) and perpendicular ($\perp$) pump–probe polarization configurations by rotating the polarization of the pump using a Berek compensator.

The fluorescence lifetime of PPBI was determined by time-correlated single-photon counting (TCSPC) measurements using a PicoQuant FluoTime 200 spectrometer.

6.2.4 Computational methods

Quantum chemical calculations were performed using the Turbomole 7.0 program.[73,74] The ground-state minimum energy structure of the dyad was optimized using second-order Møller-Plesset perturbation theory (MP2)[75] under the resolution of the identity (RI) approximation with the spin-component scaling (SCS) modification (RI-SCS-MP2)[76–81] and the def2-SVP[82] basis set using the X-ray structure of the dyad[64] as starting point. Subsequent excited-state energy and structure calculations were undertaken using the second-order algebraic diagrammatic construction method ADC(2) in the same variant (RI-SCS-ADC(2)).[83–87] The ADC(2) method has previously been found to reliably describe excited-state inter-chromophore interactions, including charge transfer[88] and excitonic interactions,[89] at moderate computational costs without suffering from some of the shortcomings found with density functional theory methods. The calculated UV absorption spectrum was broadened with Gaussians with full widths at half maximum of 0.23 eV and frequency-scaled with a factor of 0.89 to obtain best agreement with the experimental spectrum. Transition dipole vectors employed for the determination of the theoretical Förster orientation factor were obtained within the dipole-length formalism. The electronic transitions were further visualised by considering the primary natural transition orbital (NTO) electron and hole pairs[90] along with their percentage contributions to the overall transitions. Shown below are only NTO pairs with >10 % contribution.

6.3 Results

6.3.1 Static spectra

The UV absorption spectra of the PPBI–DPNP dyad, its individual components PPBI and DPNP, and an equimolar mixture of PPBI and DPNP in ACN solution are displayed in Fig. 6.2. As shown, the spectrum of the dyad is virtually identical to the sum of the spectra of its constituents, indicating only weak electronic coupling between the units in the ground state. Importantly, DPNP shows minimal absorption at λ = 310 nm, where PPBI has its first absorption maximum. Thus, the absorption of the dyad at λ_{pump} = 310 nm is predominated ($\sim$ 88 %) by the PPBI component, allowing for a selective excitation of the PPBI chromophore in the dyad at this wavelength.

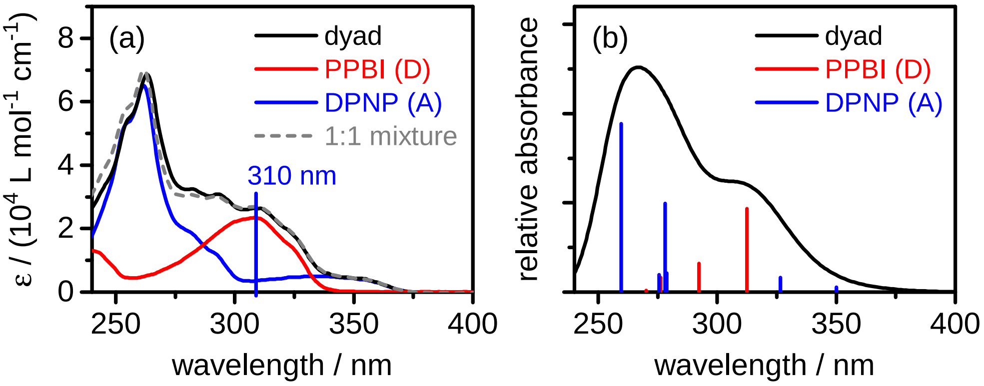

Fig. 6.2 Static UV absorption spectra of the PPBI–DPNP dyad (black) and the reference compounds PPBI (red) and DPNP (blue) in ACN. (a) Measured absorption spectra. The dashed grey line shows the spectrum of an equimolar mixture of the PPBI and DPNP. (b) Calculated absorption spectrum for the dyad at the RI-SCS-ADC(2) level of theory after applying a frequency-scaling factor of 0.89 to obtain best agreement with the experimental spectrum. The coloured vertical lines represent the electronic transitions localized on the PPBI donor (red) and the DPNP acceptor (blue) moieties. The Gaussian-broadened overall absorption spectrum of the dyad is shown in black.

The observed fluorescence spectra after excitation at λ_{exc} = 310 nm are given in Fig. 6.10 (ESI). The emisson of PPBI has a pronounced maximum at λ_{FL} = 365 nm. The emission of DPNP obtained under the same conditions is $\sim$200 times weaker. The emission spectrum of the dyad shows no significant difference in shape from its constituents. However, the fluorescence quantum yield (see ESI) is much lower (Φ_{DA}= 0.005) compared to that of PPBI alone (Φ_{D} = 0.36), i.e. the fluorescence from the PPBI donor unit is strongly quenched after linking to the DPNP acceptor. The main parameters characterising the static absorption and fluorescence spectra of the molecules are summarized in Table 6.1.

Table 6.1 Spectral properties of the PPBI–DPNP dyad and its individual constituents PPBI and DPNP: wavelenghts of peak absorption (λ_{max}) and fluorescence (λ_{FL}), molar decadic absorption coefficients ($\varepsilon_{\mathrm{max}}$) at λ_{max} and fluorescence quantum yields (Φ_{FL}).

	λ_{max}/nm	λ_{FL}/nm	$\varepsilon_{\mathrm{max}}$/M^{-1} cm^{-1}	Φ_{FL}
PPBI–DPNP	262, 350	363	26 400	0.005
PPBI	310	371	23 300	0.360
DPNP	262, 350	365	4 640	—

6.3.2 Ultrafast transient absorption measurements

The measured two-dimensional spectro-temporal transient absorption maps for the PPBI–DPNP dyad, the individual constituents PPBI and DPNP, and an equimolar mixture of the two in ACN showing the change in optical density ΔOD after excitation at λ_{pump} = 310 nm as function of probe wavelength and pump–probe delay time are displayed in Fig. 6.3. The pump wavelength was chosen in order to minimize the contribution arising from direct excitation of the DPNP moiety in the dyad measurement. The data were recorded up to Δt = 1.6 ns, but, since any further changes other than slow decays are negligible, are displayed here only from Δt = –1 to 200 ps, using a linear time scale up to 3 ps and a logarithmic time scale from 3 to 200 ps. The probe spectrum covered the range from 350 to 700 nm. Since all transient absorption data were taken with the same experimental setup under otherwise identical experimental conditions, but with different sample concentrations, the maps for the reference compounds and their equimolar mixture in Fig. 6.3 were normalized to the same concentration as the dyad using scaling factors (0.75 for PPBI, 0.40 for DPNP, and 0.80 for the equimolar mixture) to reflect the ΔOD values between the dyad and its building blocks under the same conditions. The unscaled raw data for the experimental sample concentrations are given in Fig. 6.12 (ESI).

At early pump–probe delay times, the TEA map of the PPBI–DPNP dyad in Fig. 6.3(a) features a prominent excited-state absorption (ESA) band centered at λ_{probe} = 420 nm and a weak one around λ_{probe} = 650 nm. Slightly later, however, this first ESA band decays within $\Delta t \sim 3 - 10$ ps and a second intense ESA band grows in around λ_{probe} = 440 nm. For comparison, Figs. 6.3(b) – (d) demonstrate unambiguously that the excited-state properties of the 1:1 mixture of PPBI and DPNP and the separate reference compounds PPBI and DPNP differ profoundly from that of the dyad. The TEA map for PPBI in Fig. 6.3(c) shows an intense ESA band at λ_{probe} = 420 nm and a weaker one at λ_{probe} = 650 nm, which change only little in shape and amplitude within the displayed 200 ps time window. The map for the free DPNP sample in Fig. 6.3(d) exhibits two very short-lived ESA signals around λ_{probe} = 380 and 520 nm (cf. Fig. 6.4(d)), which both disappear within $\Delta t \leq 1$ ps to be replaced by a new ESA band around λ_{probe} = 440 nm that lasts until the end of the time frame. Further, the spectro-temporal features of the equimolar mixture of PPBI and DPNP in Fig. 6.3(b) look almost the same as those for PPBI alone, reflecting the predominant photoexcitation of the PPBI molecules, the practically negligible excitation of the DPNP molecules, and the virtual absence of EET from the excited PPBI molecules to the DPNP molecules in the mixture.

By comparison with the spectro-temporal maps of its monomeric chromophores, the two early ESA bands of the PPBI–DPNP dyad at λ_{probe} = 420 and 650 nm seen immediately after excitation are safely assigned to the PPBI*–DPNP donor-excited state of the dyad that

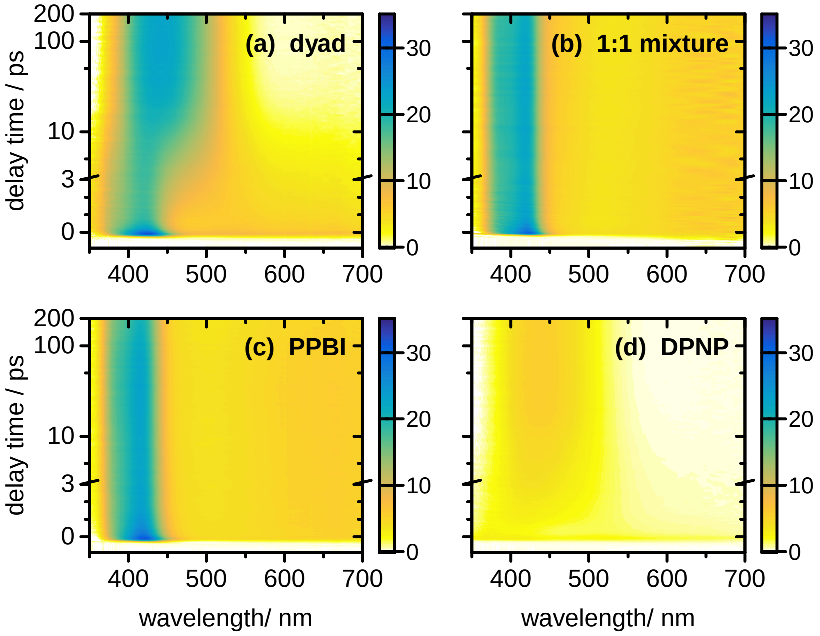

Fig. 6.3 Two-dimensional spectro-temporal transient absorption maps showing the change in optical density ΔOD for (a) the PPBI–DPNP dyad, (b) an equimolar mixture of PPBI and DPNP, (c) PPBI and (d) DPNP in ACN after photoexcitation at λ_{pump} = 310 nm for probe wavelengths between 350 and 700 nm and pump–probe delay times from –1 to 200 ps. The results are displayed using a linear time scale from –1 to 3 ps and a logarithmic time scale from 3 to 200 ps. The data for the reference compounds in panels (b) – (d) were normalized to the same effective sample concentration as for the dyad using scaling factors of 0.80 (1:1 mixture), 0.75 (PPBI) and 0.40 (DPNP).

is prepared by the absorption of a 310 nm pump photon. In contrast to the case for the free PPBI sample, however, both these ESA bands are short-lived in the dyad case and disappear within $<$ 10 ps. The delayed ESA band centered around λ_{probe} = 440 nm that grows in within the same time, on the other hand, has to originate from the excited population of the DPNP moiety in the dyad, since it matches with the corresponding ESA seen in the free DPNP measurement. However, the DPNP ESA contribution in the dyad features a four-fold higher intensity than in the DPNP sample at similar molar concentrations, indicating that the DPNP ESA band seen in the dyad case does not result from direct photoexcitation, but from efficient EET from the PPBI*–DPNP donor-excited state to a PPBI–DPNP* acceptor-excited state of the dyad. As shown by Fig. 6.3(b), this EET does not occur in the equimolar mixture of PPBI and DPNP. The much stronger transient absorption seen in the dyad case (Fig. 6.3(a)) than

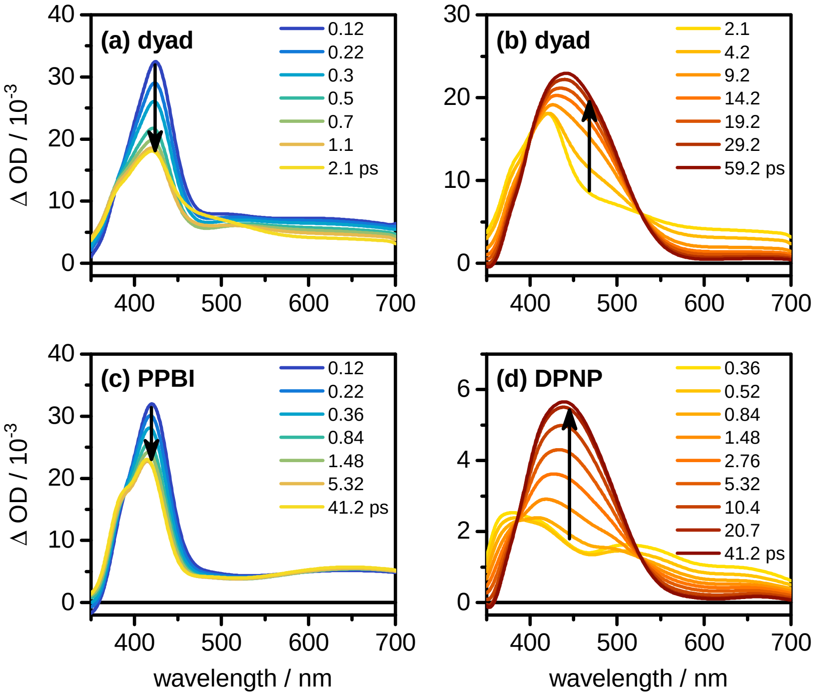

Fig. 6.4 Transient absorption spectra of (a, b) the PPBI-DPNP dyad, (c) PPBI and (d) DPNP at selected pump–probe delay times between $\Delta t \sim 0.1$ to 50 ps after excitation. The temporal evolution of the spectra goes from blue to yellow in the left panels and from yellow to red in the right panels. The data for PPBI and DPNP were normalized to the same effective sample concentrations as in Fig. 6.3.

in the free DPNP case (Fig. 6.3(d)) is a direct consequence of the higher molar absorption coefficient of PPBI compared to DPNP at the 310 nm excitation wavelength (cf. Fig. 6.2(a)).

The transient absorption spectra of the dyad and the reference compounds at selected pump–probe delay times in Fig. 6.4 reveal the spectro-temporal evolution in further detail. As can be seen, the shape of the ESA bands of the dyad around λ_{probe} = 420 nm and 650 nm at early times ($\Delta t < 2$ ps) after excitation given in Fig. 6.4(a) are very similar to those of the free PPBI chromophore in Fig. 6.4(c). At longer delay times ($\Delta t > 2$ ps; Fig. 6.4(b)), on the other hand, the dyad spectra evolve towards very similar late-time spectra as measured for free DPNP in Fig. 6.4(d). This dramatic qualitative and quantitative change in the transient spectra (see also Fig. 6.3(a)) again clearly indicates that the DPNP excited state in the PPBI–DPNP dyad is populated indirectly by intramolecular EET from the initial PPBI*–DPNP donor-excited state to a PPBI–DPNP* acceptor-excited state. The subsequent slower spectral evolution in the dyad seen up to Δt = 60 ps in Fig. 6.4(b) can be explained by subsequent

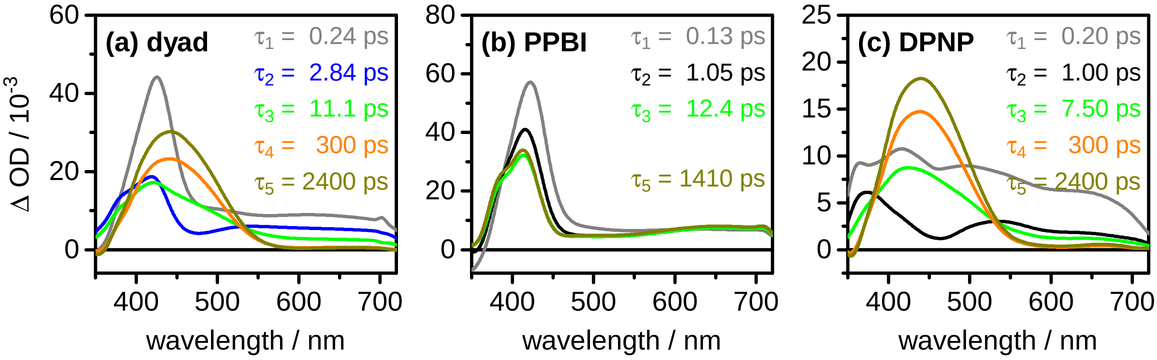

Fig. 6.5 Evolution-associated difference spectra (EADS) for (a) the PPBI-DPNP dyad, (b) PPBI and (c) DPNP belonging to the time constants $\tau_1 - \tau_5$ obtained from the SVD-based global multi-exponential analysis.

processes involving the excited DPNP* moiety (cf. Fig. 6.4(d)) after the EET, including in particular the known ring-opening reaction of DPNP.[60,62,63]

The dynamics of the dyad and its constituents were quantitatively evaluated by SVD-based global analyses assuming sequential kinetic models of the form

$$\mathrm{A} \xrightarrow{\tau_1} \mathrm{B} \xrightarrow{\tau_2} \mathrm{C} \xrightarrow{\tau_3} \mathrm{D} \xrightarrow{\tau_4} \mathrm{E} \xrightarrow{\tau_5} \mathrm{F}, \qquad (6.3.2.1)$$

where A is the initially photoexcited state with lifetime τ_1 in the Franck-Condon (FC) window, B a relaxed excited state with lifetime τ_2 that is reached by the ultrafast motion of the initially excited wavepacket away from the FC region, C – E stand for subsequent intermediate states with lifetimes $\tau_3 - \tau_5$, and F represents, eventually, the final state(s) reached by internal conversion (IC) and/or the respective photoreactions. The obtained distinct sets of time constants derived by non-linear least-squares fitting to the SVD time profiles (Fig. 6.13, ESI) are listed in Table 6.2, the respective evolution-associated difference spectra (EADS) are given in Fig. 6.5. To assist with the interpretation of the data, Fig. 6.14 (ESI) also gives the experimental and fitted time traces belonging to the main ESA bands of the dyad and the reference compounds.

The transient data for the dyad required five independent components for satisfactory fitting. Comparing the respective EADS and associated time constants, the first spectral component (EADS1; see figure legend for colour codings) belonging to the dyad clearly corresponds to the optically excited state of the PPBI chromophore. As can be seen, this state shows an ultrafast relaxation to EADS2 with τ_1 = 0.24 ± 0.01 ps in the dyad compared to τ_1 = 0.13 ± 0.02 ps in free PPBI. However, the second component of the dyad (EADS2), associated with τ_2 = 2.84 ± 0.70 ps, differs in spectral shape from all EADS components for

PPBI and, considering especially the 350 – 450 nm region, from the EADS components for DPNP as well. Further, the EADS belonging to the dyad at later times (EADS3, τ_3 = 11.1 ± 1.1 ps; EADS4, τ_4 = 300 ± 120 ps; EADS5, τ_5 = 2.4 ± 0.1 ns) all have clearly corresponding EADS with free DPNP. In particular, EADS3 of the dyad is the first that shows substantial absorption in the spectral range from λ_{probe} = 400 to 500 nm, as observed for DPNP. These observations strongly suggest that τ_2 = 2.84 ps, which describes the transition from EADS2 to EADS3, should be assigned to the EET process in the dyad from the PPBI*–DPNP donor-excited state to a PPBI–DPNP* acceptor-excited state.

The SVD analysis of the transient absorption data for PPBI taken for comparison required only four independent spectral components, as the 300 ps component (τ_4) was missing. Accordingly, the slowest decay component of τ_5 = 1.41 ± 0.02 ns is unambiguously identified as the excited-state lifetime of the molecule, when compared with the measured (TCSPC) fluorescence lifetime of τ_{FL} = 1.38 ± 0.02 ns (cf. Fig. 6.11, ESI). The much shorter components of τ_1 = 0.13 ± 0.02 ps, τ_2 = 1.05 ± 0.01 ps and τ_3 = 12.4 ± 2.6 ps therefore belong to fast processes in the excited state, including wavepacket motion from the initial FC state to the S_1 state potential energy minimum, vibrational relaxation, and/or solvent reorganization processes in the S_1 state. The ensuing vibrational cooling is reflected by a slight blue-shift of the ESA (Fig. 6.5). These processes are not at the center of attention in the present paper, however. Moreover, the ESA band fits in Fig. 6.14 indicate that the contribution of τ_3 is almost negligible.

Likewise, the analysis of the transient absorption data for DPNP again required five independent components for adequate fitting. Here, however, the observed behaviour is in excellent accordance with previous measurements in the literature.[60–63] Accordingly, time constants τ_2 = 1.00 ± 0.3 ps and τ_3 = 7.5 ± 0.9 ps are associated with the ring opening dynamics of the naphtopyran CF to the merocyanine OF product, followed by slower (τ_4 = 300 ± 120 ps and τ_5 = 2.4 ± 0.1 ns) relaxation and interconversion processes of the *trans-cis* and *trans-trans* isomers (OF_{TC} and OF_{TT}, respectively). Most importantly, these processes

Table 6.2 Globally fitted time constants describing the transient electronic absorption maps for the PPBI–DPNP dyad and the reference compounds PPBI and DPNP after excitation at λ_{pump} = 310 nm with 2σ error limits given as error of the last significant digit in parentheses.

sample	τ_1/ps	τ_2/ps	τ_3/ps	τ_4/ps	τ_5/ps
PPBI–DPNP	0.24(1)	2.84(70)	11.1(11)	300(120)	2400(100)
PPBI	0.13(2)	1.05(01)	12.4(26)	—	1410(020)
DPNP	0.20(3)	1.00(22)	7.5(09)	300(120)	2400(100)

are also observed in the transient absorption data for the PPBI–DPNP dyad molecule after the selective excitation of the PPBI donor *and* the fast EET to the DPNP acceptor unit. The time constant parameters τ_4 and τ_5 for DPNP could in fact be fixed in the fitting of the SVD time profiles at the values obtained before for the dyad.

6.3.3 Anisotropy decay measurement

Time-resolved measurements of the transient absorption anisotropy decay,

$$r(t) = \frac{\mathrm{S}_{\|}(t) - \mathrm{S}_{\perp}(t)}{\mathrm{S}_{\|}(t) + 2\,\mathrm{S}_{\perp}(t)}, \tag{6.3.3.1}$$

where $\mathrm{S}_{\|}(t)$ and $\mathrm{S}_{\perp}(t)$ denote the respective transient absorption signals with parallel and perpendicular relative polarizations of the pump and probe, provided an additional test for the EET. For randomly oriented molecules with well-defined transition dipole moments, an initial anisotropy value at $t = 0$ after excitation of $r(0) = 0.40$ is expected. Deviations from this value arise, when two or more transitions with different dipole moment orientations contribute.[91–96] Intramolecular EET in the PPBI–DPNP dyad will therefore lead to a decay of $r(t)$ from the intial value, if the transition dipole moments of the initial donor-excited state and the final acceptor-excited state(s) exhibit different relative orientations.

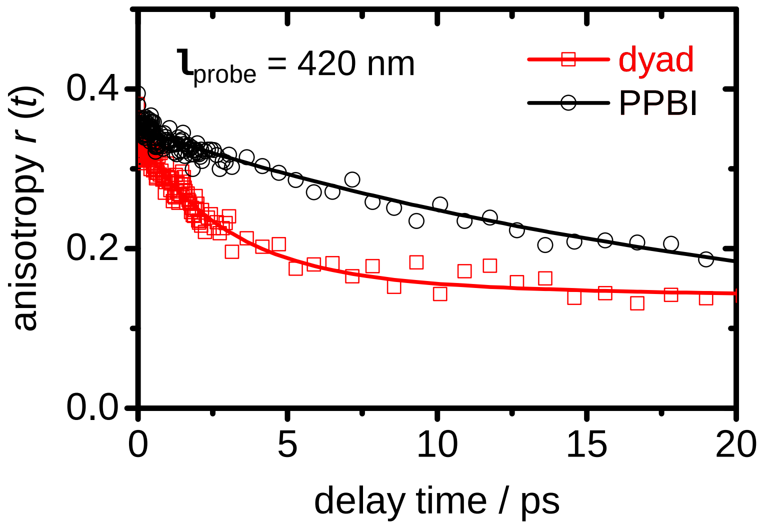

Fig. 6.6 Transient absorption anisotropy decay profiles observed at $\lambda_{\text{probe}} = 420$ nm for the PPBI–DPNP dyad (red squares) and free PPBI (black circles) with corresponding best fits (solid lines) after excitation at $\lambda_{\text{pump}} = 310$ nm. After ∼400 ps (not shown here for clarity), both curves reached asymptotic values of $r_{\infty} \sim 0.07$.

The experimental anisotropy decay curves for the dyad and for PPBI as reference compound are shown in Fig. 6.6. The data were evaluated at $\lambda_{\text{probe}} = 420$ nm, the peak absorption wavelength of PPBI (cf. Figs. 6.3 and 6.4). As can be seen, $r(t)$ for free PPBI shows an initial value near $r(0) \sim 0.4$ and decays with a time constant of $\tau_r = 22 \pm 1$ ps. In contrast, the $r(t)$ curve for the dyad requires two exponentials for adequate fitting. A fast initial decay takes place with $\tau_r' = 3.1 \pm 0.2$ ps, followed by a second slower decay with $\tau_r'' = 144 \pm 28$ ps.

The very rapid anisotropy decay for the dyad indicates a significant switching of the polarization of the observed transition dipole moments within $\tau_r' = 3.1$ ps. The observed temporal behaviour is fully consistent within experimental errors with the SVD result from the spectro-temporal absorption map above ($\tau_2 = 2.84$ ps). The slower τ_r'' value of 144 ps can be ascribed to subsequent rotational diffusion, which also explains the 22 ps τ_r for PPBI.

6.3.4 Computational results

The calculated gas-phase minimum energy structure of the PPBI–DPNP molecule in its electronic ground state is shown in Fig. 6.9 (ESI) along with the previously reported crystallographic structure[64] and with the computed cartesian nuclear coordinates in Table 6.5. A characteristic feature in the X-ray structure of the PPBI moiety is a small out-of-plane torsional angle of 7.8 ° between the benzimidazole and pyridine subunits, which is well reproduced in the calculated structure at 11.1 ° as determined by the dihedral angle $\angle(\text{N}^2\text{CCC})$ spanned by the imidazole-N^2 and the pyridine-CH. Visual inspection further reveals that the PPBI–DPNP torsional angle is somewhat closer to perpendicular in the optimized structure. This is accompanied by an overall decrease in the PPBI–DPNP center-of-mass distance from 9.66 to 8.76 Å. Small changes in the phenyl bond angles of the DPNP moiety became evident as well.

The computed vertical excitation energies (VEEs) and oscillator strengths based on the optimized ground-state structure are compiled in Table 6.3. Compared with the experimental UV spectrum of the dyad, the calculations are on the high side by ~ 0.4 eV, likely as a result of the limited basis set and the lack of a solvent correction. Importantly, however, a visual inspection of the corresponding NTO pairs shown in Fig. 6.7 suggests that all calculated transitions are localized essentially either on the acceptor or on the donor moiety, in good agreement with the finding that the experimental UV spectrum of the dyad molecule agrees well with that of a 1:1 mixture of PPBI and DPNP. Minor contributions from orbitals delocalized over both moieties seem to produce small spurious charge transfer (CT) contributions for all transitions, but a recent benchmark study found that the ADC(2) method tends to overestimate CT characters of excited states, when compared to higher-level methods.[97] For the present purpose, the small CT contributions may therefore be ignored.

A frequency-scaled calculated absorption spectrum is given in Fig. 6.2 next to the experimental spectrum. As shown, both are in excellent qualitative agreement, considering the sum of the spectra of the constituents and the dyad molecule as a whole. Most importantly, the computed spectrum reveals that excitation at λ_{pump} = 310 nm primarily populates the $\pi\pi^*$ (S_3) state localized on the PPBI chromophore. This conclusion is confirmed by the NTO pair for the $S_0 \rightarrow S_3$ transition in Fig. 6.7. The experimentally observed ultrafast structural relaxation on the time scale of τ_1 = 0.24 ps subsequently reduces the energy of the photoexcited state by ~0.3 eV compared to the FC region. The computed structure of the molecule in the resulting relaxed PPBI*–DPNP donor-excited state is given in Fig. 6.8 (see Table 6.6 for cartesian nuclear coordinates), together with the transition dipole vectors for the fluorescence from the PPBI*–DPNP donor-excited and the absorption to the PPBI–DPNP* acceptor-excited state. The structure of the relaxed donor-excited state closely resembles the ground-state minimum structure, as is exemplified by the nearly unchanged PPBI–DPNP center-of-mass distance of 8.72 Å. However, the torsional angle between the PPBI subunits is now reduced to nearly coplanar (0.8 °).

6.4 Discussion

The detailed time-resolved transient absorption data above provide clear evidence for the proposed fast electronic energy transfer process in the PPBI–DPNP dyad molecule. The measurements covered a range of pump–probe delay times up to $\Delta t \sim 2$ ns after excitation with an experimental time resolution of ~50 fs at probe wavelengths between λ = 350

Table 6.3 Calculated RI-SCS-ADC(2)/def-2-SVP vertical excitation energies (VEE) and oscillator strengths (f) of the PBBI–DPNP dyad molecule in its ground-state minimum energy structure. D and A indicate the excited molecular units.

state	VEE/eV	f	type	moiety
S_1	3.98	0.027	$\pi\pi^*$	A
S_2	4.27	0.082	$\pi\pi^*$	A
S_3	4.46	0.468	$\pi\pi^*$	D
S_4	4.77	0.160	$\pi\pi^*$	D
S_5	5.00	0.106	$\pi\pi^*$	A
S_6	5.01	0.496	$\pi\pi^*$	A
S_7	5.04	0.081	$\pi\pi^*$	D
S_8	5.06	0.097	$\pi\pi^*$	A
S_9	5.16	0.010	$n\pi^*$	D
S_{10}	5.36	0.943	$\pi\pi^*$	A

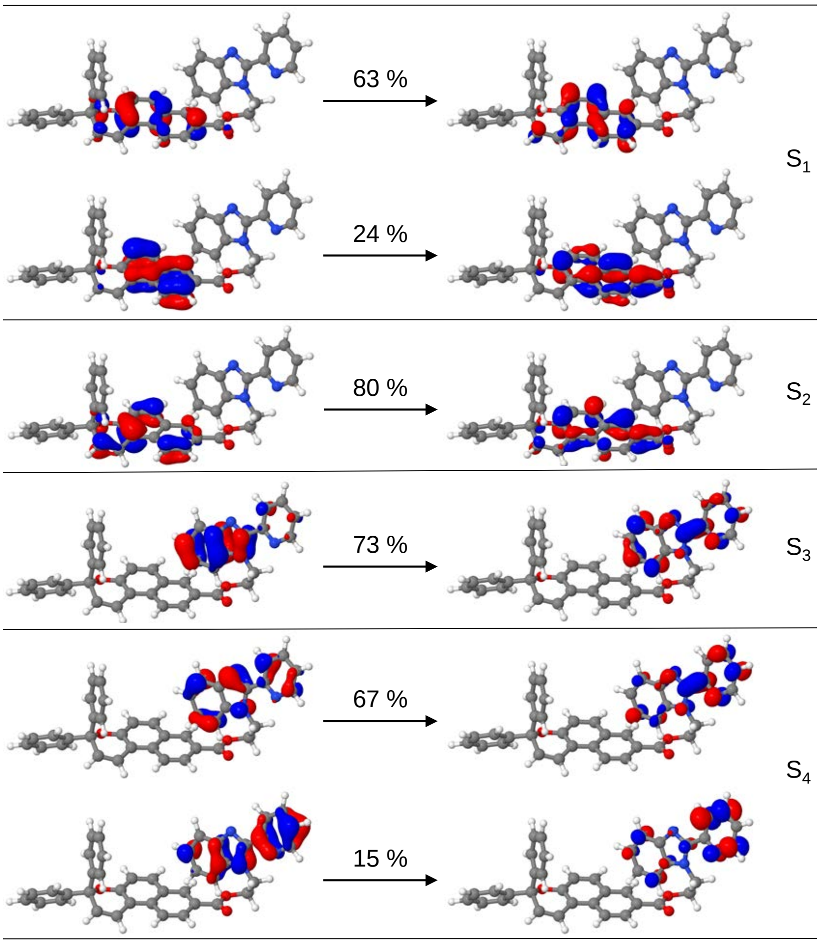

Fig. 6.7 Primary NTO pairs describing the first four $S_0 \rightarrow S_n$ electronic transitions of the dyad molecule from the ground state minimum energy structure. The percentage contributions of the individual NTO pairs to the individual transitions are given above the arrows.

and 700 nm. The results indicate that the EET from the selectively photoexcited PPBI chromophore as donor to the locally unexcited DPNP unit as acceptor takes place in the short time of only $\sim$ 2.8 – 3.1 ps (τ_2 and τ_r', respectively). For a more in-depth discussion, we shall first consider the results for the two reference compounds PPBI and DPNP, followed by the results for the dyad. Eventually, we shall compare the experimental EET time with a theoretical estimate based on the Förster resonance energy transfer (FRET) model.

6.4.1 Excited-state dynamics of free PPBI and DPNP

With its fluorescence lifetime of τ_{FL} = 1.38 ns and quantum yield of Φ_{FL} = 0.36, free PPBI in ACN solution turns out as a reasonably efficient "normal" organic fluorophore. The

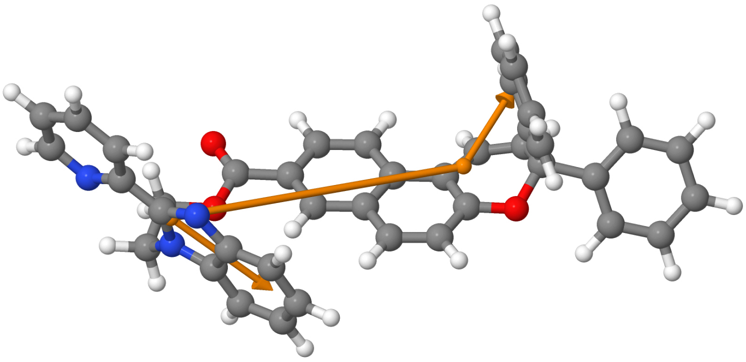

Fig. 6.8 Calculated minimum energy structure of the dyad molecule in the PPBI*–DPNP donor-excited state derived from the photoexcited S_3 state at the FC geometry. The orange line indicates the distance between the centers of mass of the PPBI and DPNP groups, the orange arrows show the calculated transition dipole moment vectors for the emission of the PBBI donor and the absorption of the DPNP acceptor units magnified by factors of 6.0 and 1.5, respectively, for better visibility. The dihedral angle between the donor emission and acceptor absorption transition dipole vectors is $\Theta_{DA} = 86\,°$, the angles between the transition dipole vectors and the line connecting the centers of mass are $\Theta_A = 44\,°$ and $\Theta_D = 43\,°$.

fluorescence decay time is in excellent agreement with the longest excited-state lifetime of $\tau_4 = 1.41$ ns inferred from the transient absorption experiment. The shorter time components $\tau_1 = 0.13$ ps, $\tau_2 = 1.05$ ps and $\tau_3 = 12.4$ ps belong to faster processes in the excited state, including wavepacket relaxation from the initial FC state (τ_1) and vibrational relaxation and/or solvent reorganization (τ_2, τ_3). These processes are not in our focus here.

For DPNP, an inspection of the UV spectrum (Fig. 6.2) shows that our pump pulses at $\lambda_{\mathrm{probe}} = 310$ nm deposit a fair amount of excess vibrational energy into the $\pi\pi^*$ excited state of the molecule. Hence, the shortest lifetime component ($\tau_1 = 0.20$ ps) is again assigned to ultrafast wavepacket motion away from the initial FC window. At reaction times of 1 ps and beyond, however, the photo-induced ring opening from the closed (CF) to the open (OF) form comes into play. This reaction has been investigated in some detail before.[56,60–63] The most direct comparison of our data is possible with the very similar transient absorption results of Herzog et al.,[62] who proposed a simplified reaction scheme in good agreement with theoretical studies. Accordingly, time constants $\tau_2 = 1.00$ ps and $\tau_3 = 7.5$ ps are associated with the ring opening of the naphtopyran CF to the merocyanine OF. The fast reaction is reflected by the sub-picosecond decay of the transient absorption bands at probe wavelengths below 380 and above 520 nm (cf. Fig. 6.4) and the following build-up of the characteristic product absorption band peaking at about 440 nm. The accompanying slower time constants

τ_4 = 300 ps and τ_5 = 2.4 ns can be related to slower relaxation and interconversion processes among the *trans-cis* and *trans-trans* OF isomers (OF_{TC} and OF_{TT}, respectively).[63] For further details, the reader is referred to the cited papers.

6.4.2 Electronic energy transfer dynamics in the PPBI–DPNP dyad molecule

The comparison of the measured spectro-temporal absorption map and transient spectra for the PPBI–DPNP dyad with the corresponding data for the free reference compounds in Section 6.3.2 showcases the EET process from the excited state of the PPBI donor to the DPNP acceptor unit of the dyad molecule. The main features for which the dyad stands out are (*i*) an initial photo-excited state that resembles the excited state of the reference compound PPBI, and (*ii*) a final state, whose spectral and temporal properties are similar to those of the reference compound DPNP (cf. Figs. 6.3 and 6.4). In particular, the observed and computed UV spectra (Fig. 6.2) show that the initial electronic excitation that is created in the dyad molecule in the FC window by the 310 nm pump is localized on the PPBI moiety. The prepared wavepacket subsequently moves to a relaxed region on the excited-state potential energy hypersurface (PEHS) in only $\sim$0.24 ps (τ_1), just slightly more slowly than in free PPBI itself. Thereafter, however, the SVD analysis revealed the occurence of the EET process in the dyad molecule by the EADS component with $\tau_2 = 2.84 \pm 0.70$ ps. This component has no analogue in the cases of free PPBI or DPNP. At the same time, the measured absorption anisotropy decay shows the switching from the donor to the acceptor transition dipole in the dyad molecule due to the EET in $\tau_r' = 3.1 \pm 0.2$ ps, in excellent agreement with the above SVD result. The subsequent slower depolarization with τ_r'' = 144 ps is explained as rotational diffusion. Averaging the two EET time constant values gave to a rate constant for the intramolecular electronic energy transfer from the PPBI donor to the DPNP acceptor chromophore of

$$k_{DA} = (3.4 \pm 0.9) \times 10^{11}\,\mathrm{s}^{-1}.$$

After the EET, the excitation is located on the DPNP unit of the dyad. The spectro-temporal absorption map and transient spectra thereafter consequently resemble the transient absorption map and spectra of free DPNP. This is highlighted, in particular, by the rise of the characteristic absorption around λ_{probe} = 450 nm (Fig. 6.4). The data thus show the ring opening and formation of the OF_{TC} and OF_{TT} isomers of the dyad molecule.[62,63] Interestingly, the time constant τ_3 = 11.1 ps that can be assigned to the ring opening in the dyad is slightly longer than in free DPNP (τ_3 = 7.5 ps). This delay is indeed expected, simply because the ring-opening in the dyad molecule requires the prior EET. Further, the same values for the longer time constants τ_4 = 300 ps and τ_5 = 2.4 ns could be used within experimental errors for modeling the dyad and the free DPNP data at late times.

Finally, the $\mathrm{OF_{TC}}$ and $\mathrm{OF_{TT}}$ merocyanine isomers are able of a reverse electrocyclic ring closure reaction to return to the naphtopyran CF. This may happen either thermally in the dark or photochemically under illumination by visible light. The ring closure involves two consecutive steps, namely $\mathrm{OF_{TT}} \xrightarrow{h\nu} \mathrm{OF_{TC}} \xrightarrow{h\nu/\Delta} \mathrm{CF}$. The predominating $\mathrm{OF_{TC}}$ isomer shows a faster reversion time (20 μs – 10 s) compared to the minor proportion of the $\mathrm{OF_{TT}}$ isomer, which is thermally stable.[54,56,57,61,98] The forward CF-to-OF transformation is accompanied by the rise of the merocyanine absorption band between $\sim$360 and 550 nm. Consequently, a larger spectral overlap between the PPBI emission and the DPNP-OF absorption bands and a possibly even more efficient quenching of the photoexcited state of the PPBI donor molecule by EET may be expected. This, unfortunately, hampers an application of the PPBI–DPNP dyad for bi-directional fluorescence on-off switching.

6.4.3 Förster resonance energy transfer

The very weak coupling between the PPBI and DPNP chromophores of the dyad molecule shown by the UV spectrum and the NTOs indicates the absence of direct electron exchange between the two sites and suggests that the observed EET is governed by the Förster resonance energy transfer mechanism via dipole-dipole coupling.

Using the model developed by Förster, the FRET rate constant k_{DA} can be calculated as[99–102]

$$k_{\mathrm{DA}} = \frac{9\ln(10)\,\kappa^2\,\Phi_{\mathrm{D}}\,J_{\mathrm{DA}}}{128\,\pi^5\,N_{\mathrm{A}}\,n^4\,\tau_{\mathrm{D}}\,{R_{\mathrm{DA}}}^6}\,, \tag{6.4.3.1}$$

where κ^2 is an orientation factor depending on the relative directions of the donor and acceptor transition dipole moments, Φ_{D} is the fluorescence quantum yield of the donor chromophore in the absence of the acceptor, J_{DA} is the spectral overlap integral between the donor emission and acceptor absorption bands, n is the refractive index of the medium, τ_{D} is the fluorescence lifetime of the donor, R_{DA} is the center-of-mass distance between the donor and acceptor units, and N_{A} is Avogadro's number.

Since all required quantities are known or can be determined, Eq. 6.4.3.1 allows us to predict the value of k_{DA} for comparison with the experimental result. The employed input parameters for the calculation are compiled in Table 6.4. However, some prior discussion appears in order:

First, assuming an uncorrelated, random mutual orientation of the donor and acceptor dipoles, the orientation factor attains a directionally and motionally averaged value of $\kappa^2 = 2/3$.[102–104] This value is used in most calculations for isotropic systems or when further

Table 6.4 Parameters for the calculation of the Förster EET rate coefficient of the PPBI–DPND dyad molecules.

τ_D/ps	Φ_D	R_{DA}/Å	J_{DA}/cm^6 mmol^{-1}	Θ_{DA}/°	Θ_D/°	Θ_A/°	κ^2
1.38	0.36	8.72	2.19×10^{-15}	86.00	42.85	44.16	2.28

information is missing. For our calculated excited state structure (cf. Fig. 6.8), however, we may also evaluate κ via[103–105]

$$\kappa = \hat{\mu}_A \cdot \hat{\mu}_D - 3\,(\hat{\mu}_A \cdot \hat{R}_{DA})(\hat{\mu}_D \cdot \hat{R}_{DA})\,, \tag{6.4.3.2}$$

where $\hat{\mu}_A$ and $\hat{\mu}_D$ are the unit vectors of the respective transition-dipole moments and $\hat{R}_{DA}$ is the unit vector along the line connecting the centers of mass. In terms of the dihedral angle Θ_{DA} between μ_A and μ_D and the angles Θ_D and Θ_A of the dipole moment vectors with the line through the centers of mass, Eq. 6.4.3.2 gives

$$\kappa^2 = (\cos\Theta_{DA} - 3\,\cos\Theta_D\,\cos\Theta_A)^2\,. \tag{6.4.3.3}$$

Taking our calculated excited-state structure of the dyad molecule (Fig. 6.8), we thus obtain a value of κ^2 = 2.28, almost 3.5 times larger than the isotropic average of 2/3. In reality, however, considering the flexible propyl linker between the PPBI donor and DPNP acceptor chromophores in our dyad molecule, we may assume the above values as limiting values, so that we have $2/3 \leq \kappa^2 \leq 2.28$.

Second, the center-of-mass distance of the chromophores (Förster distance) in the calculated structure is R_{DA} = 8.72 Å. The effective value of R_{DA} may be somewhat smaller, however, given the flexibility of the propyl linker. Third, the fluorescence lifetime of τ_D = 1.38 ps and the fluorescence quantum yield of Φ_D = 0.36 in the absence of the acceptor classify the free PPBI molecule as a moderately strong fluorophore. In contrast, the dyad of PPBI and DPNP is almost non-fluorescent (Φ_{DA} = 0.005), for practical purposes. Last, the determination of the spectral overlap integral (J_{DA} = 2.19×10^{-15} cm^6 mmol^{-1}) between the area-normalized donor emission ($\int_0^\infty f_D(\lambda)\,d\lambda$ = 1) and the molar extinction coefficient of the acceptor $\varepsilon_A(\lambda)$ according to[106,107]

$$J_{DA} = \int_0^\infty f_D(\lambda)\,\varepsilon_A(\lambda)\,\lambda^4\,d\lambda \tag{6.4.3.4}$$

has been illustrated in the ESI.

With these premises, the FRET rate constant for the PPBI–DPNP dyad molecule could be evaluated following Eq. 6.4.3.1 using both limiting values for κ^2. Taking, on the one hand, the isotropically averaged value of κ^2 = 2/3 as lower limit gave a rate constant of k_{DA} = 2.4 × 10^{11} s^{-1}, corresponding to a time constant of τ_{DA} = 4.2 ps, and only slightly smaller than the experimental k_{DA} = 3.4 × 10^{11} s^{-1} (τ = 2.9 ps). The prediction using the theoretically calculated upper limit of κ^2 = 2.28, on the other hand, provided a value of k_{DA} = 8.2 × 10^{11} s^{-1} (τ = 1.2 ps), about 2.4 times the experimental k_{DA} value. Considering the uncertainties of the orientation factor κ^2 as well as the effective Förster distance R_{DA}, both estimates are close to the experimental value for k_{DA}, and may indeed be concluded to be in good agreement. The accordance strongly supports FRET as the decisive intramolecular electronic energy transfer mechanism in the PPBI–DPNP dyad system. Moreover, it not only strengthens our weak-coupling assumption between the donor and acceptor chromophores, but also indicates that the applied point dipole approximation is still a helpful approximation for modeling EET in molecular systems, where the distance between the donor and acceptor chromophores is comparable with their own sizes, but their dipoles are near-orthogonal (86 °). Last but not least, the observed and calculated large FRET rate constants agree well with the high Förster resonance energy transfer efficiency of $E = 1 - \Phi_{\mathrm{DA}} / \Phi_{\mathrm{D}}$ = 98.6 % measured by the respective fluorescence quantum yields. The short Förster distance of R_{DA} = 8.7 Å appears to be a major factor determining this efficiency.

6.5 Conclusions

A model dyad for the investigation of fast intramolecular electronic energy transfer, consisting of 1-propyl-2-(2′-pyridyl)-benzimidazole (PPBI) as energy donor linked to 3,3-diphenyl-[3*H*]-naphtho[2,1-b]pyran (DPNP) as energy acceptor, has been studied in acetonitrile solution by means of static and time-resolved spectroscopies down to the femtosecond regime complemented by quantum chemical calculations. An inspection of the observed UV absorption spectra and the calculated excited electronic states confirm only very little electronic coupling between the two chromophores before excitation. After selective photoexcitation of the PPBI donor in the dyad molecule at λ_{pump} = 310 nm, however, a fast disappearance of the normally long-lived (τ = 1.4 ns for free PPBI) transient absorptions of the PPBI chromophore in the dyad was uncovered by the measured two-dimensional spectro-temporal transient electronic absorption map of the dyad that hints at a highly efficient energy transfer from the PPBI*-DPNP donor-excited state to the previously unexcited PPBI-DPNP* acceptor-excited state. A singular value decomposition-based global analysis of the data map allowed us to extract a time constant value for the EET process of τ = 2.84 ± 0.70 ps. The switching of the transition dipole moment determining the observed transient absorption signals after excitation due to the EET from the PPBI to the DPNP chromophore was confirmed by absorption anisotropy decay measurements, which gave a time constant of τ = 3.1 ± 0.2 ps, in excellent agreement with the global SVD result above. Averaging the two time constant values gave a rate constant for the intramolecular electronic energy transfer of $k_{\mathrm{DA}} = (3.4 \pm 0.9) \times 10^{11}$ s^{-1}. Last but not least, a quantitative prediction of this rate constant assuming the Förster dipole–dipole resonance energy transfer model provided estimates in the range 2.4×10^{11} $\mathrm{s}^{-1} \leq k_{\mathrm{DA}} \leq 8.2 \times 10^{11}$ s^{-1}, nicely enclosing the experimental result. The good agreement supports the validity of the FRET model for the observed ultrafast intramolecular electronic energy transfer in the PPBI–DPNP dyad molecule after selective excitation of the PPBI chromophore. The obtained quantitative mechanistic insight should be helpful for future developments of artificial light harvesting antenna systems with improved performance.

Conflicts of interest

The authors declare no conflicts of interest.

Acknowledgements

This work has been supported by the Deutsche Forschungsgemeinschaft through sub-project A1 of the Collaborative Research Centre (SFB) 677 “Function by Switching” (SW, FR, FT) and by a PhD grant (Grant no. 201306620029) by the China Scholarship Council (SW). The authors thank Lorenz Pietsch for the synthesis of the reference compound PPBI.

Bibliography

[1] T. Brixner, J. Stenger, H. M. Vaswani, M. Cho, R. E. Blankenship, G. R. Fleming, *Nature* **2005**, *434*, 625–628.

[2] G. D. Scholes, G. R. Fleming, A. Olaya-Castro, R. van Grondelle, *Nat. Chem.* **2011**, *3*, 763–774.

[3] D. A. Bryant, D. P. Canniffe, *J. Phys. B: At. Mol. Opt. Phys.* **2018**, *51*, 033001.

[4] G. S. Engel, T. R. Calhoun, E. L. Read, T.-K. Ahn, T. Mančal, Y.-C. Cheng, R. E. Blankenship, G. R. Fleming, *Nature* **2007**, *446*, 782–786.

[5] M. Sarovar, A. Ishizaki, G. R. Fleming, K. B. Whaley, *Nat. Phys.* **2010**, *6*, 462.

[6] D. Gust, T. A. Moore, A. L. Moore, *Acc. Chem. Res.* **2009**, *42*, 1890–1898.

[7] T. P. Chou, Q. Zhang, G. E. Fryxell, G. Z. Cao, *Adv. Mater.* **2007**, *19*, 2588–2592.

[8] S. Günes, H. Neugebauer, N. S. Sariciftci, *Chem. Rev.* **2007**, *107*, 1324–1338.

[9] H. Xin, F. S. Kim, S. A. Jenekhe, *J. Am. Chem. Soc.* **2008**, *130*, 5424–5425.

[10] G. J. Hedley, A. Ruseckas, I. D. W. Samuel, *Chem. Rev.* **2016**, *117*, 796–837.

[11] J. Otsuki, *J. Mater. Chem. A* **2018**, *6*, 6710–6753.

[12] C. S. Ponseca, P. Chábera, J. Uhlig, P. Persson, V. Sundström, *Chem. Rev.* **2017**, *117*, 10940–11024.

[13] S. Verma, H. N. Ghosh, *J. Phys. Chem. Lett.* **2012**, *3*, 1877–1884.

[14] K. Cnops, B. P. Rand, D. Cheyns, B. Verreet, M. A. Empl, P. Heremans, *Nat. Commun.* **2014**, *5*, 3406.

[15] G. Charalambidis, K. Karikis, E. Georgilis, B. L. M'Sabah, Y. Pellegrin, A. Planchat, B. Lucas, A. Mitraki, J. Bouclé, F. Odobel, A. G. Coutsolelos, *Sustainable Energy Fuels* **2017**, *1*, 387–395.

[16] M. R. Wasielewski, *Acc. Chem. Res.* **2009**, *42*, 1910–1921.

[17] D. Gust, T. A. Moore, A. L. Moore, *Acc. Chem. Res.* **2001**, *34*, 40–48.

[18] N. Banerji, S. V. Bhosale, I. Petkova, S. J. Langford, E. Vauthey, *Phys. Chem. Chem. Phys.* **2011**, *13*, 1019–1029.

[19] D. Villamaina, S. V. Bhosale, S. J. Langford, E. Vauthey, *Phys. Chem. Chem. Phys.* **2013**, *15*, 1177–1187.

[20] C. Azarias, L. Cupellini, A. Belhboub, B. Mennucci, D. Jacquemin, *Phys. Chem. Chem. Phys.* **2018**, *20*, 1993–2008.

[21] C. Wiebeler, F. Plasser, G. J. Hedley, A. Ruseckas, I. D. W. Samuel, S. Schumacher, *J. Phys. Chem. Lett.* **2017**, *8*, 1086–1092.

[22] K. J. Lee, J. H. Woo, E. Kim, Y. Xiao, X. Su, L. M. Mazur, A.-J. Attias, F. Fages, O. Cregut, A. Barsella, F. Mathevet, L. Mager, J. W. Wu, A. D'Aléo, J.-C. Ribierre, *Phys. Chem. Chem. Phys.* **2016**, *18*, 7875–7887.

[23] E. A. Ermilov, M. Schlak, R. Steffen, X.-Q. Liu, J.-Y. Liu, B. Röder, *RSC Adv.* **2015**, *5*, 67141–67148.

[24] M. Fakis, J. S. Beckwith, K. Seintis, E. Martinou, C. Nancoz, N. Karakostas, I. Petsalakis, G. Pistolis, E. Vauthey, *Phys. Chem. Chem. Phys.* **2018**, *20*, 837–849.

[25] B. Albinsson, J. Martensson, *Phys. Chem. Chem. Phys.* **2010**, *12*, 7338–7351.

[26] T. Förster, *Naturwissenschaften* **1946**, *33*, 166–175.

[27] T. Förster, *Annal. Phys.* **1948**, *2*, 55–75.

[28] T. Förster, *Discuss. Faraday Soc.* **1959**, *27*, 7–17.

[29] A. Lapini, P. Fabbrizzi, M. Piccardo, M. di Donato, L. Lascialfari, P. Foggi, S. Cicchi, M. Biczysko, I. Carnimeo, F. Santoro, C. Cappelli, R. Righini, *Phys. Chem. Chem. Phys.* **2014**, *16*, 10059–10074.

[30] J. E. A. Webb, K. Chen, S. K. K. Prasad, J. P. Wojciechowski, A. Falber, P. Thordarson, J. M. Hodgkiss, *Phys. Chem. Chem. Phys.* **2016**, *18*, 1712–1719.

[31] A. A. Hussain, A. R. Pal, *J. Mater. Chem. C* **2017**, *5*, 1136–1148.

[32] D. N. H. Meineke, M. L. Bossi, H. Ta, V. N. Belov, S. W. Hell, *Chem. Eur. J.* **2017**, *23*, 2469–2475.

[33] D. L. Dexter, *J. Chem. Phys.* **1953**, *21*, 836–850.

[34] M. Inokuti, F. Hirayama, *J. Chem. Phys.* **1965**, *43*, 1978–1989.

[35] S. Speiser, *Molecules* **1996**, *64*, 1481–1487.

[36] G. D. Scholes, *Annu. Rev. Phys. Chem.* **2003**, *54*, 57–87.

[37] H.-J. Xu, A. Bonnot, P.-L. Karsenti, A. Langlois, M. Abdelhameed, J.-M. Barbe, C. P. Gros, P. D. Harvey, *Dalton Trans.* **2014**, *43*, 8219–8229.

[38] B. P. Krueger, G. D. Scholes, G. R. Fleming, *J. Phys. Chem. B* **1998**, *102*, 5378–5386.

[39] W. Ortiz, B. P. Krueger, V. D. Kleiman, J. L. Krause, A. E. Roitberg, *J. Phys. Chem. B* **2005**, *109*, 11512–11519.

[40] S. Tretiak, C. Middleton, V. Chernyak, S. Mukamel, *J. Phys. Chem. B* **2000**, *104*, 9540–9553.

[41] F. J. Kleima, E. Hofmann, B. Gobets, I. H. Van Stokkum, R. Van Grondelle, K. Diederichs, H. Van Amerongen, *Biophys. J.* **2000**, *78*, 344–353.

[42] V. Sundstrom, T. Pullerits, R. van Grondelle, *J. Phys. Chem. B* **1999**, *103*, 2327–2346.

[43] A. Young, H. Frank, *J. Photochem. Photobiol. B Biol.* **1996**, *36*, 3–15.

[44] M. Carmen Ríos Rodríguez, F. Rodríguez-Prieto, M. Mosquera, *Phys. Chem. Chem. Phys.* **1999**, *1*, 253–260.

[45] D. Panda, *Chem. Phys. Lett.* **2006**, *422*, 446–450.

[46] T. K. Mukherjee, A. Datta, *J. Phys. Chem. B* **2006**, *110*, 2611–2617.

[47] T. N. Burai, T. K. Mukherjee, P. Lahiri, D. Panda, A. Datta, *J. Chem. Phys.* **2009**, *131*, 034504.

[48] V. Khorwal, U. Nudurupati, S. I. Mondal, A. Datta, *J. Phys. Chem. C* **2017**, *121*, 5379–5388.

[49] T. Ohno, K. Nozaki, M. Haga, *Inorg. Chem.* **1992**, *31*, 548–555.

[50] M. D. Hossain, M.-a. Haga, B. Gholamkhass, K. Nozaki, M. Tsushima, N. Ikeda, T. Ohno, *Collect. Czech. Chem. Commun.* **2001**, *66*, 307–337.

[51] Z. Assefa, T. Yaita, R. Haire, S. Tachimori, *J. Solid State Chem.* **2005**, *178*, 505–510.

[52] E. S. S. Iyer, D. Samanta, A. Dey, A. Kundu, A. Datta, *J. Phys. Chem. B* **2012**, *116*, 1586–1592.

[53] K. Mitra, S. Gautam, P. Kondaiah, A. R. Chakravarty, *ChemMedChem* **2016**, *11*, 1956–1967.

[54] G. Ottavi, G. Favaro, V. Malatesta, *J. Photochem. Photobiol. A* **1998**, *115*, 123–128.

[55] S. Jockusch, N. J. Turro, F. R. Blackburn, *J. Phys. Chem. A* **2002**, *106*, 9236–9241.

[56] J. Hobley, V. Malatesta, K. Hatanaka, S. Kajimoto, S. L. Williams, H. Fukumura, *Phys. Chem. Chem. Phys.* **2002**, *4*, 180–184.

[57] H. Görner, A. K. Chibisov, *J. Photochem. Photobiol. A* **2002**, *149*, 83–89.

[58] S. Delbaere, J.-C. Micheau, G. Vermeersch, *J. Org. Chem.* **2003**, *68*, 8968–8973.

[59] L. Bekere, V. Lokshin, M. Sigalov, R. Gvishi, P. Zhao, D. J. Hagan, E. W. V. Stryland, V. Khodorkovsky, *New J. Chem.* **2016**, *40*, 1143–1148.

[60] P. L. Gentili, E. Danilov, F. Ortica, M. a. J. Rodgers, G. Favaro, *Photochem. Photobiol. Sci.* **2004**, *3*, 886–891.

[61] B. Moine, J. Réhault, S. Aloïse, J.-C. Micheau, C. Moustrou, A. Samat, O. Poizat, G. Buntinx, *J. Phys. Chem. A* **2008**, *112*, 4719–4726.

[62] T. T. Herzog, G. Ryseck, E. Ploetz, T. Cordes, *Photochem. Photobiol. Sci.* **2013**, *12*, 1202.

[63] S. Brazevic, M. Sliwa, Y. Kobayashi, J. Abe, G. Burdzinski, *J. Phys. Chem. Lett.* **2017**, *8*, 909–914.

[64] S. Wang, Y. Si, C. Tong, G. Wang, B. Qi, G. Yang, *Opt. Mater.* **2013**, *35*, 1504–1512.

[65] Q. Cao, D. S. Bailie, R. Fu, M. J. Muldoon, *Green Chem.* **2015**, *17*, 2750–2757.

[66] W. R. Dawson, M. W. Windsor, *J. Phys. Chem.* **1968**, *72*, 3251–3260.

[67] R. Rusakowicz, A. C. Testa, *J. Phys. Chem.* **1968**, *72*, 2680–2681.

[68] G. A. Crosby, J. N. Demas, *J. Phys. Chem.* **1971**, *75*, 991–1024.

[69] A. M. Brouwer, *Pure Appl. Chem.* **2011**, *83*, 2213–2228.

[70] F. Renth, M. Foca, A. Petter, F. Temps, *Chem. Phys. Lett.* **2006**, *428*, 62–67.

[71] F. Renth, R. Siewertsen, F. Strübe, J. Mattay, F. Temps, *Phys. Chem. Chem. Phys.* **2014**, *16*, 19556.

[72] K. Röttger, S. Wang, F. Renth, J. Bahrenburg, F. Temps, *Appl. Phys. B* **2015**, *118*, 185–193.

[73] R. Ahlrichs, M. Bär, M. Häser, H. Horn, C. Kölmel, *Chem. Phys. Lett.* **1989**, *162*, 165–169.

[74] TURBOMOLE V7.0 2015, a development of University of Karlsruhe and Forschungszentrum Karlsruhe GmbH, 1989-2007, TURBOMOLE GmbH, since 2007; available from `http://www.turbomole.com`.

[75] C. Møller, M. S. Plesset, *Phys. Rev.* **1934**, *46*, 618–622.

[76] M. Häser, R. Ahlrichs, *J. Comput. Chem.* **1989**, *10*, 104–111.

[77] F. Weigend, M. Häser, *Theor. Chem. Acc.* **1997**, *97*, 331–340.

[78] F. Weigend, M. Häser, H. Patzelt, R. Ahlrichs, *Chem. Phys. Lett.* **1998**, *294*, 143–152.

[79] S. Grimme, *J. Chem. Phys.* **2003**, *118*, 9095–9102.

[80] C. Hättig, *J. Chem. Phys.* **2003**, *118*, 7751–7761.

[81] C. Hättig, A. Hellweg, A. Köhn, *Phys. Chem. Chem. Phys.* **2006**, *8*, 1159–1169.

[82] A. Schäfer, H. Horn, R. Ahlrichs, *J. Chem. Phys.* **1992**, *97*, 2571–2577.

[83] J. Schirmer, *Phys. Rev. A* **1982**, *26*, 2395–2416.

[84] C. Hättig, A. Köhn, *J. Chem. Phys.* **2002**, *117*, 6939–6951.

[85] H. Christof, *Adv. Quantum Chem.* **2005**, *50*, 37–60.

[86] A. B. Trofimov, J. Schirmer, *J. Phys. B: At. Mol. Opt. Phys.* **1995**, *28*, 2299.

[87] A. Hellweg, S. A. Grün, C. Hättig, *Phys. Chem. Chem. Phys.* **2008**, *10*, 4119–4127.

[88] A. A. J. Aquino, I. Borges, R. Nieman, A. Kohn, H. Lischka, *Phys. Chem. Chem. Phys.* **2014**, *16*, 20586–20597.

[89] A. N. Panda, F. Plasser, A. J. A. Aquino, I. Burghardt, H. Lischka, *J. Phys. Chem. A* **2013**, *117*, 2181–2189.

[90] R. L. Martin, *J. Chem. Phys.* **2003**, *118*, 4775–4777.

[91] D. M. Jonas, M. J. Lang, Y. Nagasawa, T. Joo, G. R. Fleming, *J. Phys. Chem* **1996**, *100*, 12660–12673.

[92] O. Varnavski, G. Menkir, T. Goodson III, P. Burn, *Appl. Phys. Lett.* **2000**, *77*, 1120–1122.

[93] T. G. Goodson III, *Acc. Chem. Res.* **2005**, *38*, 99–107.

[94] E. Collini, G. D. Scholes, *Science* **2009**, *323*, 369–373.

[95] B. Keller, A. McLean, B. G. Kim, K. Chung, J. Kim, T. Goodson, *J. Phys. Chem. C* **2016**, *120*, 9088–9096.

[96] I. Hwang, U. Selig, S. S. Chen, P. E. Shaw, T. Brixner, P. L. Burn, G. D. Scholes, *J. Phys. Chem. A* **2013**, *117*, 6270–6278.

[97] S. A. Mewes, F. Plasser, A. Krylov, A. Dreuw, *J. Chem. Theory Comput.* **2018**, *14*, 710–725.

[98] S. Delbaere, B. Luccioni-Houze, C. Bochu, Y. Teral, M. Campredon, G. Vermeersch, *J. Chem. Soc. Perkin Trans. 2* **1998**, *2*, 1153–1158.

[99] A. Olaya-Castro, G. D. Scholes, *Int. Rev. Phys. Chem.* **2011**, *30*, 49–77.

[100] *Principles of Fluorescence Spectroscopy*, (Ed.: J. R. Lakowicz), Springer, **2006**.

[101] T. Mirkovic, E. E. Ostroumov, J. M. Anna, R. van Grondelle, Govindjee, G. D. Scholes, *Chem. Rev.* **2016**, *117*, 249–293.

[102] S. E. Braslavsky, E. Fron, H. B. Rodríguez, E. S. Román, G. D. Scholes, G. Schweitzer, B. Valeur, J. Wirz, *Photochem. Photobiol. Sci.* **2008**, *7*, 1444–1448.

[103] R. Dale, J. Eisinger, W. Blumberg, *Biophys. J.* **1979**, *26*, 161–193.

[104] B. van der Meer, *Rev. Mol. Biotechnol.* **2002**, *82*, 181–196.

[105] D. Andrews, *Chem. Phys.* **1989**, *135*, 195–201.

[106] R. P. Haugland, J. Yguerabide, L. Stryer, *Proc. Natl. Acad. Sci. U.S.A* **1969**, *63*, 23–30.

[107] H. Du, R.-C. A. Fuh, J. Li, L. A. Corkan, J. S. Lindsey, *Photochem. Photobiol.* **1998**, *68*, 141–142.

6.6 Electronic supplementary information

6.6.1 Syntheses

The syntheses of the PPBI–DPNP dyad by Steglich esterification and the monomeric, free constituent DPNP were reported in previous work.[1] The reference compound PPBI was synthesized according to a literature procedure.[2]

PPBI−DPNP

A mixed solution of 1-(2-hydroxyethyl)-2-(2-pyridyl)benzimidazole (1.19 g, 5 mmol), 3,3-diphenyl-[3*H*]naphtho[2,1-b]pyran-8-carboxylic acid (1.89 g, 5 mmol) and 4-dimethylaminopyridine (DMAP, 0.07 g, 0.6 mmol) in a mixture of tetrahydrofuran (THF, 20 mL) and dichloromethane (DCM, CH_2Cl_2, 8.0 mL) was stirred in an ice-water bath for 1 h. N,N'-dicyclohexycarbodiimide (DCC, 1.23 g, 6.0 mmol) was added, and the reaction mixture was warmed up slowly to room temperature and stirred continuously for 36 h. The precipitate was filtered off and the solvent was evaporated. The residue was dissolved in CH_2Cl_2 and the solution was dried with anhydrous Mg_2SO_4. The white solid product was obtained by column chromatography on silica (1 : 2 EE/petroleum ether). 1.8 g, yield 90 %. ^{1}H NMR (500 MHz, DMSO−d_6): δ 8.71 − 8.69 (d, 1H, $J = 5.5$ Hz), 8.31 − 8.28 (d, 1H, $J = 8$ Hz), 8.06 − 8.03 (t, 2H), 7.91 − 7.88 (m, 1H), 7.85 − 7.83 (d, 1H, $J = 8$ Hz), 7.80 − 7.77 (d, 1H, $J = 9$ Hz), 7.75 − 7.72 (d, 1H, $J = 8$ Hz), 7.58 − 7.55 (m, 1H), 7.50 − 7.46 (m, 5H), 7.45 − 7.42 (m, 1H), 7.40 − 7.34 (m, 5H), 7.31 − 7.27 (m, 3H), 6.65 − 6.62 (d, 1H, $J = 10$ Hz), 5.57 − 5.55 (d, 1H, $J = 8$ Hz), 5.39 − 5.36 (t, 2H), 4.74 − 4.72 (t, 2H).

1-propyl-2-(2′-pyridyl)benzimidazole (PPBI)

A mixed solution of 2-(2-pyridyl)benzimidazole (1.11 g, 5.69 mmol) and K_2CO_3 (1.17 g, 8.47 mmol) in N,N-dimethylformamide (DMF, 12 mL) was stirred for 30 min. 1-Bromopropane (0.62 mL, 6.79 mmol) was added dropwise and the resultant mixture was then stirred for 5 h at 295 K. After the solvent was removed by evaporation, water (30 mL) was added and the organic product was extracted with ethyl acetate (EE, 30 mL). The organic layer was dried over $MgSO_4$. The purified product was obtained as a pale yellow oil by column chromatography on silica (1 : 1 DCM/ EE). 430 mg, yield 32 %. ^{1}H NMR (500 MHz, $CDCl_3$): δ 8.69 (m, 1H), 8.43 (dt, 1H, $J = 8$ Hz), 7.85 (m, 2H), 7.45 (m, 1H), 7.33 (m, 3H), 4.8 (m, 2H), 1.91 (m, 2H), 0.93 (t, 3H, $J = 7.4$ Hz).

1-(2-hydroxyethyl)-2-(2′-pyridyl)benzimidazole (HPBI)

A mixed solution of 2-(2-pyridyl)benzimidazole (4.48 g, 23 mmol) and sodium hydroxide (2 g, 50 mmol,) in DMF (50 mL) under nitrogen was stirred at 35 °C for 1 h. A solution of 2-bromoethyl alcohol (3.12 g, 25 mmol) in DMF (10 mL) was added dropwise, and then the reaction mixture was heated up to 120 °C for half an hour. The mixture was cooled to room temperature and poured carefully into ice-cold water (300 mL). The solution was neutralised to pH $6-7$ with HCl solution, the precipitate was collected by filtration and dissolved in $CHCl_3$ (200 mL). The filtrate was extracted with $CHCl_3$ (300 mL) and the combined $CHCl_3$ solutions were dried over Mg_2SO_4. The purified pale brown crystals were obtained by column chromatography on silica (2 : 1 EE/petroleum ether). 3.5 g, yield 69 %. ^{1}H NMR (500 MHz, $CDCl_3$): δ 8.70 (s, 1H), 8.56 (s, 1H), 7.96 (m, 2H), 7.52 (m 2H), 7.43 (m, 2H), $4.86-4.89$ (m 2H), 4.24 (t, 2H).

3,3-diphenyl-[3*H*]naphtho[2,1-b]pyran-8-carboxylic acid (DPNP)

A mixed solution of 6-hydroxynaphthalene-2-carboxylic acid (0.98 g, 5 mmol) and 1,1-diphenylprop-2-yn-1-ol (1.14 g, 5 mmol) in CH_2Cl_2 (70 mL) was stirred under nitrogen at 35 °C. A catalytic amount of *p*-toluenesulphonic acid (PTSA, 100 mg) was added and the reaction mixture was stirred for two days. The crude product was collected by filtering. The purified product was obtained by column chromatography on silica (8 : 2 DCM/ EE). White powder, 0.99 g, yield 50 %. ^{1}H NMR (500 MHz, DMSO$-d_6$): δ 8.49 (s, 1H), 8.18 (d, 1H, $J = 8.5$ Hz), 7.99 (d, 1H, $J = 9$ Hz), $7.96-7.94$ (m, 1H), $7.52-7.48$ (m, 5H), 7.40 (d, 1H, $J = 8.5$ Hz), $7.37-7.34$ (m, 4H), 7.26 (m, 2H), 6.64 (d, 1H, $J = 10$ Hz).

6.6.2 Ground- and excited-state structures of the PPBI–DPNP dyad molecule

Cartesian coordinates of the calculated ground- and excited-state structures

Table 6.5 Cartesian coordinates of the calculated RI-SCS-MP2/def2-SVP ground-state minimum structure of the dyad molecule.

atom	x / Å	y / Å	z / Å
C	7.1533346	7.4316864	6.1503460
C	8.0179067	6.3574474	5.8207896
C	9.2757282	6.2375979	6.4506778
H	9.9363790	5.4032251	6.2022824

C	9.6357537	7.2157188	7.3735813
H	10.6061604	7.1577038	7.8750409
C	8.7640747	8.2948491	7.6840675
H	9.0815508	9.0401936	8.4191931
C	7.5149307	8.4268412	7.0799571
H	6.8417817	9.2427962	7.3507574
C	6.2468118	6.0982408	4.6347702
C	5.3159731	5.5251352	3.6428527
C	5.7935341	4.5153018	2.7811600
H	6.8335779	4.1975485	2.8642880
C	4.9097844	3.9524864	1.8613286
H	5.2467469	3.1653637	1.1812265
C	3.5869766	4.4167369	1.8188284
H	2.8615299	4.0053650	1.1129946
C	3.2102726	5.4248691	2.7111984
H	2.1850746	5.8113805	2.7108529
C	4.8496475	8.1106902	5.4457627
H	4.3969359	8.2051791	4.4528709
H	5.1943252	9.1027008	5.7732198
C	3.8182520	7.5665099	6.4180522
H	2.9798745	8.2735357	6.5299410
H	3.4186596	6.6089502	6.0566438
C	3.7467302	6.8265579	8.6568504
C	4.5755819	6.4934706	9.8524687
C	5.9609741	6.4623992	9.7941911
H	6.4796328	6.7086578	8.8659328
C	6.7261197	6.1083418	10.9395189
C	6.0590817	5.7810917	12.1646750
C	4.6315507	5.8077731	12.1854832
H	4.0991564	5.5327105	13.0990129
C	3.9060837	6.1487421	11.0602432
H	2.8136546	6.1539180	11.0764556
C	6.8418006	5.4353136	13.3167259
C	8.2315951	5.3682165	13.1947043
C	8.8929837	5.7075002	11.9864653
H	9.9845063	5.6584041	11.9607985

C	8.1537094	6.0684561	10.8791548
H	8.6473698	6.3217856	9.9366435
C	8.4297013	4.1108376	15.1926291
C	7.0607746	4.6233217	15.5949059
H	6.7247227	4.4869975	16.6265798
C	6.2964286	5.2309863	14.6592967
H	5.3087095	5.6235521	14.9149280
C	8.3880287	2.7410607	14.5096661
C	9.5781038	2.2691023	13.9226501
H	10.4777087	2.8889940	13.9700271
C	9.6081296	1.0250908	13.2871346
H	10.5362470	0.6691880	12.8305192
C	8.4503061	0.2315842	13.2360762
H	8.4733996	-0.7425149	12.7395174
C	7.2672523	0.6943386	13.8216967
H	6.3606777	0.0835808	13.7820833
C	7.2334293	1.9482903	14.4531015
H	6.3016263	2.3085547	14.8954737
C	9.3461846	4.0789885	16.4098165
C	9.2616991	3.0013427	17.3097867
H	8.5889454	2.1661245	17.0948068
C	10.0492854	2.9822902	18.4670139
H	9.9789543	2.1362698	19.1567399
C	10.9300640	4.0392408	18.7371156
H	11.5502335	4.0218699	19.6376686
C	11.0146567	5.1139928	17.8430475
H	11.7000464	5.9419059	18.0467053
C	10.2203342	5.1418778	16.6880035
H	10.2815811	5.9816149	15.9942975
N	7.4281036	5.5476236	4.8795872
N	6.0286236	7.2563467	5.3667368
N	4.0465103	5.9700559	3.6081532
O	4.4857183	7.3811297	7.6683260
O	2.5554158	6.6305025	8.5615051
O	9.0187899	5.0475667	14.2623963

Table 6.6 Cartesian coordinates of the calculated RI-SCS-ADC(2)/def2-SVP excited-state minimum energy structure of the dyad molecule.

atom	x / Å	y / Å	z / Å
C	4.9685464	8.1891381	5.6149527
H	5.1322202	9.1146941	5.0475089
H	4.8871444	8.4184557	6.6914206
C	3.7015967	7.5099511	5.1190214
H	2.8163733	8.1408491	5.3226306
H	3.7610763	7.3299800	4.0328633
C	2.5606959	5.4737674	5.4893700
C	2.6262102	4.1436340	6.1646607
C	3.7451980	3.7359618	6.8760204
H	4.6102402	4.4009585	6.9736635
C	3.7875159	2.4533966	7.4892637
C	2.6646882	1.5711028	7.3672865
C	1.5330850	2.0177378	6.6188721
H	0.6723232	1.3532096	6.4842200
C	1.5128040	3.2674366	6.0275827
H	0.6474846	3.6006064	5.4432173
C	2.7150305	0.2832180	7.9989587
C	3.8857633	-0.1021980	8.6571816
C	4.9920676	0.7756697	8.7911728
H	5.8729759	0.4229385	9.3402890
C	4.9441481	2.0287118	8.2142148
H	5.7970325	2.7156762	8.2965832
C	3.2558893	-2.3869568	8.6225756
C	1.8231890	-1.9387847	8.4115994
H	1.0124334	-2.6682923	8.5329416
C	1.5885053	-0.6485197	8.0772475
H	0.5627410	-0.2872236	7.9350949
C	3.9890363	-2.7204368	7.3204898
C	5.3700634	-2.9881574	7.4024907
H	5.8662946	-2.9513508	8.3802854
C	6.1004005	-3.2969964	6.2512284
H	7.1763043	-3.5010703	6.3251220

C	5.4585568	-3.3500499	5.0020145
H	6.0309286	-3.5936247	4.0980455
C	4.0862372	-3.0891840	4.9169022
H	3.5792997	-3.1242777	3.9441232
C	3.3526640	-2.7692951	6.0720582
H	2.2813650	-2.5530183	5.9915857
C	3.2871569	-3.5706977	9.5822038
C	3.0213323	-4.8633550	9.0941414
H	2.8614008	-5.0202835	8.0199062
C	2.9795211	-5.9557196	9.9700911
H	2.7766515	-6.9601857	9.5771649
C	3.2047429	-5.7685149	11.3420199
H	3.1785675	-6.6248785	12.0275762
C	3.4682036	-4.4815077	11.8299543
H	3.6457984	-4.3268345	12.9020014
C	3.5010555	-3.3833914	10.9576287
H	3.7009793	-2.3780088	11.3409534
O	3.6041216	6.2677847	5.8264320
O	1.6861707	5.8203166	4.7273201
O	3.9825778	-1.3164204	9.2710790
N	6.1257367	7.3160890	5.4455643
C	6.5918805	6.4925485	6.4019301
C	6.8539604	6.9993617	4.2083250
C	7.6404863	5.6963038	5.7510625
C	6.2591308	6.3435499	7.7744138
N	7.7590529	6.0293595	4.4438634
C	6.6537532	7.6410737	2.9583171
C	8.3398935	4.7324881	6.4999494
C	6.9790654	5.3771425	8.4936634
H	5.4568261	6.9213298	8.2434880
N	5.6996473	8.6259324	2.8405724
C	7.4576409	7.2271229	1.8417291
C	7.9999127	4.5958622	7.8676527
H	9.1196923	4.1232264	6.0311139
H	6.7627117	5.2182819	9.5571678
C	5.5437877	9.1889012	1.6378058

C	7.2664347	7.8381569	0.6126222
H	8.2008371	6.4364151	1.9905605
H	8.5385901	3.8571196	8.4752598
H	4.7733715	9.9734883	1.5769179
C	6.2829533	8.8509903	0.4930850
H	7.8697848	7.5384020	-0.2543751
H	6.0985416	9.3630933	-0.4590205

Crystallographic and calculated ground-state structures

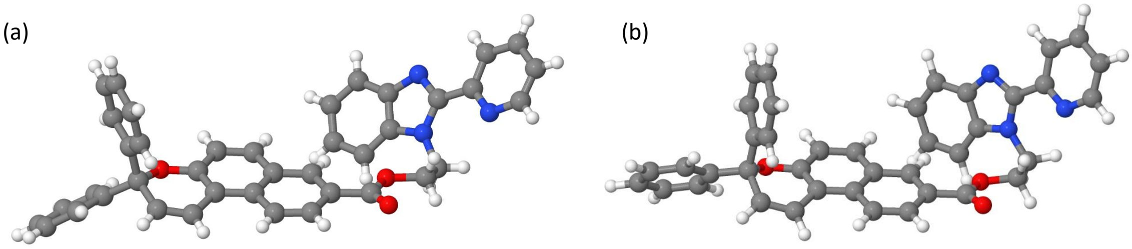

Fig. 6.9 (a) Crystallographic structure of the PPBI–DPNP dyad molecule from Ref. [1] (CCDC number: 870473). (b) Optimized molecular structure in the ground state at the MP2/def2-SVP level of theory.

6.6.3 Fluorescence data

Static fluorescence spectra and spectral overlap integral

Fluorescence quantum yields

The fluorescence quantum yields (Φ_{FL}) of free PPBI and the PPBI-DPNP dyad molecule were measured relative to 2-aminopyridine ($\Phi_{\mathrm{FL}} = 0.66$) resp. phenanthrene ($\Phi_{\mathrm{FL}} = 0.125$) as fluorescence standards. The characteristic parameters of the reference compounds are listed in Table 6.7. The standards were chosen because they absorb and emit in similar spectral regions as the samples. All pairs of measurements were made using the same instrument settings (slit widths, integration time, excitation wavelength, etc.).

From the measurements, the fluorescence quantum yields are given by

$$\Phi_{\mathrm{FL}} = \frac{I_{\mathrm{FL}}\, f_{\mathrm{ref}}\, n^2}{I_{\mathrm{FL,ref}}\, f\, n_{\mathrm{ref}}^2}\, \Phi_{\mathrm{FL,ref}}\,, \qquad (6.6.3.1)$$

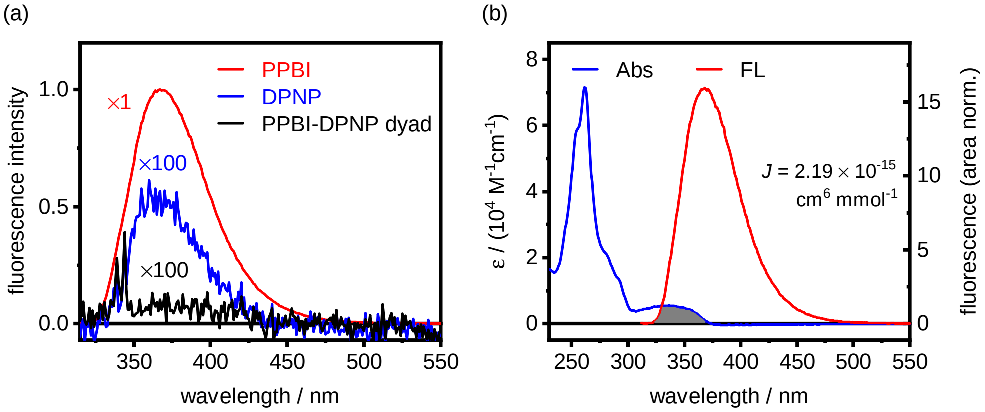

Fig. 6.10 (a) Static fluorescence spectra of PPBI (red), DPNP (blue) and the PPBI–DPNP dyad (black) measured under the same experimental conditions (apparatus settings and sample concentrations) in ACN upon excitation at λ_{exc} = 310 nm. The fluorescence intensities for DPNP and the dyad are shown with 100-fold magnifications. (b) Determination of the spectral overlap integral $J = 2.19 \times 10^{-15}$ cm^6 mmol^{-1} between the area-normalized fluorescence of PPBI (red) and the molar extinction coefficient of DPNP (blue).

Table 6.7 Properties of the employed fluorescence standards 2-aminopyridine and phenanthrene.

	emission	excitation	solvent	λ_{exc}	value	references
2-aminopyridine	315 – 480	285	H_2SO_4 (0.1 M)	280 – 315	0.66 ± 0.05	Ref. [3]
phenanthrene	345 – 410	260 – 335	EtOH	254, 313	0.125 ± 0.007	Ref. [4]

where the subscript “ref” denotes the fluorescence standard, $f = 1 - 10^{-A}$ is the absorption factor (with A = absorbance), I_{FL} is the spectrally integrated fluorescence intensity, and n denotes the refractive index of the respective solution. The obtained results are listed in Table 6.8.

Fluorescence lifetime of PPBI

The fluorescence lifetime τ_{D} of the free donor compound PPBI was measured by time-correlated single photon counting (TCSPC) using a PicoQuant FluoTime 200 instrument. The excitation pulses at λ_{exc} = 290 nm and 10 MHz repetition rate were delivered by a PLS 290-10 laser diode. The measured pulse duration was 840 ps (full width at half maximum, fwhm). The recorded fluorescence–time profiles (see Fig. 6.11 for an example) were modeled by a sum of two exponentials (cf. Table 6.9) convoluted with the instrument response function

Table 6.8 Results of the fluorescence quantum yield measurements.

	$A(\lambda_{\mathrm{exc}})$	I_{FL} / (10^5)	n	Φ_{FL}
2-aminopyridine	0.0348	81.0	1.334	0.660
PPBI	0.0405	50.7	1.344	0.360
phenanthrene	0.0181	37.2	1.362	0.125
PPBI–DPNP dyad	0.0450	3.5	1.344	0.005

(IRF). The measurements gave an amplitude-weighted lifetime of

$$\langle \tau_{\mathrm{D}} \rangle = 1.38 \pm 0.02 \text{ ns.}$$

Table 6.9 Fit parameters describing the measured fluorescence decay time profiles of PPBI.

parameter	value
α_1 / counts	146500
τ_1 / ns	1.37
α_2 / counts	368
τ_2 / ns	4.16
$\langle \tau_{\mathrm{D}} \rangle$ / ns	1.38

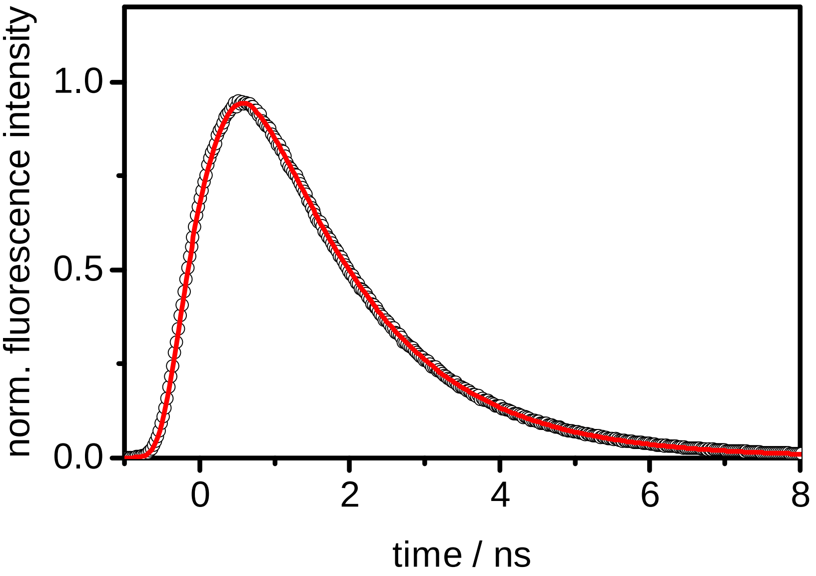

Fig. 6.11 TCSPC fluorescence–time profile of PPBI in ACN.

6.6.4 Femtosecond transient absorption results

Unscaled experimental spectro-temporal transient absorption maps

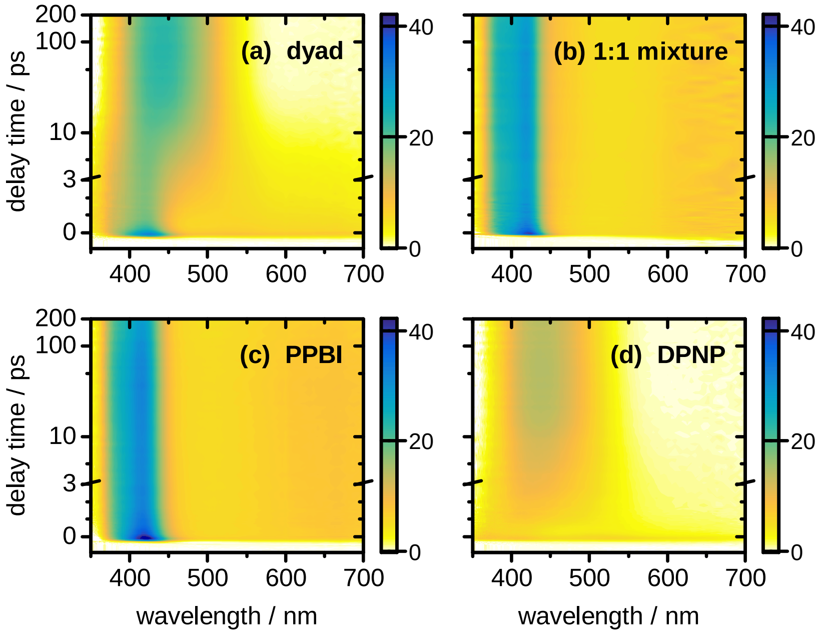

Fig. 6.12 Two-dimensional spectro-temporal transient absorption maps showing the change in optical density ΔOD for (a) the PPBI–DPNP dyad, (c) an equimolar mixture of PPBI and DPNP, (c) PPBI and (d) DPNP in ACN after photoexcitation at $\lambda_{\text{pump}} = 310$ nm for probe wavelengths between 350 and 700 nm and pump–probe delay times from –1 to 200 ps. The sample concentration are: 0.12 mM (OD = 0.31) for the dyad, 0.16 mM (OD = 0.38) for PPBI, 0.30 mM (OD = 0.11) for DPNP, and 0.15 mM each (OD = 0.39) for the 1:1 mixture.

SVD analysis of the transient absoption matrices for the dyad and its constituents PPBI and DPNP

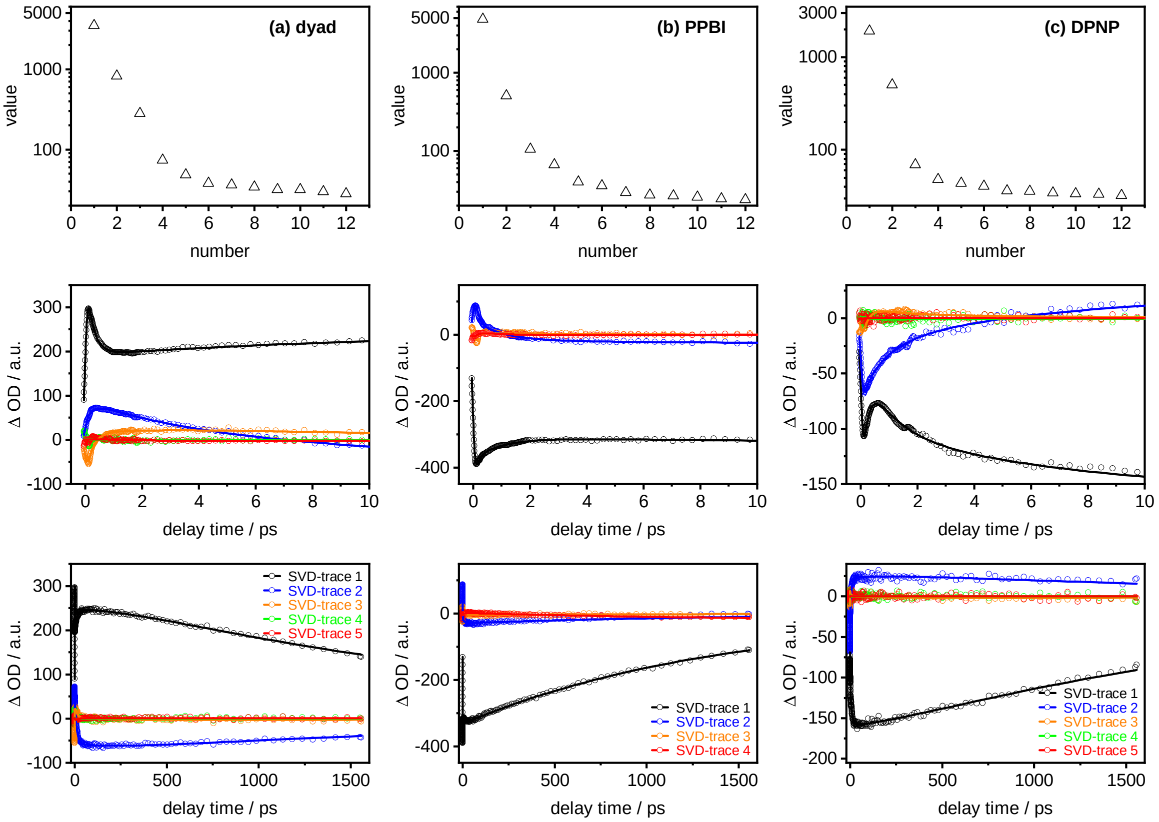

Fig. 6.13 Top row: Singular-value scree plots for (a) PPBI–DPNP, (b) PPBI and (c) DPNP resulting from the SVD analysis on a logarithmic scale. Middle and bottom rows: SVD time traces for the dyad and its constituents PPBI and DPNP described by simultaneous non-linear least-squares fitting using a sum of exponentials convoluted with the IRF.

Time traces for the dyad and its constituents PPBI and DPNP

Figure 6.14 shows a set of experimental and fitted time traces for the dyad and its constituents PPBI and DPNP following excitation at $\lambda_{\text{pump}} = 310$ nm after integration over the distinct ESA bands in the spectro-temporal absorption maps of Fig. 3. Simultaneous non-linear least-squares fits to the main ESA bands gave exactly the same time constants as the global SVD analysis. The data for PPBI indicate a delayed rise with a time constant of $\tau_3 = 12.4$ ps (orange, Fig. 6.14(b)) appearing at about $\Delta t \sim 30$ ps, which can be assigned to a minor (2% in amplitude) excited-state hydrogen bonding interaction of PPBI with residual water in the ACN.

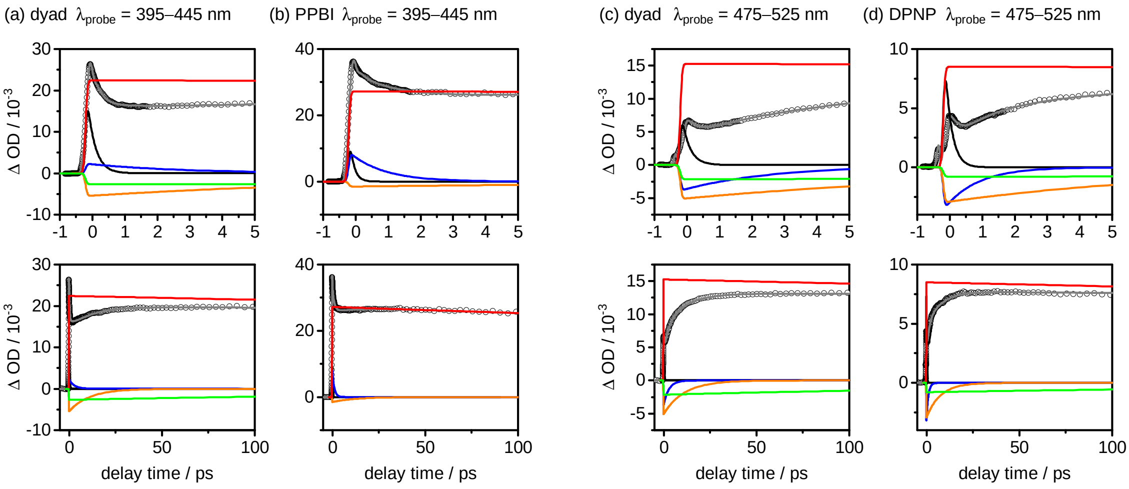

Fig. 6.14 Transient absorption time traces of PPBI–DPNP, PPBI and DPNP after excitation at $\lambda_{\text{pump}} = 310$ nm in the probe windows from 395 – 445 nm for (a) the dyad and (b) PPBI and from 475 – 525 nm for (c) the dyad and (d) DPNP.

Bibliography

[1] S. Wang, Y. Si, C. Tong, G. Wang, B. Qi, G. Yang, *Opt. Mater.* **2013**, *35*, 1504–1512.

[2] Q. Cao, D. S. Bailie, R. Fu, M. J. Muldoon, *Green Chem.* **2015**, *17*, 2750–2757.

[3] R. Rusakowicz, A. C. Testa, *J. Phys. Chem.* **1968**, *72*, 2680–2681.

[4] W. R. Dawson, M. W. Windsor, *J. Phys. Chem.* **1968**, *72*, 3251–3260.

Chapter 7

Summary and outlook

The goal of this thesis was to elucidate the photochemical properties and the ultrafast dynamics of particular classes of photoswitches under the influence of different environmental conditions. First, several azobenzene (AB) derivatives were investigated under different circumstances, which might influence or compete with the desired photoisomerization. In particular, the potential impacts, such as steric interactions, geometrical constraints, external forces, that may occur in typical functional systems where chromophores are embedded into polymer matrices. Second, the molecular dynamics of the sunscreen constituent—ferulic acid (FA)—have been revealed by a combination of femtosecond time-resolved spectroscopic techniques and DFT calculations. Third, the nature of excited states and possible deactivation mechanisms including electronic energy transfer (EET) of a molecular dyad composed of 1-propyl-2-(2′-pyridyl)-benzimidazole (PPBI) as energy donor linked to the photoswitch 3,3-diphenyl-[3*H*]-naphtho[2,1-b]pyran (DPNP) as energy acceptor have been investigated by static and time-resolved spectroscopies in combination with quantum chemical calculations.

7.1 Summary

Ultrafast photoisomerization of azobenzenes in a thin solid polymer film

The photo-induced switching of photochromic dyes in rigid polymer matrices forms the basis of many potential applications, but is often found to be impaired compared to the case in solution. We developed an experimental setup and data collection strategy combined with a background subtraction scheme for femtosecond time-resolved transient absorption spectroscopy on thin solid polymer film samples. This setup allows us to study the excited-state dynamics and *E/Z*-isomerisation of azobenzenes (DR1 and **1E** in Fig. 7.1) embedded into thin solid polymethylmethacrylate (PMMA) films with high chromophore load upon S_1 and/ or S_2 excitation. The photoswitching properties are compared to the observed dynamics of the molecules in solution as a reference.

A more detailed look into the photoisomerization and deactivation dynamics of DR1 doped in polymer films following photo-excitation at $\lambda_{\text{pump}} = 473$ nm was provided by a non-linear least-squares fitting analysis. The obtained time constants are shown in Table 7.1. DR1 in solution has been investigated previously in this workgroup by means of transient absorption and fluorescence up-conversion spectroscopy (*cf.* J. Bahrenburg, K. Röttger,

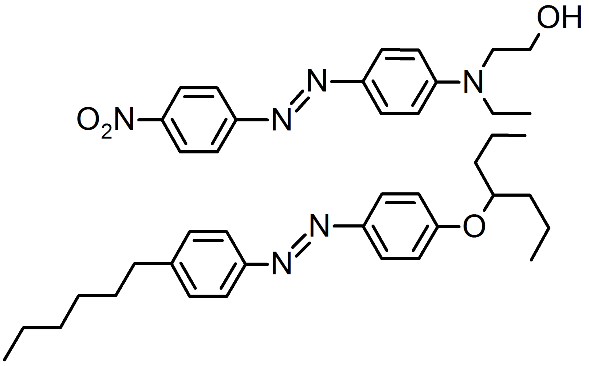

Fig. 7.1 Top: Chemical structure of Disperse Red 1 (4-[*N*-ethyl-*N*(2-hydroxyethyl)amino]-4′-nitro-azobenzene, DR1). Bottom: 4-hexyl-4′-(1-propylbutoxy) azobenzene (**1E**).

R. Siewertsen, F. Renth and F. Temps, *Photochem. Photobiol. Sci.,* **2012**, 11, 1210 – 1219). The femtosecond time-resolved transient absorption results of DR1 embedded into PMMA revealed that the excited-state dynamics characterized by time constants of $\tau_1 = 0.06$ and $\tau_2 = 1.0$ ps, is almost identical as in solution, but vibrational cooling in the ground state is moderately slowed down by a factor of 2 (time constant $\tau_3 = 14$ ps resp. $\tau_3 = 6$ ps in solution) due to the constraining polymer environment. The photoisomerization of **1Z** and **1E** embedded into thin polymer films was studied by static and femtosecond time-resolved transient absorption spectroscopy following to the $S_1\,(n\pi^*)$ and the $S_2\,(\pi\pi^*)$ state, respectively. The studies of **1E** and **1Z** embedded into PMMA films as well as those obtained in *n*-hexane solution, revealed molecular dynamics that are summarized in Table 7.2. For **1Z**, the excited-state dynamics, characterized by the time constants τ_1 and τ_2, are surprisingly similar in solution and in the polymer film, while the electronic ground-state process (τ_3) is slowed down by a factor of 2 in the polymer film. The excited-state relaxation pathways of **1Z** in both environments (PMMA and *n*-hexane) are unchanged, indicating that the *cis* → *trans* isomerization is less hindered in the PMMA matrix due to a barrierless isomerization pathway. The observed permanent absorption changes can be fitted almost perfectly with the corresponding static UV/VIS difference spectrum showing that the modified azobenzene

Table 7.1 Global time constants for DR1 embedded in PMMA films and in 2-fluorotoluene following $\pi\pi^*$ excitation at $\lambda_{\text{pump}} = 473$ nm.

medium	τ_1 / ps	τ_2 / ps	τ_3 / ps
2-fluorotoluene	0.08(3)	0.99(2)	6(0)
PMMA	0.06(1)	1.0(1)	14(1)

Table 7.2 Time constants from global fits to the spectro-temporal absorption data of **1Z** following S_1 ($n\pi^*$) excitation at $\lambda_{\text{pump}} = 460$ nm and **1E** following S_2 ($\pi\pi^*$) excitation $\lambda_{\text{pump}} = 330$ nm in *n*-hexane and PMMA with 2σ error limits given as error of the last significant figure in parentheses.

	medium	τ_0 [a] / ps	τ_1 / ps	τ_2 / ps	τ_3 / ps
1E, S_2 ($\pi\pi^*$)	*n*-hexane	0.09(1)	1.17(16)	3.84(12)	–
	PMMA	–	1.17(34)	23.4(61)	–
1Z, S_1 ($n\pi^*$)	*n*-hexane	–	0.20(1)	1.77(11)	12.3(20)
	PMMA	–	0.08(5)	1.29(36)	24.5(80)

[a] internal conversion from $S_2 \rightarrow S_1$

derivative with long terminals performs robust photoswitching behavior and undergoes *cis* → *trans* photoisomerization successfully in a PMMA matrix.

In contrast to the ground-state dynamics of **1Z** slowed down by a factor of ~ 2, a significant six-fold increase of the excited-state lifetimes ($\tau_2 = 23.4$ ps resp. $\tau_2 = 3.84$ ps) was observed for **1E**, whereas, the volume constraints in the polymer film do not affect the early excited-state dynamics decribed by τ_0 and τ_1 very much. The wavepacket needs to overcome a higher energy barrier to reach an intermediate excited state with τ_2 on the S_1 PES in comparison to the *n*-hexane solution.

Dynamics of UV-excited *trans*- and *cis*-ferulic acid in aqueous solutions

The photochemical properties of FA have been studied using combinations of theory and ultrafast time-resolved spectroscopy. While gas-phase investigation can reveal the ultrafast excited-state photophysics of FA, condensed-phase studies take us a step closer to the actual environment in which FA is prevailing in its application as a sunscreen consitituent.

The present comprehensive study of the photo-excited neutral, anionic and dianionic forms of *trans*- and *cis*-ferulic acid in aqueous solutions using femtosecond time-resolved emission and absorption spectroscopies and DFT calculations yielded detailed insight into the ensuing ultrafast processes promoting the deactivation. In all cases (Fig. 7.2), initial excitation with UV light populates the first $^1\pi\pi^*$ state followed by very similar *trans-cis* isomerism pathways. For the dianionic *cis*-isomer cFA^{2-}, the observed permanent absorption changes show unambiguously that the *trans*-isomer photo-product is formed. The electronic deactivation of cFA^{2-} happens with a time constant of 1.4 ps, making a barrierless excited-state pathway along a *cis* → *trans* isomerisation coordinate likely. In all other cases, excited-state deactivation happens more than ten times slower, on a time scale of ≈ 20 ps, (Table

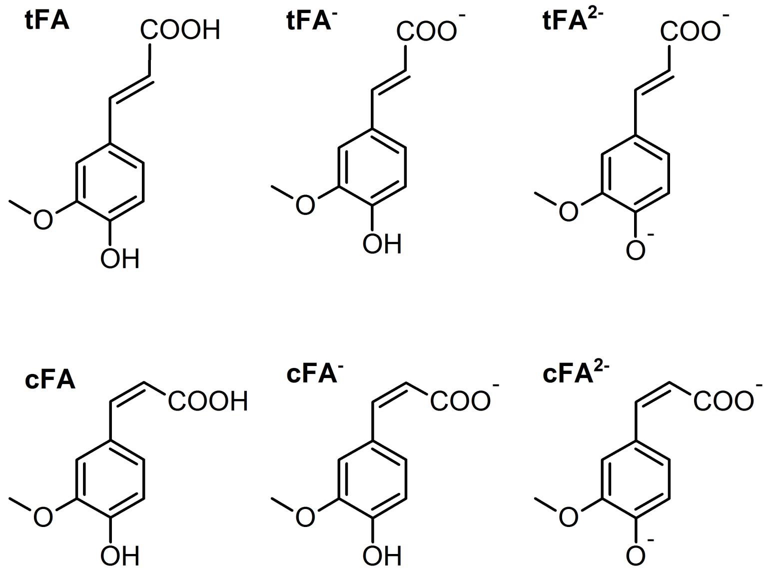

Fig. 7.2 Top row: Neutral, anionic and dianionic forms of *trans*-ferulic acid (3-methoxy-4-hydroxycinnamic acid) (tFA, tFA$^-$ and tFA^{2-}). Bottom row: Corresponding forms of *cis*-ferulic acid (cFA, cFA$^-$ and cFA^{2-}).

Table 7.3 Globally fitted time constants for the transient absorption (TA) SVD time traces of tFA, tFA$^-$ and tFA^{2-} with 2σ error limits given as error of the last significant figure in parentheses.

	τ_1 / ps	τ_2 / ps	τ_3 / ps	τ_4 / ps
tFA	0.16(1)	0.58(3)	4.0(1)	20(1)
tFA$^-$	0.12(1)	0.45(2)	11.5(9)	23(1)
tFA^{2-}	0.11(1)	0.57(2)	5.5(2)	25(1)
cFA	0.10(1)	0.49(6)	3.4(3)	17(2)
cFA$^-$	0.10(1)	0.26(5)	–	17(3)
cFA^{2-}	0.16(1)	–	–	1.4(1)

7.3) suggesting pathways with an excited-state energy barrier. More efforts to extend such measurements include using structure-sensitive methods such as time-resovlved vibrational spectroscopy, measurements in other solvent environments, or anisotropy measurements. Given the variety of relaxation pathways discussed in the literature for this class of molecules, it is clear that further high-level theoretical studies are neccessary.

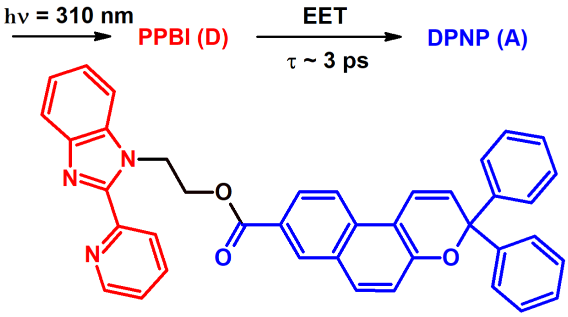

Fig. 7.3 Scheme of electronic energy transfer (EET) process from PPBI moiety to DPNP moiety in the PPBI–DPNP molecular dyad.

Electronic energy transfer in donor–acceptor systems

A donor–acceptor dyad composed of 1-propyl-2-(2′-pyridyl)-benzimidazole (PPBI) as energy donor linked to 3,3-diphenyl-[3*H*]-naphtho[2,1-b]pyran (DPNP) as energy acceptor, has been synthesized and systematically characterized by static and femtosecond time-resolved absorption spectroscopy in combination with quantum chemical calculations. UV/VIS absorption spectroscopy and computational studies revealed only a weak electronic interaction between the chromophores of the dyad in the ground-state. However, the electronic energy transfer (EET) from the PPBI*–DPNP donor-excited state to a PPBI–DPNP* acceptor-excited state of the dyad following the selective excitation of the PPBI donor moieties at $\lambda_{\text{pump}} = 310$ nm resulted in a fast decay and disappearance of the usually long-lived transient absorption features of the PPBI donor in the dyad compared to pure PPBI. The SVD-based global analysis of the measured transient absorption data of the dyad and its two building blocks as reference compounds allowed us to determine the EET process with a time constant of 2.84 ± 0.7 ps. Furthermore, transient absorption anisotropy study showed the switching of the transition dipole from donor to acceptor due to the EET in the dyad, with the time constant of $\tau_r' = 3.1 \pm 0.2$ ps, in excellent agreement with the SVD result. Last but not least, the Förster dipole–dipole resonance energy transfer model was adopted to explain the photo-induced EET event in the dyad, and yielded an EET rate of in the range 2.4×10^{11} s^{-1} $\leq k_{\text{DA}} \leq 8.2 \times 10^{11}$ s^{-1} ($4.2 \text{ ps} \geq \tau \geq 1.2$ ps), which nicely encloses the experimental result. The accordance strongly supports FRET as the decisive intramolecular electronic energy transfer mechanism in the PPBI–DPNP dyad system. Moreover, it not only strengthens our weak-coupling assumption between the donor and acceptor chromophores, but also indicates that the applied point dipole approximation is still a helpful approximation for modeling EET in molecular systems, where the distance between the donor and acceptor chromophores is comparable with their own sizes, but their dipoles are near-orthogonal.

7.2 Outlook

The results presented in this Thesis initiated a number of ongoing and future investigations regarding the ultrafast dynamics of molecular switches in complex environments in our group. As a general concept, photochromic transitions are slower in a polymer matrix in comparison to that in solution. This effect is broadly attributable to the limited free volume available for segmental motion of chromophores in a polymer matrix. The matrix environment imposes steric constraints by limiting the mobility of the molecules and therefore their ability to isomerize. A modified time-resolved transient absorption setup and data collection strategy, that allows for the investigation of solid film samples, has beeen developed and successfully performed on PMMA films doped with the azobenzene derivatives (DR1 and **1E (1Z)**) and the results were discussed in comparison with corresponding solution phase experiments. The variation of the dye content (from 10 – 60 wt.-%) embedded into polymer matrices will hopefully allow for the investigation of photoswitching behaviour influenced by the particular molecular environment (free volume) and specific multi-chromophore interactions. Polymer films doped with a series of AB derivatives should be measured to further shed light on the effect of mechanical forces on the photoswitching properties of different types of chromophores. The solvent, i.e., methyl isobutyrate with a similar chemical environment to poly(methyl methacrylate) (PMMA) will be employed in future work as reference, which allows for more reliable comparison. Further measurements of PMMA films doped with **1E (1Z)** and carbon nanotube nanoparticles are underway in cooperation with the group of F. Faupel.

The photoswitching behavior and the ultrafast dynamics of azobenzene derivatives, such as diazocines referred to as bridged azobenzenes (12*H*-dibenzo[*b*,*f*][1,4,5]oxadiazocine and 12*H*-dibenzo[*b*,*f*][1,4,5]thiadiazocine), which were designed and synthesized in collaboration with the group of R. Herges, will be investigated in complex environments by means of static and time-resolved spectroscopies. The dynamics of the bi-functional AB (4,4′-bis(pentamethyldisiloxane)azobenzene) covalently attached into the main chain of the polymer (poly(4,4′-azobenzene-alt-hexamethyl-trisiloxane)) which was designed and synthesized in collaboration with the group of A. Staubitz will be invertigated by time-resolved transient absorption spectroscopy. Due to the strong effects of mechanical forces, the electronic excited state lifetimes of AB covalently linked into the polymeric micronetworks will be expected to be much longer compared to those in solution and embedded into a polymer matrix. One aim of this project is to provide a fundamental understanding of design and development of functional photosensitive systems, which allow for exhibiting superior photophysical properties and improved performance even under strong mechanical forces.

Photochromic compounds behave the structural and electronic changes, accompanying the photo-induced and reversible transformations under irradiation with UV/VIS light. These properties can be engineered to control the emission of complementary fluorophores in fluorophore-chromophore dyads. Ideally, these molecules can be designed that the absorption spectrum of only one isomer of the photochromic compound overlaps with the emission of fluorophore moiety. Under these conditions, the emission of the fluorophore can be modulated by interconverting the photochromic moiety under optical control via intramolecular excitation energy transfer mechanism. Increasing the lifetime of the thermally unstable isomer ($>$ ms) or alternative photochromic compounds containing both thermally stable isomers (i.e., diarylethene) will satisfy the requirements for the time-resolved measurements of both isomers performed in a flow cell. The design and the syntheses of the photochromic fluorescence switches are already planned in our group. The unambiguous clarification of the EET process mechanism and the possible charge transfer will be possible with a two-dimensional electronic spectroscopy, which is currently under construction in our laboratory. The aim of this project is to address underlying energy transf ermechanisms and to provide some thoughts on directions for future developments in this area.

Acknowledgements

First of all, I would like to express my gratitude to Prof. Dr. F. Temps who gave me the opportunity to work on these challenging subjects. I would always remember the joy when, Oct. 4th 2012, I got the email of acceptance as a PhD student in AK Temps. It was such excited. I am so grateful to you for offering the opportunity. Doing the PhD in Temps' research group is an honor. The brilliant, inspiring and helpful discussions together with professor have given solid scientific foundation to every project.

Thank you very much Falk, your dedication to the consistent guidance and your commitment for my study life in general have been remarkable. I have grown a lot as a researcher under your help. Your valuable tips will be applied in many different aspects of my scientific research career. Thanks for your versatile help, engagement and patience throughout the entire duration of this five-year study.

I would like to thank Prof. Dr. B. Hartke for being my co-supervisor within the integrated research training group of the CRC677 and accepting to be referee for this work.

My sincere thank you to Ole, Megow, Schatz for your diligent proofreading of this thesis and the final proofreading contribution from Dennis, Pascal, Birthe is significant in my case. Megow, Hendrik, Mats, Rebecca and Lorenz, thanks for your contributions and the helpful discussions regarding the dyad chapter; Carsten and Tim, thanks for your contributions in the FA chapter.

My deep appreciation goes out to Katharina and Julia for welcoming me in fs-lab, for having carefully introduced and explained me how things work at the fs lab. Special thanks go to Anja, Uta, Mats, Dennis, Megow. Without your contributions, the support during the experiments, and the productive discussions this work would not have some very interesting aspects. My sincere thanks go to Dr. Joachim Gripp answering all chemical subjects. Without their help and advice it would not have been possible for me to accomplish these studies.

Thanks for the great time at many activities done together – soccer watching, playing and gambling. So pround of being one member of the "a little bit dangerous" team. I am indebted to Tanja who was always so helpful and provided me with her assistance throughout my studies. Thanks Monika, Mats, Hendrik and Xiaonan for being officemate! Because of your passion to learn new things, it was really satisfactory. your names will be always present in my personal Office of Fame. Thanks for your help, advices, and reassurances. We had a

wonderful and supportive working atmosphere in our office.

I would like to acknowledge all members of the involved working groups for sharing experiences and knowledge, for their readiness to help and for the friendly atmosphere. Becoming part of this group was a big privilege. These people have always kindly given me strength, courage and support; therefore I will reserve them my gratitude in more appropriate ways and circumstances.

Also a lot of thanks go to current and former group members: Jonas, Hendrik Rapp, Mayra, Thrun, Rebecca Marschan, Amke, Carsten, Sabine, Jessica, Elisabeth, Jana, and Tomoko for your help in daily life and resolving scientific problems. Thank you for the great time spent together.

I gratefully acknowledge the funding received towards my PhD from CSC and SFB.

Last but not least, I would like to express my deepest gratitude and love to my entire family for their understanding, their invaluable support and encouragement, and great patience with me throughout these challenging times. Linan, thank you. I am so fortunate to have you in my life.